



Mesures géodésiques et modélisation de la convergence oblique au travers de failles transformantes. Application au bord Nord du Plateau Tibétain et à la Californie du Sud

Simon Daout

► To cite this version:

Simon Daout. Mesures géodésiques et modélisation de la convergence oblique au travers de failles transformantes. Application au bord Nord du Plateau Tibétain et à la Californie du Sud. Sciences de la Terre. Université Grenoble Alpes, 2016. Français. NNT : 2016GREAU025 . tel-01560620

HAL Id: tel-01560620

<https://theses.hal.science/tel-01560620>

Submitted on 11 Jul 2017

HAL is a multi-disciplinary open access archive for the deposit and dissemination of scientific research documents, whether they are published or not. The documents may come from teaching and research institutions in France or abroad, or from public or private research centers.

L'archive ouverte pluridisciplinaire **HAL**, est destinée au dépôt et à la diffusion de documents scientifiques de niveau recherche, publiés ou non, émanant des établissements d'enseignement et de recherche français ou étrangers, des laboratoires publics ou privés.

THÈSE

Pour obtenir le grade de

DOCTEUR DE L'UNIVERSITÉ GRENOBLE ALPES

Spécialité : Géosciences

Arrêté ministériel : 7 Août 2006

Présentée par

Simon Daout

Thèse dirigée par **Marie-Pierre Doin**
et codirigée par **Cécile Lasserre et Anne Socquet**

préparée au sein de **l'Institut des Sciences de la Terre**
et de l'école doctorale **Terre Univers Environnement**

**Mesures géodésiques et modélisation
de la convergence oblique au travers
de failles transformantes.**

Application au bord Nord du Plateau Tibétain
et à la Californie du Sud.

Thèse soutenue publiquement le **21 Novembre 2016**,
devant le jury composé de :

Bénédicte Fruneau

Maître de Conférence, Université Paris Est Marne la Valée, Paris/France, Rapporteur

Ramon Hanssen

Professeur, Faculty of Civil Engineering and Geosciences, Delft/Pays-Bas, Rapporteur

Henriette Sudhaus

Investigateur Principal, Christian-Albrechts-University, Kiel/Allemagne, Examinateur

Yann Klinger

Directeur de recherche CNRS, IPG Paris/France, Examinateur

Marie-Pierre Doin

Chargée de Recherche CNRS à l'ISTerre, Université Grenoble-Alpes, Grenoble/France

Anne Socquet

Physicienne des Observatoires à ISTerre, Université Grenoble-Alpes, Grenoble/France

Cécile Lasserre

Chargée de Recherche CNRS à l'ISTerre, Université Grenoble-Alpes, Grenoble/France

Hervé Leloup

Directeur de recherche CNRS, LGTPE UCB, Lyon/France, Président



Remerciements

Je remercie tout d'abord l'ensemble du jury d'avoir accepté de juger ce travail, en premier lieu les deux rapporteurs Bénédicte Fruneau et Ramon Hanssen, mais aussi les examinateurs, Henriette Sudhaus, Yann Klinger et Hervé Leloup. J'adresse ensuite mes remerciements aux nombreuses personnes qui m'ont accompagné dans ma recherche ces dernières années. Tout d'abord, merci Marie-Pierre Doin de démontrer quotidiennement qu'il est possible d'être l'une des meilleures dans son domaine tout en restant des plus modestes. Je te suis reconnaissant pour ton encadrement : libre mais bien orienté. J'admire ta rigueur et tes capacités techniques dans les parties difficiles de ce travail. Merci aussi Cécile Lasserre pour tes qualités pédagogiques et tes idées. Merci de m'avoir pris en stage de Master, de m'avoir envoyé à ma première conférence à l'autre bout du monde, puis guidé jusqu'à aujourd'hui. Merci Anne Socquet pour ton énergie, ta présence et pour les discussions que tu inities. Je remercie ensuite Sylvain Barbot et Paul Tapponnier qui ont initié la première partie de ma thèse. Merci Sylvain pour ta présence, ton dynamisme et pour tout ce que tu m'as appris depuis mon premier séjour à Singapour jusqu'à aujourd'hui. Merci Paul de m'avoir partagé ta passion sur le Tibet. C'est avec grande satisfaction que j'apprécie la maturation et l'évolution de nos travaux aujourd'hui. Je remercie aussi sincèrement Gilles Peltzer qui a été un pilier de ma thèse et que j'ai sollicité tant pour le traitement interférométrique, que pour le permafrost, la modélisation, ou bien l'interprétation tectonique du Tibet et de la Californie. J'admire ton extraordinaire et unique capacité à faire le lien entre la tectonique, les observations géodésiques et les modèles numériques, et te remercie pour ton implication et ta précieuse aide. Merci Romain Jolivet pour tes cours d'interférométrie et de modélisation et ton efficacité. Ton manuscrit de thèse a toujours été à porté de main. Merci Matthieu Volat pour ta contribution dans la chaîne de traitement NSBAS, pour tes petits cours en programmation et ta présence au labo. De mon Master à aujourd'hui tu as complètement transformé la chaîne NSBAS et tu as fait un sacré joli travail. Merci Sandrine de nous mettre au petit soin si efficacement. Merci Erwan pour tes cours de QGIS et tes petites blagues qui font du bien. Il va de soi que d'autres personnes ont comptés d'une manière plus générale. Merci par exemple à Baptiste pour ces trois années ensemble au bureau et en montagne sans une seule minute de conflit. Merci aussi Shengyi pour ton soutien et tes cours d'illustrator et d'anglais. Puis je finirai assurément par une pensée vers mes parents qui m'ont toujours aidé, réconforté et orienté tout au long de mon parcours.

Résumé

La convergence oblique entre deux blocs tectoniques engendre la coexistence de failles décrochantes, chevauchantes et normales dans un même système. Bien que cette complexité soit observable en surface, son organisation géométrique et la manière dont elle accumule les déformations en profondeur sont mal connues. Ici, je me focalise sur trois grands systèmes de failles transformantes obliques au Tibet et en Californie du Sud, et ce, afin de mieux comprendre et quantifier les relations entre les différentes failles qui les définissent. L’interférométrie radar à Synthèse d’Ouverture (InSAR) dispose du potentiel pour cartographier et localiser précisément la déformation sur des zones étendues et ainsi contraindre la géométrie des structures profondes. Cependant son utilisation en milieu naturel se trouve fortement entravée par la décorrélation due à la végétation, au relief, et aux cycles de gel et dégel, mais aussi par les délais troposphériques et les rampes orbitales résiduelles. Différencier ces signaux parasites de la déformation tectonique est particulièrement difficile s’ils sont spatialement corrélés. J’ai développé des méthodes pour palier ces limitations. Au Tibet, j’ai ainsi traité les archives du satellite Envisat au niveau de deux zones de lacune sismique, à la bordure Nord du plateau, se présentant comme des zones intéressantes pour étudier le partitionnement de la convergence : le système de faille de Haiyuan au north-est Tibet et la faille sénestre de l’Altyn Tagh, au nord-ouest du plateau. Une attention spécifique sur les déformations liées au pergélisol m’a permis de (1) retrouver la continuité du signal sur de grandes zones, notamment au travers des basins sédimentaires, (2) de quantifier le comportement temporel des cycles de gel et dégel des sédiments recouvrant le pergélisol, (3) d’isoler les zones stables des sédiments se déformant. Je montre que les déformations saisonnières sont fortement dépendantes des unités géomorphologiques et que la quantité d’eau dans la couche active contrôle l’amplitude et le moment où la subsidence est maximale. J’analyse aussi le signal saisonnier au travers la marche topographique afin de définir un proxy pour les incertitudes de la correction atmosphérique, principale difficulté pour accéder à la déformation tectonique de l’Altyn Tagh. Une propagation des erreurs individuelles dans l’analyse de vitesse permet d’estimer la vitesse tectonique avec une meilleure confiance. J’observe un gradient de déformation au travers la faille de l’Altyn Tagh de l’ordre de 10-14 mm/an et un alignement clair de la déformation dans le Tarim, parallèle à la faille de l’Altyn Tagh, ainsi que des soulèvements de l’ordre de 1 mm/an associés à des chevauchements. Ces résultats suggèrent que la déformation transpressive, dans ce coin nord-ouest du plateau, est découplée en une composante décrochante et de raccourcissement, mergeant probablement en profondeur en une frontière lithosphérique unique. Ce travail montre aussi un gradient

de déformation associé à la terminaison ouest de la faille du Kunlun, redéfinissant ainsi la géométrie des blocs tectoniques dans cette région. Parallèlement à cette acquisition de données, je développe des outils d'inversion basés sur des algorithmes de Monte Carlo afin d'explorer l'ensemble des géométries en accord avec les observations et d'estimer la compatibilité de la déformation actuelle avec des modèles tectoniques long-termes. Je montre ainsi une convergence uniforme de 10 ± 1.5 mm/an et d'orientation $N89 \pm 8^\circ$ E à travers le système de faille d'Haiyuan et quantifie son partitionnement le long des différentes structures. Par ailleurs, j'applique mon approche en Californie du Sud, au niveau du « Big Bend » de la faille de San Andreas où, en analogie avec des modèles structuraux géologiques, j'utilise des lois de conservations du mouvement pour contraindre la géométrie des chevauchements aveugles. Je montre la compatibilité du champs de déformation actuel avec un décollement grande échelle partitionnant la déformation intersismique profonde et quantifie une accumulation de contrainte de 2.5 ± 1.0 mm/an le long de la structure majeure sous Los Angeles. L'objet de mes travaux souligne l'importance de la géométrie des failles pour les modèles géodésiques et vise à combler, quelque peu, le fossé qui existe entre les modèles de cycles sismiques et la géologie structurale.

Abstract

Oblique convergence between two tectonic blocks leads to slip partitioning with the coexistence of strike-slip, normal, and thrust motion in major fault system. While such complexity has been observed at the surface, the question is to understand how faults interact and accumulate strain at depth. Here, I focus on three major oblique transform faults in Tibet and in Southern California, in order to better measure and quantify the present-day strain accumulation on these fault systems. Interferometric synthetic Aperture Radar (InSAR) has the potential to map and localize precisely the deformation over wide areas and thus constrain the deep geometry of these structures. However, its application in natural environments is hindered by strong decorrelation of the radar phase due to vegetation, relief, and freeze and thaw cycles, but also due to variable tropospheric phase delays across topographic features and long-wavelength residual orbital ramps. Here, I develop methodologies to circumvent these limitations and separate tectonic from other parasitic signals. In Tibet, I process data from the Envisat satellite archives, at the boundary of the Tibetan plateau, over two seismic gaps, which appear interesting to study the partitioning of the convergence : the Haiyuan Fault system in northeastern Tibet and the left-lateral Altyn Tagh Fault, in northwestern Tibet. A specific focus on the permafrost related deformation signal allows us to : (1) correctly unwrap interferograms from north to south, in particular across sedimentary basins, (2) quantify the temporal behavior of the freeze/thaw cycles, and (3) isolate bedrock pixels that are not affected by the permafrost signal for further tectonic analysis. I show that the seasonal subsidence depends greatly on the geological land unit and that water/ice content in permafrost active layer controls amplitude and timing of maximum subsidence. I also analyze the atmospheric signal across the high plateau margin to define a proxy for the uncertainty on atmospheric corrections, which is the main challenge to access the Altyn Tagh Fault slip rate. The propagation of individual errors in the time series analysis allows to estimate tectonic velocities with higher reliability. I observe a strike-slip deformation of around 10-14 mm/yr across the Altyn Tagh fault, a clear line of concentrated strike-slip deformation of around 3 mm/yr within the Tarim basin, trending parallel to the Altyn Tagh Fault trace, as well as thrust signal uplifting terraces at a rate of 1 mm/yr. These findings suggest that the transpressive deformation along the northern edge of Tibet may be decoupled into transform and compressive deformation on deep-seated structures, which may merge at depth into a single lithospheric boundary. This work also shows a strain accumulation around the western extension of the south trace of the Kunlun Fault, redefining the block boundaries in northwestern Tibet. In parallel to this data acquisition,

I develop a Monte Carlo inversion tool in order to explore the various geometries in agreement with observations and estimate the compatibility of actual surface displacements with long-term slip partitioning models. I thus show a uniform convergence rate of 10 ± 1.5 mm/yr with a N $89 \pm 8^\circ$ E across the Haiyuan fault system and quantify the partitioning along the various structures. I also apply my approach to Southern California, across the « Big Bend » of the San Andreas Fault, where, in analogy with structural geological models, I use conservation of motion to help constraining the geometry and the kinematics of blind thrust faults. I show the compatibility of surface displacements with a large-scale décollement that partitions a more uniform deep-seated motion and quantify a loading rate of 2.5 ± 1.0 mm/yr along the major thrust structure developing under Los Angeles. This work underlines the importance of first order fault-geometry for geodetic models and represents of step forward towards bridging the gap between earthquake cycle modeling and structural geology.

Table des matières

| | |
|--|-----------|
| Introduction générale | 13 |
| 1 Principes généraux et contexte | 17 |
| 1.1 La géodésie | 18 |
| 1.1.1 L'interférométrie Radar à Synthèse d'ouverture (InSAR) | 18 |
| 1.1.1.1 Généralités | 18 |
| 1.1.1.2 Notions indispensables du traitement SAR | 20 |
| 1.1.1.3 La chaîne de traitement NSBAS | 22 |
| 1.1.2 Le GPS | 24 |
| 1.2 Réconcilier les modèles géodésiques avec les modèles tectoniques | 25 |
| 1.2.1 La phase intersismique du cycle sismique | 25 |
| 1.2.2 Modèles géodésiques et limitations | 26 |
| 1.2.3 Aspect rhéologique de la déformation | 28 |
| 1.2.4 De la géologie structurale aux modèles de cycle sismique | 31 |
| 1.2.5 Une approche Bayésienne d'exploration géométrique | 32 |
| 1.3 Contexte et état de l'art au Nord Tibet | 34 |
| 1.3.1 Contexte géodynamique | 34 |
| 1.3.2 Contexte tectonique | 39 |
| 1.3.3 État de l'art sur la déformation active | 40 |
| 1.3.4 Le système de failles de Haiyuan | 43 |
| 1.3.5 La faille de l'Altyn Tagh | 46 |
| 1.4 Contexte tectonique et état de l'art en Californie du Sud | 49 |
| 1.4.1 Contexte tectonique | 49 |
| 1.4.2 Etat de l'art sur la déformation active | 50 |
| 1.4.3 Le « Big Bend » | 52 |
| I Modèles géodésiques de partitionnement au Tibet et en Californie | 55 |
| 2 Modèles de partitionnement au travers de la faille d'Haiyuan | 57 |
| 2.1 Introduction | 59 |
| 2.2 GPS velocity field | 62 |
| 2.3 InSAR velocity field | 63 |

| | | |
|-----------|--|------------|
| 2.4 | 2D models | 64 |
| 2.4.1 | Model geometry | 66 |
| 2.4.2 | Free parameters | 66 |
| 2.4.3 | Inversion method | 67 |
| 2.4.4 | Inversion results | 68 |
| 2.5 | Discussion | 69 |
| 2.5.1 | InSAR and Bayesian methods | 69 |
| 2.5.2 | Lateral variations of the slip partitioning | 72 |
| 2.5.3 | Comparison with geological time scales | 75 |
| 2.5.4 | Influence of the M~8, 1920 Haiyuan and 1927 Gulang earthquakes | 76 |
| 2.6 | Conclusions | 77 |
| 2.7 | Supplementary Material | 78 |
| 3 | Modèles de partitionnement au travers le « Big Bend » | 93 |
| 3.1 | Introduction | 94 |
| 3.2 | Tectonic constraints | 96 |
| 3.3 | Deformation data | 97 |
| 3.4 | Description of the model | 97 |
| 3.5 | Slip partitioning constraints | 99 |
| 3.6 | Prior Assumptions | 100 |
| 3.7 | Inversion method | 100 |
| 3.8 | Posterior models | 102 |
| 3.9 | Discussion | 103 |
| 3.10 | Conclusion | 106 |
| 3.11 | Supplementary Material | 107 |
| II | Traitemet et Analyses InSAR au Nord-Ouest Tibet | 123 |
| 4 | Analyse atmosphérique au travers la faille de l'Altyn Tagh | 125 |
| 4.1 | Introduction | 126 |
| 4.2 | Data set and formation of wrapped interferograms | 129 |
| 4.3 | Atmospheric corrections before unwrapping | 130 |
| 4.4 | Time series of delays elevation ratios | 133 |
| 4.5 | Atmospheric delays analysis | 135 |
| 4.6 | Validation of the ERA-I derived uncertainties using empirical estimate | 137 |
| 4.7 | Conclusion | 139 |
| 5 | Mesure du permafrost du plateau Tibétain par InSAR | 145 |
| 5.1 | Introduction | 146 |
| 5.2 | Data processing | 148 |
| 5.3 | Results and Discussions | 149 |
| 5.3.1 | Amplitude of the seasonal ground movements | 149 |
| 5.3.2 | Months of subsidence peak | 150 |
| 5.3.3 | Multi-annual trend of ground subsidence | 155 |

| | |
|--|------------|
| 5.4 Conclusion | 156 |
| 5.5 Supplementary Materials | 157 |
| 6 Déformation intersismique au Nord-Ouest Tibet | 173 |
| 6.1 Introduction | 175 |
| 6.2 InSAR processing | 178 |
| 6.2.1 Tests on atmospheric corrections | 183 |
| 6.2.2 Tests on residual orbital ramps | 184 |
| 6.3 Analysis of the tectonic signal | 186 |
| 6.3.1 GPS data | 186 |
| 6.3.2 InSAR velocity field | 188 |
| 6.3.3 2D model | 196 |
| 6.4 Discussions and Conclusions | 201 |
| Conclusions et perspectives | 205 |
| Bibliographie | 209 |

Introduction générale

La communauté de chercheurs étudiant les failles actives de la Terre regroupe des domaines de compétences variées depuis le géomorphologue de terrain et tectonicien cartographiant et datant les décalages des failles en surface sur plusieurs milliers d'années, en passant par le géophysicien et le géodésien imageant et mesurant les glissements et déformations actuelles, sans oublier le géologue structural et le géodynamicien intégrant le rôle d'une faille dans l'évolution tectonique d'une région sur quelques millions d'années. Les diverses natures des observations provenant de ces différentes techniques et spécialités, ainsi que les incertitudes sur la nature de la déformation profonde rendent les interprétations ambiguës et stimulent la créativité des chercheurs. De nombreux modèles sont ainsi confrontés aux observations. Bien que les interprétations régionales sur quelques millions d'années soient loin de l'échelle d'observation en géodésie, la prise en compte de l'histoire d'une région, et des contraintes cinématiques, complémentent la vision limitée du comportement actuel des failles actives du globe et, de fait, l'estimation de leur potentiel sismique.

Depuis les premières mesures par GPS de la tectonique des plaques, les capacités d'observation par géodésie spatiale ont mis en évidence une diversité spatiale et temporelle des déplacements tectoniques de surface. La segmentation des ruptures, les glissements lents, et les déformations distribuées questionnent les représentations classiques du cycle sismique. Par exemple, les champs de déformation distribués observés aujourd'hui dans des zones connues pour leurs séismes historiques ou les biais entre les mesures tectoniques long-terme et les mesures court-terme géodésique, traduisent la vision restreinte de la déformation actuelle et les ambiguïtés d'interprétation. Les modèles considèrent bien souvent les failles comme un plan sans aucune liaison avec d'autres failles, bien loin de la vision des géologues structuraux. Toutefois, la géométrie des failles, leurs répartitions et leurs interactions, doivent désormais être prises en compte afin de mieux interpréter le champ de déformation actuelle observé. Comment s'enracinent les failles en profondeur ? Quels sont les paramètres qui guident leur propagation vers la surface et leur géométrie ? Les données géodésiques demeurent des éléments clés pour caractériser le fonctionnement sismique des failles actives car elles localisent et quantifient la déformation actuelle. Toutefois, les données GPS sont espacées et ne permettent pas de répondre à toutes les problématiques, en particuliers pour parvenir à bien identifier la location de la déformation au travers une faille ou d'une série de failles, et de bien identifier les interactions entre ces failles.

INTRODUCTION

L'InSAR, de ce fait, présente un potentiel majeur car elle apporte une cartographie en continu de la déformation au travers d'un ensemble de structures, avec une forte résolution spatiale et une grande sensibilité aux déformations verticales. L'étendue de ces observations permet de caractériser la complexité géométrique d'une faille (e.g. le basin en pull-part de Tianzhu de la faille d'Haiyuan (chapitre 2), le "Big-bend" de la faille de San Andreas (chapitre 3)), des zones d'inter-segments (en terminaison de ruptures sismiques ou de segment de creep ou fortement couplé) ou encore des zones de tectonique complexe situées à la terminaison de grandes failles (comme par exemple l'interaction entre la terminaison ouest de la faille du Kunlun et la faille de l'Atyn Tagh sur le plateau de Tibétain (chapitre 6)). Parvenir à cartographier des déformations à grande échelle présente aussi un enjeu pour la communauté en Science de la Terre afin de mieux contraindre la nature des déformations profondes produisant des déplacements grandes longueurs d'onde à la surface. La nouvelle génération de satellites SAR (ALOS-2 et Sentinel-1) permet maintenant d'acquérir un large flux de données sur de grandes fauchées d'une largeur de $\sim 400\ km$. Il s'agit donc aujourd'hui d'une opportunité unique pour couvrir aisément de grandes zones affectées par de la déformation. Cependant, cette méthode de mesure des déplacements de surface nécessite des développements méthodologiques et comporte elle aussi des limites dont la décorrélation temporelle (par exemple due aux cycles de pergélisol, à la végétation, à la neige), les délais atmosphériques, les résidus orbitaux et les difficultés de déroulement, limitant la continuité du signal. Bien que les méthodes InSAR multi-temporelles permettent de contrer certains de ces problèmes et aboutissent à une mesure de déformation plus fine, certaines limitations restent encore à résoudre pour étendre l'applicabilité de l'InSAR à la mesure de faibles déformations en milieu montagneux et sur des zones étendues. Jusqu'à présent peu d'études se sont attachés à l'extraction par InSAR du signal tectonique à grande échelle en raison des fortes ambiguïtés entre les rampes orbitales, les délais atmosphériques et la topographie corrélés à la déformation.

De part sa facilité d'accès, le domaine intracontinental reste le laboratoire privilégié des géodésiens. Pour ce travail de thèse, je me suis intéressé à des grands systèmes de failles transformantes obliques à la convergence locale produisant un fort partitionnement de la déformation en surface. Le terme "slip partitioning" s'utilise, en effet, pour décrire un mouvement oblique accommodé par la coexistence de failles décrochantes, chevauchantes et normales au sein d'un même système (Fitch, 1972). Bien que la complexité du déplacement et du champ de déformation soit observable sur le terrain ou par la géodésie, son organisation géométrique et les mécanismes de cette déformation en profondeur sont mal connus. Les modèles géologiques et tectoniques extrapolent des observations de surfaces en profondeur et, de fait, dans le passé. Les mesures géophysiques donnent de faibles résolutions en profondeur et se limitent à des gammes de fréquences spécifiques de l'appareil de mesure. La géodésie apporte quant à elle peu de contraintes sur la géométrie des structures et sur la nature de la déformation en profondeur. Pourtant de nombreuses questions restent à élucider afin de mieux comprendre le lien entre l'accumulation des contraintes en profondeur, leur relâchement en surface sous forme d'un séisme ou d'événements asismiques, tout au long du cycle sismique d'une faille active. Quelle est l'origine et quels sont les paramètres qui gouvernent la complexité de surface ? Est-elle le résultat

d'un cisaillement profond localisé se partitionnant vers la surface (Bowman *et al.*, 2003) ou la conséquence d'une déformation distribuée en profondeur (Bourne *et al.*, 1998)? Ainsi, est-il préférable de considérer toutes les structures indépendantes ou faut-il les associer au sein d'un même cycle d'accumulation et de relâchement de la déformation? La nature visqueuse ou ductile de la déformation profonde a fait l'objet de nombreux débats, notamment au Tibet, lesquels demeurent encore aujourd'hui en raison des faibles résolutions des données et modèles en profondeur et de la non-unicité des modèles après inversion des données de surface. Les modèles extrêmes distribuées ou de blocs de la tectonique des plaques se basent sur des observations géologiques ou géophysiques ne pouvant pas être négligées par la communauté de géologues structuraux ou de modélisateurs, et doivent être aujourd'hui intégrées dans un modèle unique afin de ne pas sous-estimer l'importance des déformations continues d'une zone ni sa capacité à produire un séisme. Dans cette perspective, les modèles géodésiques de cycle sismique ont aujourd'hui un large fossé à combler afin de se rapprocher au plus près des observations des géologues structuraux ou bien des modèles mécaniques de la déformation de la lithosphère.

Dans ce manuscrit, je m'intéresserai aux failles transformantes du plateau Tibétain et de la Californie du Sud, imposantes tant par leur morphologie, par la topographie régionale qu'elles délimitent que par leurs ruptures historiques. Je proposerai une approche pluridisciplinaire afin d'intégrer au mieux l'ensemble des observations dans des modèles cinématiques de déformation actuelle. Au Tibet (chapitre 2 - faille de Haiyuan - chapitre 6 - faille de l'Altyn Tagh -), les objectifs, tant méthodologiques que thématiques, seront de traiter de longues séries d'images (800 km de long, 8 ans d'observation) afin de capturer par Interférométrie Radar à Synthèse d'Ouverture (InSAR) la distribution spatiale des déformations. L'extraction de petits signaux dans des zones à très faible cohérence et à forte décorrélation nécessitera l'intégration des algorithmes les plus récents de l'interférométrie radar ainsi que le développement de méthodologies particulières pour des applications à la grande échelle. Je me focaliserai tout particulièrement sur (1) les signaux atmosphériques au travers de la bordure du plateau (chapitre 4) et (2) les cycles de gel et de dégel des sédiments recouvrant le pergélisol (chapitre 5). Une fois corrigés des signaux perturbateurs, de par sa précision, sa couverture spatiale et sa sensibilité aux mouvements verticaux, l'InSAR apportera des informations complémentaires au GPS bien adaptées aux problèmes d'exploration géométrique des structures en profondeur. Afin de tirer au maximum parti de ces données traitées, je développerai des outils d'inversion basés sur des algorithmes de Monte Carlo dans le but d'explorer la diversité des géométries des structures profondes en accord avec le signal observé, et ce afin d'évaluer la compatibilité de ce signal avec des modèles tectoniques long-terme. J'exploiterai aussi le réseau dense de données disponibles en Californie du Sud (chapitre 3) pour exporter mes outils au système de failles de San Andreas. Je me focaliserai sur le "Big Bend" où l'obliquité de la faille nourrit le développement de chevauchements aux alentours et sous la région de Los Angeles. Une analogie avec les failles tibétaines et l'introduction de contraintes cinématiques long-terme de conservation du mouvement dans mes modèles m'amènera enfin à proposer un modèle de déformation régionale en accord avec les observations de surface actuelles.

Chapitre 1

Principes généraux et contexte

Sommaire

| | | |
|------------|---|-----------|
| 1.1 | La géodésie | 18 |
| 1.1.1 | L'interférométrie Radar à Synthèse d'ouverture (InSAR) | 18 |
| 1.1.2 | Le GPS | 24 |
| 1.2 | Réconcilier les modèles géodésiques avec les modèles tectoniques | 25 |
| 1.2.1 | La phase intersismique du cycle sismique | 25 |
| 1.2.2 | Modèles géodésiques et limitations | 26 |
| 1.2.3 | Aspect rhéologique de la déformation | 28 |
| 1.2.4 | De la géologie structurale aux modèles de cycle sismique | 31 |
| 1.2.5 | Une approche Bayésienne d'exploration géométrique | 32 |
| 1.3 | Contexte et état de l'art au Nord Tibet | 34 |
| 1.3.1 | Contexte géodynamique | 34 |
| 1.3.2 | Contexte tectonique | 39 |
| 1.3.3 | État de l'art sur la déformation active | 40 |
| 1.3.4 | Le système de failles de Haiyuan | 43 |
| 1.3.5 | La faille de l'Altyn Tagh | 46 |
| 1.4 | Contexte tectonique et état de l'art en Californie du Sud | 49 |
| 1.4.1 | Contexte tectonique | 49 |
| 1.4.2 | Etat de l'art sur la déformation active | 50 |
| 1.4.3 | Le « Big Bend » | 52 |

1.1 La géodésie

La géodésie est la science qui mesure et représente la surface de la Terre. Elle introduit l'ellipsoïde de référence approximant au mieux la forme de la Terre (géoïde) et positionne tout point du globe par rapport à un repère, une projection en carte et des points de référence. Le GPS et l'InSAR sont deux techniques de mesures par satellite.

1.1.1 L'interférométrie Radar à Synthèse d'ouverture (InSAR)

1.1.1.1 Généralités

L'interférométrie Radar à Synthèse d'ouverture (InSAR) se définit comme une technique de géodésie spatiale à large couverture. Le signal émis par le satellite est rétro diffusé par le sol, puis enregistré par le satellite (Fig. 1.1). Les mesures traduisent des temps de trajet entre l'émission et le retour du signal. Ce temps de trajet dépend des paramètres d'acquisitions (orbites, altitude des satellites, longueur d'onde du signal, etc..), de l'altitude du point éclairé, de la composition atmosphérique et ionosphérique (pour les plus basses longueurs d'ondes) et de la déformation du sol le long de la ligne de visée du satellite (LOS). L'InSAR nécessite le passage répété d'un satellite sur une même zone. La différence entre les deux images acquises à deux périodes distinctes correspond à l'interférogramme qui contient, notamment, le signal de déplacement de la surface du sol entre ces deux périodes (Fig. 1.2). L'information est contenue dans la différence de phase des deux images radar acquises. L'amplitude du signal varie en fonction des caractéristiques du capteur (longueur d'antenne, longueur d'onde, angle d'incidence) et des propriétés de la surface éclairée (relief ou rugosité, présence d'eau ou de végétation). L'amplitude de l'image radar demeure insensible aux conditions atmosphériques en raison de la longueur d'onde du signal électromagnétique variant du centimètre à une cinquantaine de centimètre (5.6 cm pour le satellite Envisat dont j'ai traité les données). Son angle de visée (ou d'incidence) lui confère un pouvoir de détection des objets du sol dans la direction perpendiculaire à l'orbite (Fig. 1.1).

De par sa résolution, sa couverture et sa précision, cette technique offre de nombreuses possibilités dans des endroits reculés difficiles d'accès. Dans le cas d'une grande série d'acquisitions, l'InSAR retrace également l'évolution temporelle des déplacements. En effet, depuis le premier interferogramme mesurant les déplacements de surface liés au séisme de Landers, en Californie ([Massonnet et al., 1993](#)), de nombreux développements dans le traitement interférométrique ont permis l'amélioration du rapport signal sur

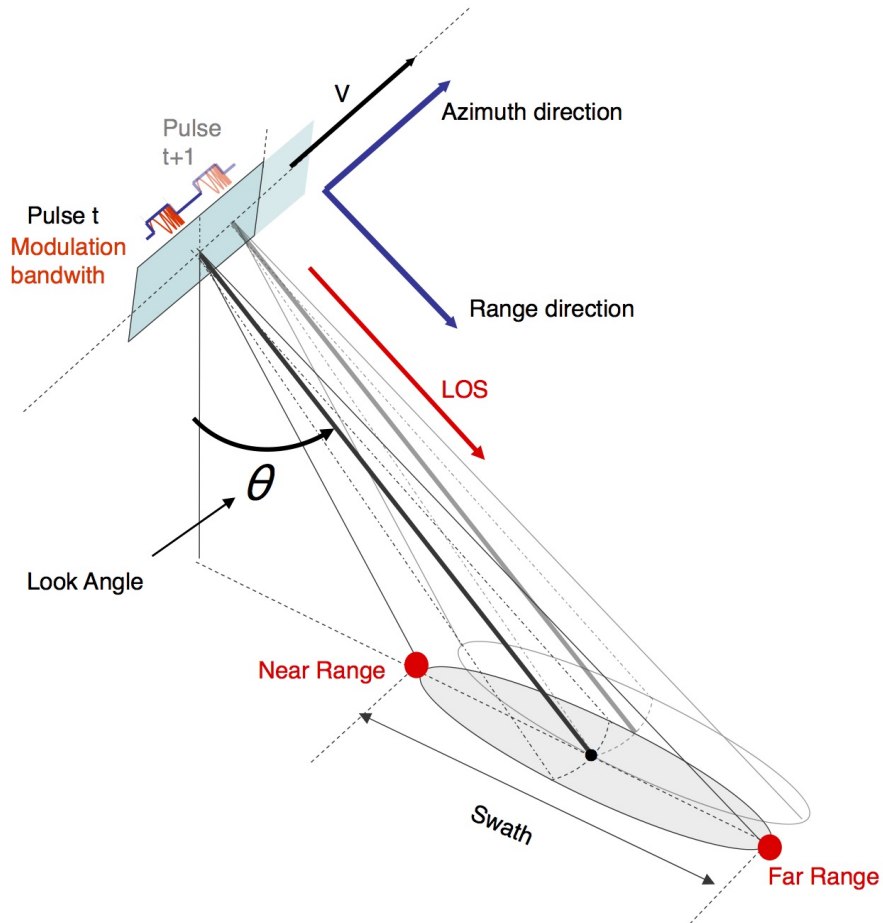


FIGURE 1.1 – Représentation schématique de l’acquisition radar. Au temps, t , une impulsion radar modulé en fréquence (« chirp ») est envoyé vers le sol dans la direction en portée (range) avec un angle d’incidence central θ . La cible au sol est éclairée à une fréquence doppler f_0 . Au temps $t+1$, le satellite s’est déplacé à une vitesse v dans la direction azimuthale et envoie une nouvelle impulsion. La cible est de nouveau éclairée mais à une fréquence plus faible f_1 . Les réponses impulsionales présentent ainsi une redondance d’information à fréquence Doppler variables exploitable pour augmenter la résolution en azimuth. (Modifié de, [Massonnet et Souyris, 2008](#)).

bruit, en passant notamment d’un signal de déplacement entre deux dates d’acquisition (l’interférogramme) à un signal retracant l’évolution spatio-temporelle des déplacements (la série temporelle). Le traitement par InSAR consiste en l’extraction de la plus petite et précise information possible (jusqu’au mm/an près) et de différencier le signal contenant la déformation du sol des autres signaux parasites, dont l’amplitude est très souvent supérieure, comme celle du signal atmosphérique ou orbital.

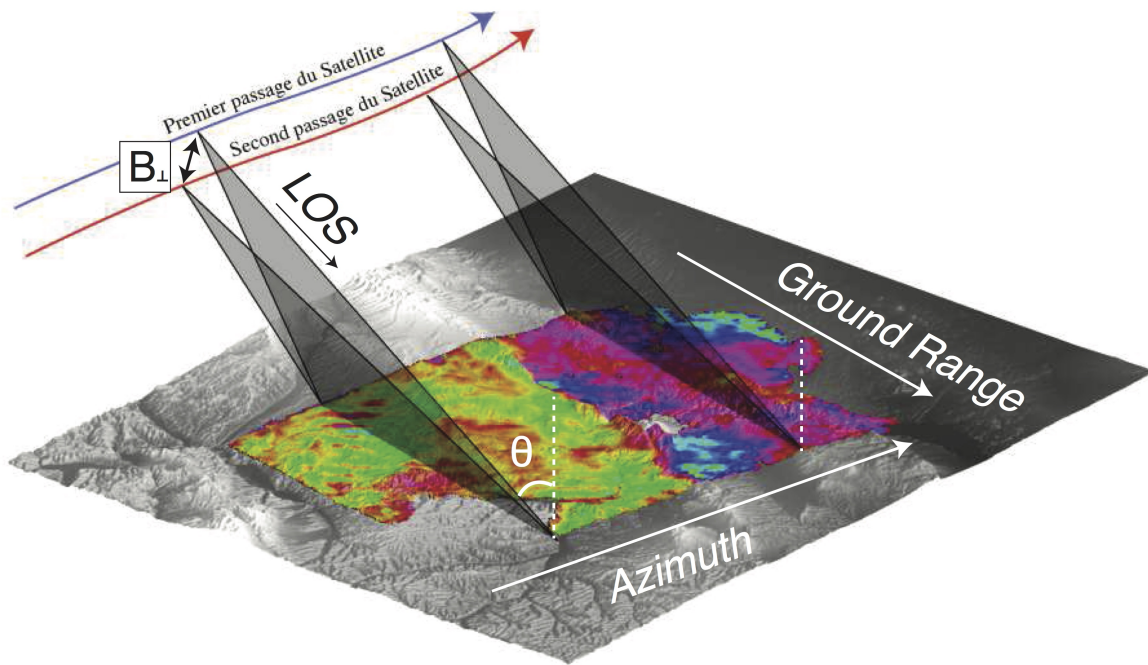


FIGURE 1.2 – Représentation schématique de l’InSAR. B_{\perp} : ligne de base perpendiculaire. θ : angle d’incidence en portée distale (far range). Tous points de l’interférogramme se positionnent par de deux axes (azimuth, range) en géométrie radar ou sur un modèle géométrique de terrain (Modifié de, [Jolivet, 2011](#)).

1.1.1.2 Notions indispensables du traitement SAR

La technologie SAR améliore significativement la résolution en portée des images (une vingtaine de mètres en distance pour le satellite Envisat par exemple) en envoyant une onde modulée de fréquence variable (« chirp ») (Fig. 1.1). En azimuth, à l'image d'une correction « Normal Move Out » en sismique réflexion, l'utilisation de la redondance d'information à fréquences Doppler variables réduit la résolution d'une moitié de la longueur d'antenne, soit 5 mètres pour le satellite Envisat (Fig. 1.1). L'amélioration de la résolution des images brutes (« Raw ») s'effectue lors de la première étape de traitement, dite de focalisation ([Zebker et Rosen, 1994](#)). L'image résultante, appelée une Single Look Complex (SLC), intègre une valeur de phase et d'amplitude pour chaque pixel.

Avant le calcul des interférogrammes, il est nécessaire de recaler toutes les images de manière à ce que tous les pixels correspondent au même objet (Fig. 1.3). Au cours de cette étape, dite de coregistration, les images sont décalées en portée et en azimuth (« offset ») afin de maximiser le produit de corrélation en amplitude. Après le calcul

du meilleur champ de décalage, toutes les images sont ré-échantillonnées et recalées. Les interférogrammes peuvent ensuite être générés.

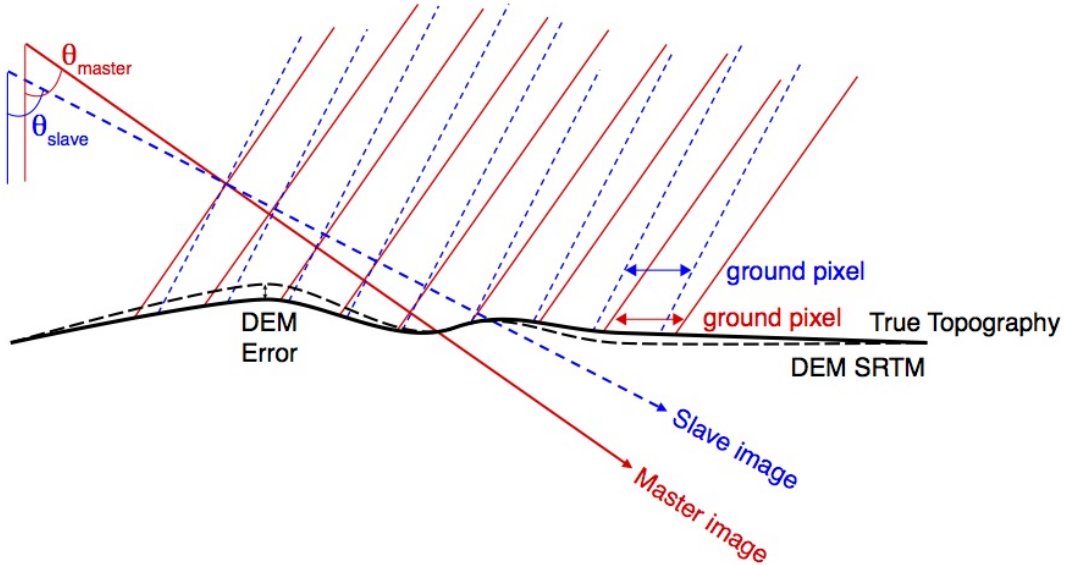


FIGURE 1.3 – Représentation schématique des distorsions géométriques introduites par les changements d’orbite du satellite entre une image appelée « master » et une image appelée « slave », ainsi que les distorsions introduites par la topographie. Une augmentation de l’angle d’incidence, diminue la taille d’un pixel au sol alors que la sensibilité à la pente topographique varie selon l’orientation de la pente par rapport à l’angle d’incidence. Afin de calculer l’interférogramme entre ces deux acquisitions, il faut rendre les deux images superposables en décalant et ré-échantillonnant les pixels tout en prenant en compte un modèle de topographie (e.g DEM SRTM) qui présentent lui aussi des erreurs (Modifié de, [Massonnet et Souyris, 2008](#)).

L’interférogramme est le produit de corrélation complexe de deux images SLCs, u_1 et u_2 , pour chaque pixel, tel que :

$$\rho(x, r) = \frac{u_1(x, r)u_2^*(x, r)}{\sqrt{|u_1(x, r)|^2|u_2(x, r)|^2}} \quad (1.1)$$

La phase du produit de corrélation est connue modulo 2π et doit être « déroulée » au cours du traitement. Le module du produit de corrélation contient la cohérence spatiale de l’interférogramme. Elle vaut 1 (resp., 0), lorsque la phase est constante (resp. aléatoire) entre les deux acquisitions. La perte de cohérence peut être liée au rapport signal sur bruit des images, à la décorrélation temporelle (changement des propriétés de rétrodiffusion des réflecteurs) et à la décorrélation géométrique (différences d’angles de vues). De la même manière la cohérence spatiale peut se calculer sur une petite fenêtre

PRINCIPES GÉNÉRAUX ET CONTEXTE

afin d'estimer la variabilité de la phase sur cette cellule (Ducret *et al.*, 2014).

Le traitement interférométrique requiert des observations cohérentes dans le temps (Hanssen, 2001). Cependant, dans un environnement dynamique (neige, glace, dunes), la cohérence sur une longue période de temps est rare, impliquant l'utilisation possible de quelques points uniquement. Deux grandes techniques conventionnelles diffèrent par leurs approches. La technique Persistent Scatterers (PS) identifie les pixels à fortes réponses impulsionales avant que les paramètres de déformation soient estimés (Ferretti *et al.*, 2000; Hooper *et al.*, 2004; Hooper, 2008). Cette technique est très efficace en zone urbaine et permet de repérer un réflecteur stable au milieu d'une zone incohérente. Elle est cependant moins utilisée en milieu naturel. A l'inverse la technique « Small Baseline Subset » (SBAS) (Berardino *et al.*, 2002) réduit la quantité de bruit due aux décorrélations géométriques, à l'atmosphère, à la topographie ou encore aux orbites, avant l'estimation de la déformation. Elle requiert la sélection d'un réseau de paires d'images ni trop espacées en temps, ni en géométrie d'acquisition afin d'optimiser la cohérence de l'interférogramme.

A la fin du traitement, l'évolution de la phase au cours du temps est retrouvée par analyse en série temporelle augmentant significativement le rapport signal sur bruit. Le signal séculaire se dérive à partir de cette évolution des déplacements dans le temps et correspond à la vitesse de déformation du sol. Dans la récente méthode d'inversion « Multiscale InSAR Time Series (MInTS) » (Hetland *et al.*, 2012), les auteurs proposent de décomposer chaque interférogramme par une série de coefficients d'ondelettes afin de prendre en compte la covariance spatiale du signal. Ils modélisent ensuite directement la phase interférométrique par une combinaison de nombreuses fonctions temporelles allant d'un terme linéaire à des fonctions splines. La paramétrisation du modèle est alors guidée par l'utilisateur en fonction du problème scientifique et ne permet pas, contrairement à l'analyse en série temporelle, de retrouver la phase reconstruite au cours du temps.

1.1.1.3 La chaîne de traitement NSBAS

Le traitement et les développements méthodologiques ont été réalisés pour cette étude avec la chaîne « New Small Baseline Subset » (NSBAS) (Doin *et al.*, 2011), développé au laboratoire ISTerre principalement par Marie-Pierre Doin et Cécile Lasserre. La chaîne incorpore de nombreuses améliorations assurant une meilleure cohérence et un meilleur rapport signal sur bruit en zones montagneuses et/ou à fort couvert végétal (Cavalié *et al.*, 2007; López-Quiroz *et al.*, 2009). Elle s'appuie sur le logiciel « Repeat Orbit Inter-

ferometry PACkage » (ROI_PAC) développé par le Jet Propulsion Laboratory/Caltech en Californie ([Rosen et al., 2004](#)). Elle a démontré ses performances dans de nombreuses zones en permettant de mesurer pour la première fois par InSAR le couplage intersismique à travers la chaîne Himalayenne ([Grandin et al., 2012](#)) ou les glissements lents à travers la faille de Haiyuan ([Jolivet et al., 2012, 2013](#)).

Les caractéristiques de l'étape de coregistration incluent, d'abord, (1) une simulation de la distortion et donc de la phase liée à la topographie avant la génération des interférogrammes et (2) l'estimation d'une translation en range, qui s'ajoute à la simulation de la topographie, et l'estimation d'une surface de distortion quadratique en azimut. Toutes les SLCs sont projetées, ré-échantillonnées et corrigées des effets topographiques dans la géométrie d'acquisition d'une image maîtresse choisie avec une ligne de base temporelle et perpendiculaire médiane par rapport à l'ensemble des images. Ensuite, un filtrage adaptatif en range est implémenté avant le calcul des interférogrammes ([Guillaso et al., 2006, 2008](#)), augmentant significativement la cohérence des interférogrammes à grandes lignes de base perpendiculaires. La chaîne NSBAS autorise ainsi un réseau d'interférogrammes formé avec des lignes de base critiques plus grandes qu'une approche SBAS classique.

Le traitement comporte ensuite une cascade de corrections sur la phase enroulée visant à diminuer sa variabilité (i.e d'augmenter sa cohérence) et le risque d'erreur lors de la phase critique de déroulement :

- correction des erreurs locales de topographie ([Ducret et al., 2014](#)),
- correction des délais atmosphériques ([Cavalié et al., 2008; Jolivet et al., 2011; Doin et al., 2015](#)),
- filtrage de la phase ([Grandin et al., 2012; Doin et al., 2015](#)).

Il est aussi possible d'extraire, par analyse en composantes principales d'une série d'interférogramme bien déroulés, la forme typique de la déformation et le comportement temporel associé. Cette forme ou « template » peut aider à l'analyse et au déroulement (chapitre 5).

Les interférogrammes peuvent ensuite être déroulés en suivant un chemin de déroulement allant des zones les plus au moins cohérentes (8), évitant ainsi de se propager dans des zones incohérentes, telles que les zones montagneuses ou les zones de dunes ([Grandin et al., 2012; Doin et al., 2015](#)).

A la fin du traitement, l'analyse en série temporelle permet de retracer l'évolution temporelle des déplacements avec ([Cavalié et al., 2008; Jolivet et al., 2012](#)) ou sans

PRINCIPES GÉNÉRAUX ET CONTEXTE

contrainte de lissage ([López-Quiroz et al., 2009](#); [Doin et al., 2015](#)). Cette étape est cruciale, car elle vérifie la consistance du signal sur chaque interférogramme et détecte les erreurs de déroulement ([López-Quiroz et al., 2009](#); [Doin et al., 2011](#)). Les cartes de séries temporelles obtenues donnent la possibilité de séparer par itérations les termes spatiaux, comme les rampes résiduelles ou les termes proportionnels à la topographie, des termes temporels, comme le terme linéaire, le terme saisonnier, et le terme proportionnel à la ligne de base perpendiculaire (chapitre 5).

1.1.2 Le GPS

Le système GNSS (Global Navigation Satellite System) est un dispositif de positionnement par satellite localisant tout point du globe par l'intermédiaire d'un récepteur. Il est abusivement appelé GPS (Global Positionning System), du nom des premiers systèmes développés par les Etats-Unis. Aujourd'hui, la constellation de satellite européenne, Galileo, dispose de 12 satellites fonctionnels sur une orbite polaire située à 23,222 km de la Terre. Le signal GPS spécifique à chaque satellite (PRN pour Pseudo Random Noise), est porté par des ondes électromagnétiques et est accompagné d'autres signaux, tels que le temps à l'émission ou le signal de navigation du satellite. Les distances satellites-récepteurs donnent des mesures de temps de trajet du signal par corrélation du signal PRN reçu avec une réplique interne au récepteur. Elles traduisent aussi des conversions de phase de l'onde porteuse, à l'identique de l'InSAR que nous étudierons par la suite. La position du récepteur sur l'ellipsoïde de référence se fait par trilateration en combinant l'information d'au moins quatre satellites. Une mesure en distance (avec le code PRN) est moins précise ($\sim 3 \text{ m}$) qu'une mesure en phase ($\sim 2 \text{ mm}$) mais ne présente pas les désavantages de l'InSAR liés à l'ambiguïté de 2π de la phase. Bien que les étapes de traitement soient quelque peu similaires à l'InSAR, je n'ai réalisé aucun traitement GPS au cours de ce travail. J'utiliserai des données publiées soit de campagne, constituées de la mesure répétée d'un point fixe au sol à différentes périodes, soit permanentes, enregistrant en continu le positionnement de la station. Ces mesures seront corrigées des signaux parasites, référencées dans le système de référence ITRF (International Terrestrial Reference Frame) du globe et je présenterai leurs incertitudes et leurs erreurs liées à leurs modes d'acquisition et à leurs traitements.

1.2 Réconcilier les modèles géodésiques avec les modèles tectoniques

1.2.1 La phase intersismique du cycle sismique

Le cycle sismique d'une faille se divise classiquement en 3 périodes. La période intersismique sépare deux ruptures de la faille. Celle-ci se trouve alors bloquée en surface et glisse en profondeur (Fig. 1.4a). Ainsi, elle emmagasine de manière élastique une quantité de contrainte correspondant au mouvement sur cette période de temps entre les deux blocs qu'elle délimite. Durant la période cosismique (Fig. 1.4b), la partie précédemment bloquée rompt et relâche l'énergie élastique accumulée sous forme d'un séisme. Enfin durant la phase post-sismique, certaines zones du plan de faille continuent à glisser (afterslip) ou bien rééquilibrent localement les pressions de fluides (effets poro-elastiques), alors que la partie inférieure et ductile de la croûte se relâche de manière visqueuse (relaxation visco-élastique). Finalement, la faille retourne à l'état bloqué en surface et démarre un nouveau cycle. La phase intersismique, qui est l'objet de mon étude, est la phase la plus longue. Contrairement aux phases co- et post-sismiques, elle reste la plus difficile à mesurer du fait des faibles taux de déformations qui la caractérisent (du mm au cm par an). De plus, la géodésie (GPS et InSAR) révèle l'existence de glissements lents transitoires durant la phase intersismique (zone de creep ([Jolivet et al., 2012](#); [Rousset et al., 2016](#)), séismes lents ([Miller et al., 2002](#); [Ito et al., 2007](#); [Ide et al., 2007](#)) dans la zone sismogénique ou de transition, accompagnées de trémors (non-volcaniques), compliquant ainsi grandement le modèle classique de cycle sismique.

La géométrie des failles demeure un paramètre clef contrôlant l'initiation, la propagation et l'arrêt d'un événement sismique. Par exemple, la nucléation et la terminaison des séismes s'observent souvent près de terminaisons géométriques le long des failles (change-
ment d'azimut majeurs, sauts en extension ou en compression, branchement d'une faille secondaire) ([King et Nabelek, 1985](#); [Wesnousky, 2006](#)). La distribution du glissement cosismique se trouve également influencée par la segmentation ([Lasserre et al., 2005](#); [Manighetti et al., 2005](#)), avec des inter-segments associés avec des minimums locaux de glissements. Ces irrégularités se compensent dans les autres phases du cycle sismique (post et inter sismique) sous forme de déformation volumique ou bien de glissement lent. L'étude de la phase inter-sismique, de sa complexité géométrique et des effets transitoires apporte des informations indispensables à notre compréhension de la phase cosismique.

PRINCIPES GÉNÉRAUX ET CONTEXTE

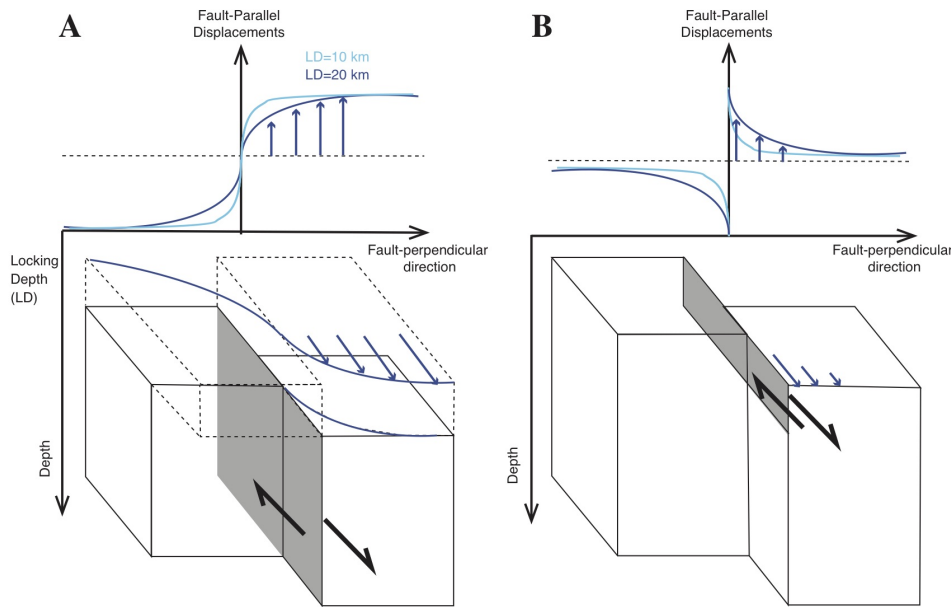


FIGURE 1.4 – Représentation schématique des 2 phases de déplacement d'une faille décrochante dextre verticale et de ses déplacements purement parallèles à la faille en surface prédit par le modèle de dislocation élastique (Segall, 2010). A : phase intersismique. B : phase coseismique.

1.2.2 Modèles géodésiques et limitations

L'accès aux champs de déformations intersismiques autour d'une faille permet de quantifier les taux d'accumulation des contraintes et à terme d'estimer l'énergie potentielle pouvant être relâchée durant le prochain séisme. La formulation d'[Okada \(1985\)](#) relie le glissement d'un segment de faille à sa déformation en surface (Fig. 1.4, 1.5). Un processus d'inversion permet de retrouver les taux de glissement ou la géométrie du plan à partir des observations de surface. Cependant, de nombreuses études se limitent à inverser le glissement de la dislocation élastique, car ce dernier est relié linéairement aux déplacements de surface. A l'inverse, l'accès aux caractéristiques géométriques des dislocations nécessite des explorations non linéaires. Aussi, les études prennent rarement en compte les interactions entre les différents types de failles et la géométrie 3D complexe des systèmes de failles. Pour une faille décrochante par exemple, elle reste souvent considérée comme verticale, sans aucune liaison avec d'autres failles. Par conséquent, ces modèles géodésiques diffèrent grandement de la vision des géologues structuraux cartographiant une région par de multiples plans de glissement à géométries variables.

La distribution spatiale des déplacements de surface dépend de la géométrie du plan

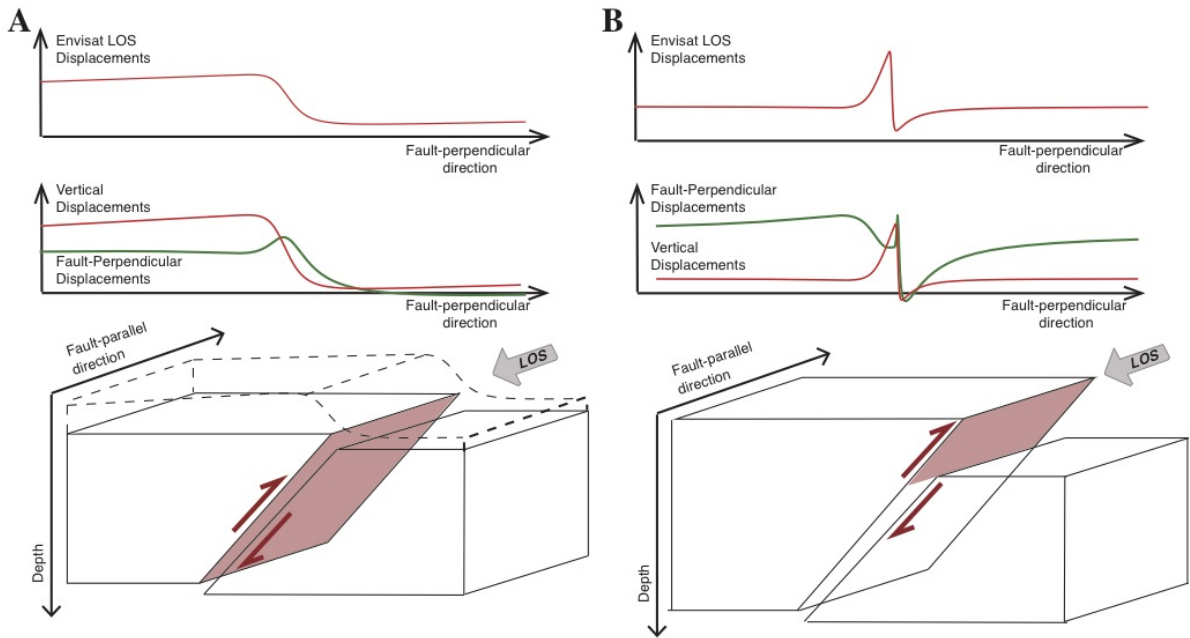


FIGURE 1.5 – Représentation schématique des deux phases de déplacement d'une faille chevauchante de pendage 60° et de ses déplacements perpendiculaires à la faille et verticaux en surface prédits par le modèle de dislocation élastique (Segall, 2010). Représentation également des mouvements observés dans la ligne de visée du satellite Envisat pour une faille d'azimut parallèle à l'orbite du satellite. A : phase intersismique. B : phase cosismique.

de faille ou du système de failles. Par exemple, le gradient des déplacements de surface constraint la profondeur des dislocations (Fig. 1.4). Les mouvements verticaux dépendent des taux de raccourcissement des structures inclinées (Fig. 1.5). De par sa résolution spatiale, sa couverture et sa sensibilité aux déplacements verticaux, l'*InSAR* mesure les faibles longueurs d'onde des déformations de surface et constraint ainsi de façon complémentaire au GPS la géométrie des failles (e.g., Fruneau *et al.*, 2001; Sun *et al.*, 2011; Simons *et al.*, 2002; Sudhaus et Jónsson, 2011). Le GPS est quant à lui plus sensible aux grandes longueurs d'onde des mouvements horizontaux. Cependant, la géodésie apporte des contraintes limitées sur la géométrie des failles comme l'illustre l'équivalence des distributions de déplacements de surface due à une même faille décrochante à pendages variables (Segall, 2010). L'angle unique de visée de l'*InSAR* conjugué au glissement de plusieurs plans de failles augmente les ambiguïtés entre les différents paramètres géométriques définissant les plans de glissement. Par exemple, de part sa plus grande sensibilité aux déplacements verticaux qu'horizontaux, l'addition d'un signal chevauchant à un signal décrochant transfère le gradient de déformation à l'avant du chevauchement

PRINCIPES GÉNÉRAUX ET CONTEXTE

(Fig. 1.6).

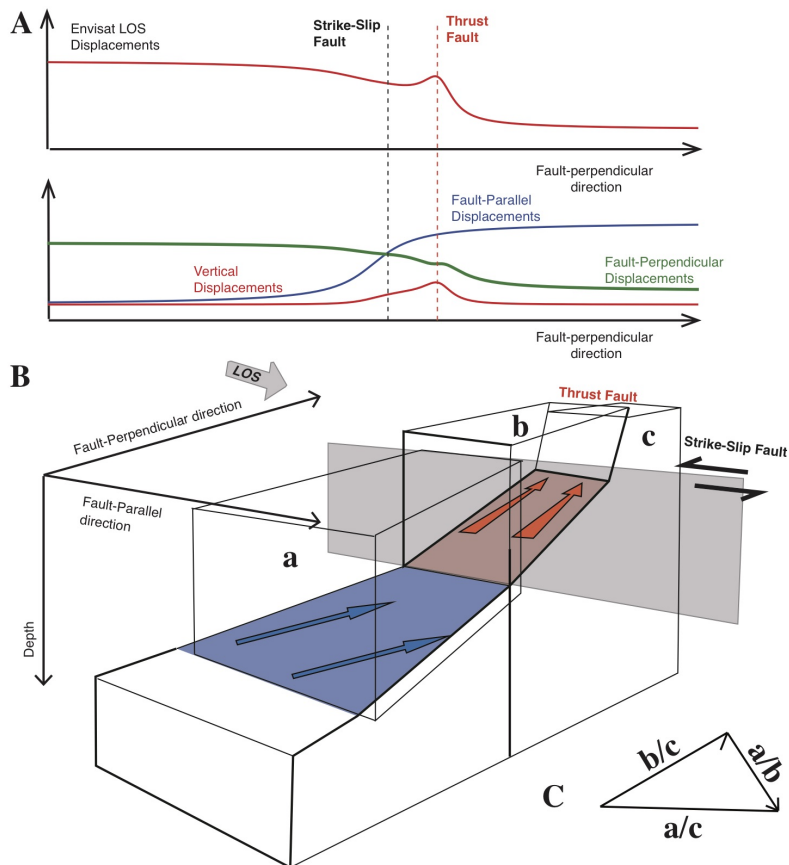


FIGURE 1.6 – Représentation schématique d'un modèle cinématique de bifurcation (Armijo *et al.*, 1986; Leloup *et al.*, 1988), composé d'une faille décrochante sénestre et d'une faille chevauchante (B) et ses déplacements de surface (A). La faille profonde glisse et accommode un mouvement composite décrochant et longitudinal alors que le chevauchement a un mouvement purement longitudinal. Les parties peu profondes des deux failles sont bloquées. C : Vecteurs glissement relatifs horizontaux entre les trois blocs a, b et c.

1.2.3 Aspect rhéologique de la déformation

Une roche se déforme lorsqu'elle subit une force orientée (compression, traction, cisaillement, torsion). Le type de déformation dépend tout d'abord de la nature compétente (e.g grès, granite) ou à l'inverse incomptente (e.g argile) de la roche. La température, la pression, l'apport de fluide et la durée de la déformation oriente ensuite la roche à se déformer de manière continue (plis, fluage, schistosité, etc..) ou d'une manière discontinue (failles, joints stylolithiques, fentes de tension et d'extension, etc ..). Les

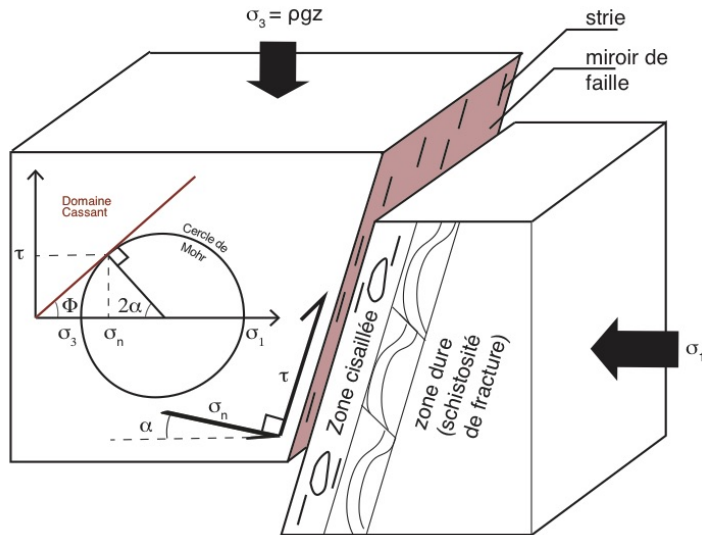


FIGURE 1.7 – Représentation schématique d'un bloc cisaillé par une une contrainte principale, σ_1 , horizontale et une contrainte secondaire, σ_2 , verticale égale à la force lithostatique. Représentation du cercle de Mohr associé aux contraintes. Pour un coefficient de friction non nul le plan de cisaillement se développe obliquement à la contrainte principale alors que pour un coefficient de friction nul le plan de cisaillement est horizontal.

mesures de terrain informent sur la direction et les taux d'allongement et de raccourcissement maximaux et donc l'orientation des contraintes permettant retracer l'histoire d'une région (e.g., [Leloup et al., 1988](#)). En milieu anisotrope, une contrainte cisaillante (τ) se développe (avec ou sans fracture) perpendiculairement à la contrainte normale (σ_n) (Fig. 1.7). τ et σ_n sont reliés par le coefficient de friction interne du matériau, ϕ , tel que : $\tau = \sigma_n \tan \phi$. Le pendage du plan de cisaillement va alors dépendre de ce coefficient de friction : plus la friction sera faible, plus le plan de cisaillement se développera à 45° de la contrainte principale, σ_1 . Si l'angle de friction augmente cet angle diminue jusqu'à ce que les (futures) failles soient subparallèles à σ_1 . Dans ce dernier cas on parlera plus de fentes que de failles.

La formation d'un décollement ou alors d'une faille listrique (faille normale à très faible pendage) nécessite de faibles frictions ou la présence d'une couche ductile à la base (gypse, argile ou roche riche en micas). Dans ce cas à frontières libres, les contraintes ne respectent plus le cercle de Mohr. Pour certaines failles décrochantes, telle que la faille de San Andreas, l'absence de contraintes tangentielles due à des phénomènes de shear heating ([Lachenbruch et Sass, 1980; Leloup et al., 1999](#)), pousse le plan de rupture à se développer perpendiculairement à l'une des contraintes principales ([Mount et Suppe,](#)

PRINCIPES GÉNÉRAUX ET CONTEXTE

1987).

En laboratoire, l'évolution des contraintes déviatoriques ($\sigma_1 - \sigma_3$) en fonction de la profondeur (pression, température) permet de retracer le profil de résistance des minéraux (et par extrapolation des couches lithosphériques). Le point d'intersection entre la droite de Byerlee (limite de rupture en déformation fragile) et la courbe de déformation ductile indique la profondeur du passage fragile-ductile et ainsi des niveaux de décollement théoriques (Fig. 1.8). En domaine continental, le Moho situé entre la croûte inférieure ductile et le manteau supérieur rigide (du fait de sa composition majoritaire en Olivine), se présente comme un bon niveau de décollement, chevauchant de grandes unités géologiques en régime de compression et formant la topographie du monde (e.g. Alpes, Andes, Tibet). A l'inverse, en domaine océanique, comme l'illustre l'absence des chaînes de montagne dans les océans et comme le prédisent les expériences de laboratoire, la composition basique des basaltes et gabbros ne permet pas la formation de niveau de décollement au dessus du manteau (Fig. 1.8b).

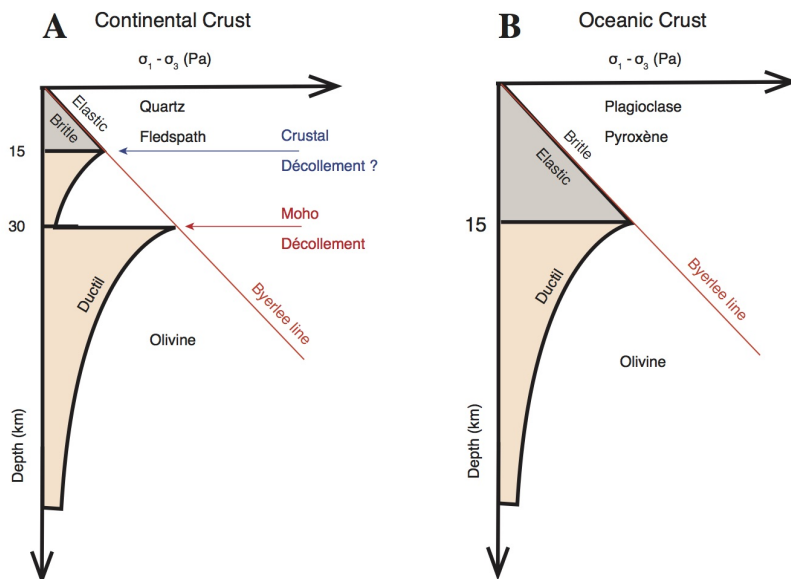


FIGURE 1.8 – Profils de résistance de la croûte continentale (A) et océanique (B) basés sur la résistance à la déformation des minéraux majoritaires présents dans les couches lithosphériques. La limite fragile-ductile correspond à l'intersection entre la droite délimitant les domaines élastiques et cassant (droite de Byerlee en rouge) et la courbe de déformation ductile. La croûte continentale présente deux niveaux de décollement alors que la croûte océanique est solidaire au manteau.

1.2.4 De la géologie structurale aux modèles de cycle sismique

Les incompatibilités entre le glissement en profondeur déduit des modèles inverses géophysiques ou géodésiques avec les décalages tectoniques mesurés en surface ont parfois conduit les chercheurs à émettre l'hypothèse que les séismes sont caractérisés par un déficit de glissement en surface accommodé par de la déformation distribuée durant la période intersismique (Fialko *et al.*, 2005). Cependant, une cartographie précise des ruptures de surface en champ proche sur le terrain ou par imagerie optique et radar haute résolution (Klinger *et al.*, 2006; Klinger, 2010) apporte des contraintes sur les changements de géométrie des ruptures vers la surface. Ces changements de géométrie contrôlent les taux de glissement et montrent que ces possibles déficits de glissement en surface s'expliquent par le partitionnement de la déformation profonde vers la surface (Bowman *et al.*, 2003; King *et al.*, 2005; Teshebaeva *et al.*, 2014; Vallage *et al.*, 2015).

Les contraintes cinématiques imposent des compatibilités long-terme des déplacements le long d'un système de faille. Similairement à la conservation du glissement le long d'une jonction triple (McKenzie et Morgan, 1969), l'intégration des déplacements en carte le long d'un chemin recoupant un certain nombre de failles, doit s'annuler. De manière identique, la cinématique apporte des contraintes sur l'évolution des structures chevauchantes. En coupe, le changement d'angle d'une structure séparant deux blocs A et B, requiert une déformation du bloc supérieur. L'évolution de ces systèmes compressifs a fait l'objet de nombreuses études. Par exemple, le modèle de Suppe (1983) fait intervenir la formation de plis dans le bloc supérieur afin d'accommoder la différence de vitesse avant et après le changement de géométrie (Fig. 3.5a). Ce pli bascule et étire les couches sédimentaires du bloc supérieur dans le scénario « slip created », et à l'inverse, raccourcit le bloc supérieur dans le cas « slip consumed ». Dans un autre modèle de blocs indéformables (Meyer *et al.*, 1998), le changement de géométrie de la structure profonde crée un troisième bloc, C, séparé des deux autres blocs A et B par une troisième structure accommodant la différence de vitesse verticale due au changement de géométrie (Fig. 3.5b). Dans ce dernier modèle, les blocs A, B et C sont supposés indéformables et ne basculent pas.

Bien que de nombreux modèles expliquent l'évolution de ces structures en fonction du contexte géologique, la conservation du mouvement demeure la règle centrale et la plus utile pour relier la géodésie aux modèles long-terme. Aussi j'introduirai la conservation du mouvement dans mes modèles afin de limiter le nombre de paramètres à explorer et de proposer des modèles géodésiques en accord avec la géologie structurale.

PRINCIPES GÉNÉRAUX ET CONTEXTE

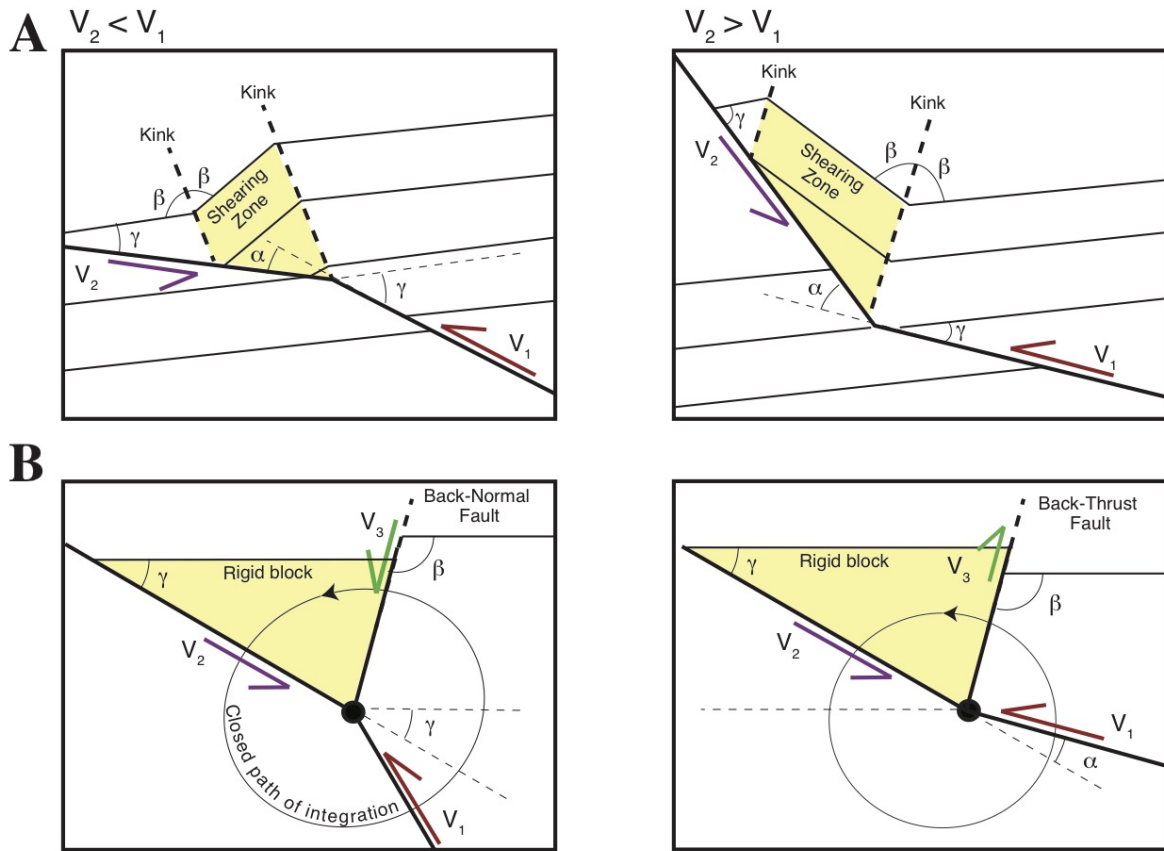


FIGURE 1.9 – Analogie entre les modèles de Suppe (1983) (A) et les modèles de bloc (Meyer *et al.*, 1998) (B) et illustration de la conservation du mouvement suite à un changement de géométrie de la rampe profonde nécessitant la déformation des couches ou du bloc supérieur.

1.2.5 Une approche Bayésienne d'exploration géométrique

La communauté géophysique doit aujourd’hui faire face à un nouveau challenge technique lié à l’explosion du nombre de données disponibles. Les données sismiques à larges bandes de fréquence, les réseaux sismiques denses, les imageries satellites, les réseaux GPS et les données de Tsunami produisent des volumes de données importantes. Ces données de natures très différentes conduisent à des systèmes géophysiques à très hautes dimensions. Les techniques traditionnelles d’optimisation des ces problèmes inverses requièrent des régularisations basées sur des choix subjectifs et non physiques qui ont des effets majeurs sur la solution, tels que l’illustre la variété des modèles disponibles dans la littérature pour un même problème (Fig. 1.10). Face à ces problèmes inverses, la meilleure solution est d’identifier l’ensemble des modèles plausibles. Dans cette pers-

pective, l'approche Bayésienne présente de nombreux avantages comparés aux optimisations classiques de solution. Elle permet entre autre de résoudre le problème inverse sans aucune régularisation et de produire l'ensemble des modèles acceptables (Fukuda et Johnson, 2008; Sudhaus et Jónsson, 2011; Minson *et al.*, 2013; Duputel *et al.*, 2014; Jolivet *et al.*, 2015a).

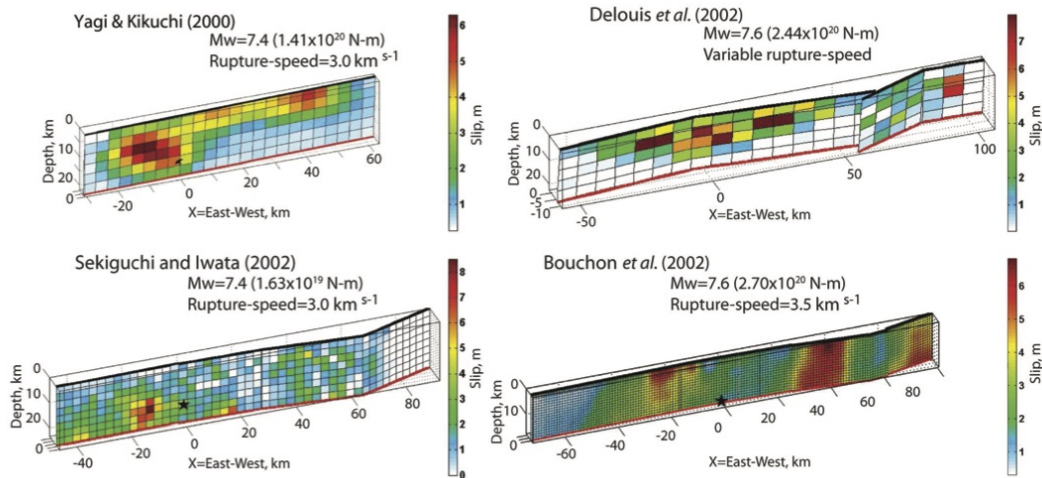


FIGURE 1.10 – Une illustration des variétés de modèles cinématiques disponibles dans la littérature pour le séisme d’Izmit de 1999. (Credit : Duputel *et al.* (2014))

Le théorème de Bayes relie l’ensemble des modèles plausibles, $p(\mathbf{m}|\mathbf{d})$, expliquant les observations, \mathbf{d} , et en accord avec nos hypothèses à priori, $p(\mathbf{m})$, tel que :

$$p(\mathbf{m}|\mathbf{d}) \propto p(\mathbf{m}) \exp \left[-\frac{1}{2} (\mathbf{d} - \mathbf{g}(\mathbf{m}))^T \mathbf{C}_D^{-1} (\mathbf{d} - \mathbf{g}(\mathbf{m})) \right], \quad (1.2)$$

où \mathbf{d} est le vecteur des données, \mathbf{m} est le vecteur des inconnues, \mathbf{C}_D est la matrice de covariance des données, et $\mathbf{g}(\mathbf{m})$ est la fonction de transfert reliant les données aux paramètres du modèles que l’on recherche \mathbf{m} .

Deux options s’offrent alors pour résoudre cette équation. En supposant des à priori Gaussiens, $p(\mathbf{d}|\mathbf{m})$, (1) il est possible d’obtenir la solution analytique de $p(\mathbf{m}|\mathbf{d})$ (Tarantola et Valette, 1982). Une deuxième approche (2) consiste à échantillonner aléatoirement la distribution à priori, $p(\mathbf{d}|\mathbf{m})$, avec des simulations de Monte Carlo et de regarder la distribution à postériori des résultats en accord avec les données Minson *et al.* (2013). Cette deuxième option, très inefficace, a un coût de calcul très élevé. Cependant, elle ne nécessite aucun choix de régularisation ni de distribution a priori Gaussienne des

inconnues.

Afin d'explorer l'ensemble des paramètres géométries non-linéaires avec les taux de déformation associés en accord avec nos observations de surface, j'ai choisi de développer des codes d'inversion basés sur des algorithmes de Monte Carlo. En l'absence d'a priori sur les paramètres à explorer, j'attribuerai ainsi des distributions uniformes entre des bornes réalistes, et à l'inverse des distributions Gaussiennes centrées sur des valeurs à priori. Ces distributions a priori seront ensuite échantillonnées avec des algorithmes de Metropolis ([Metropolis *et al.*, 1953](#)) implémentés dans la librairie PYmC de Python ([Patil *et al.*, 2010](#)).

1.3 Contexte et état de l'art au Nord Tibet

1.3.1 Contexte géodynamique

La déformation actuelle en Asie résulte de la collision entre l'Inde et l'Asie, qui s'est initiée il y a environ 55 millions d'années ([Jaeger *et al.*, 1989](#)). Depuis le début de cette collision, qui continue aujourd'hui à la vitesse de 4 cm/an ([Wang *et al.*, 2001](#)), plus de 2.500 km de convergence ont été absorbés et ont déformé l'Asie, de la chaîne Himalayenne aux massifs du Tien Shan ([Molnar et Tapponnier, 1975b; Tapponnier et Molnar, 1977; Armijo *et al.*, 1986](#)). Le plateau Tibétain est le plus large et le plus haut plateau du monde. Sa dimension alimente de nombreux débats sur les mécanismes de la déformation intracontinentale. Trois modèles opposés s'affrontent encore aujourd'hui.

Le premier et plus ancien modèle, basé sur des observations géologiques, suppose que les manteaux lithosphériques de l'Inde et du Tarim plongent simultanément sous le Tibet (Fig. 1.11). Dans ce modèle, la convergence oblique entre l'Inde et l'Asie aurait réactivé d'anciennes subductions lithosphériques à pendage Sud ([Meyer *et al.*, 1998; Peltzer et Tapponnier, 1988; Matte *et al.*, 1996; Tapponnier *et al.*, 2001](#)). Les datations suggèrent une activation de la suture du Bangong (datant du Jurassique) durant l'Eocène, puis une propagation vers la suture du Jinsha (datée du Triassique) et du Kunlun (datée du Paléozoïque) durant l'Oligo-Miocène, jusqu'à une déformation actuelle active au bord du plateau le long de la suture des Qilian Shan (datée du Paléozoïque) ([Tapponnier *et al.*, 2001](#)) (Fig. 1.11). La migration de ces réactivations successives, de direction opposée à celle de l'accrétion lithosphérique des anciennes chaînes de montagne du Paléo-Mésozoïque, demeure par conséquent compatible avec une croissance de la chaîne Tibétaine postérieure à

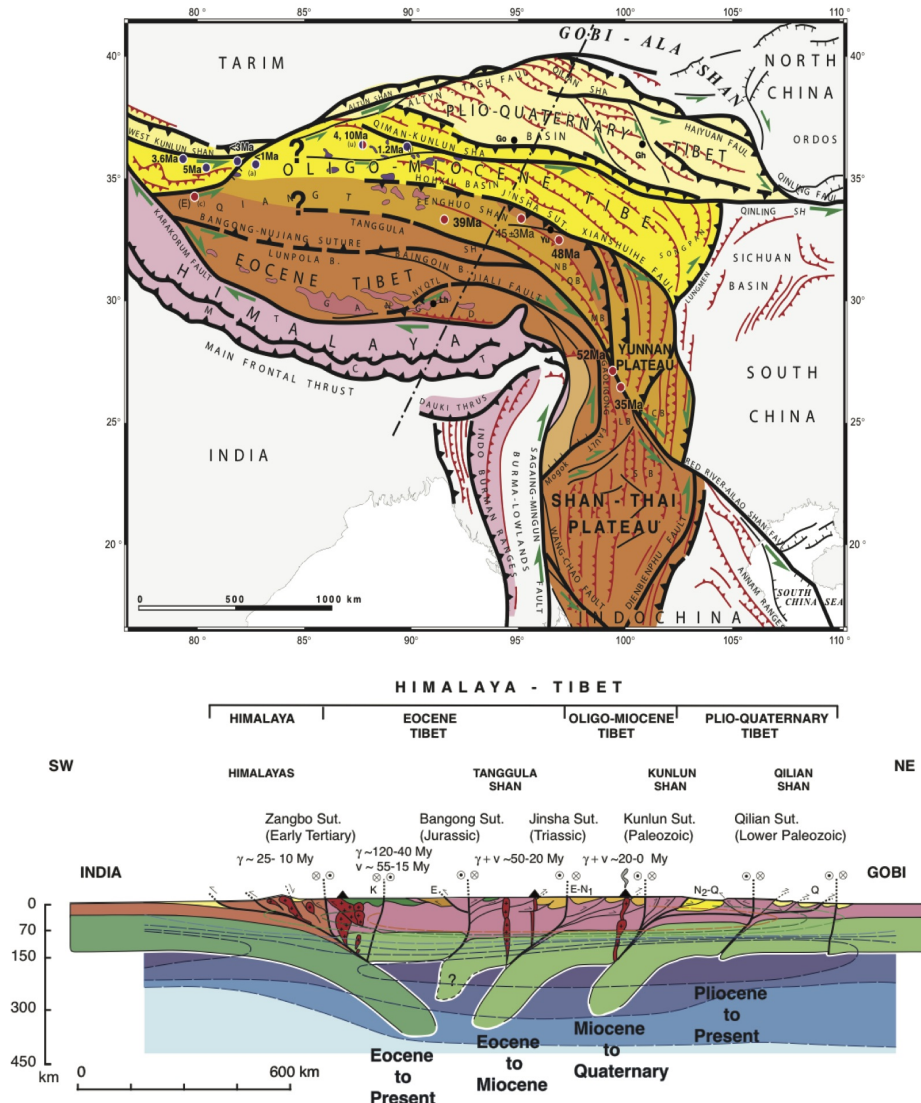


FIGURE 1.11 – Haut : Carte simplifiée des anciennes sutures géologiques déduites des majeures frontières géologiques et localisation de la section. Bas : Section lithosphérique schématique de l'évolution Cénozoïque de l'orogène Himalaya-Tibet résumant l'âge successif des anciennes subductions océaniques et de leurs réactivations suite à la collision Inde-Asie. (Credit : [Tappognier et al. \(2001\)](#))

la collision Inde-Asie ([Mattauer, 1986; Tappognier et al., 1990](#)). La déformation actuelle s'expliquerait ainsi par un raccourcissement crustal des prismes d'accrétion découpant la croûte inférieure de la croûte supérieure ou du manteau supérieur, simultanément à un extrusion Est-Ouest le long des failles décrochantes majeures, qui s'enracinaient et longeraient les zones de faiblesses lithosphériques ([Meyer et al., 1998; Gaudemer et al., 1995](#);

PRINCIPES GÉNÉRAUX ET CONTEXTE

Lasserre *et al.*, 1999, 2001). Ce modèle implique une déformation lithosphérique localisée au niveau des zones de failles délimitant des blocs tectoniques majeurs (Fig. 1.12A). Cependant, les faibles taux de déformation géodésiques court terme observés en surface sur certaines failles majeures depuis la fin du XXème siècle ont remis partiellement en question ce modèle de déformation et alimenté de nombreux débats.

Le deuxième modèle, basé sur le champ de déformation grande longueur d'onde du plateau, suppose une déformation continue et visqueuse de son intérieur (England et Houseman, 1989; England et Molnar, 1997a,c) (Fig. 1.12B). Dans ce modèle de « Tibet mou », la topographie plate du plateau se construirait par rebond isostatique suite au retrait du manteau lithosphérique depuis l'Eocène. A la manière d'un « camembert chaud », l'ensemble du plateau s'effondrerait aujourd'hui par étalement gravitaire en distribuant la déformation sur de nombreuses failles. Ce modèle simplifié à rhéologie ductile a pour avantage de reproduire au premier ordre le champ de vitesse avec une conservation mécanique et en supposant que les forces gravitaires sont supérieures aux forces tectoniques. Cependant, ce modèle à croûte solidaire du manteau (Fig. 1.12B), ignore les observations tectoniques de surface et le chevauchement de la croûte inférieure sur le manteau péricratique relativement plus rigide le long des décollements majeurs (Mattauer, 1986; Tapponnier *et al.*, 2001).

Le troisième modèle fait intervenir une couche profonde à très faible viscosité ($< 10^{18}$ Pa/s). Cependant, dans ce dernier cas, la couche mobile se trouverait piégée entre la croûte supérieure cassante et le manteau supérieur plus visqueux. La croûte inférieure serait décollée et participerait à la construction de la topographie élevée du plateau Tibétain par l'apport de matière sous sa croûte supérieure rigide et peu déformée. Les déformations post-sismiques associées à des ruptures majeures appuient ce modèle en contraignant une viscosité de la croûte inférieure faible afin d'expliquer le signal de surface observé (Royden *et al.*, 1997; Ryder *et al.*, 2007; Wen *et al.*, 2012; Huang *et al.*, 2014) (Fig. 1.12C). Cependant, ces études souffrent des ambiguïtés entre la localisation en profondeur de cette déformation et la viscosité de la couche déformée. Plus récemment, une étude de Doin *et al.* (2015) montre que la subsidence autour du lac de Siling Co, au Tibet centrale, suite à un récent changement du niveau d'eau, contraint une croûte inférieure d'une viscosité de $2 - 3 \cdot 10^{18}$ Pa/s confinée entre une croûte supérieure cassante épaisse et un manteau élasto-plastique s'étendant en profondeur. Ce modèle interprété sur la Fig. 1.12D, présenterait donc lui aussi deux niveaux de décollement. L'accès aux propriétés visqueuses de la lithosphère est malheureusement un sujet bien complexe et, de mon point de vue, loin des possibilités de quantification par la géodésie. Les caracté-

ristiques rhéologiques déduites des observations actuelles sont dérivées d'une croûte qui s'est déjà épaissie depuis longtemps et qui présente de fait un héritage structural, thermique et rhéologique variant latéralement sur tout le Tibet. Les propriétés à l'équilibre d'un fluide visqueux changeant ses propriétés dynamiques, il est également difficile de connaître avec certitude l'état rhéologique de la lithosphère durant les longues périodes séparant des événements sismiques. Bien que pouvant être un facteur de l'épaississement du Tibet, ce modèle dit de « Channel Flow », ne peut expliquer à lui seul la formation du Tibet et doit donc être intégré à l'histoire des chevauchements des unités géologiques de la croûte supérieure.

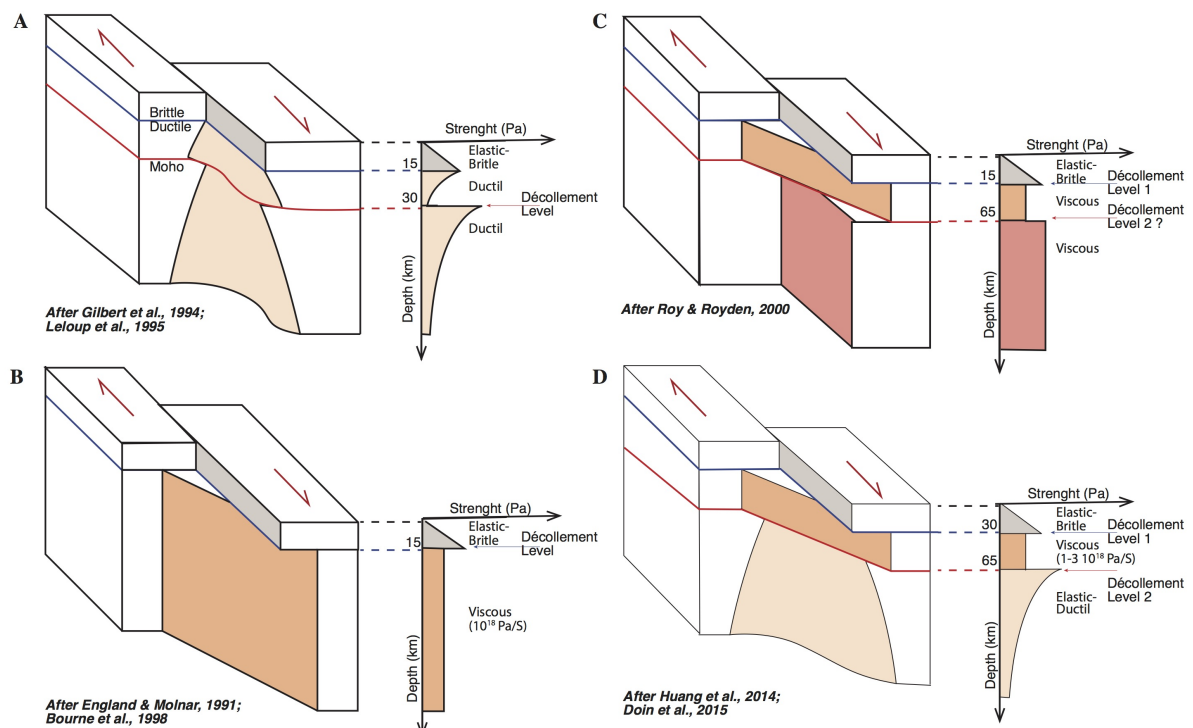


FIGURE 1.12 – Représentation schématique de décrochement lithosphérique à partir des observations et modèles présents dans la littérature du Tibet profond. Pour chaque modèle est représentée le block diagramme des déformations accompagné d'un profil de résistance schématique déduit des expériences mécaniques en laboratoire (A) ou des modèles géophysiques (B, C, D) (Crédits : Modifié du manuscript d'HDR d'Hervé Leloup).

Ainsi, les taux de déformation de ces failles majeures sont au cœur du débat sur la manière dont le plateau Tibétain se déforme. Il a été alimenté ces dernières années par les inconsistances entre les mesures géologiques basées sur des décalages morphologiques et des datations cosmogéniques (Van Der Woerd *et al.*, 1998; Mériaux *et al.*, 2004, 2005;

PRINCIPES GÉNÉRAUX ET CONTEXTE

Lasserre *et al.*, 1999, 2002), les mesures géodésiques des campagnes GPS (Bendick *et al.*, 2000; He *et al.*, 2013), les mesures InSAR (Elliott *et al.*, 2008; Wang *et al.*, 2012), ou encore les taux de glissement inversés à partir de modèles numériques basés sur des mesures long-terme et/ou court-terme (Peltzer et Saucier, 1996; Meade, 2007a). De mon point de vue, le champ de déformation uniforme aujourd’hui observé à la surface peut tant s’expliquer par un modèle de déformation distribuée que par un fort découplage des couches lithosphériques. Les modèles rhéologiques négligeant l’importance des forces tectoniques, sous estiment le potentiel sismique des nombreuses failles majeures délimitant les blocs géologiques du plateau. Ces failles sont remarquables par leurs morphologies, par leurs étendues et par la topographie qu’elles délimitent. De plus, elles sont historiquement responsables des séismes dévastateurs de M 7.5-8 de type décrochant (tels que le séisme d’Haiyuan en 1920 Qidong *et al.* (1986), le séisme de Kokoxili en 2001 (Lasserre *et al.*, 2005)), et également de type chevauchant (tel que le séisme de 1927 de Gulang (Gaudemer *et al.*, 1995), ou celui de Wenchuan en 2008 (Shen *et al.*, 2009)) qu’a connus la Chine. Les divergences entre mesures court-terme et long-terme pourraient simplement s’expliquer par l’évolution du rôle des structures au cours des temps géologiques (million d’années) ou de son cycle sismique (Meade *et al.*, 2013) ou bien de par notre perception limitée de la déformation actuelle. En effet, tout comme le montre son histoire, le Tibet ne se maintient pas dans un état d’équilibre, mais se propage depuis l’Eocène supérieure vers le Nord en développant de nouvelles failles qui orchestrent la croissance de la chaîne. Aussi, au sein même d’un cycle sismique (500 ans à mille ans ou plus), les taux de déformations intersismiques évoluent en fonction des effets viscoélastiques de la croûte et du manteau (Hetland et Simons, 2010; Meade *et al.*, 2013; DeVries et Meade, 2013). Enfin, nos observations de surfaces sont restreintes à quelques zones et ne permettent pas de déduire sans ambiguïté les taux de déformation en profondeur.

Je pense que les mesures actuelles de la déformation des failles n’apportent pas un argument suffisant pour discuter ces modèles géodynamiques. Ils ne seront donc pas plus profondément discutés dans ce manuscrit. Aussi, j’axerai mes centres d’intérêts sur le lien entre géométrie des failles et leurs comportements court-terme et long-terme. Réconcilier les modèles géodésiques et tectoniques, tout en prenant en compte les contraintes géodynamiques, seront pour ce travail une priorité afin de proposer des modèles de déformations cohérents visant à améliorer notre compréhension de l’aléa sismique.

1.3.2 Contexte tectonique

La tectonique du plateau Tibétain se caractérise par un comportement différent d'Est en Ouest.

A la bordure Nord-Est du plateau, les systèmes de failles du Kunlun et d'Haiyuan, d'orientation N120°E, limitent les chaînes du Qiman et des Qilian Shan. Ces grands systèmes montrent un raccourcissement de plus de 1.5 cm/an, accompagné par une succession de chevauchements et d'anticlinaux, discontinus, de moins de 40 km de large, et parallèles aux structures décrochantes, recouverts de sédiments datant du Miocène au Quaternaire ([Tapponnier et al., 1990](#)) (Fig. 1.13). L'activation de ces jeunes chevauchements est synchrone et gouvernée par la géométrie des failles du Kunlun et d'Haiyuan. La topographie étroite associée ainsi que la sismicité, ou bien encore les récentes études par imageries sismiques ([Ye et al., 2015; Guo et al., 2015](#)), suggèrent que ces chevauchements s'enracinent le long de décollements qui ne s'étendent pas plus loin que la croûte et qui se branchent sur les failles lithosphériques décrochantes ([Gaudemer et al., 1995; Meyer et al., 1998; Lasserre et al., 1999, 2001, 2002](#)) (Fig. 1.13).

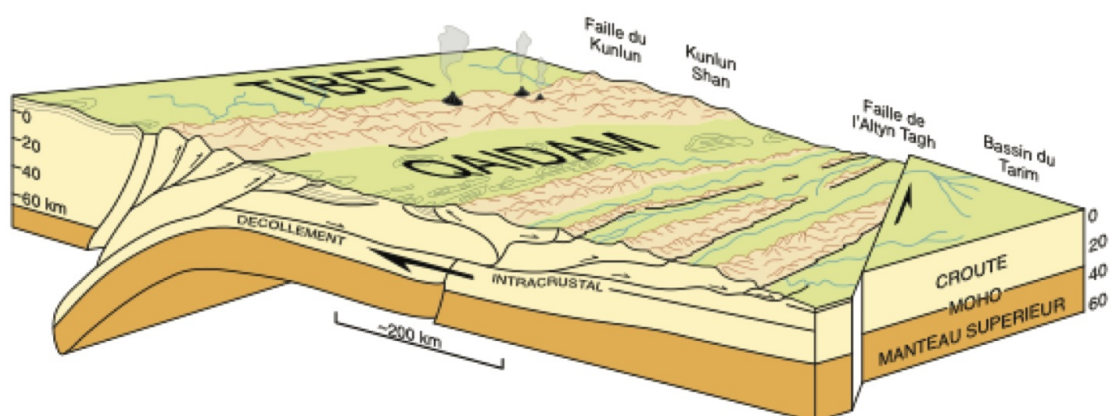


FIGURE 1.13 – Modèle de bloc schématique de la déformation actuelle de la partie Nord-Est du Tibet. Le manteau supérieur lithosphérique est en orange et la croûte allochtone est en jaune. Les chaînes de montagne étroites, autour des bassins du Qaidam, se forment par une succession d'anticlinaux associés aux rampes qui se propagent vers le Nord-Ouest le long d'un décollement intra-crustal se branchant sur la suture lithosphérique du Kunlun (Crédit : [Meyer et al. \(1998\)](#)).

La section Nord-Ouest du plateau (80°-85°E) est quant à elle environ trois fois plus

PRINCIPES GÉNÉRAUX ET CONTEXTE

petite en largeur et en longueur que la section Nord-Est (90-105°E). A cet endroit, la suture du Kunlun, datée du Paléozoïque, subducte le Tarim sous le Tibet (Wittlinger *et al.*, 1998) (Fig. 1.14). Les roches Paléozoïques de la chaîne du Kunlun montrent un décalage de quelques centaines de kilomètres d'Ouest (West-Kunlun) (Fig. 1.14) en Est (East-Kunlun) (Fig. 1.13), découpée par une des structures les plus remarquables du Tibet : la faille de l'Altyn Tagh (Peltzer *et al.*, 1989; Matte *et al.*, 1996) (Fig. 1.22). Elle se présente par sa longueur et sa morphologie comme une actrice majeure de l'extrusion du plateau. Le long de cette chaîne, la réactivation des structures chevauchantes crustales a été datée au Miocène, synchrone des chevauchements Himalayens, ainsi que de l'activation de la faille de l'Altyn Tagh (Matte *et al.*, 1996). Le long de cette bordure du plateau Tibétain, le partitionnement de la convergence Inde-Asie demeure donc des plus complexes. L'extrusion et le raccourcissement sont d'une part contrôlés, tout comme à l'Est, par la réactivation crustale de la suture du Kunlun d'orientation N110°E, subductant le Tarim sous le Tibet (Fig. 1.14). Le bassin du Tarim montre lui aussi une déformation active (Fig. 1.15) comme l'atteste le récent séisme chevauchant de Mw 6.4 du Pishan, qui a rompu un segment entre la chaîne Ouest du Kunlun et le Mazar Tagh, ainsi que les campagnes sismiques dans le Tarim, montrant une succession de failles chevauchantes dans l'ensemble du bassin (Fig. 1.16). Cependant à cet endroit, la chaîne du Kunlun est également simultanément décalée vers le Nord-Est par la faille de l'Altyn Tagh d'orientation N100°E. Ceci suggère que la déformation transpressive dans ce coin nord-est du Tibet est probablement découpée en une composante transformante, le long de l'Altyn Tagh et du Kunlun, et une composante de raccourcissement au travers du prisme d'accrétion du Tarim, le tout se branchant probablement en profondeur sur une frontière lithosphérique unique (Wittlinger *et al.*, 1998).

1.3.3 État de l'art sur la déformation active

Face aux difficultés d'obtenir des données GPS au Tibet et compte-tenu des grandes distances entre les stations (Fig. 1.17), l'interférométrie radar représente un outil remarquable pour compléter les observations de la déformation actuelle. Elle mesure les déplacements du sol avec une grande résolution spatiale et de manière continue en espace. Contrairement au GPS, la continuité du signal permet de localiser précisément la déformation. Sa couverture spatiale intègre l'ensemble des structures responsables de la déformation observée localement et apporte des contraintes sur des sources de déformations profondes produisant des déformations en surface de grandes longueurs d'onde.

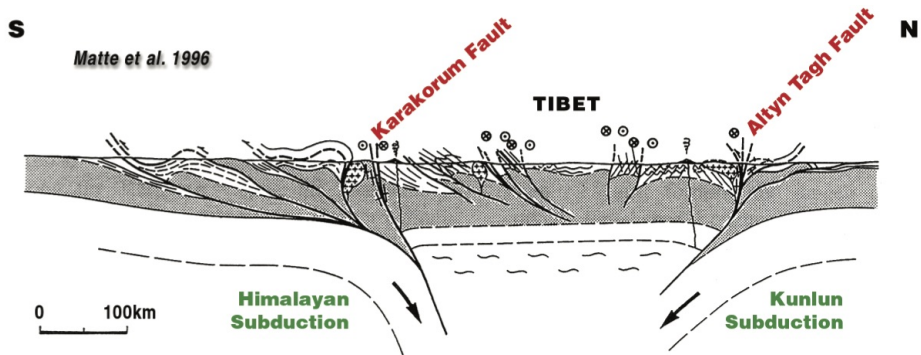


FIGURE 1.14 – Coupe schématique de la partie Nord-Ouest du Tibet. A cet endroit du Tibet, les subductions lithosphériques de l'Himalaya et du Kunlun, où viennent se brancher les chevauchements crustaux, sont décalées par les failles du Karakorum et de l'Altyn Tagh (Crédit : Matte et al. (1996)).

Cependant, en raison des nombreux défis méthodologiques, peu d'études InSAR ont été réalisées jusqu'à aujourd'hui sur les failles tibétaines et de nombreuses zones restent à explorer (Fig. 1.17). Le récent séisme de Wenchuan, qui a frappé, pour certains, de manière inattendue le Sichuan le 12 mai 2008 et qui a tué plus de 70000 personnes, souligne les limites des connaissances du risque sismique de l'ensemble des failles tibétaines et démontre l'importance de couvrir l'ensemble du plateau.

Taylor et Peltzer (2006) furent les pionniers dans l'étude par InSAR du champ de déformation associé à la faille du Gyaring Co au coeur du plateau Tibétain, et quantifièrent une zone de déformation localisée le long de failles conjuguées. Ils pointèrent les difficultés liées à l'atmosphère ou encore celles dues aux cycles de gel et dégel des basins sédimentaires. Wang et al. (2009), quand à eux, étudièrent la faille de Xianshuihe et purent localiser grâce à l'InSAR la profondeur d'accumulation des contraintes de la faille. Cavalié et al. (2008); Jolivet et al. (2012) observèrent avec succès la déformation au travers la faille d'Haiyuan, en mettant au point des techniques pour palier aux différentes difficultés, notamment atmosphériques. Ils réalisèrent des mesures de la déformation de surface au voisinage de la faille pour en déduire son chargement profond. Jolivet et al. (2012, 2013) ont également mis en évidence une zone de glissement asismique de 35 km de long de la faille, corrélée avec sa rugosité géométrique. Wright et al. (2004); Peltzer et al. (2006); Lasserre et al. (2007); Elliott et al. (2008); Wang et al. (2012) s'attachèrent quant à eux à la faille de l'Altyn Tagh, mais furent confrontés aux nombreuses ambiguïtés et trade-offs entre la déformation, les rampes orbitales et les délais atmosphériques (Fig. 1.21). Pour palier ce problème, Elliott et al. (2008) et Wang et al. (2012) inversèrent

PRINCIPES GÉNÉRAUX ET CONTEXTE

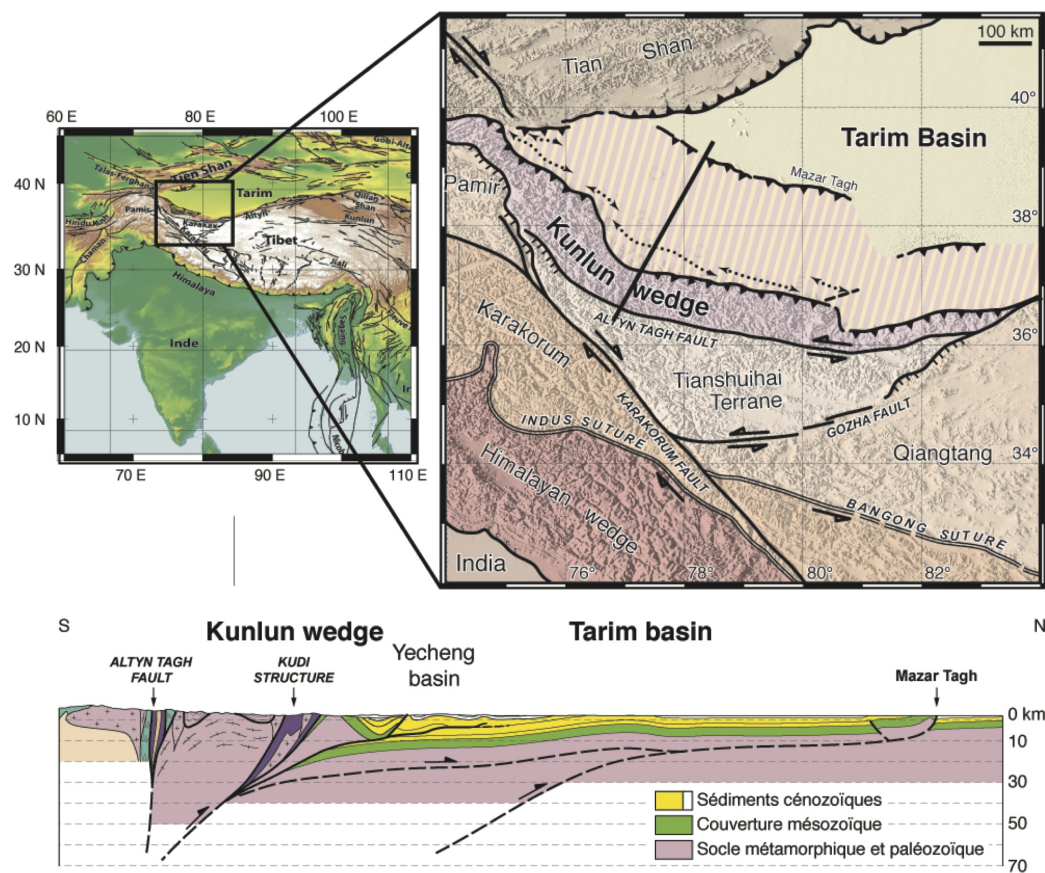


FIGURE 1.15 – Coupe schématique du prisme d'accrétion dans le bassin du Tarim s'étendant de la faille de l'Altyn Tagh, au sud, jusqu'aux chevauchements des Mazar Tagh, au nord, et illustrant le décollement du Tarim et la propagation des chevauchements vers le nord depuis le Miocène (Credit : Communications personnelles provenant de Paul Tapponnier et extrait des travaux de thèse de Thomas Coudroy à l'IPGP).

conjointement, à la fin de leur traitement, leur champ de vitesse obtenu, avec ces diverses inconnues (Fig. 1.18A,B). Cette opération mathématique mène à de grandes incertitudes sur les taux de glissement. Par ailleurs, ils ne prirent pas en compte la déformation verticale dans leurs modèles bien que l'InSAR soit plus sensible aux mouvements verticaux qu'horizontaux et que la zone présente du raccourcissement non négligeable.

Les travaux de Garthwaite *et al.* (2013) et de Wang *et al.* (2012) restent les premières tentatives d'une mesure à très grande échelle au travers de nombreuses failles (Fig. 1.17, Fig. 1.18B,C). Cependant, n'ayant pas réussi à corriger les signaux parasites présents dans le signal interférométrique avant l'extraction du signal de déformation, ils ne purent

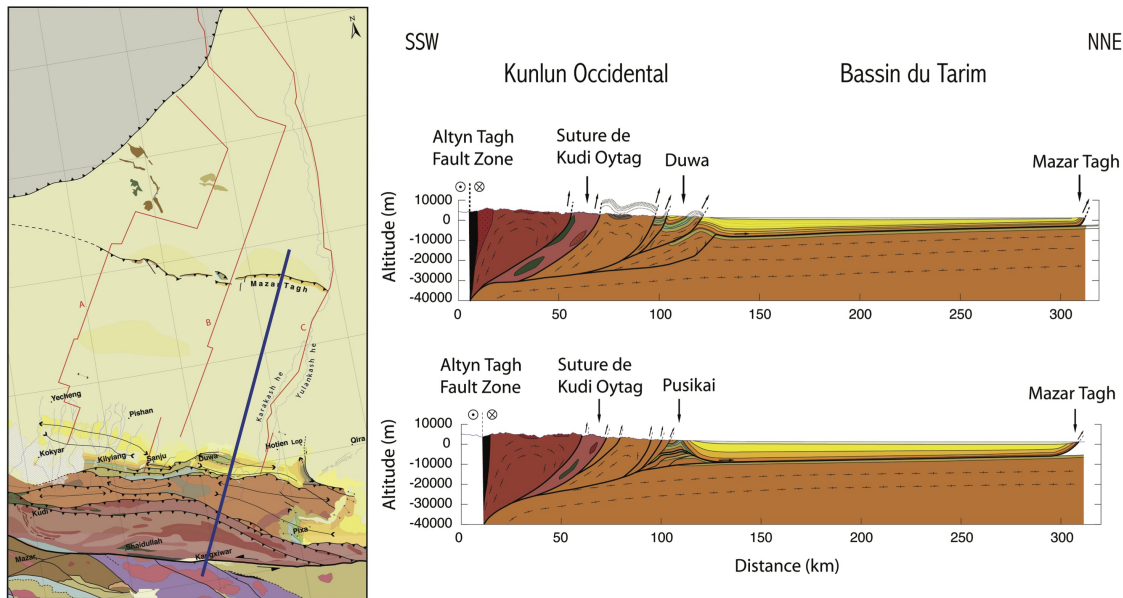


FIGURE 1.16 – Interprétations de profils sismiques imageant les chevauchements et les décollements profonds du Tarim (Credit : Communications personnelles provenant de Paul Tapponnier et extrait des travaux de thèse de Thomas Coudroy à l'IPGP).

dérouler le signal au travers de nombreuses zones, telles que les chaînes de montagnes, les dunes ou les bassins sédimentaires.

1.3.4 Le système de failles de Haiyuan

Nos travaux au Tibet s'intéressent à deux grands systèmes de failles bordant la limite Nord du plateau. La première zone d'étude se situe entre les longitudes 101°E et 105°E au Nord-Ouest du plateau Tibétain et couvre le système de faille de Haiyuan (HFS pour « Haiyuan Fault System »). Le HFS, est un système de failles de plus de 1000 km de long accommodant la déformation entre le plateau tibétain au Sud et la plate-forme de Gobi Ala Shan au Nord. Il se constitue d'une grande faille décrochante sénestre (la faille de Haiyuan), de la faille de Gulang (qui est également en décrochement sénestre connectée à la faille de Haiyuan et se terminant à l'Est par des chevauchements), et des chevauchements du bord Nord Est des Qilian Shan, aussi connectés en profondeur à la faille de Haiyuan (Gaudemer *et al.*, 1995) (Fig. 1.19).

La zone constitue une transition géométrique entre deux types de déformation et se

PRINCIPES GÉNÉRAUX ET CONTEXTE

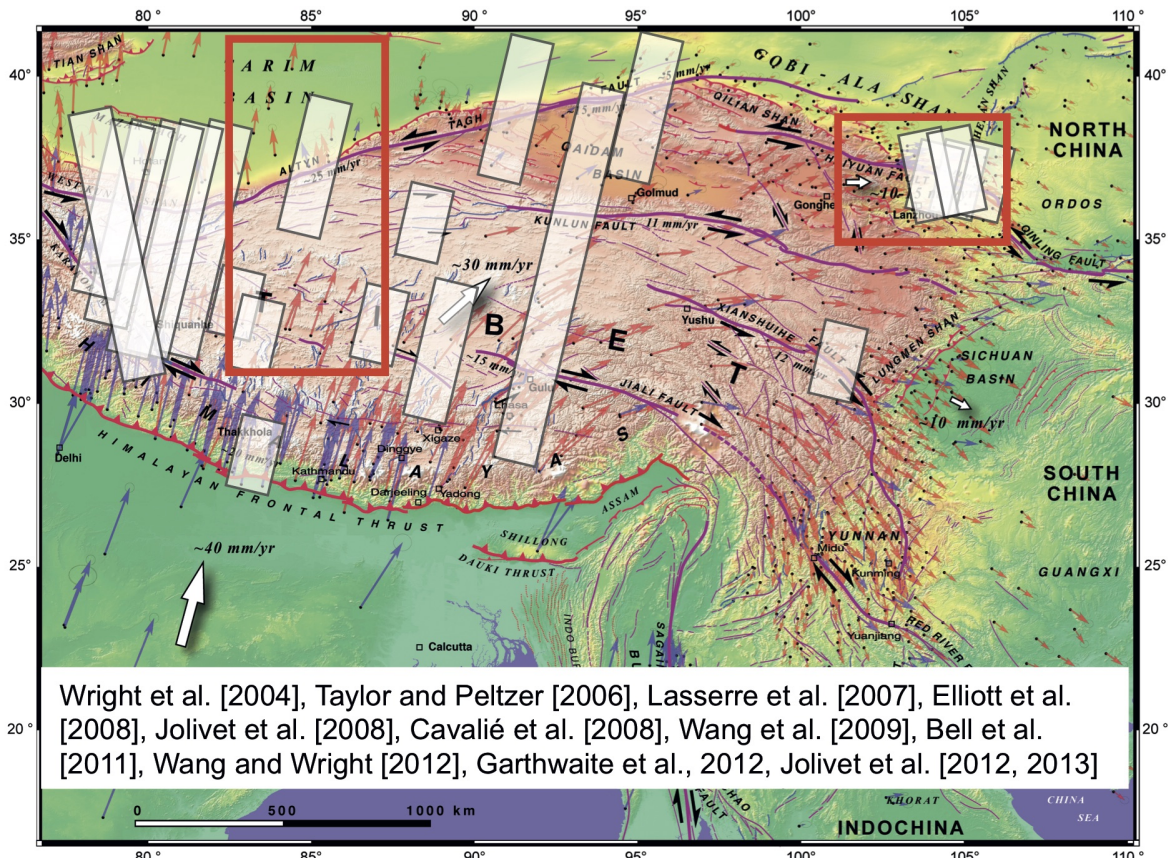


FIGURE 1.17 – Tectonique du Tibet superposé au réseau GPS et aux publications InSAR (gris clair). Les deux zones d'étude au Tibet de ce manuscrit sont encadrées en rouge.

présente comme une zone intéressante pour étudier le partitionnement de la convergence Inde-Asie sur les différentes structures, comme l'ont illustrés les deux derniers séismes de $M \sim 8$ qui cassèrent une partie de la faille de Haiyuan en 1920 et des chevauchements des Qilian Shan en 1927 (Fig. 1.19). Pour cette première étude, j'utiliserai les derniers développements apportés à la chaîne de traitement NSBAS (telles que les corrections d'erreurs locales de topographie (Ducret et al., 2014) et atmosphériques (Jolivet et al., 2011) avant le déroulement du signal) afin d'extraire un signal continu au travers de cette zone montagneuse. Ensuite, j'exploiterai l'information géodésique (GPS et InSAR) pour modéliser la déformation actuelle le long de deux profils perpendiculaires au système de failles de Haiyuan. La complémentarité des données est bien adaptée au problème. Les données GPS apportent une référence sur le champ de vitesses lointain, alors que l'InSAR améliore la résolution spatiale et contraint les déplacements verticaux. J'évaluera la

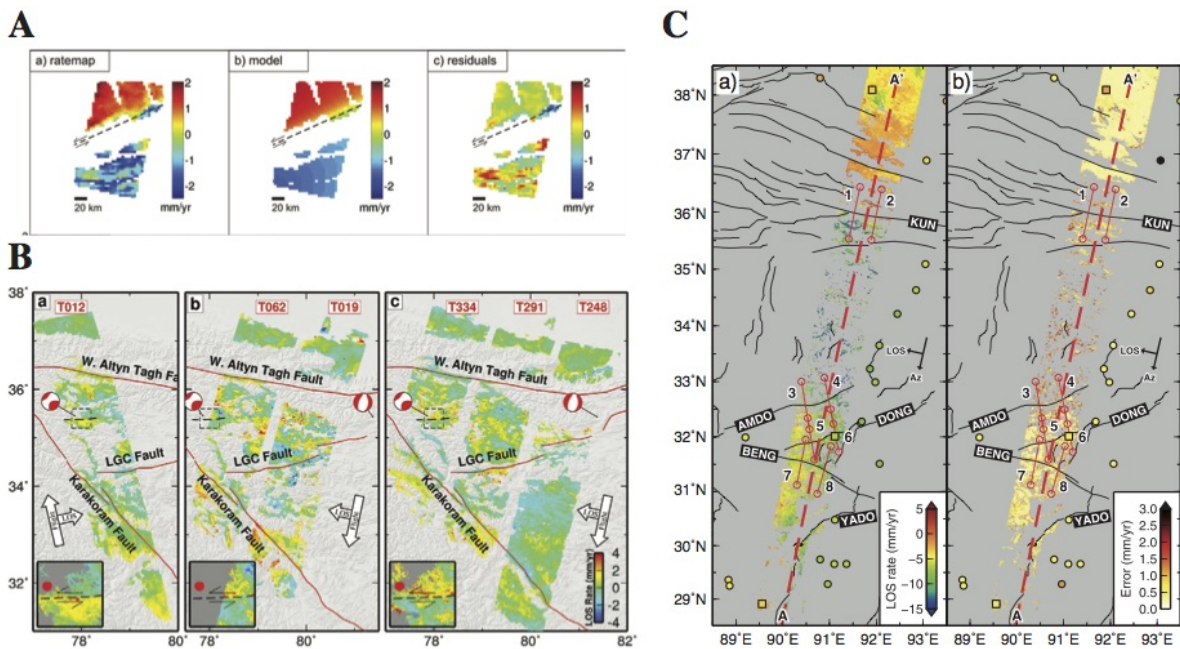


FIGURE 1.18 – Études InSAR réalisées au nord Tibet. A : Carte de vitesse et modèle de déformation associée à travers la partie centrale de l'ATF de Elliott *et al.* (2008). B : Cartes de vitesse au Nord-Ouest Tibet de Wang *et al.* (2012). C : Carte de vitesse grande échelle et erreurs associées dans la partie centrale du Tibet Garthwaite *et al.* (2013).

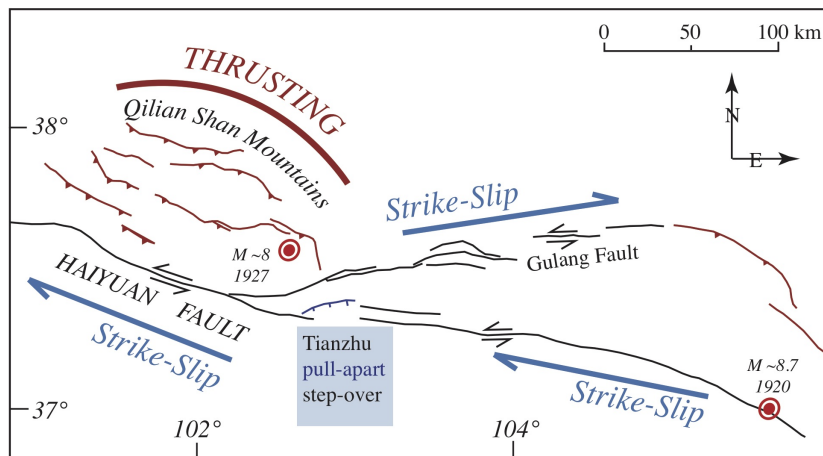


FIGURE 1.19 – Carte schématique du système de failles de Haiyuan (HFS) montrant le changement de partitionnement d'Ouest en Est entre la faille d'Haiyuan, la faille du Gulang et les chevauchements de Qilian Shan. Localisation des deux derniers évènements sismiques majeurs de M>8.

compatibilité des mesures avec les modèles tectoniques long-terme de cette zone. Pour cela, j'étudierai l'influence de la géométrie du système de failles sur le signal InSAR et GPS en développant des algorithmes Bayésiens afin d'explorer l'ensemble des géométries en adéquation avec le signal de surface observé.

1.3.5 La faille de l'Altyn Tagh

La deuxième zone d'étude s'étend du bassin du Tarim jusqu'au centre du plateau et se situe entre les longitudes 81°E (Fig. 1.22) (où la faille de l'Altyn Tagh se connecte sur la faille de la Karakax), et 88°E (où elle se branche en profondeur sur les chevauchements des Altun Shan, au Nord, et des Qiman Shan, au Sud). La zone se situe dans la partie la plus linéaire de la faille de l'Altyn Tagh, délimitée par deux changements de direction de la structure. A l'Est, le faible changement de direction de la faille crée une zone en transpression et la formation de la chaîne des Altun Shan. La zone montre une tectonique Quaternaire active, avec de jeunes chevauchements recouvrant des sédiments récents au piedmont de la chaîne de montagne. La zone Ouest demeure, quant à elle, plus complexe, avec une compression dans le bassin du Tarim (Fig. 1.15, 1.16), mais également une extension, au sud des Karakax, marquée par une sismicité importante. Le bassin du Tarim présente également quelques marqueurs de déformation récents (Fig. 1.22), avec notamment un saut topographique remarquablement linéaire s'étendant d'Est en Ouest, d'orientation parallèle à la faille de l'Altyn Tagh et s'alignant avec une zone d'oasis suggérant la présence d'une faille décrochante aveugle (Fig. 1.22).

Le plateau tibétain est, quant à lui, couvert par une succession de bassins sédimentaires, d'une altitude moyenne de 4.4 km et d'orientation quasiment Est-Ouest, au pied des chaînes de montagnes étroites pouvant atteindre 6 km d'altitude. En profondeur, ces sédiments accueillent de la glace permanente, appelée pergélisol. De plus, près de la surface, ils gèlent en hiver et dégèlent en été, et subissent de nombreux effets de cryoturbations (Fig. 1.20). Ces fortes déformations non-tectoniques limitent la continuité du signal de phase sur les interférogrammes et donc le traitement sur une grande zone (Taylor et Peltzer, 2006; Doin *et al.*, 2015). De plus, le changement d'altitude entre le désert du Tarim (inférieur à 1 km d'altitude), au Nord de l'Altyn Tagh, et le plateau Tibétain (en moyenne à 5 km), au Sud de la faille, engendre d'énormes délais troposphériques corrélés au signal attendu au travers de la faille de l'Altyn Tagh (Fig. 1.21). Cette atmosphère stratifiée limite grandement l'accès aux déformations tectoniques.

Dans cette zone, le faible nombre de GPS et la complexité géométrique du système de

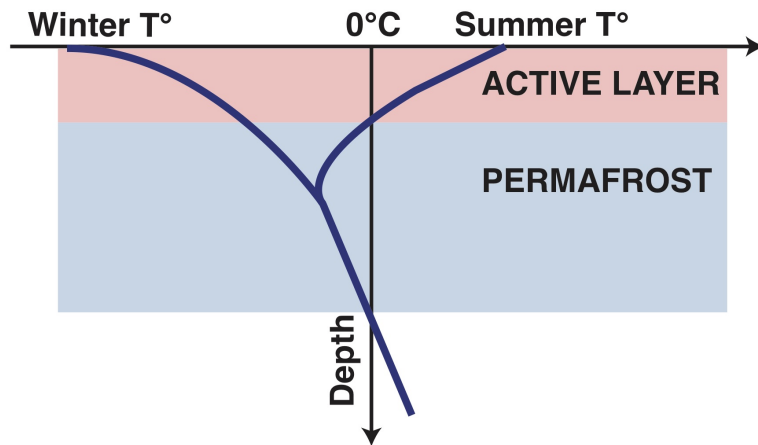


FIGURE 1.20 – Représentation schématique de la couche active recouvrant le pergélisol et soumise aux cycles de gel et dégel.

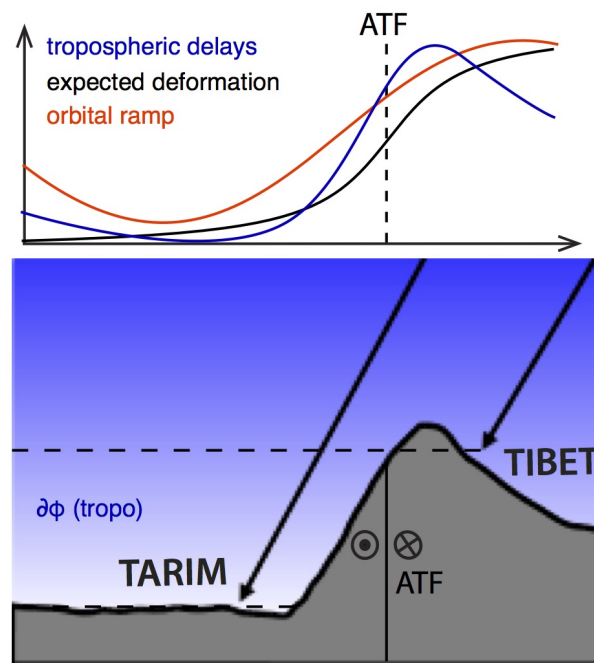


FIGURE 1.21 – Représentation schématique des ambiguïtés entre les délais troposphériques, $\delta\phi_{tropo}$, entre le bassin du Tarim et le plateau Tibétain dû au saut topographique de ~ 4 km, les rampes orbitales et la déformation attendue au travers la faille de l'Altyn Tagh (ATF).

failles (Fig. 1.17) ne permettent pas de définir clairement des limites de blocs lithosphériques et il s'avère important d'intégrer le rôle actuel de cette faille dans la tectonique

PRINCIPES GÉNÉRAUX ET CONTEXTE

régionale. D'un point de vue aléa, la faille de l'Altyn Tagh présente aussi un intérêt car une série de séismes modérés ont rompu ces dernières années en extension à son extrémité Ouest, laissant craindre une prochaine rupture sur le segment principal étudié.

L'objectif de mon étude consiste en l'extraction d'un signal continu sur cette grande zone, et ce afin de discerner les signaux parasites du signal de déformation, de mieux contraindre les modèles cinématiques de déformation et la géométrie des blocs. Dans le but de répondre aux nombreux défis méthodologiques (rampes orbitales, décorrélations temporelles dues aux dunes ou aux variations de gel et dégel des sédiments, variations atmosphériques gigantesques entre le désert du Tarim et le plateau Tibétain), je développerai pour cette seconde zone d'étude de nombreux outils spécifiques à la grande échelle.

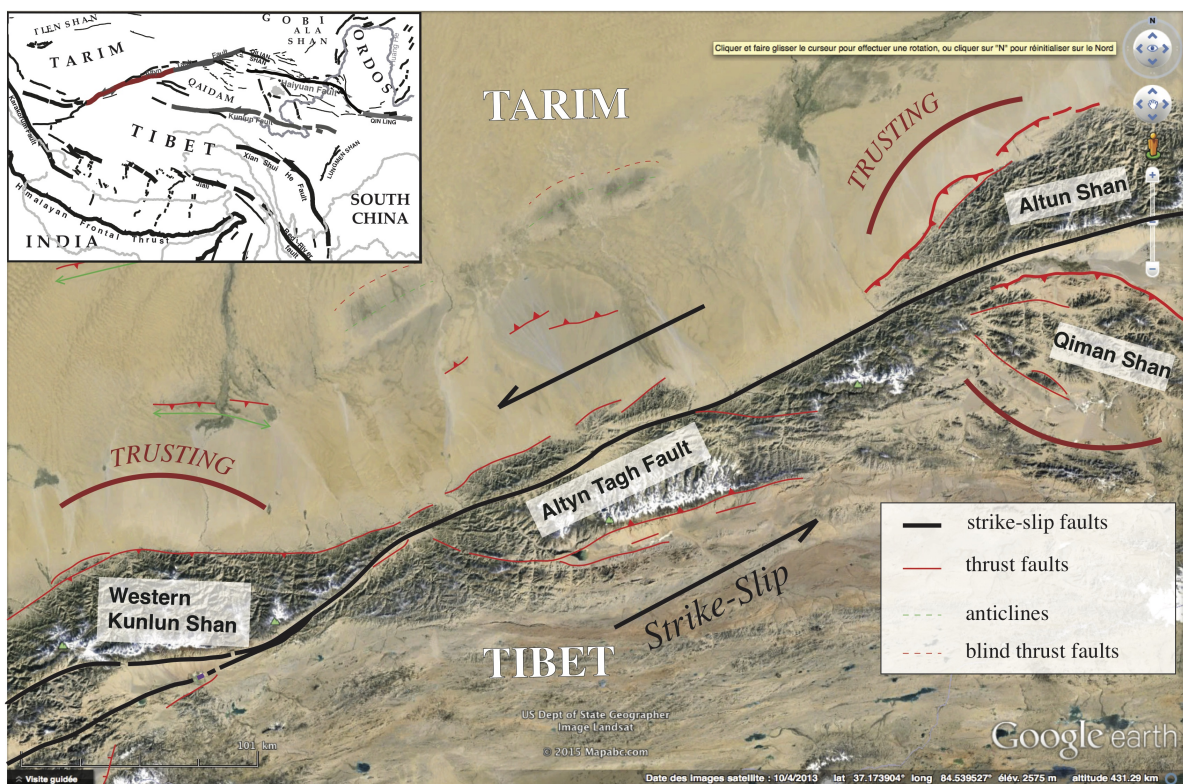


FIGURE 1.22 – Cartographie des failles actives aux alentours de la partie rectiligne de la faille de l'Altyn Tagh, superposées à une image Google Earth Landsat (Credit : Modifié à partir de communications personnelles provenant de Jérôme Van der Woerd).

1.4 Contexte tectonique et état de l'art en Californie du Sud

1.4.1 Contexte tectonique

La déformation actuelle en Californie du Sud résulte, quant à elle, de la collision entre la Plaque Océanique Pacifique (POP) et la plaque Nord Américaine (NAP) qui s'initia il y a 28 millions d'années. Le mouvement relatif entre ces deux plaques est largement pris en charge par de longues et matures failles décrochantes le long du système de failles de San Andreas (SAF) (Fig. 1.23). Les modèles long-terme géologiques et géodynamiques proposent que la faille de San Andreas (SAF) suit une ancienne zone de faiblesse crustale (suture) créée par la subduction de la plaque Farallon sous la NAP (Furlong et Hugo, 1989; Pikser *et al.*, 2012; Wang *et al.*, 2013). De par sa morphologie et les grands séismes qu'elle a provoqués et qui ont dévasté la Californie du Sud à plusieurs reprises (Sieh, 1978; Jacoby *et al.*, 1988), la faille est considérée comme une faille lithosphérique majeure où s'accumule un mouvement décrochant dextre.

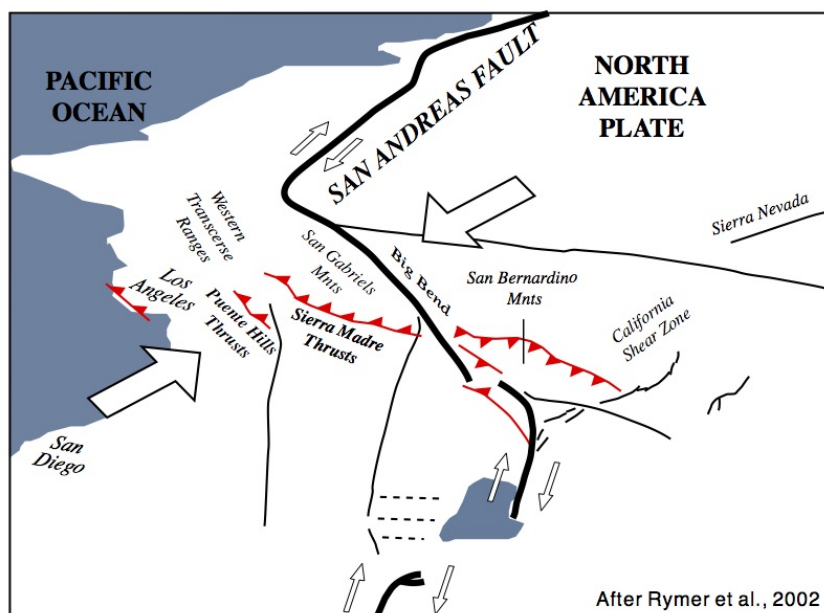


FIGURE 1.23 – Carte schématique de la Californie du Sud illustrant la zone de transpression formé par les chevauchements des Sierra Madre et des Puente Hills suite au changement de géométrie de la faille lithosphérique de San Andreas au niveau du « Big Bend ».

A certains endroits, l'obliquité de la faille crée une convergence locale, mise en évi-

PRINCIPES GÉNÉRAUX ET CONTEXTE

dence par la présence de chevauchements et de plis d'une largeur de 50-100 km, qui se développent perpendiculairement à la faille de San Andreas (Mount et Suppe, 1987) (Fig. 1.23). Le chevauchement « aveugle » des Puente Hills est reconnu comme la structure active majeure s'étendant 45 km en longueur sous Los Angeles enfoui de 3 à 7 km (Shaw *et al.*, 2002). Quatre séismes majeurs sont supposés avoir rompu durant ces 11,000 dernières années le long de ces chevauchements, produisant plus de 14 m de glissement le long de plis sédimentaires près de la surface (Dolan *et al.*, 2003). Les récents profils sismiques, opérés à travers la faille de San Andreas (LARSE), identifièrent de forts réflecteurs à faible pendage situés à 20 km de profondeur sous les montagnes des San Gabriel (Fig. 1.24). Ils s'interprétèrent comme des décollements crustaux se connectant à la base des chevauchements peu profonds et à fort pendage (Fuis *et al.*, 2001a, 2012). Les mesures GPS enregistrent actuellement à travers le « Big Bend » de la faille de San Andreas, un fort raccourcissement de 4 mm/an concentré à l'avant de la chaîne (Argus et Gordon, 2001), au niveau des Puente Hills, soulignant le risque important associé à ces structures.

Malgré les changements de direction de la faille de San Andreas, le champ de vitesse intersismique mesuré par les GPS demeure relativement uniforme en Californie du Sud du Tejon Pass au bassin de Salton Sea. En profondeur, l'accumulation de la déformation doit également être uniforme tout en se connectant à la complexité géométrique des structures de surface. Comme l'indique également les faibles taux de friction de la faille de San Andreas (Brune *et al.*, 1969), ou encore la direction perpendiculaire à la faille de San Andreas des taux de contraintes maximales, le champ de déformation uniforme suggère (tout comme au Tibet) un fort découplage de la déformation le long de structures à faibles pendages. D'autres modèles prédisent des déformations distribuées en profondeur sur de larges zones (Wilcox *et al.*, 1973; Bourne *et al.*, 1998) (Fig. 1.12B). Par exemple, dans le modèle dit de « Wrench tectonic », les plis et les chevauchements se développent obliquement à la composante de décrochement majeure en raison du fort taux de friction de la zone distribuée.

1.4.2 Etat de l'art sur la déformation active

De nombreuses études géodésiques modélisent la tectonique décrochante de la Californie du Sud avec des dislocations verticales à quasi verticales sans aucune liaison avec d'autres failles (Plesch *et al.*, 2007). Le long du « Big Bend », les mesures géologiques des taux de glissement de la faille de SA varient de 24.5+-3.5 mm/an (Weldon et Sieh, 1985)

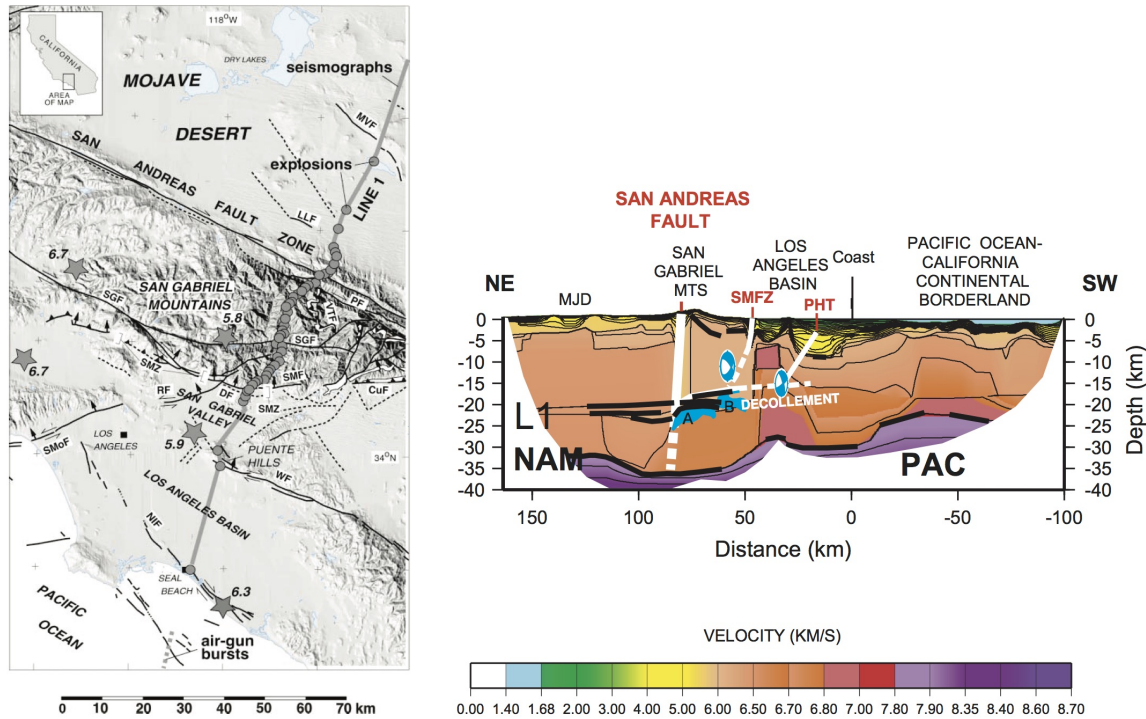


FIGURE 1.24 – Trace en surface de la ligne sismique LARSE 1 en Californie du Sud (A) et son interprétation tectonique (B) montrant un décollement majeur, s'enracinant au niveau de la faille de San Andreas à une profondeur de ~20 km et le long duquel viennent se brancher les chevauchements à forts pendages de Sierra Madre et de Puente Hill (Crédit : Modifié à partir de Fuis *et al.* (2001a) et Fuis *et al.* (2007)).

au Cajon Pass à 35 +7mm/an au Pallett Creek (Salyards *et al.*, 1992). Les mesures court-terme géodésiques indiquent des taux de déformations souvent plus faibles variant de 15 mm/an pour les modèles de blocs (Shen *et al.*, 1996; Meade et Hager, 2005), en passant par 25 mm/an pour les modèles visco-élastiques (McCaffrey, 2005; Tong *et al.*, 2014), et allant jusqu'à 32.5 mm/an pour les modèles élastiques à une seule dislocation (Savage et Lisowski, 1995).

Dans ces études, les déplacements verticaux mesurés par le GPS sont souvent négligés ou bien associés à des déformations grandes longueurs d'onde du manteau lithosphérique (Smith et Sandwell, 2006; Sandwell et Smith, 2009). Par exemple, une récente étude de Howell *et al.* (2016) explique l'ensemble des déplacements verticaux de la Californie du Sud par la flexure de la faille de San Andreas prédictive par des modèles de cycles sismiques visco-élastiques. Pour les études interférométriques, le signal vertical est soit négligé (Lundgren *et al.*, 2009; Chaussard *et al.*, 2015, 2016) ou bien systématiquement soustrait

PRINCIPES GÉNÉRAUX ET CONTEXTE

aux cartes de vitesses InSAR grâce aux GPS, afin de ne garder que les composantes horizontales de déplacements ([Fialko, 2006](#); [Lindsey et al., 2014](#); [Lindsey et Fialko, 2013](#); [Tong et al., 2014](#)).

Les taux de chargement des chevauchements restent quant à eux faiblement étudiés par géodésie du fait des faibles connaissances sur la géométrie de ces structures en profondeur ($>5\text{km}$), et des limitations de résolution géophysiques et géodésiques. Seule une étude de ([Argus et al., 2005](#)) détermina grâce au GPS, dans un modèle à dislocation unique semi-infinie et à pendage constant, un glissement des chevauchements des Puente Hills de 9 mm/an jusqu'à une distance peu profonde de 6 km. Ce modèle est en contradiction avec les mesures géologiques indiquant seulement 3 mm/an de glissement long-terme le long des Pente Hills et des chevauchements des Elysians Park.

1.4.3 Le « Big Bend »

Pour ces travaux je m'intéresserai à un profil au travers les montagnes des San Gabriels s'étendant du bloc Mojave à Palos Verdes afin de contraindre le chargement des chevauchements sous Los Angeles. Bien que disposant d'une géométrie plus mature et complexe que le système de failles de Haiyuan, le système de failles de San Andreas présente une géométrie similaire (Fig. 1.25). Ici, l'obliquité de la faille lithosphérique de SA contrôle le raccourcissement local entre le block Mojave et Los Angeles. Ce raccourcissement est accommodé par le glissement en profondeur du décollement intra-crustal se développant sous la région de Los Angeles d'où viennent se brancher les failles peu profondes à faibles pendages ([Gaudemer et al., 1995](#); [Bowman et al., 2003](#)). La géométrie de ce décollement contrôle la quantité de soulèvement de chacun des blocs qu'il délimite et le champs de déformation actuel.

J'utiliserais pour cette étude les réseaux permanents GPS du Plate Boundary Observatory (PBO) gratuitement disponible par EarthScope, ainsi qu'une carte de vitesse Envisat, produit par [Liu et al. \(2014b\)](#). Je chercherai à réconcilier les modèles géologiques des modèles géodésiques de déformation intersismique en introduisant des contraintes cinématiques long-terme à chaque changement de géométrie des structures profondes. J'identifierai d'abord un modèle dit « en fleur », fait d'un réseau de rampes et de décollements, basé sur une revue tectonique et géophysique de la région. J'explorerais ensuite avec une approche Bayésienne et une cinématique conservative, diverses géométries compatibles avec ce réseau de structures et en accord avec les observations de surface GPS et InSAR. Je présenterai ainsi des nouveaux taux de glissements pour la faille de San

Andreas et pour les chevauchements de Sierra Madre et des Puente Hills.

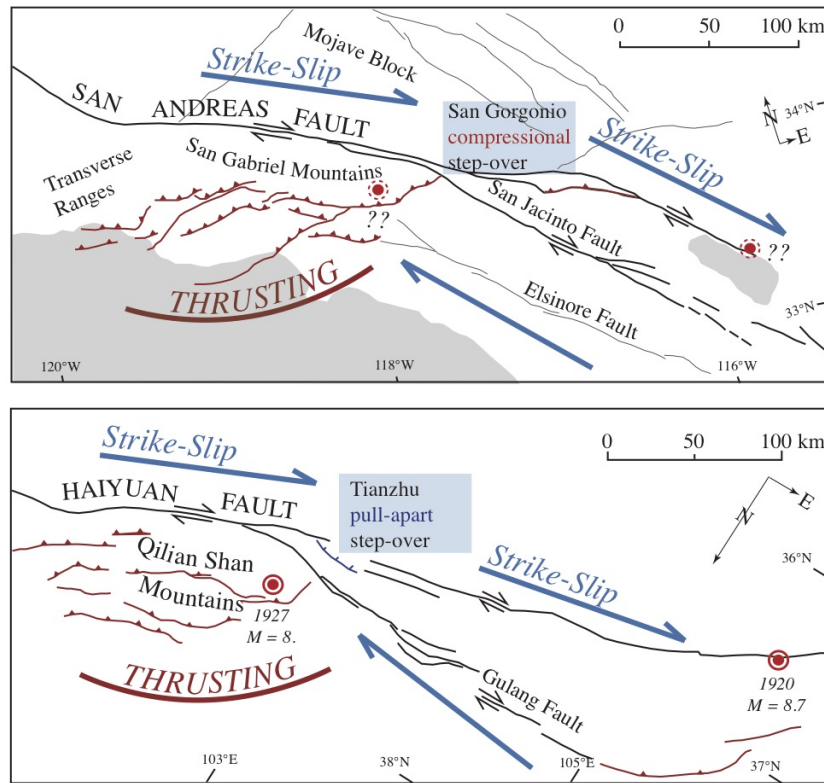


FIGURE 1.25 – Analogie entre le système de faille de Haiyuan et du « Big Bend » de la faille de San Andreas (after, [Gaudemer et al., 1995](#)).

Première partie

Modèles géodésiques de
partitionnement au Tibet et en
Californie

Chapitre 2

Along strike variations of the partitioning of convergence across the Haiyuan fault system detected by InSAR

Sommaire

| | | |
|------------|--|----|
| 2.1 | Introduction | 59 |
| 2.2 | GPS velocity field | 62 |
| 2.3 | InSAR velocity field | 63 |
| 2.4 | 2D models | 64 |
| 2.4.1 | Model geometry | 66 |
| 2.4.2 | Free parameters | 66 |
| 2.4.3 | Inversion method | 67 |
| 2.4.4 | Inversion results | 68 |
| 2.5 | Discussion | 69 |
| 2.5.1 | InSAR and Bayesian methods | 69 |
| 2.5.2 | Lateral variations of the slip partitioning | 72 |
| 2.5.3 | Comparison with geological time scales | 75 |
| 2.5.4 | Influence of the M~8, 1920 Haiyuan and 1927 Gulang earthquakes | 76 |
| 2.6 | Conclusions | 77 |
| 2.7 | Supplementary Material | 78 |

Preface

Cette étude se place dans la continuité des travaux de thèse d'Olivier Cavalié et de Romain Jolivet. [Jolivet *et al.* \(2012\)](#) identifièrent une zone de fluage dans une zone de relai entre la zone sismogénique et la zone de lacune sismique (Fig. 1.19) associée à de la micro sismicité importante et quelques M~5 ces dernières années ([Lasserre *et al.*, 2001](#)). Cette étude se place un peu plus à l'Ouest et recouvre une autre zone de relai importante, le basin en pull apart de Tianzhu, également associé à une sismicité sur des structures secondaires en arrière de la faille principale. Dans cette zone, le peu de GPS déployés ne semble pas indiquer de glissement peu profond de la faille d'Haiyuan et ne se présente pas assez dense pour caractériser le fonctionnement du système ni en champ proche ni en champ lointain. L'application de l'InSAR dans cette zone nécessite de surmonter une combinaison de multiples difficultés en raison de la zone montagneuse (les Qilian Shan), du saut topographique de part et d'autre de la faille beaucoup plus important qu'à l'Est, et d'une faible déformation corrélée à la topographie générée par un creep profond (donc de grande longueur d'onde en ambiguïté avec les résidus orbitaux). Le but de ces travaux, qui ont débuté lors de mon stage de Master 2 sous la direction de Cécile Lasserre, fut de tester, tout d'abord, les dernières améliorations pour le traitement de séries temporelles d'image radar. A l'époque, l'ensemble des ces outils ne s'imbriquaient pas dans une suite cohérente dans la chaîne de traitement NSBAS, ce qui me demanda l'écriture d'un ensemble de scripts afin d'automatiser le traitement et de vérifier l'apport de chacune des étapes. Bien que ce travail, effectué par tâtonnement et repris durant ma thèse, représente une lourde charge, il ne représente pas une partie majeure de ce chapitre et se retrouve principalement dans les suppléments. Cette étude est le résultat d'une collaboration avec Sylvain Barbot et Paul Tapponnier de l'Observatoire de Singapour, débutée lors mon séjour prédoctoral d'un an à la suite de mon Master et poursuivie tout le long de ma thèse. Elle est aussi le résultat d'une collaboration avec Romain Jolivet, qui m'a appris les techniques Bayésiennes et guidé dans l'écriture de mon premier papier. Dans ce chapitre, j'étudierai ainsi deux profils indépendants de part et d'autre de la transition géométrique de la faille d'Haiyuan. Je comparerai les conditions aux limites nécessaires à appliquer à la frontière de deux profils de part et d'autre du bassin, dans le but de reproduire le champ de vitesse observé. Je montrerai que les deux zones indiquent des conditions aux

limites similaires avec un raccourcissement moyen de direction N82°. Cette démarche indique qu'un fort partitionnement du taux de convergence, contrôlé par la géométrie de la faille lithosphérique d'Haiyuan, peut expliquer la complexité de système de failles en surface ainsi que l'uniformité des champs de déplacement. Ces travaux ont fait l'objet d'un proceedings dans la conférence "Dragon 3Mid Term Results Symposium" (Daout *et al.*, 2014), puis ont été acceptés dans la revue « Geophysical Journal International », sous le titre "Along strike variations of the partitioning of convergence across the Haiyuan fault system detected by InSAR" par S. Daout, R. Jolivet, C. Lasserre, M.-P. Doin, S. Barbot, P. Tapponnier, G. Peltzer, A. Socquet and J. Sun (Daout *et al.*, 2014, 2016c).

2.1 Introduction

Present-day tectonics in Asia results from the India-Eurasa collision, which initiated about 55 million years ago (e.g., Jaeger *et al.*, 1989) and continues today at a velocity of about 4 cm/yr (e.g., Molnar et Tapponnier, 1975a; Tapponnier et Molnar, 1977; Wang *et al.*, 2001). Oblique convergence observed across the Tibetan plateau is accommodated by extrusion along major fault systems as well as crustal thickening resulting from successive accretionary wedges from the south-west to the north-eastern boundary of the plateau (e.g., Meyer *et al.*, 1998; Tapponnier *et al.*, 2001; Métivier *et al.*, 2007). Crustal deformation is partitioned between major strike-slip faults (e.g. Haiyuan, Altyn Tagh, Kunlun, Karakorum faults) and thrust fault systems (e.g. Himalaya, Qilian Shan, Lungmen Shan thrusts). These fault systems are responsible for devastating $M \sim 7.5\text{-}8$ earthquakes, including strike-slip events (e.g. 1920 Haiyuan (Deng *et al.*, 1986) and 2001 Kokoxili earthquakes (Lasserre *et al.*, 2005)) and thrust events (e.g. 1927 Gulang (Gaudemer *et al.*, 1995) and 2008 Wenchuan earthquakes (Shen *et al.*, 2009)). Modeling the kinematics and the partitioning of the deformation on active structures is thus essential to estimate their potential seismic hazard.

Here, we focus on the southeastern end of the Qilian Shan mountain range, where the Qilian thrusts connect to the Haiyuan left-lateral fault system, at the north-eastern boundary of the Tibetan plateau (e.g., Gaudemer *et al.*, 1995; Lasserre *et al.*, 2002; Liu-Zeng *et al.*, 2007; Cavalié *et al.*, 2008; Jolivet *et al.*, 2012). We use geodetic data (SAR interferometry -InSAR- and GPS) to quantify present-day displacement rates across three main structures : (1) the Qilian thrusts, ~ 30 km north of the Haiyuan Fault, that ruptured during the $M \sim 8$, 1927 earthquake, (2) the left-lateral Gulang Fault, and (3) the central section of the left-lateral Haiyuan Fault, unbroken for more than 1000 years,

referred to as the Tianzhu seismic gap ([Gaudemer et al., 1995](#)) (Fig. 2.1). This seismic gap, which extends for more than 250 km, is divided into four segments from west to east ([Liu-Zeng et al., 2007](#)) : (1) the Leng Long Ling (LLL) segment west of the Gulang-Haiyuan triple junction, (2) the Jing Qiang He (JQH) segment, (3) the Maomao Shan (MMS) segment, and (4) the Lao Hu Shan (LHS) segment. The Haiyuan Fault is marked by a major left-lateral step over : the 10 km-wide Tianzhu pull-apart basin, separating the JQH and MMS segments (Fig. 2.1). The basin marks a geometrical transition between the eastern Haiyuan fault system, where deformation is observed on the Haiyuan and Gulang strike-slip faults connected through a décollement, and the western Haiyuan fault system, where strain is partitioned between the Haiyuan Fault and the Qilian Shan thrust fault system forming a seismically active transpressional bend ([Gaudemer et al., 1995; Lasserre et al., 2001](#)) (Fig. 2.2). Along the western fault system, [Gaudemer et al. \(1995\)](#) proposed that thrust faults and the Haiyuan Fault root on a $10 - 20^\circ$ south-dipping décollement, forming a typical “flower structure” across this strike-slip restraining bend of the fault. South of the Haiyuan Fault, slip on a sub-horizontal, intra-crustal décollement is oblique to the orientation of the Haiyuan Fault (blue vector in Fig. 2.2) and accommodates both convergence (red vectors in Fig. 2.2) and transform components (black vector in Fig. 2.2) of the relative block motion. Recent broadband seismic survey from [Ye et al. \(2015\)](#) illuminates, at the root of the Haiyuan Fault, the underthrusting of the mantle of the North China lithosphere beneath the Qilian ranges and the presence of large scale intra-crustal décollements in the crust. These results support the Haiyuan tectonic model defined by [Gaudemer et al. \(1995\)](#) or the large scale model proposed by [Tappognier et al. \(1990\)](#), [Meyer et al. \(1998\)](#) and [Tappognier et al. \(2001\)](#), in which the Tibetan plateau has formed by successive crustal thickening and shortening bounded by major lithospheric faults.

We evaluate the compatibility of contemporary geodetic displacement rates with these models at different scales, which include partitioning of slip on strike-slip and thrust structures to explain the kinematics of oblique convergence across the Haiyuan fault system. We use GPS-derived velocities from [Liang et al. \(2013\)](#) and we derive maps of the average ground velocity using InSAR data from two tracks crossing the Haiyuan fault system, acquired along descending orbits by the Envisat satellite between 2003 and 2011 (Fig. 2.1). We first describe some strategic InSAR processing steps applied to increase the signal-to-noise ratio across the Haiyuan Fault. We then develop a 2D model based on a Bayesian approach to invert two independent GPS and InSAR-derived LOS velocity profiles, on both sides of the Tianzhu basin, exploring the differences in the way slip is

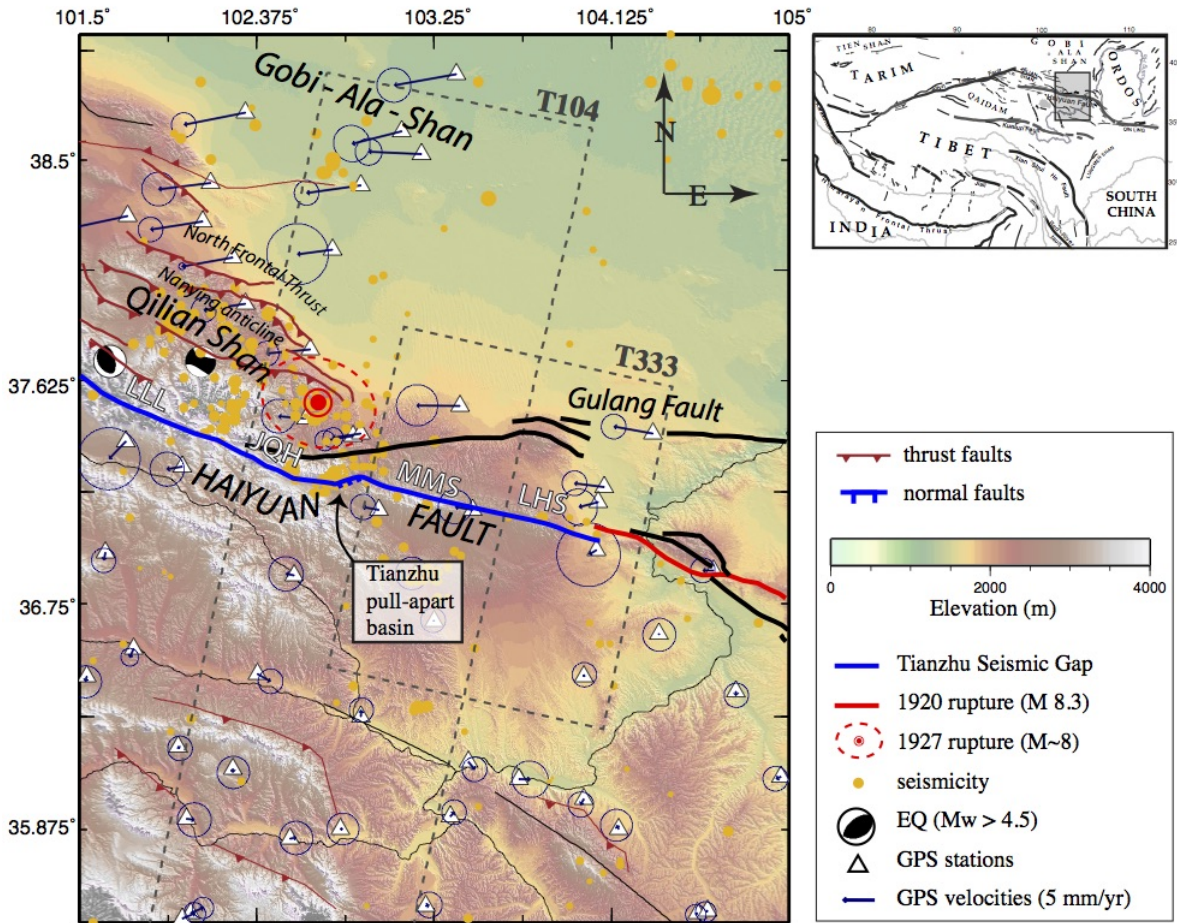


FIGURE 2.1 – Seismotectonic setting of the Haiyuan fault system. The focal mechanisms of earthquakes of magnitude > 5 from 2000 to 2014 are from USGS. Yellow dots show seismicity from 1988 to 2009 recorded by the Seismological Institute of Lanzhou. Blue arrows are GPS data from the Observation Network of China (ONOC) (Liang *et al.*, 2013) (in the South Haiyuan block reference frame). Dashed rectangles show the footprint of ENVISAT descending tracks 104 and 333. The Haiyuan-Gulang fault system is outlined in black, the Tianzhu seismic gap, unbroken since ~ 1000 years, in blue, and the 1920 and 1927 Haiyuan and Gulang rupture traces in red. The Tianzhu seismic gap is segmented in four segments from west to east : the Leng Long Ling (LLL), Jing Qiang He (JQH), Maomao Shan (MMS) and Lao Hu Shan (LHS) segments. The North Frontal Thrust (NFT) separates the Qilian Shan from the desert platform to the north. Inset at top right shows the location of the figure.

partitioned between the various active structures. We show that InSAR data helps to constrain the fault geometry and present-day kinematics, and we discuss the consistency of our interseismic deformation model with long-term tectonic models.

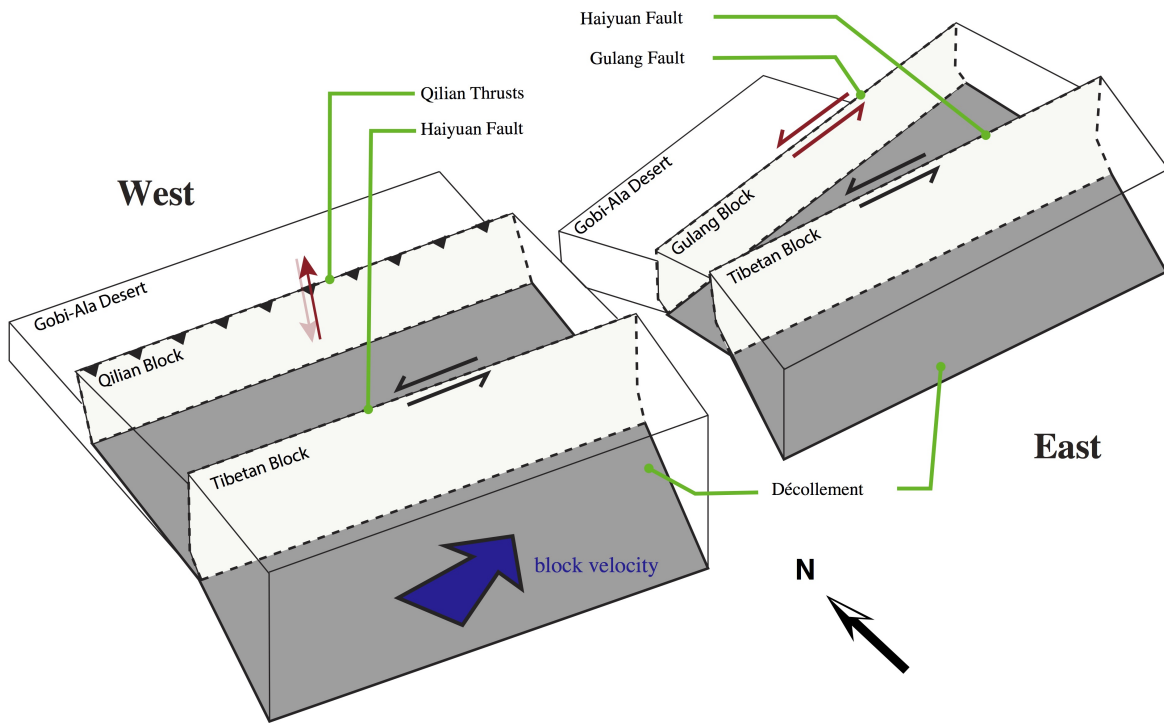


FIGURE 2.2 – Schematic block model across the Haiyuan fault system illustrating the variation of slip partitioning west (left) and east (right) of the Tianshu pull-apart basin. The oblique deep secular motion (large blue arrow) is accommodated by a deep crustal décollement below the brittle-ductile transition. The transpressional Qilian block is decoupled from Tibetan plateau by the vertical left-lateral Haiyuan fault and the south-dipping Qilian Shan thrusts. Identically, the Gulang block is bounded by the Haiyuan and Gulang left-lateral Faults that root in the décollement.

2.2 GPS velocity field

We use the GPS velocity field provided by [Liang et al. \(2013\)](#), that includes 750 continuous and campaign stations around the Tibetan Plateau spanning over 10 years since 1999. We rotate the GPS solution with respect to a rigid block bounded by the Haiyuan fault, to the south of it. To do so, we select a subset of 13 stations south of the Haiyuan fault to estimate an Eulerian rotation pole (Fig. 2.9a). All these stations are selected far from any faults to avoid trade-off between block rotation and interseismic deformation ([Socquet et al., 2006](#)). We invert for an Eulerian pole by minimizing the L1 norm of the ITRF08 velocities of this subset of stations. Our solution shows almost no residual velocities between observations and predictions indicating no internal deformation in this block south of the Haiyuan Fault (Fig. 2.9b). We then remove the predicted rotation by applying a Helmert transformation ([Bevis et Brown, 2014](#)) in order to reference the GPS

velocity field with respect to the South Haiyuan block (Fig. 2.1).

2.3 InSAR velocity field

In addition to GPS data, we use SAR data on two descending tracks of the Envisat satellite. InSAR ground velocity map on track 333 (Fig. 2.1) is from Jolivet *et al.* (2012). Moreover, we process all the 31 available SAR data acquired by the ENVISAT satellite on descending track 104, using the NSBAS chain based on the ROI_PAC software (Rosen *et al.*, 2004; Doin *et al.*, 2015). From the raw data, we first compute all Single Look Complex (SLCs) images with a common Doppler bandwidth. We coregister the SLCs to a single master image chosen on the basis of maximum theoretical coherence (Hooper *et al.*, 2007). We then compute differential interferograms, with 4 looks in range and 20 in azimuth (refer to Fig. 2.8 for interferogram network). The change in elevation between the desert of the Gobi Ala Shan platform (<1000 m), north of the Haiyuan fault (Fig. 2.1), and the mountain ranges (~ 4000 m), across and south of the fault, leads to significant atmospheric delays and possible topographic errors, affecting the coherence and our unwrapping capability of the InSAR data. To improve coherence over areas with rough topography and produce a continuous map of displacement, we use the newly developed tools in the NSBAS interferometric chain (Doin *et al.*, 2015), including corrections of atmospheric delays and local Digital Elevation Model (DEM) errors before unwrapping (Jolivet *et al.*, 2011; Ducret *et al.*, 2014). These corrections are of particular importance as they reduce the fringe rate and phase noise across regions with high topographic gradients, hence preventing unwrapping errors. Tropospheric delays are predicted from the global atmospheric re-analysis ERA-Interim (ERA-I) computed by the European Center for Medium-Range Weather Forecast (ECMWF) (Doin *et al.*, 2009; Jolivet *et al.*, 2011, 2014a). We then multilook again 8 times in range and 40 times in azimuth, apply a low pass filter and unwrap the phase. The unwrapping path varies with the phase colinearity (Pinel-Puyssegur *et al.*, 2012), avoiding the unwrapping of incoherent areas (Grandin *et al.*, 2012; Doin *et al.*, 2015). We derive the ground velocity along the Line-Of-Sight (LOS) using a modified Small Baseline Subset time series Analysis (SBAS), including a linear temporal constraint for pixels covered by disconnected subsets of interferograms (Cavalié *et al.*, 2007; López-Quiroz *et al.*, 2009). This constraint is arbitrary weighted by a small coefficient to not affect the result for connected pixels. Finally, we remove residual unwrapping errors using an iterative procedure based on misclosure analysis of the interferometric network. At each iteration, misclosure maps

are checked by visual inspection. Unwrapping errors are then corrected for each interferogram and times series analysis is iterated ([López-Quiroz et al., 2009](#); [Doin et al., 2011](#)). The reliability of each unwrapped interferogram is estimated computing the misclosure of the interferometric network. If large, we then check visually the corresponding interferogram and correct its unwrapping error by setting manually a high priority bridge along another unwrapping path with less fringe gradients. A more detailed discussion of the processing as well as additional figures that allow for assessment of the quality of InSAR corrections are available in the supplementary materials (Fig. [2.10](#) for tropospheric corrections, Fig. [2.11](#) for local DEM errors corrections and Fig. [2.12](#) for velocity map).

The LOS velocity maps provide a continuous view of the surface displacement field over each track highlighting the contribution of active structures (Fig. [2.3](#)). To first order, ground velocity suggests different patterns of strain accumulation on both sides of the 10 km-wide Tianzhu basin (Fig. [2.3](#)). In the following, we analyse two profiles of LOS velocity (50 km-wide and 300 km-long) perpendicular to the Haiyuan fault, east and west of the Tianzhu basin, where the Haiyuan fault strikes $N103^{\circ}E$ and $N112^{\circ}E$, respectively (Fig. [2.3](#), [2.4](#), [2.5](#)), and explore the apparent change of strain accumulation along strike. Along the eastern fault section (LHS and MMS segments; Fig. [2.3b](#), [2.5a](#)), we observe localized high strain along the Haiyuan fault, due to creep along the seismogenic portion of the fault ([Cavalié et al., 2008](#); [Jolivet et al., 2012, 2013, 2015a](#)). The strain pattern observed 60-70 km north of the Haiyuan fault is consistent with left-lateral motion along the Gulang Fault ([Jolivet et al., 2012](#)) (Fig. [2.3b](#)). Along the western section (LLL and JQH segments), the velocity map and profile reflect the combined effect of vertical motion associated with the Qilian Shan thrusts and of strike-slip motion on the Haiyuan fault (Fig. [2.3c](#), [2.4a](#)). With respect to the southern side of the Haiyuan fault, the northern side is moving ~ 4 mm/yr in the LOS direction away from the satellite (Fig. [2.3c](#), [2.4a](#)). A zone of local subsidence is also observed ~ 70 km north of the Haiyuan Fault in a region of sand dunes, at the foot of the Qilian thrusts. It might be of non tectonic origin, related to water pumping.

2.4 2D models

To understand the kinematics and the partitioning of the deep-secular motion on both sides of the Tianzhu pull-apart basin, we test the model proposed by [Gaudemer et al. \(1995\)](#) from geological observations (Fig. [2.2](#)). We adjust the fault geometry and estimate corresponding slip rates using a Bayesian approach on the InSAR and GPS data

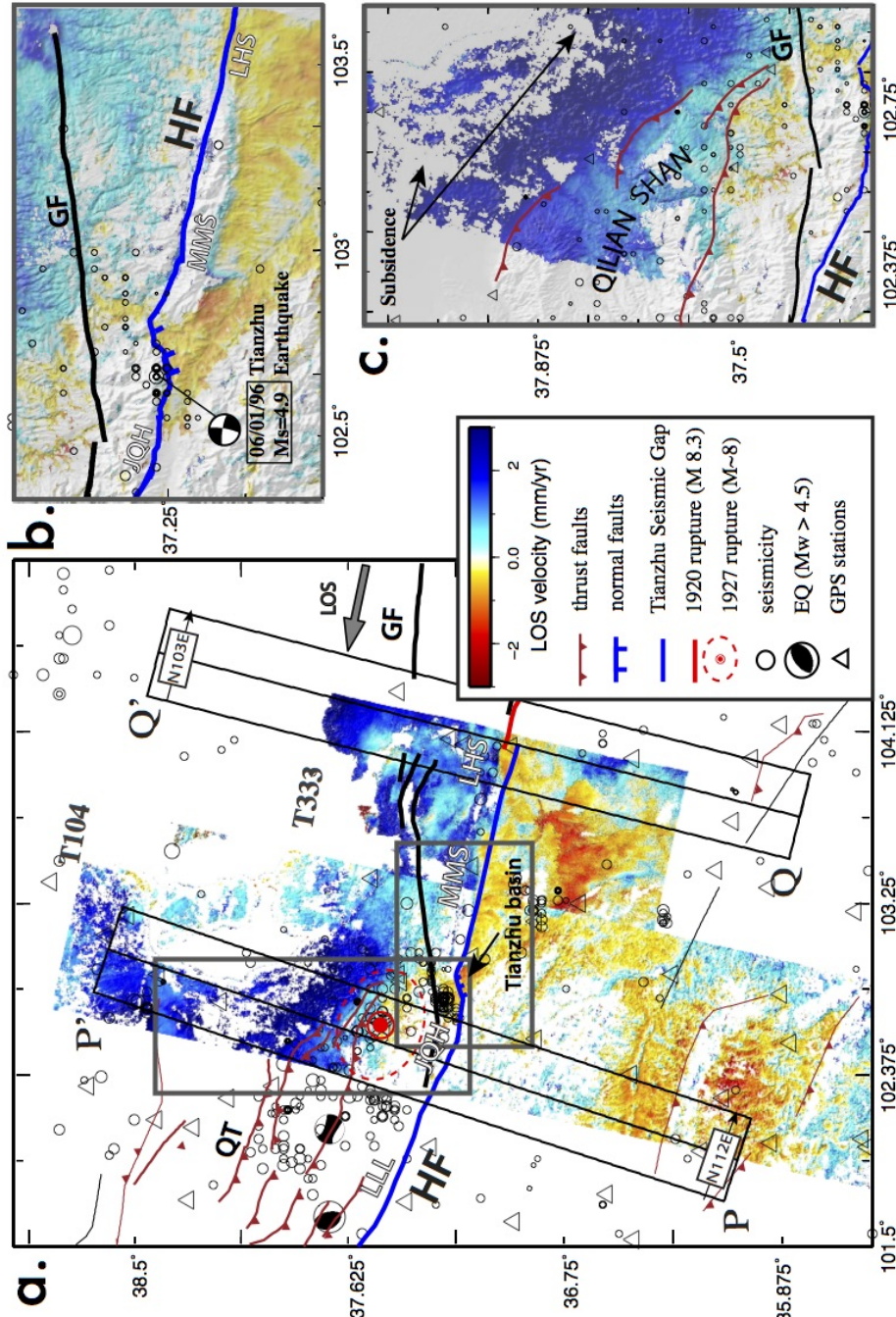


FIGURE 2.3 – a) Line Of Sight velocity maps for track 104 (left) and track 333 (right) showing a transition in the slip partitioning on both sides of the Tianzhu pull-apart basin. Positive motion is away from the satellite. Faults, GPS network and seismicity are as in Fig. 2.1. We define two profiles perpendicular to the Haiyuan fault (black rectangles), west (PP') and east (QQ') of the basin. The Jing Qiang He (JQH) segment, the Lao Hu Shan (LHS) segment, the Qilian shan Thrusts (QT) and the Gulang Fault (GF) represent the faults segments used in our model. b) Zoom around the Tianzhu pull-apart basin showing a change in the fault locking depth between the (MMS) and the (LHS) segments. c) Zoom around the Qilian Shan front bounding a zone of seismicity and uplift to the south and a zone of subsidence north of the thrusts. b) and c) are superimposed to the SRTM Digital Elevation Model.

projected on two independent profiles. The two profiles are on both sides of the Tianzhu pull-apart basin and perpendicular to the Haiyuan Fault. We test whether the apparent east-west variability of the strain pattern is consistent with the model of partitioning of the convergence on the structures observed at the surface (Fig. 2.3).

2.4.1 Model geometry

For both profiles, the model consists of two-dimensional dislocations, infinite in the along-strike dimension, embedded in a homogeneous elastic half-space. The model includes both semi-infinite and finite dislocations accounting for deformation at shallow depth. We model the flat décollement by a horizontal semi-infinite dislocation, limited to the north by the Haiyuan fault, with oblique motion (both strike-slip and dip-slip). We extend the décollement with a ramp, connecting the northern tip of the décollement to the down-dip end of locked faults in the seismogenic part of the crust (Fig. 2.4b - Fig. 2.5b). A detailed description of each dislocation used to build the models in Fig. 2.4b and Fig. 2.5b is available in the supporting information (Fig. 2.13). For the eastern profile, the ramp points toward the Gulang Fault, oblique to the profile. We allow for creep on the shallow portion of the Haiyuan Fault on a vertical finite segment up to a shallow locking depth. For the western profile, the ramp points toward the foot of the Qilian Shan thrusts.

2.4.2 Free parameters

We assume a horizontal décollement, so that the dip-slip component on this flat structure, \dot{U}_{short} , is an effective estimate of the shortening rate perpendicular to the fault system (Fig. 2.4b - Fig. 2.5b). For both profiles, we estimate the depth, H_1 , of the semi-infinite dislocation representing the décollement, as well as the slip rate parallel, \dot{U}_{s1} , and perpendicular, \dot{U}_{short} , to the Haiyuan fault system. Note that surface displacements due to the strike-slip component, \dot{U}_{s1} , are not influenced by the dip-angle of the structure. We test values of depth, H_1 , between 0 and 30 km, left-lateral velocity, \dot{U}_{s1} , between 0 and 20 mm/yr, and of shortening rate, \dot{U}_{short} , between 0 and 10 mm/yr. For the shallow ramps, we estimate the horizontal distance between the tip of the décollement and the bottom of the locked section of the frontal fault, D (also called *width* of the system), the locking depth of the frontal fault, H_2 , and the along-strike component of slip, \dot{U}_{s2} . The dip angles of the ramps are deduced from the parameters D , H_1 and H_2 . The along-

dip component of slip along the frontal structure is defined as the projection of the shortening, \dot{U}_{short} , along this dipping plane (McCaffrey, 2002).

For the eastern profile (Fig. 2.5b), we test values of strike-slip motion on the Gulang Fault, \dot{U}_{s2} , between 0 and 10 mm/yr, of locking depth, H_2 , between 0 and 30 km and of horizontal distance to the Haiyuan fault, D , between 25 and 75 km. On the vertical dislocation modeling creep on the Haiyuan fault, we test values of locking depth, H_c , between -0.5 and 10.5 km, and strike-slip component, \dot{U}_c , between 0 and 10 mm/yr. Note that we allow for non-physical negative values for the locking depth in order to better sample the 0 km value (full creeping of the seismogenic zone). Slip on the shallow dislocation, \dot{U}_c , is set lower or equal to \dot{U}_{s1} , allowing for a slip deficit on the creeping segment. Strike-slip on the Gulang fault is on a semi-infinite dislocation and the total strike-slip on the décollement is thus equal to the sum of \dot{U}_{s1} and \dot{U}_{s2} (Fig. 2.5b and Fig. 2.13B).

For the western profile, we test values of locking depth of the Qilian Shan thrusts, H_2 , between 0 and 30 km, of horizontal distance to the Haiyuan fault, D , between 0 and 60 km. Preliminary tests show that no creep is required on the western segment, so that we assume that the Haiyuan Fault is fully locked on this section. We consider no strike-slip motion on the Qilian Shan thrusts, consistent with geomorphological long-term observations (Gaudemer *et al.*, 1995) (Fig. 2.4a and Fig. 2.13A).

2.4.3 Inversion method

We use a Bayesian approach to explore the range of models allowed by geodetic data, to provide realistic estimates of uncertainties and to avoid some of the issues related to the regularization of the inverse problem such as the choice of damping factor or normality assumptions (Minson *et al.*, 2013). Bayes' rule writes the posterior probability density function (PDF) of a model, $p(\mathbf{m}|\mathbf{d})$ (i.e what we know from the prior and the data), as proportional to the prior PDF, $p(\mathbf{m})$ (i.e the knowledge before input from data), and the likelihood (i.e a measure of the misfit), such as :

$$p(\mathbf{m}|\mathbf{d}) \propto p(\mathbf{m}) \exp \left[-\frac{1}{2} (\mathbf{d} - \mathbf{g}(\mathbf{m}))^T \mathbf{C}_d^{-1} (\mathbf{d} - \mathbf{g}(\mathbf{m})) \right], \quad (2.1)$$

where \mathbf{d} is the vector of data, \mathbf{m} is the vector of model parameters, \mathbf{C}_d is the covariances matrix in the data space, and $\mathbf{g}(\mathbf{m})$ is the surface displacements predicted using a model \mathbf{m} .

For both profiles, the model, \mathbf{m} , includes the parameters previously described for geometry and slip rates, as well as InSAR and GPS reference frames. An azimuthal ramp is included for the InSAR data to explore trade-off between residual long-wavelength orbital errors and slip rates. The data vector, \mathbf{d} , is made of the LOS displacement rates and GPS velocities projected into profile-perpendicular and profile-parallel components along each profile. The data covariance (i.e describing uncertainties on observations), \mathbf{C}_d , includes the variance of the GPS measurements on its diagonal. For InSAR data, the covariance includes data variance as diagonal terms and data spatial correlation in the off-diagonal components. From data-model residuals of a preliminary inversion, we compute empirical covariance as a function of the distance between InSAR points on the residual velocity map (Lohman et Simons, 2005; Sudhaus et Sigurjón, 2009). We then estimate the best-fit exponential function to build the full data covariance (Chiles et Delfiner, 2009; Jolivet et al., 2015b). Phase residual distributions, empirical covariances, best-fit functions and covariance matrix for InSAR data are shown in Fig. 2.14.

For each profile independently, we draw random samples from uniform distributions between the minimum and the maximum values defined for all parameters and evaluate the posterior PDF using the Metropolis algorithm implemented in the pymc library (Metropolis et al., 1953; Patil et al., 2010). Our Markov chain has 20,000 iterations, rejecting the first 10,000 samples to minimize the effect of the initial model.

2.4.4 Inversion results

The complete comparison between the prior and posterior model distributions, as well as the first moments of the marginal posterior distributions, are summarized in Table 2.1 of the supplementary materials. All the uncertainties are documented with their 95% confidence interval.

For the western profile (Fig. 2.4), the mean posterior model suggests a depth of the décollement, H_1 , of 25 [19 – 30] km, and sets the tip of the shallow ramp, H_2 , at 15 [9 – 22] km. Our estimates also indicate a well-constrained width, D , of 24 [17.5 – 30] km, corresponding to a dip angle of the ramp of 21 [8 – 34]° below the Qilian Shan. The left-lateral slip-rate, \dot{U}_{s1} , on the western section of the Haiyuan Fault (JQH segment) is 8.6 [6.9 – 10] mm/yr and the mean shortening rate across the whole system, \dot{U}_{short} , is 3.5 [2.3 – 4.8] mm/yr. All the 5 PDFs (Fig. 2.4c) resemble normal distributions centered on the mean model, with higher skewnesses for the PDFs of D and H_2 (Table 2.1).

For the eastern profile (Fig. 2.5), the mean model includes 5.6 [4.5 – 6.9] mm/yr of

strike-slip motion along the Haiyuan Fault. The creep rate, \dot{U}_c , is of 4.6 [3.5–5.6] mm/yr between 0.5 [0.2–0.7] km (H_c) and 24 [14–30] km (H_1) depth. The depth of the Haiyuan Fault, H_1 , is not well constrained, as illustrated in the Figure 2.5c and described by the first moments of the marginal distribution (Table 2.1). The corresponding shortening rate across the fault system, \dot{U}_{short} , is of 2.6 [0.2–4.6] mm/yr. Left-lateral velocity on the Gulang segment is of 4.6 [2.6–6.3] mm/yr with a locking depth of 9 [2.5–14.5] km. The width, D , is constrained at 61 [54–72] km, corresponding to a dip angle of 13.5 [5–21]°. PDFs of \dot{U}_{s1} , \dot{U}_{short} , H_c , H_2 , \dot{U}_{s2} , \dot{U}_c , resemble normal distributions centered on the mean model (Fig. 2.5c, Table 2.1).

2.5 Discussion

2.5.1 InSAR and Bayesian methods

In areas of high relief, significant atmospheric delays and DEM errors lead to spatial aliasing of the wrapped and filtered interferometric phase, resulting in unwrapping errors (Grandin *et al.*, 2012). By flattening the interferometric phase with local DEM (Ducret *et al.*, 2014) and tropospheric corrections (Doin *et al.*, 2009; Cavalie *et al.*, 2007; Jolivet *et al.*, 2011), we significantly reduce the unwrapping errors and increase the total area of unwrapped phase over the Qilian ranges. This allows us to produce a continuous map across a region with more than 3000 m of elevation change and to study at large scale the kinematics of the fault system integrating all the structures. Unlike GPS measurements, InSAR has a strong sensitivity to vertical displacements and its high spatial resolution finely constrains strain localization and first order patterns of fault geometry. Moreover, the Bayesian method derives the range of possible values exploring the influence of fault geometry on surface displacements. To illustrate the contribution of InSAR data, we compare posterior model PDFs derived using GPS data only with those derived with InSAR data only, and those derived using both GPS and InSAR data (Fig. 2.4c, Fig. 2.5c). On the eastern profile, due to the lack of GPS stations in the far-field, the Gulang fault parameters are only controlled by InSAR. Without InSAR data, D and H_c , the width of the system and the depth of creep, are not constrained, with uniform posterior PDFs close to the prior uniform model. InSAR constrains the localisation of the deformation on a kilometric-wide zone and reveals no deformation between faults. For the other parameters, posterior PDFs obtained without InSAR data resemble normal distributions but are much wider than with the information enclosed

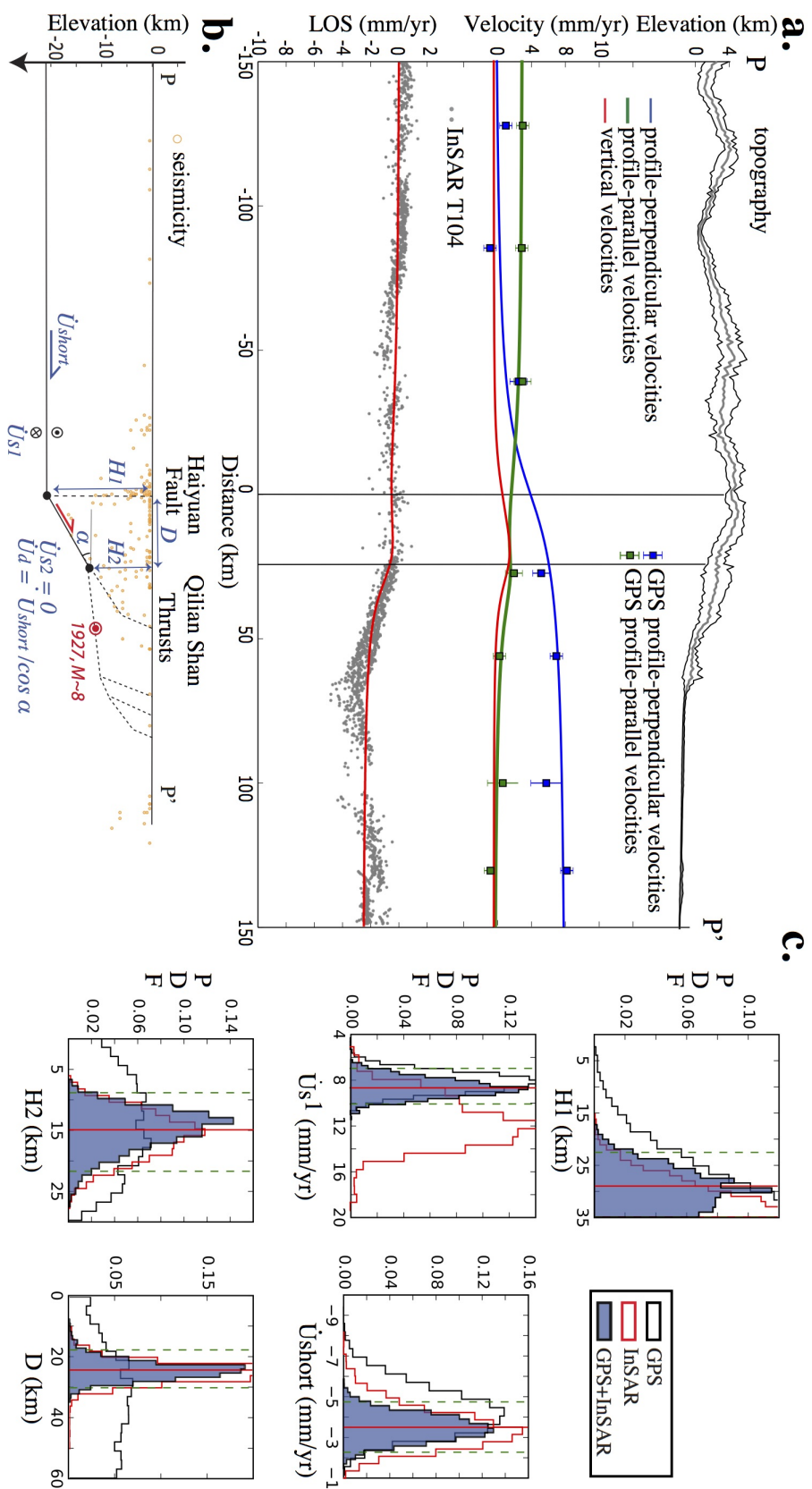


FIGURE 2.4 – Inversion model and results for profile PP', west of the Tianshu basin. a) Top : Topography (grey line for the average topography and black dash-lines for the maximum and minimum topography). Middle : profile-parallel (green square markers) and profile-perpendicular (blue square markers) GPS velocities with their associated 1σ uncertainties. Average model obtained (corresponding blue, green and red lines) along profiles. Bottom : LOS velocities (grey points). b) Fault geometry and fault velocities parameters explored in the inversion ; solid (resp. dashed) lines represent slipping (resp. locked) sections of the faults; free parameters are in blue; arrows indicate relative direction of slip on faults. c) Posterior marginal PDF using the GPS data only or the InSAR data only (black and red unfilled histograms, respectively) or the GPS+InSAR data (blue histograms), illustrating the slip partitioning across the fault system and the benefits of including the InSAR data. See text for further details on model setting.

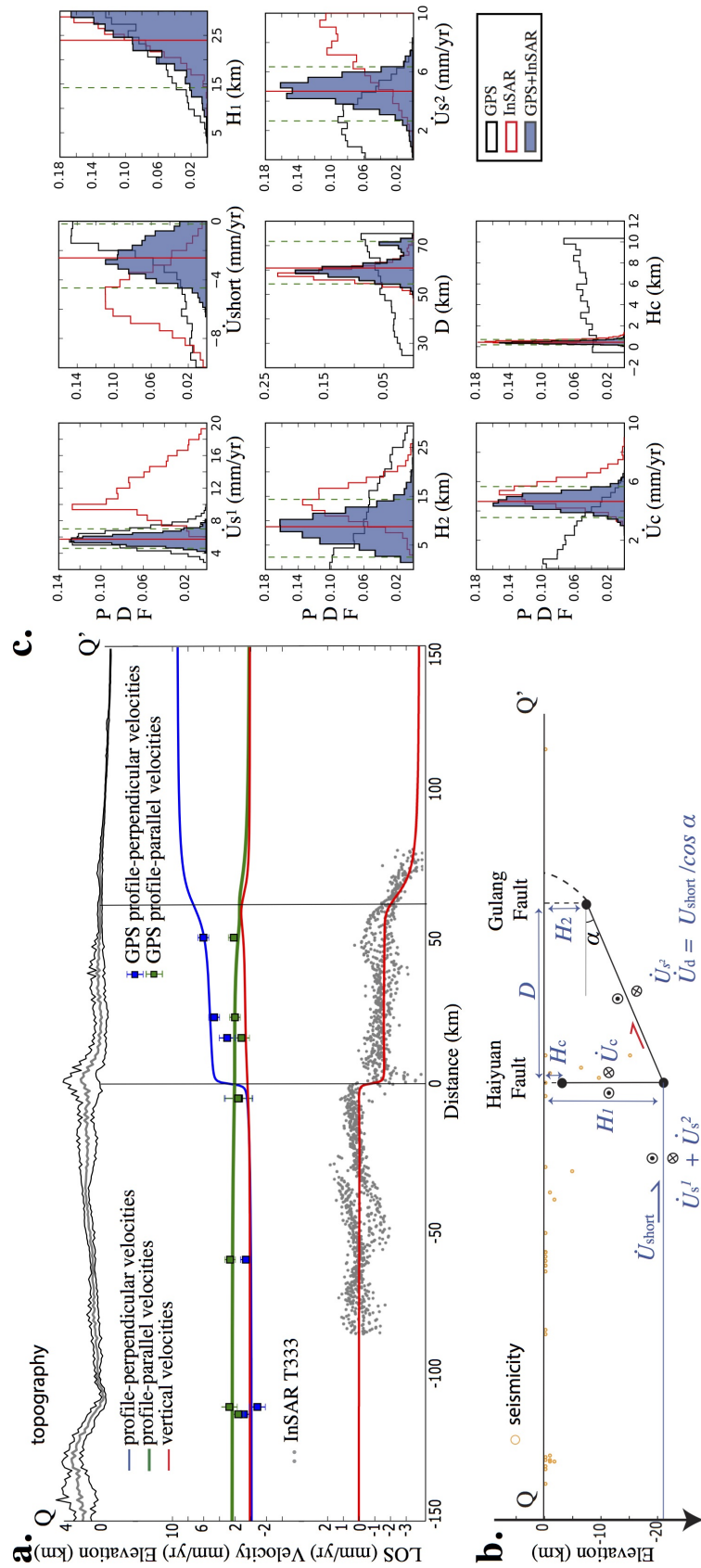


FIGURE 2.5 – Same as Fig. 2.4 for the eastern profile Q-Q'.

in the InSAR data. Although limited by the spatial correlation of the noise, the LOS velocity maps help to constrain the gradient of deformation and thus the locking depths of fault segments. For example, the 2σ uncertainties of H_2 are equal to ~ 14 km with GPS data only for the western and the eastern profiles, whereas while adding the InSAR data, uncertainties shrink to ~ 6 km. However, using InSAR data only results in wider and biased PDFs for slip rates with respect to those obtained using GPS data only, because of the trade-off between long-wavelength residual signal and the deformation (see posterior correlation coefficient matrix of the free parameters for the western and eastern profiles (Tables 2.2 and 2.3) and joint marginal PDFs (Fig. 2.16) for illustrations of these trade-offs). GPS data thus constrain the horizontal slip rates and the combination of InSAR and GPS together fixes the fault-system geometry.

2.5.2 Lateral variations of the slip partitioning

Our mean model indicates that horizontal shortening rates and left-lateral slip rates are differently distributed west and east of the Tianshu basin. Along the western section, oblique convergence is purely partitioned with 3.5 [2.3 – 4.8] mm/yr of shortening across the north-eastern Qilian Shan thrust system and 8.6 [6.9 – 10] mm/yr of left-lateral strike-slip motion on the Haiyuan Fault (Fig. 2.6a). In contrast, along the eastern section, our parameter exploration indicates that the left-lateral Gulang Fault accounts for 4.6 [2.6 – 6.3] mm/yr of strike-slip rate and 2.6 [0.2 – 4.6] mm/yr of shortening rate in directions perpendicular and parallel to the profile, respectively, whereas the Haiyuan Fault slips at a left-lateral rate of 5.6 [4.5 – 6.9] mm/yr at depth. This two-dimensional model implies a long-term slip vector along the Gulang fault system of 5.4 [3.7 – 7.0] mm/yr with an azimuth of 28 [1 – 51]° with respect to the N103E°-striking Haiyuan Fault. This result is in agreement with the geometry of the Gulang Fault at the surface, which forms an angle of $\sim 20 – 30$ ° with the MMS and LHS segments of the Haiyuan Fault (Fig. 2.3a,b, Fig. 2.15) and absorbs the shortening component by its obliquity (see velocity vectors sum in Fig. 2.6b). In agreement with studies by Cavalié *et al.* (2008) and Jolivet *et al.* (2012, 2013, 2015a), our model shows that slip rate on the vertical creeping segment, \dot{U}_c , is on the same order as the Haiyuan Fault deep-seated rate, \dot{U}_{s1} . We evaluate the probability that no strain is presently accumulating on the Haiyuan Fault along the eastern profile (i.e. \dot{U}_c is equal to \dot{U}_{s1} and H_c is null). We found that 88% of the models have a creep rate \dot{U}_c equal to \dot{U}_{s1} within 2 mm/yr and have a locking depth, H_c , shallower than 1 km, confirming a low probability of slip deficit buildup along the LHS portion of

the Haiyuan Fault ([Cavalié et al., 2008](#); [Jolivet et al., 2012](#)).

We then evaluate the probability for the far-field tectonic motion across the whole Haiyuan fault system (blue vector in Fig. 2.2) to be consistent on both sides of the Tianzhu pull-apart, comparing the azimuth and the norm of the convergence vectors for the eastern and the western profiles. To the west, the far-field tectonic convergence vector on the décollement is the sum of strike-slip motion along the Haiyuan Fault, \dot{U}_{s1} , and shortening across the fault system, \dot{U}_{short} (Fig. 2.6a). To the east, the total convergence on the décollement is the sum of the combined strike-slip motion along the Haiyuan, \dot{U}_{s1} , and Gulang Fault, \dot{U}_{s2} , and the shortening component across the fault system, \dot{U}_{short} (Fig. 2.6b). We find that 64% of the models explaining the geodetic data show similar convergence rates within 2 mm/yr and similar azimuth within 20°. On average, to the west we estimate a convergence rate of 9.3 [7.8 – 10.8] mm/yr with a N89.5 [82 – 98] °E azimuth (Fig. 2.7) across the 24 [17.5 – 30] km-wide fault-system partitioned between the $N112E^\circ$ -striking left-lateral Haiyuan fault and the Qilian Shan thrusts that connect at a depth of 25 [19 – 30] km. To the east, we estimate a convergence rate of 10.7 [8.2 – 13.1] mm/yr with a N89 [77 – 103] °E azimuth (Fig. 2.7) across the 61 [54 – 72] km-wide fault-system distributed in between the $N103E^\circ$ -striking Haiyuan Fault and the Gulang Fault that merge at a depth of 24 [14 – 30] km. The present-day geodetic displacements may thus be explained with a long-term “flower structure” model, with a uniform convergence rate of 10 [8.6 – 11.5] mm/yr with a N89 [81 – 97] °E across the whole fault system (Fig. 2.6, Fig. 2.7). Such consistency of the far-field tectonic motion implies that the connected thrusting and strike-slip faulting are thus complementary facets of the same deep-seated deformation process, participating into the growing and rising of the Tibetan plateau ([Tapponnier et al., 2001](#)).

In previously proposed block models with only vertical faults, results mostly depend on the prior choice of the number and shape of rigid blocks ([Meade, 2007a](#); [Thatcher, 2007](#); [Loveless et Meade, 2011](#)). These models can describe the first order geodetic deformation and account for 3D spatial interaction between faults. However, they do not allow for local complexity of the structures, such as partitioning, or do not explore the lateral variations of locking depths, which leads to a uniform strike-slip rate along the various vertical segments of the Haiyuan Fault of ~ 9 mm/yr ([Meade \(2007a\)](#), without off-fault distributed deformation) or ~ 6 mm/yr ([Thatcher \(2007\)](#), [Loveless et Meade \(2011\)](#), with internal micro-plate strain modeled by off-fault distributed deformation). In comparison, our model explores the geometry of the fault-system at depth and the partitioning of the uniform deep-seated motion in between the various segments intervening in the up-

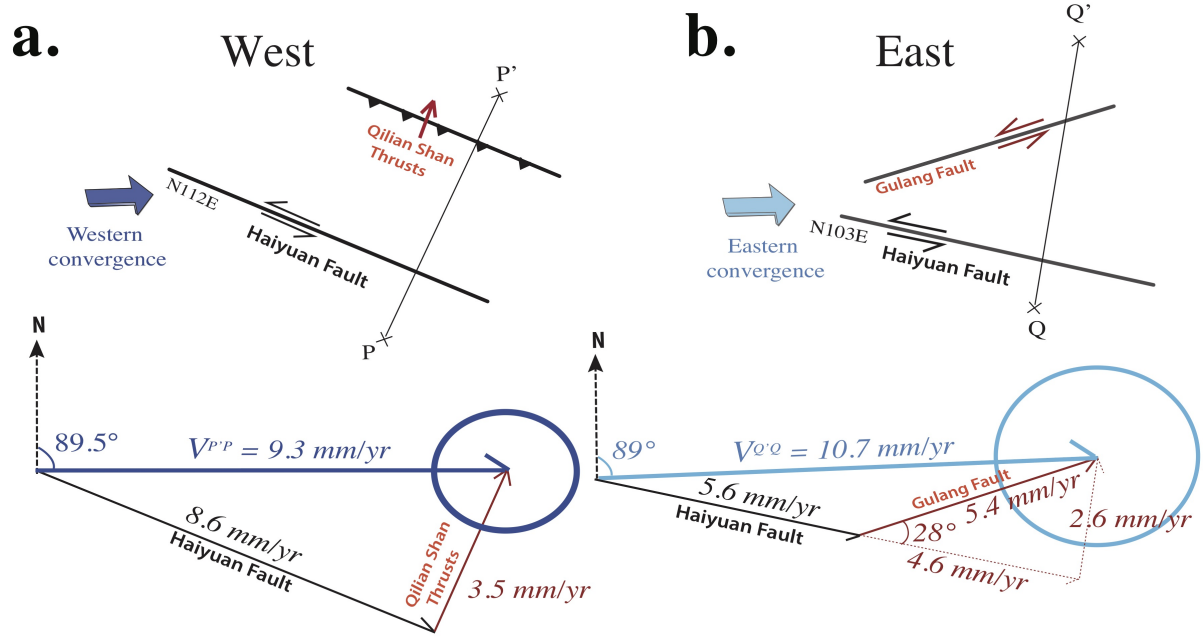


FIGURE 2.6 – Kinematic sketch summarizing the longitudinal or lateral change in slip partitioning between the various branches of the fault system west (a) and east (b) of the Tianzhu pull-apart basin (after Gaudemer *et al.*, 1995). Profiles PP' and QQ' are shown in map view in Fig. 2.3.

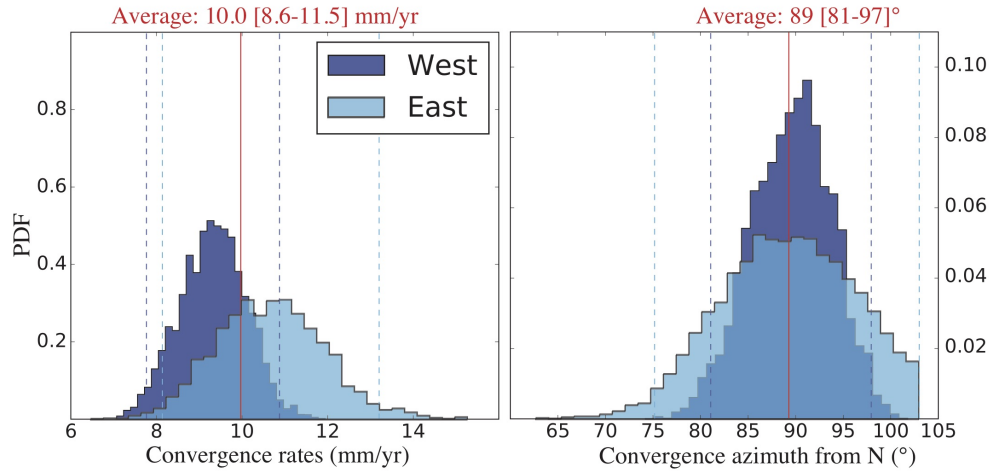


FIGURE 2.7 – Posterior PDFs for the norm and the azimuth of the convergence vectors across the Haiyuan fault system for both profiles (blue vectors $V_{P'P}$ and $V_{Q'Q}$ on Fig. 2.6). Data constraints include both GPS and InSAR velocities.

per crust. Our model allows us to investigate both along-strike and fault-perpendicular variations of slip along the fault system and the corresponding trade-offs between fault

rates and geometry. We show a decrease of the locking depth from 25 [19 – 30] km along western section (thus fully locked) to 0.5 [0.2 – 0.7] km along the eastern creeping section of the Haiyuan Fault, with different slip partitioning on both sides of the basin (Fig. 2.6a). Our model does not require any internal deformation to explain the current displacement rates and shows that most of the complexity of the surface velocity field across the Haiyuan fault system may be accounted for by partitioning, laterally and at depth.

2.5.3 Comparison with geological time scales

The geometry of our most likely model, assumed to be representative of the geometry over several seismic cycles, is consistent with the variation of the long-term topography observed on both sides of the Tianshu basin. To the west, we infer a $21[8 - 34]^\circ$ dip angle of the ramp, while to the east, our model suggests a dip angle of $13.5[5 - 21]^\circ$. Topography is more pronounced to the west (max. of 4200 m in the Qilian Shan) than to the east (max. of 3000 m in the LHS). Shortening may be accommodated on a steeper ramp to the west than to the east, which is consistent with the idea that the change of geometry of the Haiyuan Fault from west to east controls the way convergence motion is partitioned, thus the amount of growing and extrusion of the Tibetan plateau ([Meyer et al., 1998](#); [Tapponnier et al., 2001](#)).

The proposed ramp-décollement geometry is conceptual and represents a way of describing both elastic and permanent parts of surface displacement field at the present time. Over geological time scale, this geometry is unstable and non conservative. The faults will propagate toward the north, deform and adapt for new configurations. Near the slope break at depth, the horizontal slip incompatibility may be accommodated by distributed deformation and by a kink-fault forming a fault-bend fold structure ([Suppe, 1983](#); [Thompson et al., 2002](#)). In another model, this residual velocity between the ramp and the décollement may also create a back-thrust or a normal fault decoupling the Qilian Shan block from the Tibetan block (Fig. 2.2) and forming a typical transpressive “flower structure” tectonic model ([Gaudemer et al., 1995](#)).

InSAR and GPS indicate as much as $3.5[2.3 - 4.8]$ mm/yr of deep-seated shortening motion accumulated during the interseismic period for the western section of the Haiyuan Fault. We find that 80% of the models are in agreement with the 2.8 ± 1.3 mm/yr long-term slip rates measured by [Champagnac et al. \(2010\)](#) on the North Frontal Thrust (NFT) of the Qilian Shan (Fig. 2.1). More recently, [Hu et al. \(2015\)](#) measured, north

of the Nanying anticline and south of the NFT (Fig. 2.1), a shortening rate of 0.9 ± 0.3 mm/yr, but we find no model in agreement with this range of values. On the other hand, we find that 99% of the models lie within the shortening rate of 4.0 ± 2 mm/yr deduced by Gaudemer *et al.* (1995), from a kinematic sketch based on strike-slip rates of the Haiyuan and Gulang faults and the surface geometry of the fault system. This suggests that the shortening rate on the décollement might be accommodated by various thrust structures (Champagnac *et al.*, 2010) or by folding (Hu *et al.*, 2015) at different periods of the seismic cycle.

Based on leveling measurements of offset-terrace risers, Gaudemer *et al.* (1995) estimate a Holocene slip rate for the N112°E eastern JQH segment of the Haiyuan Fault of 11 ± 4 mm/yr. In comparison, our mean model shows a lower left-lateral rate of $8.6 [6.9 - 10]$ mm/yr along the western profile. However, we find than 96% of the models explaining our geodetic data exhibit a strike-slip motion along the JQH segment that lies within the range of geological rates, between 7 and 15 mm/yr. Some discrepancies between short-term and long-term rates may come from the complex link between present-day measurements of strain accumulation at the surface, the long-term accumulation and release of strain along fault and surrounding medium, the temporal variations of interseismic slip rates throughout the seismic cycle of the fault (e.g., Hetland et Simons, 2010; Meade *et al.*, 2013; DeVries et Meade, 2013), as well as the effect of the steep topography on the surface velocity field (Thompson *et al.*, 2015).

2.5.4 Influence of the M~8, 1920 Haiyuan and 1927 Gulang earthquakes

Transient processes triggered by previous earthquakes may also influence observed interseismic slip rates of the fault. Creep can potentially be initiated by coseismic stress changes as post-seismic afterslip from several years to decades after a large event (Hetland et Simons, 2010; Çakir *et al.*, 2012). Creep on the Haiyuan Fault is located at the western tip of the 1920 Haiyuan earthquake (Jolivet *et al.*, 2012). Also we cannot exclude a possible residual post-seismic deformation in the area that ruptured during the 1927 M ~ 8 Gulang earthquake, which caused major stress changes and is still seismically active (Fig. 2.1) (Lasserre, 2000; Lasserre *et al.*, 2001). Integrating post-seismic deformation from previous large earthquakes in a comprehensive 3D visco-elastic deformation model (Trubienko *et al.*, 2013), may be important to further characterize the average interseismic strain accumulation in this region and take into account the interactions between

faults, but is beyond the scope of the present work.

2.6 Conclusions

We produce a time series analysis of InSAR data across a challenging mountainous area in northern Tibet. The processing procedure is based on a small baseline approach. To improve the signal-to-noise ratio and the phase unwrapping capability across the fault, we correct for tropospheric delays (using the ERA Interim Global Atmospheric Models) and local Digital Elevation Model errors before unwrapping and apply a series of filtering steps. We produce a velocity map of the present-day interseismic strain accumulation across the central Haiyuan Fault consistent with GPS data. The velocity map provides a continuous map of deformation over a large zone with a strong sensitivity to vertical motion, useful to assess the geometry of faults. We explain the present-day surface displacements with a slip partitioning model derived from a long-term structural and tectonic model. In the model, strike-slip and thrust faults branch off at depth on a deep décollement, which moves aseismically during the interseismic period. Using a fully Bayesian approach, we investigate the trade-off between fault geometry parameters and slip rates. InSAR data help to constrain the gradient and the localisation of the deformation. We constrain the variations of geometry and locking depths and highlight the benefits of adding InSAR data in the inversion, which decreases the uncertainties on the model parameters. We show the compatibility of the present-day displacement field with a long-term tectonic model and quantify a uniform convergence rate of 10 [8.6 – 11.5] mm/yr with a N89 [81 – 97] °E, across the whole fault system, partitioned differently west and east of the Tianzhu basin. To the west, oblique convergence is purely partitioned between the Haiyuan Fault, which accommodates left-lateral slip at a rate of 8.6 [6.9 – 10] mm/yr, and the Qilian Shan thrusts, which absorb 3.5 [2.3 – 4.8] mm/yr of shortening. To the east (i.e where the azimuth of the Haiyuan Fault changes slightly), the oblique convergence is partitioned between 5.6 [4.5 – 6.9] mm/yr of left-lateral motion along the Haiyuan Fault, 4.6 [2.6 – 6.3] mm/yr of left-lateral velocity along the Gulang Fault, and 2.6 [0.2 – 4.6] mm/yr of shortening along the oblique fault-system. These results illustrate the importance of the geometry of the Haiyuan fault system, controlling eastward motion and the growth of the crustal wedge at this boundary of the Tibetan plateau.

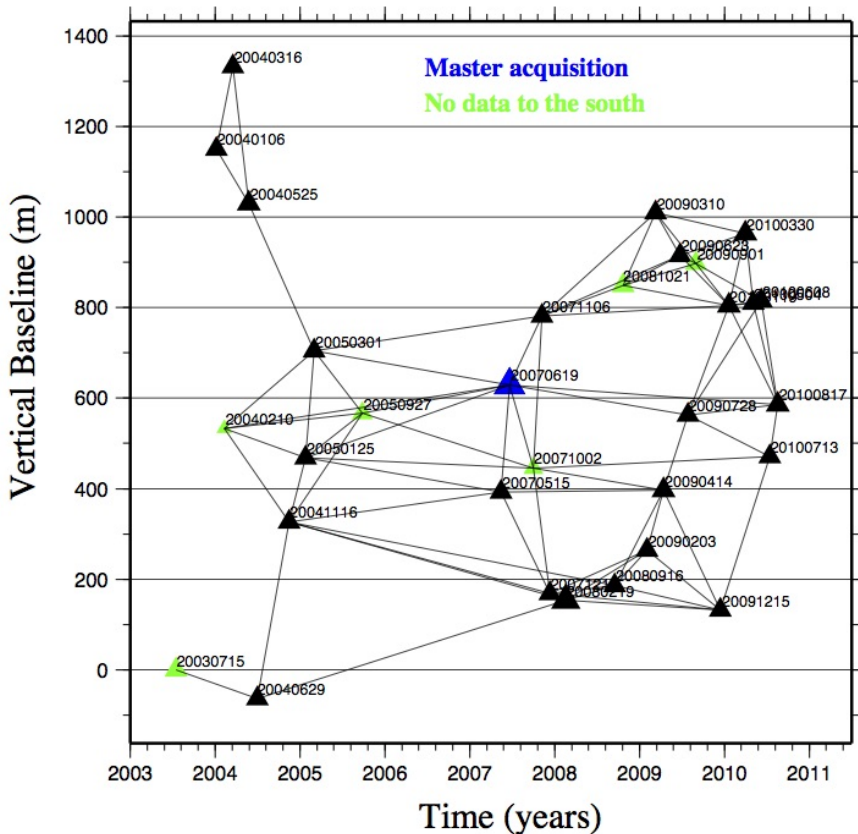


FIGURE 2.8 – Computed interferograms from 31 images along track 104. Triangles are SAR acquisitions, with sizes and colors according to their spatial extend : black triangles for a full coverage and green triangles for images covering the northern part of the track only.

2.7 Supplementary Material

Small Baseline network

We define an optimal small baseline network of interferograms using a perpendicular baseline constraint, B_{perp} , of 600 m and temporal baseline constraint, B_t , of 4 years (Fig. 2.8). Chosen image pairs are a compromise between interferogram redundancy, which allows error detection, and processing constraints (Doin *et al.*, 2011) as links between large-covered images or large B_{perp} to help improving the local DEM error correction.

GPS referencing

To reference the GPS, we select a subset of stations south of the Haiyuan fault to estimate the Eulerian pole (Fig. 2.9a : G092, G083, G081, G080, G096, G098, G101, G105, G106, G108, G111, XNIN, G112) and invert for the position and rotation rate of an Eulerian pole by minimizing the L1 norm of the ITRF08 velocities of this subset of stations. Our best-fitting solution locates the Euler pole between the ITRF08 ([Altamimi et al., 2011](#)) and the Southern block at (7.9°N, 80.1°E) with a clockwise rigid rotation of 0.710°/Myr and shows almost no residual velocities between observations and predictions, indicating no internal deformation in this block south of the Haiyuan Fault (Fig. 2.9b). We then remove the predicted rotation by applying a Helmert transformation ([Bevis et Brown, 2014](#)) in order to reference the GPS velocity field with respect to the South Haiyuan block. Note that we also tried to reference the GPS solution to the northern block. Our results indicate less dispersion between the observations and the predictions and a more robust solution for the southern block than for the northern block. This result is not surprising as GPS stations in the northern block are located in the sand dunes area that are affected by hydrological deformations. Also, the northern block is deformed by the Qilian Shan thrusts and sheared by the Gulang and the continuity of the Altyn Tagh Faults, making it more difficult to find a tectonically stable region.

Quality of InSAR corrections

Fig. 2.10 shows two examples of wrapped interferograms before and after atmospheric corrections predicted from the ERA-I reanalysis of atmospheric data ([Jolivet et al., 2011](#)). Before corrections, the short wavelength topographic structures coincide with phase gradients and the mean phase/elevation ratio, calculated on small windows of $\sim 17 \text{ km}^2$, reaches -3 rad/m and 6.5 rad/m on average for both interferograms. After corrections, the stratified signal is in majority removed, the phase/elevation ratio is close to zero and the local scatter in phase/elevation ratios decreases.

DEM errors are estimated based on the relationship between interferometric phase and perpendicular baseline ([Ducret et al., 2014](#)). This correction step is applied on the wrapped interferograms after than flat earth and the topographic contribution has been removed using predict orbit and a DEM and aims to correct for residual DEM errors due to the imperfect knowledge of the topography. Note that for Envisat data the deformation may not be included in the DEM error coefficient as the the perpendicular baseline

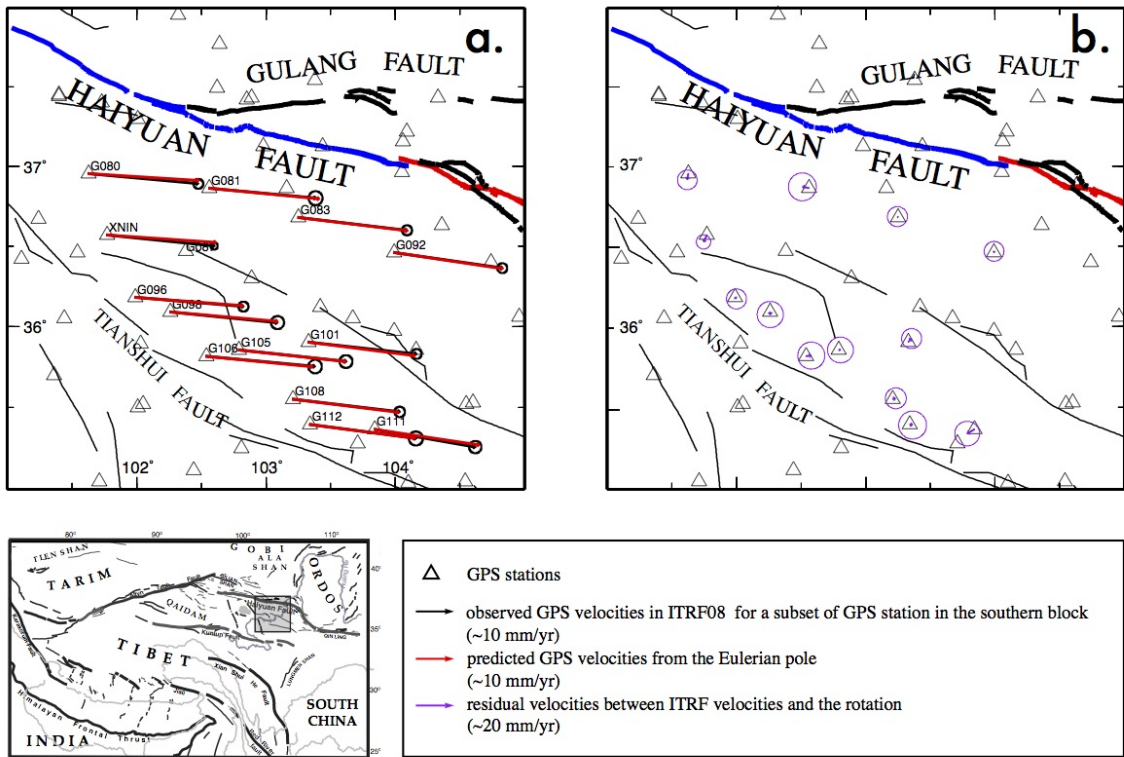


FIGURE 2.9 – GPS referencing. (a) Subset of 13 reference stations used to define a reference frame south of the Haiyuan Fault. (b) Residual velocities between the observations and the predictions. Faults map and colors as Fig.1. Insert at the bottom left shows the location of the figure.

drifting is very small. To highlight the efficiency of the correction across the mountain range, we display in Fig. 2.11, on a selected area across the Tianzhu basin, the coefficient's map used to correct for local DEM errors, the temporal coherence map, and two examples of correction. The correction increases the apparent phase coherence across the Tianzhu pull-apart and the mountainous areas.

After this series of cascading corrections that aim at enhancing the coherence of wrapped phase, unwrapping process is performed using a specific scheme. First, we multilook by a factor of 8 in range and 40 in azimuth, replacing the amplitude of the interferograms by the colinearity as defined by Pinel-Puyssegur *et al.* (2012). We then low pass filter using the average temporal coherence extracted from the DEM correction as weight. In contrast to the cut-tree algorithm (Rosen *et al.*, 2004), here we impose an unwrapping path going from the high to low coherence areas defined by the filter, avoiding unwrapping to propagate into incoherent areas, as snow-capped mountain ridges or sand covered deserts. Unwrapping is performed iteratively in successive sub-regions above a decreasing

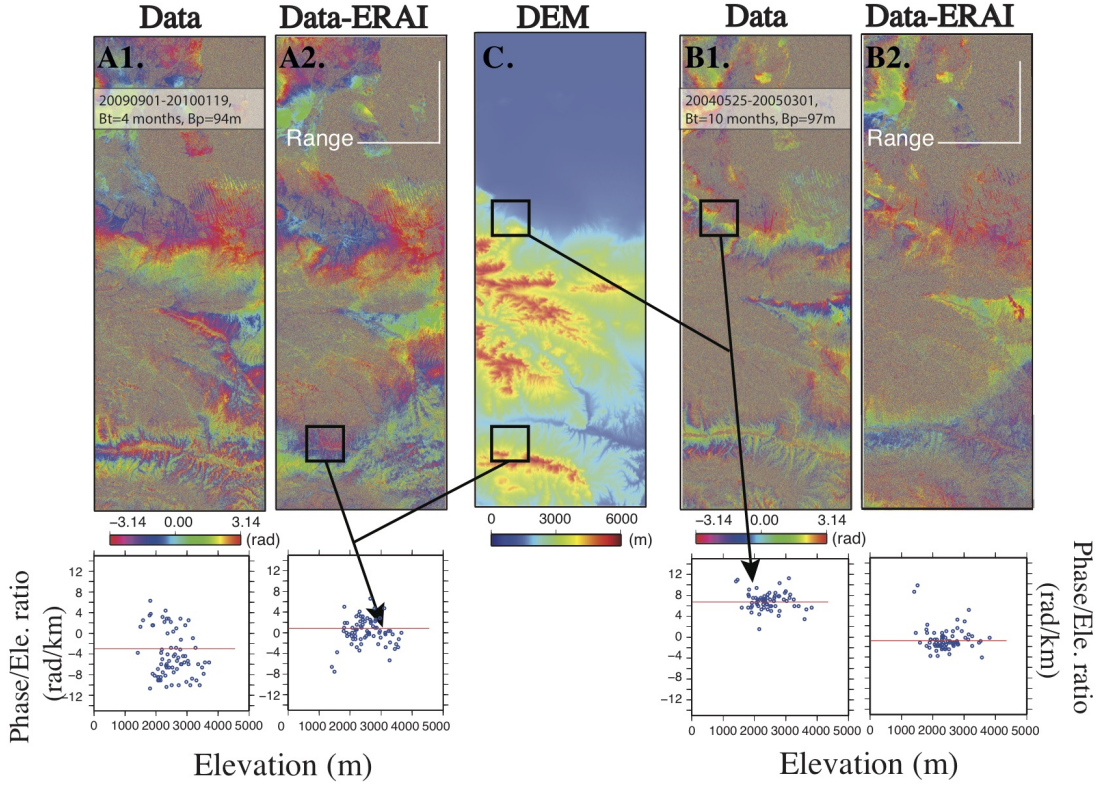


FIGURE 2.10 – Top : Example of two wrapped interferograms (A :20090901-20100119 and B :20050125-20050927), multi-looked by a factor of 4, before (A1-B1) and after (A2-B2) atmospheric corrections predicted using the ERA-I model. Digital Elevation Model is shown in C. Bottom : comparison of the local ratio phase/elevation as a function of elevation before and after correction. Each blue dot correspond to a local estimate in a sub-window of $\sim 17 \text{ km}^2$.

coherence threshold. Each newly unwrapped area is added to already unwrapped areas. The coherence threshold iteratively slightly decreases to propagate unwrapping further away (Grandin *et al.*, 2012; Doin *et al.*, 2015). If necessary, high priority bridges are set manually by visual inspection of interferograms. Finally, unwrapped interferograms are inverted into phase time series for each acquisition date following López-Quiroz *et al.* (2009) and Jolivet *et al.* (2012) approach. We use an iterative procedure to remove all residual unwrapping errors. At each iterations, misclosure of the interferometric network are computed for each interferograms. If large, we then check visually the corresponding interferogram and correct its unwrapping errors. Times series analysis is then iterated again until no large network inconsistencies remain (Doin *et al.*, 2015). From the final time series, we derive a linear term, which corresponds to the ground velocity in the LOS direction.

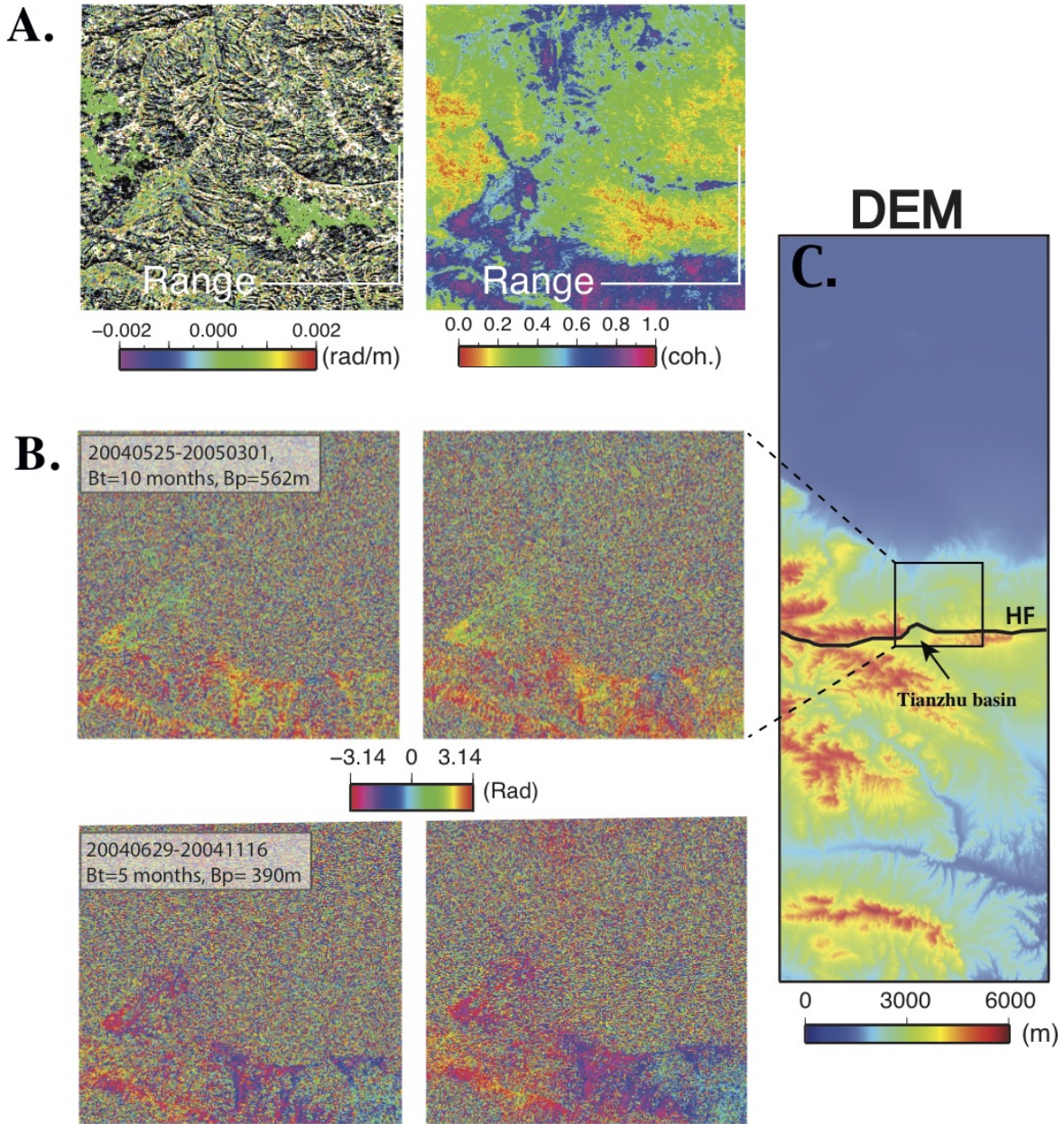


FIGURE 2.11 – A) Map of the DEM error coefficient (in rad/m) (left). The error $\delta h = \frac{\alpha\lambda\tan\theta}{4\pi}$ is 11 m on average. Average temporal coherence map (right) across the pull-apart basin. B) Effect of local DEM correction for two interferograms with large perpendicular baseline across the Tianshu pull-apart basin before (left) and after (right) DEM errors correction.

To quantify the quality of the inverted velocity map, we estimate the local velocity-elevation ratios and compute a global Root Mean Square (RMS) network misclosure map for the inversion (Cavalié *et al.*, 2007; López-Quiroz *et al.*, 2009; Doin *et al.*, 2011)

(Fig. 2.12). Fig. 2.12A shows local LOS velocity-elevation ratios on small sub-windows of 17×14.5 km as a function of elevation. We observe a variability of local velocity-elevations ratios of 0.002 rad/yr/km centered on average on zero, indicating no short scale tropospheric signal in the velocity map. RMS misclosure between the observed interferometric phase and the reconstructed phase from time series inversion (Fig. 2.12B) gives the phase reliability for each pixel. On average the RMS misclosure is lower than 0.4 rad for the whole map, indicating the absence of unwrapping errors in the produced interferograms and a low phase noise. We mask pixels with RMS larger than 0.4 rad .

Inverse model

We define two profiles perpendicular to the $N103^\circ E$ and $N112^\circ E$ segments of the Haiyuan fault and centered at $(104.018^\circ, 37.021^\circ)$ and $(102.469^\circ, 37.282^\circ)$, east and west of the Tianzhu basin, respectively. The modeling is two dimensional with infinite dislocations in the along-strike direction. In cross section, the model includes both semi-infinite dislocations and a finite dislocation with both strike-slip and dip-slip components (Fig. 2.13). For the eastern profile, we add a vertical finite segment to model the shallow creep in the LHS section of the Haiyuan Fault. On this segment, we invert for the locking depth, H_c , as well as the strike-slip rate, \dot{U}_c , allowing for a slip deficit $(\dot{U}_{s1} - \dot{U}_c)$. All the prior distributions allowing to recreate the two models (Fig. 2.13) are summarized in the Table 2.1.

Data Covariance matrix

To take into account residual atmospheric signal delays on the two InSAR profiles, we compute the full covariance matrix for the two InSAR tracks. To characterize the noise distribution, we map the residuals of a preliminary inversion of the InSAR data set only, mask subsidence areas and remove residual long-wavelength ramps. Residual velocity distribution shown in (Fig. 2.14 A1, B1) has standard deviations, ε , of 0.41 mm/yr and 0.70 mm/yr for the western and eastern profile respectively. Following Jolivet *et al.* (2012), we compute the empirical semi-variogram of each residual LOS velocity map, using the following equation :

$$\gamma(x) = \frac{1}{2 |N(x)|} \sum_{(i,j) \in N(x)} (z_i - z_j)^2, \quad (2.2)$$

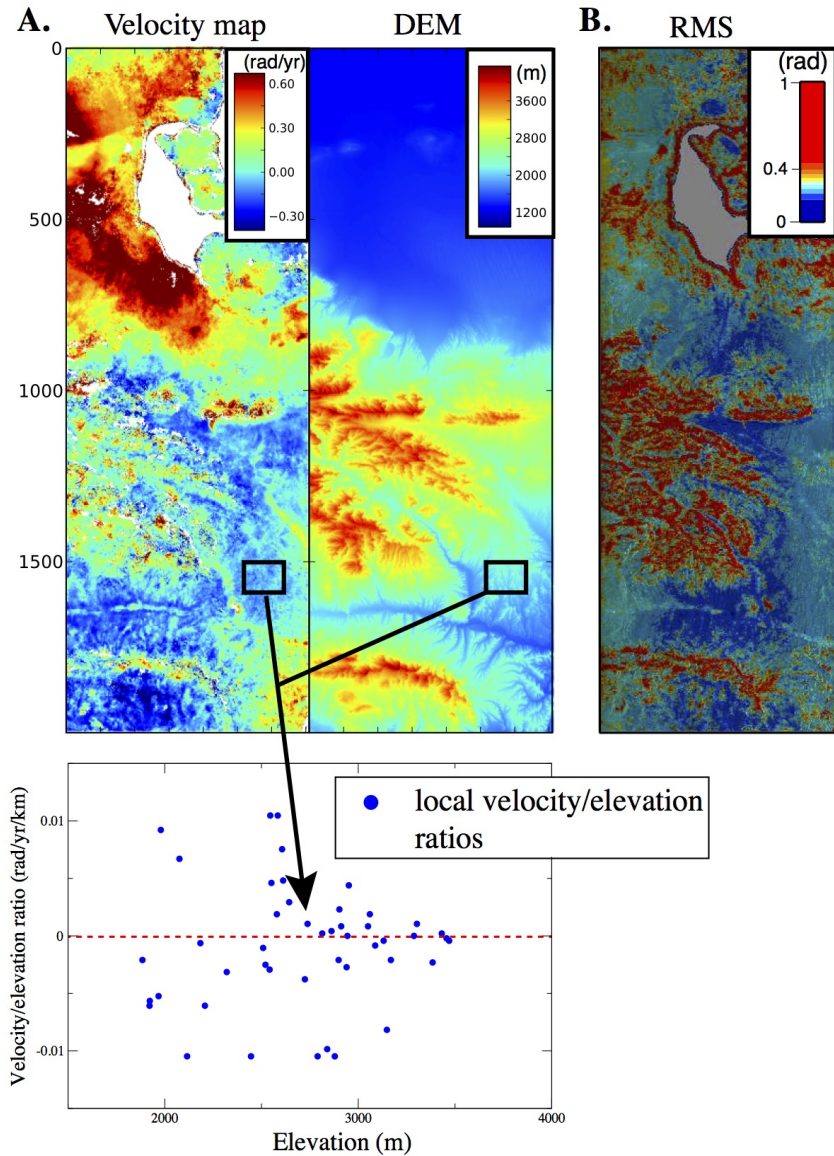


FIGURE 2.12 – Quality of the LOS velocity map. A) Estimation of the local velocity-elevation ratios. Top : LOS velocity map (left) and Digital Elevation Model (DEM, right). Bottom : Local velocity-elevation ratios as a function of elevation. Each blue dot corresponds to the average velocity-elevation ratio in a local sub-window of 17×14.5 km. B) Root Mean Square (RMS) network misclosure map between the interferometric phase and the reconstructed phase from time series inversion ([Doin et al., 2011](#)). The LOS velocity map in Fig. 3 has been masked on pixels with RMS superior to 0.4 rad, that may be contaminated by errors and phase noise.

where $N(x)$ denotes the set of pairs of observations i, j separated by a distance x , $|N(x)|$ is the number of pairs in the set, and z_i, z_j are the LOS velocities of pixels i and j ([Chiles et Delfiner, 2009](#)). Assuming the covariance between two points only depends

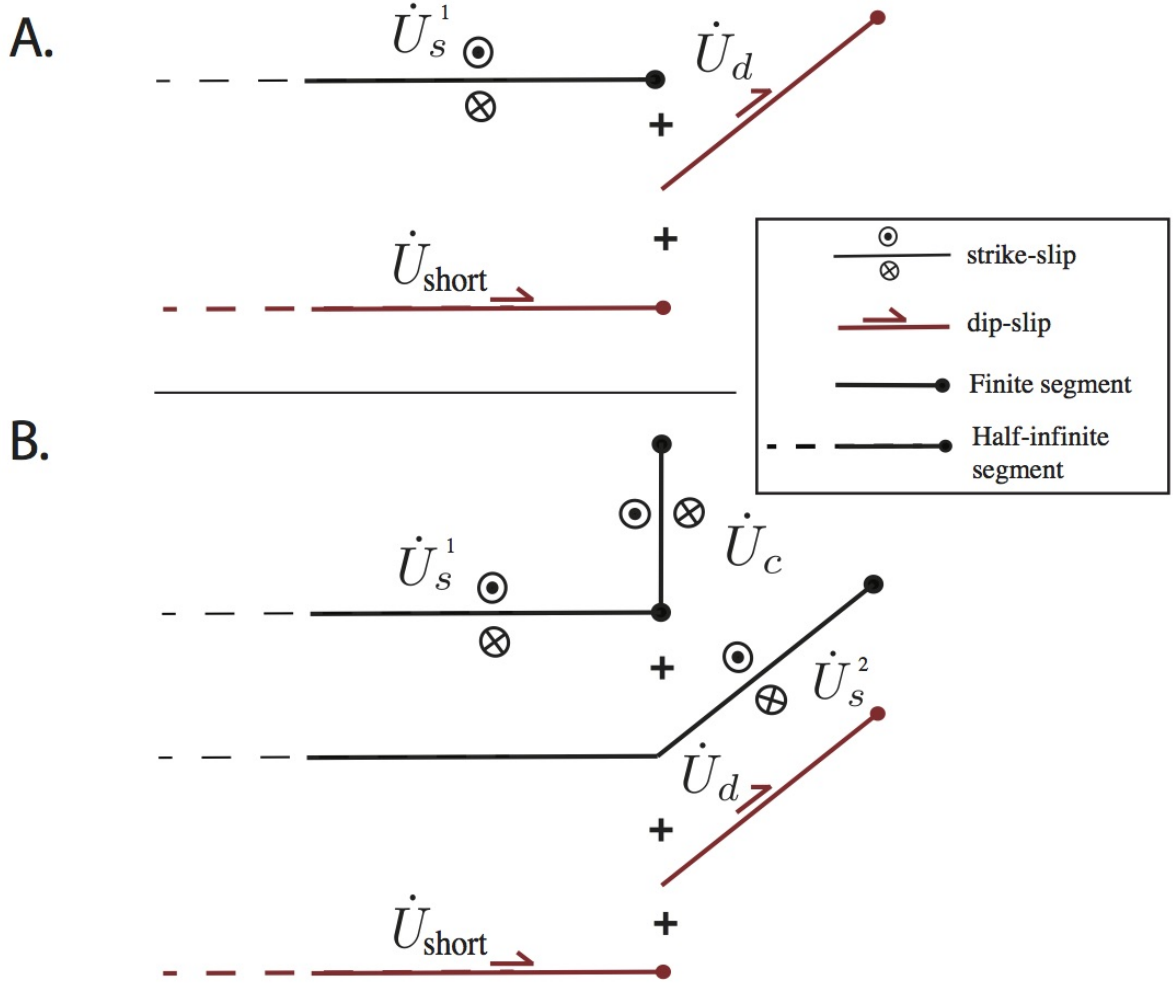


FIGURE 2.13 – Schematic decomposition of each dislocations forming the inverse model for the western (A) and eastern profiles (B). Strike-slip on the Haiyuan and Gulang dislocations are semi-infinite to model the far-field displacements and reproduce rigid-blocks. In case B, slip on the décollement is the sum of \dot{U}_{s1} and \dot{U}_{s2} to ensure the compatibility of the strike-slip motion between the ramp and the décollement. In contrary, slip on the vertical dislocation, \dot{U}_c , is inferior or equal to \dot{U}_{s1} , allowing for a slip deficit on the creeping segment. In both case, the dip-slip motion, \dot{U}_d , is the projection of the shortening component on the ramp.

on the distance between them (Lohman et Simons, 2005) (Fig. 2.14 A2, B2), we estimate the covariance function, defined as :

$$\text{Cov}(x) = \gamma_s - \sigma^2 \exp^{-\frac{(z_i - z_j)^2}{\lambda}}, \quad (2.3)$$

where $\text{Cov}(x)$ is the covariance function, γ_s is the sill value of the semi-variogram over a characteristic length scale of noise, λ , σ^2 is the auto covariance of the measurement,

and z_i , z_j the LOS velocities for two pixels i and j. As we observe a sill value, γ_s , lower or close to σ^2 , suggesting very low white noise in the InSAR data set, we force the sill value, γ_s , to be equal to the auto covariance, σ^2 . Empirical covariograms indicate then an error, σ , of 0.44 mm/yr and 0.50 mm/yr close to the standard deviation of the residual velocity, with a characteristic correlation distance, λ , of 11 km and 8.5 km for the track T104 and T333, respectively. We then build the full covariance matrix for InSAR data sampled by the profiles ([Sudhaus et Sigurjón, 2009](#)) (Fig. 2.14, A3, B3), such as :

$$\text{Cov}(i,j) = \sigma^2 \exp^{-\frac{\|i,j\|^2}{\lambda}}, \quad (2.4)$$

where $\|i,j\|^2$, is the distance between two pixels i and j.

For GPS data, the covariance matrix is diagonal with terms compute with the 1σ error of the measurements.

Inversion results

GPS and InSAR velocity map for the data, model and residual between data and model across the western and eastern profiles covered respectively by the track T104 and T333 are presented in the Fig. 2.15. The model is limited by the 2D structural simplification but shows on average a good agreement with both GPS and InSAR data. Posterior 95% confidence intervals as well as first moments are available in the Table 2.1. Tables 2.2 and 2.3 give the correlation coefficient matrix of the variables for the western and eastern profiles respectively, and Fig. 2.16 displays some selected joint marginal PDFs.

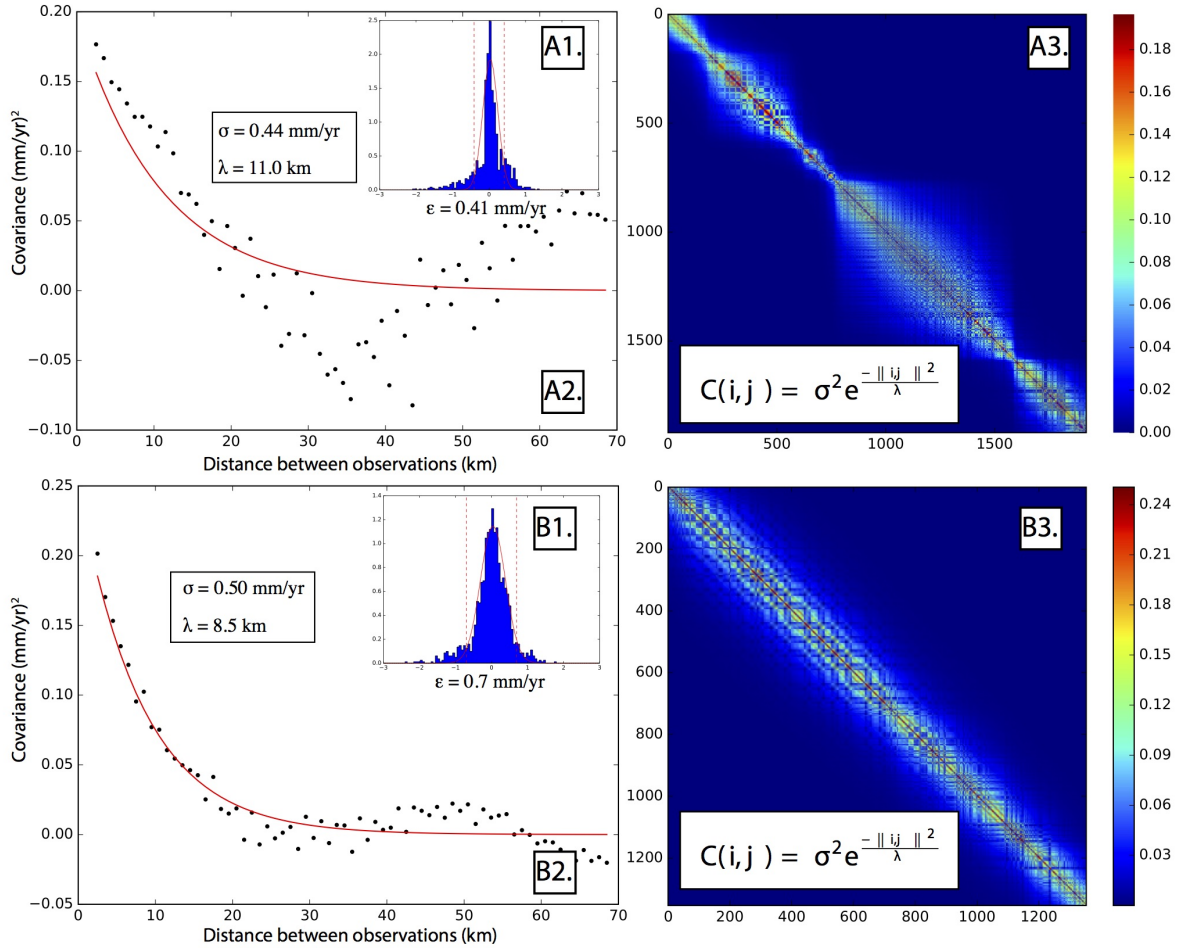


FIGURE 2.14 – Distribution of the residual between a preliminary model and the InSAR data for InSAR tracks 104 (A1) and 333 (B1). Empirical covariance and associated best-fit exponential functions for the InSAR residual velocity maps (A2, B2). Associated data covariance matrix built from the exponential functions for points sampled in the studied profiles (A3, B3).

TABLE 2.1 – Summary of the prior probability distributions (first column), the posterior 95% confidence intervals (second column), as well as the mean, the variance and the skewness (third, fourth and fifth columns) of the marginal posterior distributions for the western (Top) and eastern (Bottom) profiles.

| West parameters | prior | 95% confidence | mean | variance | skewness |
|----------------------------------|---------------------------|---|-----------------------|-----------------------|----------|
| \dot{U}_{s1} (mm/yr) | $\mathcal{U}(0, 20)$ | [6.9, 10] | 8.6 | 0.66 | -0.11 |
| \dot{U}_{short} (mm/yr) | $\mathcal{U}(0, 10)$ | [2.3, 4.8] | 3.5 | 0.41 | -0.40 |
| H_1 (km) | $\mathcal{U}(0, 30)$ | [19, 30] | 25 | 9.5 | -0.48 |
| D (km) | $\mathcal{U}(0, 60)$ | [17.5, 30] | 24 | 10 | -0.76 |
| H_2 (km) | $\mathcal{U}(0, 30)$ | [9, 22] | 15 | 11 | 0.60 |
| T104 ramp | $\mathcal{U}(-1, 1)$ | $[-2.2 \times 10^{-05}, 5.9 \times 10^{-03}]$ | 3.2×10^{-03} | 2.2×10^{-06} | -0.11 |
| East parameters | prior | 95% confidence | mean | variance | skewness |
| \dot{U}_{s1} (mm/yr) | $\mathcal{U}(0, 20)$ | [4.5, 6.9] | 5.6 | 0.4 | 0.44 |
| \dot{U}_{short} (mm/yr) | $\mathcal{U}(0, 10)$ | [0.2, 4.6] | 2.6 | 1.42 | -0.21 |
| H_1 (km) | $\mathcal{U}(0, 30)$ | [14, 30] | 24 | 23 | -0.80 |
| \dot{U}_c (mm/yr) | $\mathcal{U}(0, 10)$ | [3.5, 5.6] | 4.6 | 0.3 | -0.12 |
| H_c (km) | $\mathcal{U}(-0.5, 10.5)$ | [0.2, 0.7] | 0.5 | 0.02 | 0.55 |
| \dot{U}_{s2} (mm/yr) | $\mathcal{U}(0, 10)$ | [2.6, 6.3] | 4.6 | 0.9 | -0.30 |
| D (km) | $\mathcal{U}(25, 75)$ | [54, 72] | 61 | 22 | 0.85 |
| H_2 (km) | $\mathcal{U}(0, 30)$ | [2.5, 14.5] | 9 | 10 | 0.24 |
| T333 ramp | $\mathcal{U}(-1, 1)$ | $[-3.7 \times 10^{-03}, 1.1 \times 10^{-02}]$ | 3.3×10^{-03} | 1.3×10^{-05} | 0.02 |

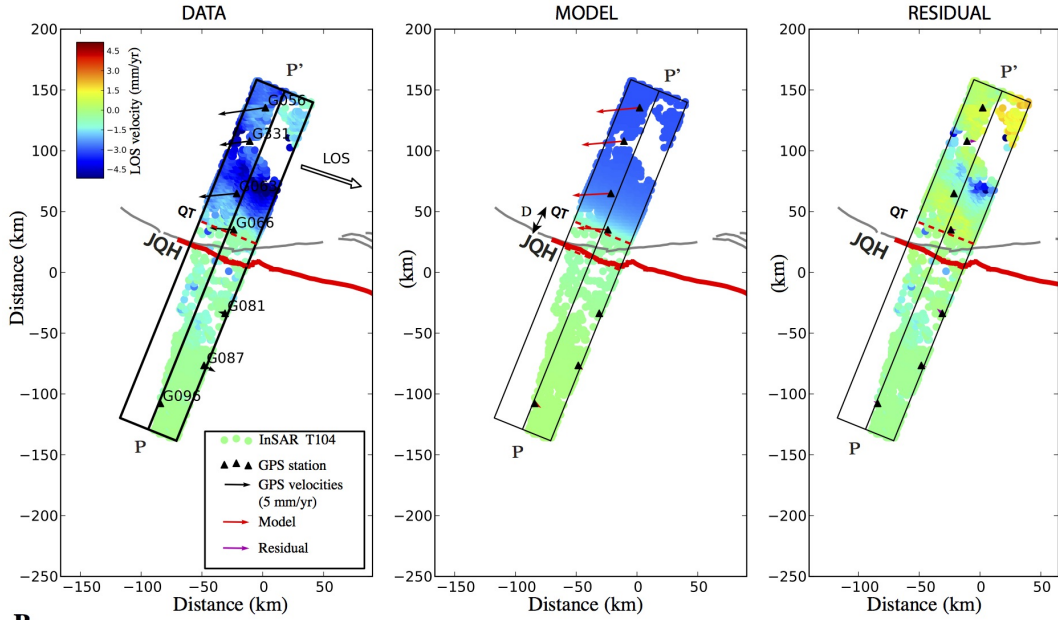
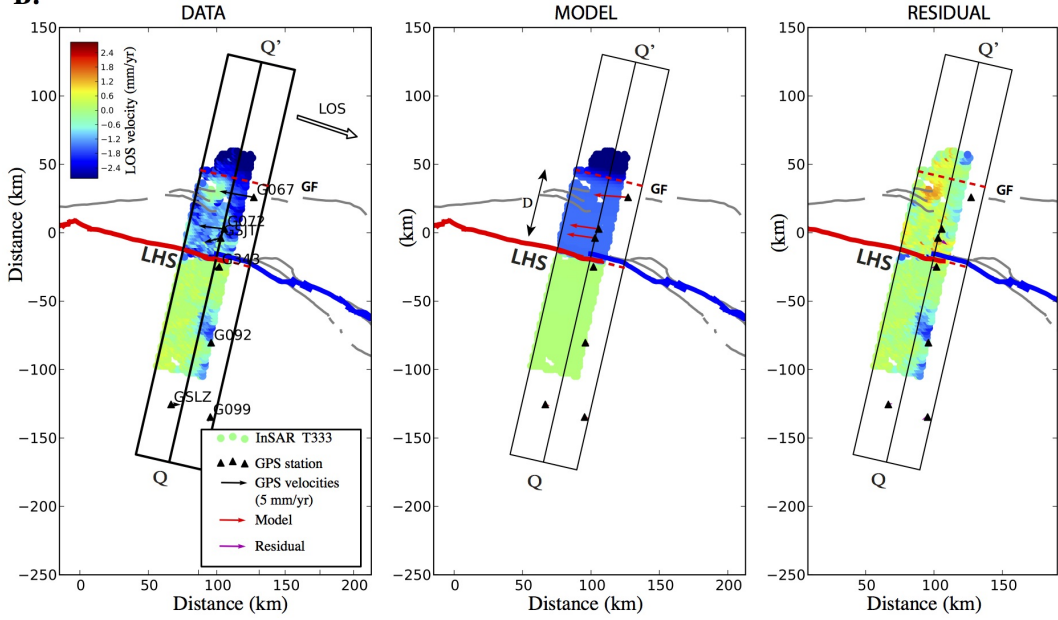
A.**B.**

FIGURE 2.15 – Joint inversion map of the GPS and InSAR data across the western (PP') and the eastern (QQ') profiles covered respectively by the track 104 (A) et 333 (B). GPS network is referred to the southern block. InSAR positive motion is away from the satellite. Red dashed lines are associated to 2D dislocation lines for each fault segment and extract from Fig.4 and 5. The Jing Qiang He (JQH) segment, the Lao Hu Shan (LHS) segment, the Qilian shan Thrusts (QT) and the Gulang Fault (GF) represent the faults segments used in our model

TABLE 2.2 – Correlation coefficient matrix of the western profile parameters.

| West parameters | \dot{U}_{s1} | \dot{U}_{short} | H_1 | D | H_2 | T104 ramp |
|--------------------------|----------------|--------------------------|-------|-------|-------|-----------|
| \dot{U}_{s1} | 1 | -0.02 | 0.48 | 0.05 | 0.25 | 0.76 |
| \dot{U}_{short} | -0.02 | 1 | 0.27 | 0.34 | -0.47 | -0.15 |
| H_1 | 0.48 | 0.27 | 1 | 0.02 | 0.41 | 0.16 |
| D | 0.05 | 0.34 | 0.02 | 1 | -0.59 | 0.0 |
| H_2 | 0.25 | -0.47 | 0.41 | -0.59 | 1 | 0.12 |
| T104 ramp | 0.76 | -0.15 | 0.16 | 0 | 0.12 | 1 |

TABLE 2.3 – Correlation coefficient matrix of the eastern profile parameters.

| East parameters | \dot{U}_{s1} | \dot{U}_{short} | H_1 | \dot{U}_c | H_c | \dot{U}_{s2} | D | H_2 | T333 ramp |
|--------------------------|----------------|--------------------------|-------|-------------|-------|----------------|-------|-------|-----------|
| \dot{U}_{s1} | 1 | 0.09 | 0.12 | 0.09 | 0.05 | 0.48 | 0.25 | -0.09 | 0.49 |
| \dot{U}_{short} | 0.09 | 1 | -0.12 | -0.07 | -0.02 | 0.25 | 0.52 | -0.65 | 0.56 |
| H_1 | 0.12 | -0.12 | 1 | 0.03 | -0.01 | -0.03 | -0.04 | 0.33 | -0.27 |
| \dot{U}_c | 0.09 | -0.07 | 0.03 | 1 | 0.51 | 0.01 | 0.0 | -0.03 | 0.09 |
| H_c | 0.05 | -0.02 | -0.01 | 0.51 | 1 | 0.01 | 0.01 | -0.02 | 0.03 |
| \dot{U}_{s2} | 0.48 | 0.25 | -0.03 | 0.01 | 0.01 | 1 | 0.36 | -0.12 | 0.55 |
| D | 0.25 | 0.52 | -0.04 | 0.0 | 0.01 | 0.36 | 1 | -0.58 | 0.2 |
| H_2 | -0.09 | -0.65 | 0.33 | -0.03 | -0.02 | -0.12 | -0.58 | 1 | -0.39 |
| T333 ramp | 0.49 | 0.56 | -0.27 | 0.09 | 0.03 | 0.55 | 0.2 | -0.39 | 1 |

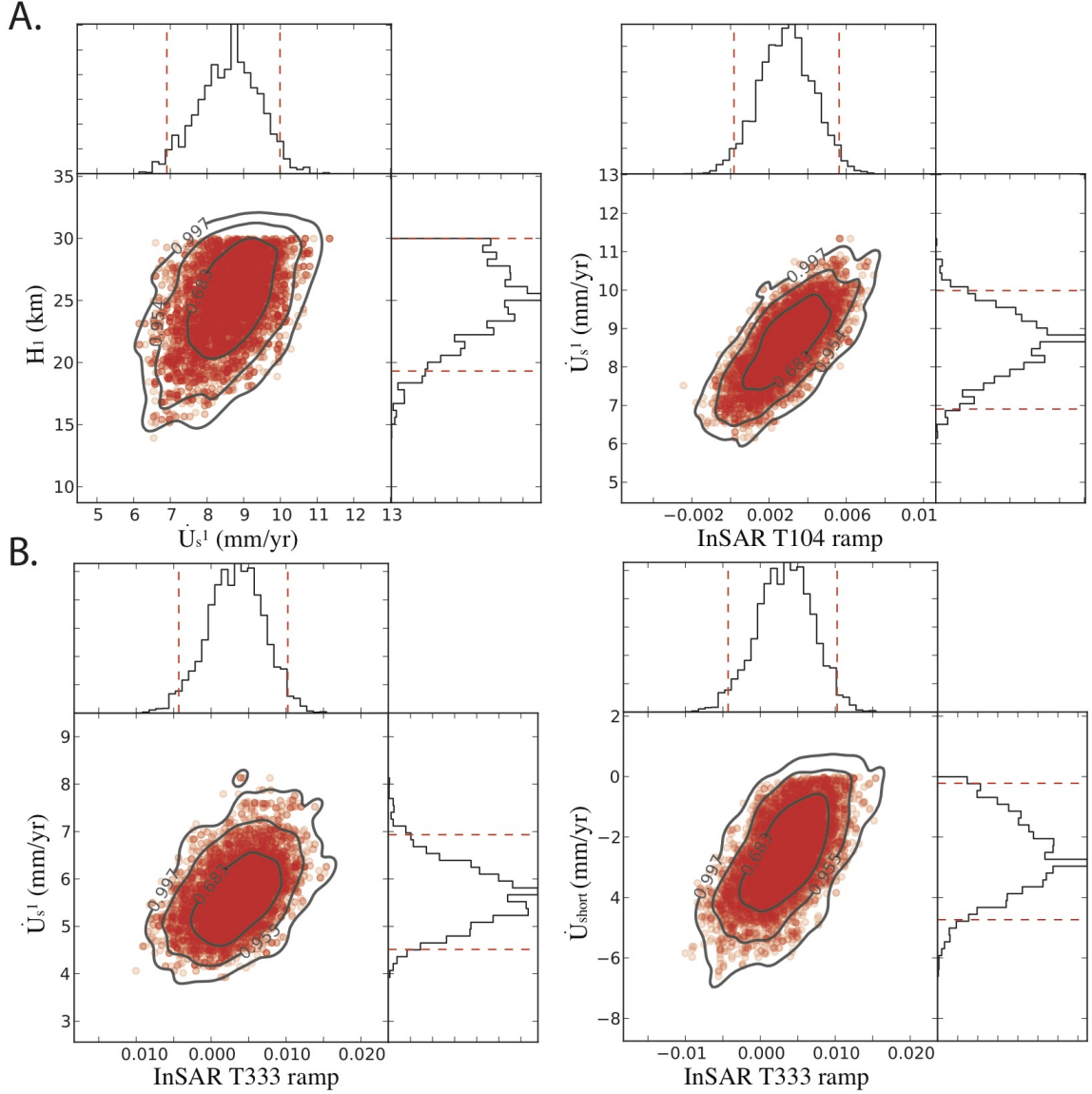


FIGURE 2.16 – Joint PDFs for the western (A) and eastern profiles (B) showing trade-offs between some parameters. For the western profile (A) the strike-slip rate of the Haiyuan Fault, \dot{U}_{s1} , indicates a correlation with the locking depth, H_1 , (left) and with the InSAR azimuthal ramp (right). For the eastern profile (B), joints PDFs reveal a correlation between the InSAR ramp and the strike-slip rates of the Haiyuan Fault, \dot{U}_{s1} , (left) as well as between the InSAR azimuthal ramp and the shortening component across the fault system, \dot{U}_{short} (right).

Chapitre 3

Constraining the Kinematics of Metropolitan Los Angeles Faults with a Slip-Partitioning Model

Sommaire

| | | |
|------|-------------------------------|-----|
| 3.1 | Introduction | 94 |
| 3.2 | Tectonic constraints | 96 |
| 3.3 | Deformation data | 97 |
| 3.4 | Description of the model | 97 |
| 3.5 | Slip partitioning constraints | 99 |
| 3.6 | Prior Assumptions | 100 |
| 3.7 | Inversion method | 100 |
| 3.8 | Posterior models | 102 |
| 3.9 | Discussion | 103 |
| 3.10 | Conclusion | 106 |
| 3.11 | Supplementary Material | 107 |

Preface

Ces travaux se basent sur l'analogie de [Gaudemer et al. \(1995\)](#) et [Bowman et al. \(2003\)](#) entre le système de faille de Haiyuan et la Californie du Sud. Les auteurs proposent que la complexité tectonique observée en surface en Californie du Sud peut s'expliquer par un fort taux de partitionnement de la déformation profonde dans la croûte. Tout comme au Tibet, la morphologie et la dimension de la faille de San Andreas suggèrent que cette dernière s'enracine en profondeur en ayant ainsi la force de contrôler la tectonique régionale de par sa géométrie. Au niveau du « Big Bend », l'obliquité de la faille de SA créerait ainsi une convergence locale accommodée par le glissement asismique et à faible pendage d'un décollement découplant la croûte supérieure de la croûte inférieure et reliant les failles peu profondes et à forts pendages. J'utiliserai pour ces travaux, les quantités de données géologiques, géodésiques et géophysiques disponibles dans cette région. Je présenterai ainsi de nouveaux taux de glissements pour la faille de San Andreas et pour les chevauchements de Sierra Madre et des Puente Hills. Ces résultats sont en accord avec les mesures géologiques long-termes et expliquent précisément les déplacements actuels de surface. Notre approche novatrice constitue ainsi une méthodologie intéressante visant à étudier la complexité géométrique de tels systèmes de failles embranchées et limite la gamme de modèles possibles en accord avec les données de surface en introduisant des contraintes long-terme cinématiques. Cette étude débuta à l'Observatoire de Singapour lors de mon expérience post-Master puis se poursuivit durant ma thèse dans le cadre d'un échange financé par le Labex OSUG@2020 de l'Université de Grenoble et par la bourse "National Research Foundation of Singapore" de Sylvain Barbot. Elle est aussi le résultat d'une étroite collaboration avec Gilles Peltzer, expert de la tectonique et de la déformation actuelle de la région. Le manuscrit a été accepté dans le journal « Geophysical Research Letter » sous le titre « Constraining the Kinematics of Metropolitan Los Angeles Faults with a Slip-Partitioning Model » par S. Daout, S. Barbot, G. Peltzer, M.-P. Doin, Z. Liu et R. Jolivet ([Daout et al., 2016a](#)).

3.1 Introduction

The Pacific Plate (PAP) made its first contact with the North America Plate (NAP) about 28 Ma ago, when the Farallon slab, which was separating them, fully subducted beneath the American continent. The San Andreas Fault (SAF) follows the previous suture zone of the downgoing Farallon slab beneath the western NAP ([Furlong et Hugo,](#)

1989) and accounts for a large fraction of the relative motion between the PAP and the NAP (Lisowski *et al.*, 1991; Tong *et al.*, 2013). The crustal expression of this transform boundary in Southern California is complex and involves a large number of faults (Plesch *et al.*, 2007) with multiple strands (Mount et Suppe, 1992; Teyssier et Tikoff, 1998). Most of the deformation along the SAF system is accommodated by long and mature strike-slip faults, but some of the relative convergence is absorbed by thrusts or oblique strike-slip faults (Walls *et al.*, 1998).

Despite the surface complexity of the SAF system, the far-field interseismic horizontal velocity field is relatively uniform along the SAF from the Coachella to the Mojave segment of the SAF (Fig. 6.1A). GPS velocity vectors in the ITRF08 reference frame are closely aligned with the Coachella segment of the SAF and the San Jacinto Fault (SJF). Farther north, near the Mojave segment of the SAF, GPS velocity vectors between the Mojave Block and Los Angeles (LA) have a similar orientation, despite the remarkable change of strike of the SAF of 18° (blue vector PP' of Fig. 6.1B). The projection of this vector on the fault-perpendicular and fault-parallel directions indicates ~ 7 mm/yr of far-field contraction (Bock *et al.*, 1997; Argus *et al.*, 2005) (red vector of Fig. 6.1B, Table S1) and ~ 26 mm/yr of transform motion (black vector of Fig. 6.1B, Table S1). This relatively uniform orientation of the surface velocity vectors in Southern California is in contradiction with the complex superficial geometry of the fault system and might be the result of slip partitioning in the mid- and lower crust (Fig. 6.1C) (Mount et Suppe, 1987; Crouch et Suppe, 1993; Bowman *et al.*, 2003). At depth, the long-term average cumulative horizontal velocity vectors must be accommodated by the interplay of strike-slip and thrust faults.

Both the transform and convergent components of deformation are responsible for significant seismic hazard in Southern California (Dolan *et al.*, 1995; Walls *et al.*, 1998). Strike-slip faults can generate long seismic ruptures, such as during the 1812 Mw 6.9 San Juan Capistrano and the 1857 Mw 7.9 Fort Tejon earthquakes (Sieh, 1978; Toppozada *et al.*, 2002), and reverse faulting is at the origin of the 1971 M_L 6.6 San Fernando, the 1987 M_L 5.9 Whittier Narrows, the 1991 M_L 5.8 Sierra Madre, and the 1994 Mw 6.7 Northridge earthquakes (Rubin *et al.*, 1998). Reconciling all these structures in a self-consistent kinematic model would improve our assessment of seismic hazard in Southern California (e.g., Gaudemer *et al.*, 1995; Deng et Sykes, 1997; Loveless et Meade, 2011).

The purpose of this study is to better constrain the loading rate on the buried faults below Los Angeles (LA) using geodetic data and a conservative slip-partitioning model. We consider a profile that crosses the Big Bend, the segment of the SAF that is

~N63°W compared to ~N45°W direction along the Coachella segment (Fig. 6.1). We first identify the broad features of a ramp-décollement system across the San Gabriel mountains (SGM) to explain the topography, seismicity and tomography data in cross section. We then provide quantitative estimates of the loading rate and the range of geometries consistent with surface velocities observed by InSAR and GPS using a Bayesian framework and assuming conservation of motion across the fault network.

3.2 Tectonic constraints

The Big Bend is bounded to the south in the LA Basin by several blind thrust faults and to the north in the Mojave desert by the beginning of the San Bernardino Mountains (SBM). Several observations are in agreement with a large scale décollement south of the transpressional bend, formed as the result of the obliquity between the relative plate motion and the local orientation of the strike-slip faults (Fig. 6.1,B) (Mount et Suppe, 1992; Teyssier et Tikoff, 1998). Crouch et Suppe (1993) first suggested a low-angle décollement below high-angle faults in the LA region from geological investigations of the Western Transverse Ranges, which has undergone more than 90° of clockwise rotation during the late Cenozoic (Crouch et Suppe, 1993; Nicholson et al., 1994; Atwater, 1998; McQuarrie et Wernicke, 2005), earlier than the activation of the present strike-slip faults. The variation of topography between flat sediments (i.e., the LA Basin) and high topography (i.e., the SBM and SGM) across small distances imply major changes from sub-horizontal structures to dipping ramps (Fig. 6.1C, Fig. 3.2A). The Moho shows a strong thickening of the crust (Tape et al., 2012) from 20 km beneath the LA Basin to 35 km beneath the SGM (Fig. 3.2A). The Sierra Madre Thrusts (SMT), the Whittier Fault (WF), the Elysian Park Thrust (EPT) and the Puente Hills Thrusts (PHT) (Fig. 6.1) may be regarded as partitioned strike-slip and thrust faults above a low-angle décollement (Shaw et Suppe, 1996; Shaw et Shearer, 1999) at the bottom of the ~ 15 km-thick seismogenic upper crust (Fig. 3.2A). This décollement may extend farther west, as indicated by the uplift of the larger banks, ridges and islands on the inner Continental Borderland region, offshore LA (Namson et Davis, 1988; Davis et al., 1989). Numerous earthquakes in this area have pure dip-slip thrust focal mechanisms and their hypocenter locations cluster between 10 to 15 km depth along shallow northeast dipping planes (Astiz et Shearer, 2000). At the junction between the Mojave and the Coachella segment, Yule et Sieh (2003) inferred from geological measurements, from the southward deepening of microseismicity (~10°S (Corbett, 1984)) and from several small, deep earthquakes with

shallow nodal planes (Webb et Kanamori, 1985), that the crustal structure of the complex San Gorgonio Pass (SGP) (Fig. 6.1) may also involve a low-angle décollement at depth that undercuts the North Frontal Thrust (NFT) and decouples the upper and the lower crust. More recently, results from the LARSE seismic refraction surveys (Kohler, 1999; Fuis et al., 2001b,a, 2012) have confirmed the presence of a low angle reflective layer below the SGM, which originates at the SAF and terminates near the hypocenters of the 1971 San Fernando and 1987 Whittier Narrows thrust earthquakes (Fuis et al., 2003). This large-scale décollement may branch on the SAF in a weak upper mantle, with a depth commensurate with the width of the SGM (\sim 25 km), following the old suture zone created by the subduction of the Farallon Plate beneath the NAP (Fuis et al., 2012), and may terminate offshore (Fig. 6.1C, Fig. 3.2A).

3.3 Deformation data

To constrain the activity and geometry of the structures below Los Angeles, we use geodetic data within a 60 km-wide and 200 km-long swath oriented perpendicular to the local azimuth of the SAF. These include the three-dimensional GPS velocity field from the Plate Boundary Observatory (PBO) and a line-of-sight (LOS) velocity map derived from Envisat and ERS descending pass spanning 18 years (Liu et al., 2014b). The InSAR data analysis is based on a small baseline approach and includes a series of corrections for atmospheric, orbital errors, and oscillator frequency drift (cf. supplementary materials).

3.4 Description of the model

We assume that the shallow vertical and high-angle faults, which formed a complex three-dimensional system at the surface, are locked during the interseismic period, while the segments that connect the down-dip end of locked faults, at the bottom of the seismic upper-crust, slip aseismically, partitioning the observed uniform velocity field (Fig. 6.1).

Several scenarios might be possible to accommodate shortening across the mountain range including a ramp-décollement system (Crouch et Suppe, 1993), distributed deformation (Wilcox et al., 1973), and out-of-sequence thrusts within the wedge (e.g., Whipple et al., 2016). Following our interpretation of geological, seismological, and surface deformation data, we divide the region in three rigid blocks delimited by two triple

MODÈLES DE PARTITIONNEMENT AU TRAVERS LE « BIG BEND »

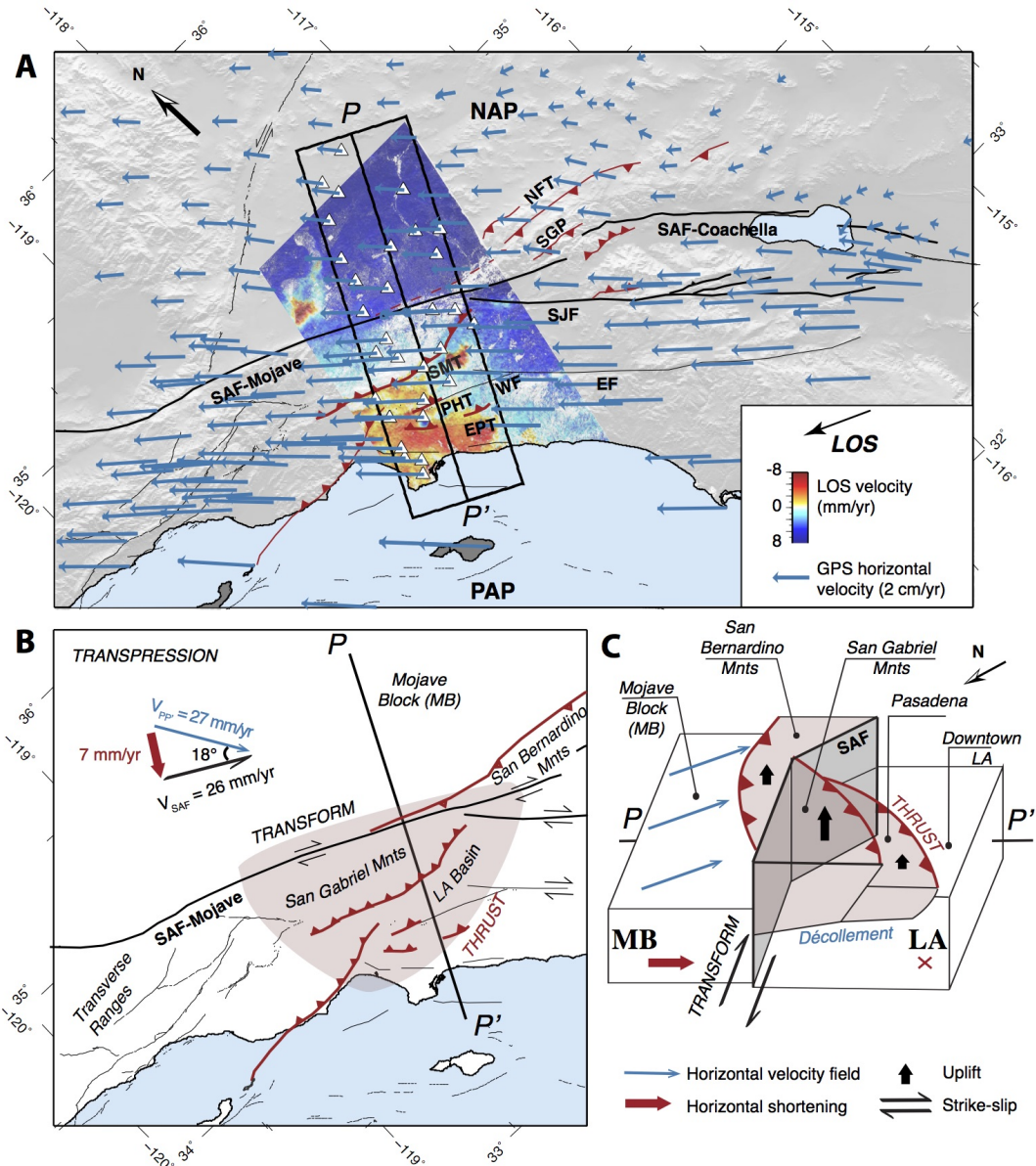


FIGURE 3.1 – Seismotectonic setting of the Southern California fault system. A : GPS data in the ITRF08 reference frame highlighting a uniform velocity field despite the complex 3-dimensional geometry of the faults systems. InSAR velocity map is derived from Envisat descending track 170 (from Liu *et al.*, 2014b). Black rectangle defines the profile perpendicular to the SAF. Major strike-slip faults including the San Andreas Fault (SAF), Whittier Fault (WF), San Jacinto Fault (SJF) and the Elsinore Fault (EF) are in black. Major thrust faults including the Sierra Madre Thrust fault (SMT), the Elysian Park Thrust (EPT), the Puente Hills Thrusts (PHT), San Gorgonio Pass (SGP) and the North Frontal Thrusts (NFT) are in red. B : Simplified kinematic sketch illustrating how the obliquity of the SAF creates a local shortening (red vector) between the Mojave Block (MB) and Los Angeles (LA). C : Simplified three-dimensional model across the profile PP' illustrating how the geometry of the ramp-décollement system partitions the uniform velocity field and controls the amount of shortening and uplift along the various blocks.

junctions and one frontal ramp (Fig. 6.1C, Fig. 3.2A). The first ramp and the back-thrust extrude the San Gabriel and the San Bernardino ranges (Fig. S2b), while a flat décollement lies under the LA Basin (Fig. S2c), connecting to the down-dip end of the SM and the PH ramps (Fig. S2d). As we have no constraints on the geometry and the mechanics of the deep seated shear zone below the SAF, we model the motion by a horizontal semi-infinite dislocation, limited to the west by the SAF (Fig. 3.2A). The surface strain due to the strike-slip component, SS_{SAF} , is not influenced by the dip angle of the fault (Fig. S3) (Segall, 2010). However the longitudinal component on this flat structure, V_{short} , can accommodate the local convergence caused by the oblique angle between the SAF and far-field plate motion near the Big Bend (Fig. 6.1B, Fig. 3.2A). We also allow a strike-slip component on the ramp-décollement system by adding a strike-slip motion on a semi-infinite dislocation, SS_{PH} . The deep-seated strike-slip motion below the SAF locking depth that controls the far-field motion is equal to the sum of strike-slip rates on the two dislocations, $SS_{SAF} + SS_{PH}$. We estimate the depth of locking H_{SAF} of the SAF. For other segments, we estimate the horizontal and the vertical distance between the triple junction and the tip of the segments (D and H) (Fig. 3.2A).

3.5 Slip partitioning constraints

Geodetic data offer limited constraints on fault geometry at depth (Savage, 1990; Segall, 2010). But slip partitioning brings additional kinematic constraints to enforce long-term compatibility of displacements along various segments of faults. At a triple junction, the partitioning of the velocity V_1 along a deep-seated fault into a velocity V_2 along a ramp, and V_3 along a back-fault implies the conservation of the horizontal and vertical motion along the three segments (Fig. 3.2A, Fig. S1). In analogy to the fault-bend folds models of Suppe (1983), we consider a kinematic model that conserves motion across the block boundaries. Assuming rigid blocks and no tilt of the hanging wall, the ratio of slip velocities on the faults bounding the blocks are

$$\begin{aligned}\frac{V_2}{V_1} &= \frac{\sin(\beta - \gamma + \alpha)}{\sin(\beta - \gamma)} \\ \frac{V_3}{V_1} &= \frac{\sin \alpha}{\sin(\beta - \gamma)},\end{aligned}\tag{3.1}$$

where γ and β are the dip angles of the ramp and the back fault, respectively. We denote α the angle between the deep-seated fault and the ramp.

3.6 Prior Assumptions

Dip angles are determined from the horizontal and vertical distances, D and H , and the along-dip components of slip are thus constrained using the conservation of motion across each junctions from equation (3.5) (cf. supplement materials).

We first define the convergence across the fault system, V_{short} , as the local horizontal shortening perpendicular to the Mojave segment of the SAF (Fig. 6.1B, Fig. 3.2, Fig. S2a) measured by the GPS between the Mojave Block and LA encompassing the profile PP'. Our prior assumption is that the deep-seated rates of motion are normally distributed centered on the far-field horizontal motion (Fig. 6.1B). This gives a shortening rate of $V_{\text{short}} = 7 \text{ mm/yr}$ with a 1σ uncertainty of 1.5 mm/yr and a deep-seated strike-slip motion of 26 mm/yr with an uncertainty of 5 mm/yr . For other parameters, we assume uniform prior distributions bounded by realistic values. According to the geological and seismological setting, we force the décollement below the LA Basin to be horizontal (Fig. 3.2A). Prior distributions for all parameters are summarized in Table S2.

3.7 Inversion method

We explore the range of models allowed by geodetic data and derive the posterior probability describing the full ensemble of possible models, $p(\mathbf{m}|\mathbf{d})$, that explain the observations, \mathbf{d} , and agree with a prior knowledge, $p(\mathbf{m})$, implementing a Bayesian approach (Minson *et al.*, 2013; Jolivet *et al.*, 2015a; Lin *et al.*, 2015; Daout *et al.*, 2016c), such as

$$p(\mathbf{m}|\mathbf{d}) \propto p(\mathbf{m}) \exp \left[-\frac{1}{2}(\mathbf{d} - \mathbf{g}(\mathbf{m}))^T \mathbf{C}_D^{-1} (\mathbf{d} - \mathbf{g}(\mathbf{m})) \right], \quad (3.2)$$

where \mathbf{d} is the data vector, \mathbf{m} is the vector of model parameters, \mathbf{C}_D is the covariance matrix of the data, and $\mathbf{g}(\mathbf{m})$ is the surface displacements predicted from model \mathbf{m} . The model parameters include the ones previously described for geometry and slip rates and the InSAR and GPS reference frames. We add an unknown azimuth linear trend to InSAR data that ties far-field LOS velocities to GPS data (Table S2). As the InSAR velocity field profile flattens in the far field, we did not add a quadratic term (Chaussard *et al.*, 2015). The data vector, \mathbf{d} , is made of the LOS displacement rates, the GPS vertical velocities, and the GPS horizontal velocities projected into profile-perpendicular and profile-parallel components (Table S1). The data covariance matrix includes the

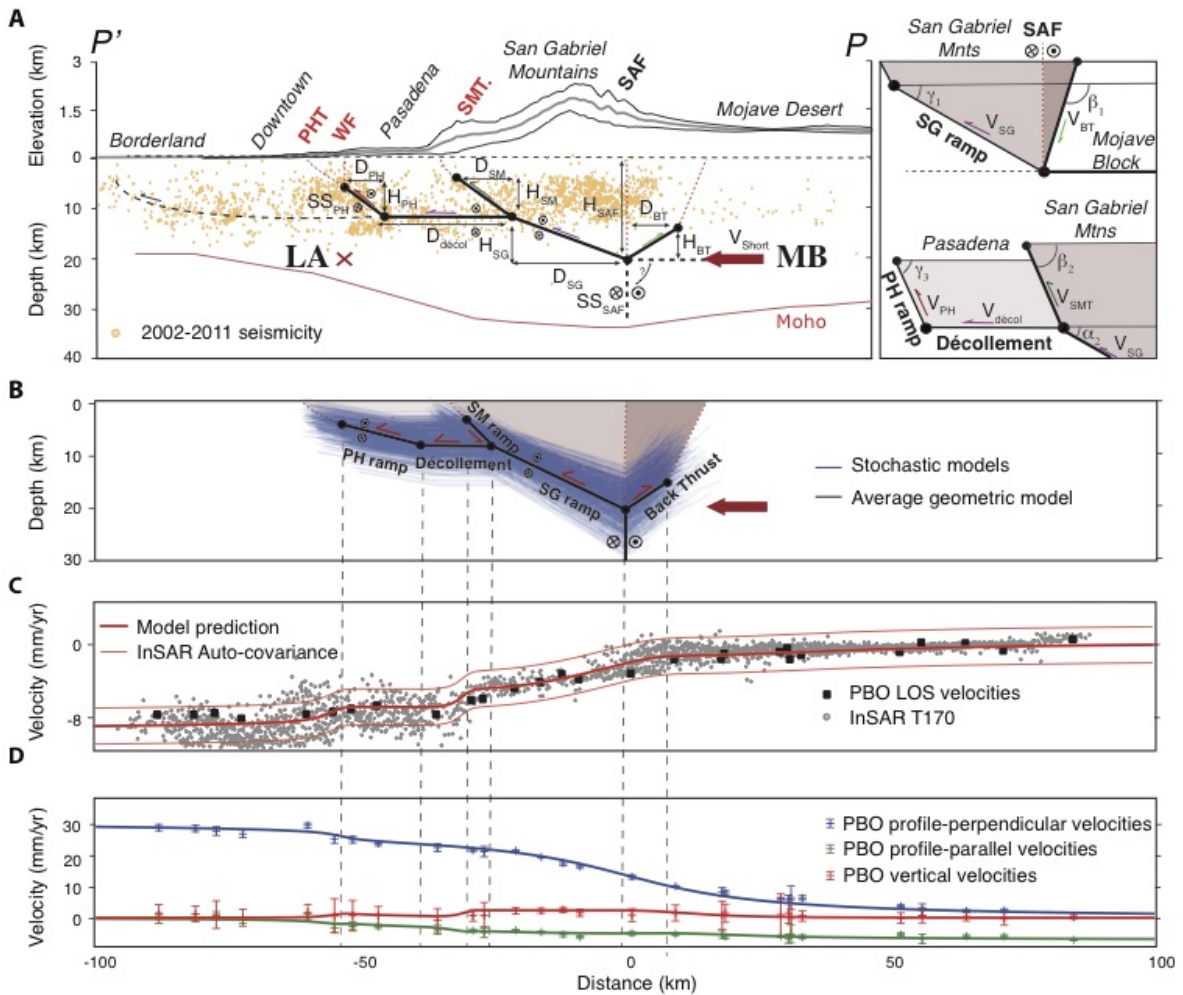


FIGURE 3.2 – Comparison between the prior and posterior models. A : 2D prior model based on the tectonic review along the profile PP' defined in Fig. 6.1. Black lines (red dashed lines resp.) represent slipping (locked resp.) sections of the faults ; arrows indicate relative direction of the movement on faults. The SAF is associated with two thick black-dashed lines and an question mark as we have no constraints of its deep geometry. We use this configuration and the conservation of motion along each junction to explore the various parameters defined in this figure. Insert is a simplified two-dimensional block model illustrating the relation between the block geometries and longitudinal velocities along the structures. B : Posterior geometries in agreement with the data (blue lines) and average geometry (black lines). C : InSAR LOS velocities (grey points) and GPS projected in the LOS direction (black squares) and average model obtained. D : Profile-perpendicular (blue markers), profile-parallel (green markers), and vertical (red markers) GPS velocities with their associated uncertainties. Average model obtained (blue, green and red lines) along profiles.

variance of the GPS and InSAR measurements on its diagonal and InSAR data spatial correlation in the off-diagonal components (cf. supplement materials and Figs. S4 and S5).

We then draw random samples from prior distributions previously defined (Table S2) and evaluate the posterior PDFs using the Metropolis algorithm, implemented in the *PYmC* library ([Patil et al., 2010](#)), guided by the geodetic data and the associated uncertainties.

3.8 Posterior models

We sample the model space with 40,000 samples, rejecting the first 30,000 (after the starting of the convergence) to minimize the effect of the initial model. A large range of possible models in agreement with the data and the conservation of motion are shown in blue lines in Fig. 3.2B. The comparison between the prior and posterior models is summarized in Table S2 and Fig. S6. Except for parameters $D_{\text{décol}}$, D_{SM} , and H_{PH} , all posterior PDFs show normal distributions centered on the mean models (red vertical lines in Fig. S6) away from the prior limits. Posterior PDFs are narrowed in comparison to the prior PDFs highlighting the gain of information from the data and the conservation of motion. The sensitivity of InSAR to vertical deformation and its dense spatial sampling makes it a valuable complementary data sets to GPS. We compare these results with inversions that consider GPS alone in the supplementary materials (Fig. S6 and S7). The comparison between surface observations and predictions from the mean value of the posterior model are shown in Figs. 3.2C and D. There is in general a good agreement between observations and predictions. Predicted velocity maps and GPS vectors are also presented in Fig. S8, while the full posterior covariance of the model parameters and the joint posterior probabilities between slip rates and locking depths are displayed in Figs. S9 and S10. The GPS residuals are smaller than 1 mm/yr, indicating that the model explains horizontal deformation well. In contrast, InSAR residuals reveal subsidence within the LA Basin bounded by the Whittier and the Palos Verdes Faults (Fig. 3.2B, Fig. S8).

The average posterior model indicates a locking depth of 20 ± 3.5 km and 3.5 ± 2.5 km for the SAF and Whittier-Puente Hills fault-system, respectively (all the uncertainties are documented $\pm 1\sigma$). These depths are associated with strike-slip rates of 25.5 ± 0.5 mm/yr on the SAF and 3.1 ± 0.6 mm/yr on the WF. We find that the 6.6 ± 0.6 mm/yr of shortening rate is partitioned between 3.1 ± 0.5 mm/yr on the $40 \pm 5^\circ$ SW-dipping back-thrust segment and 4.7 ± 0.7 mm/yr on the $25 \pm 5^\circ$ NE ramp segment below the SGM. Then, slip on the ramp partitions into 2.7 ± 0.9 mm/yr on the $48 \pm 5^\circ$ NE Sierra Madre ramp and 2.5 ± 1.0 mm/yr on the $16 \pm 10^\circ$ NE-dipping Puente Hills ramp (Fig. 3.2B). The 8 ± 3.5 km depth flat décollement below the LA Basin connecting the down-dip end of

the PH ramp with the tip of the SG ramp creeps at 2.4 ± 0.7 mm/yr. To summarize, among the 6.6 ± 0.6 mm/yr of local shortening across the profile, the backthrust structure accommodates around 2.4 mm/yr of horizontal convergence while the SMT and the PHT absorb 1.8 mm/yr and 2.4 mm/yr of shortening, respectively.

We explore the influence of adding a strike-slip creeping segment on the SAF between the junction of SG ramp with the SAF and a shallow locking depth of the SAF, but our results indicate a strike-slip motion on this shallower segment close to zero.

3.9 Discussion

The average slip rates and the most likely geometry of the fault system is shown in Fig. 3.11 and Fig. 3.2B. Note that although our model is two-dimensional, it explains the three-dimensional interseismic velocity field remarkably well (Fig. S8).

Our mean posterior model indicates a deep-seated strike-slip rate of 28.6 ± 0.5 mm/yr partitioned into 25.5 ± 0.5 mm/yr on the SAF, locked at 20 ± 3.5 km depth, and 3.1 ± 0.6 mm/yr on the ramp-décollement system, creeping from the SG-SAF junction to the tip of the PH ramp at 3.5 ± 2.5 km depth. The rate of the SAF is near the high end of the range of rates previously estimated for the Mojave section of the SAF using single fault models (e.g., Savage et Lisowski, 1995), two-dimensional, GPS-constrained, block models (e.g., Shen et al., 1996; McCaffrey, 2005; Meade et Hager, 2005), or viscoelastic half-space models (e.g., Tong et al., 2014). Long-term geologic slip rates along the SAF range from 24.5 ± 3.5 mm/y (Weldon et Sieh, 1985) in the Cajon Pass to 35 ± 7 mm/y in the Pallett Creek (Salyards et al., 1992). The modeled strike-slip component on the ramp-décollement system is also comparable with the 2.5 ± 0.5 mm/yr of long-term strike-slip motion measured on the Whittier fault zone (Walls et al., 1998). The deep-seated strike-slip motion is in agreement with geometry of the Big Bend. If we consider 34 mm/yr of strike-slip component along the central segment observed both geologically and geodetically (Sieh et Jahns, 1984; Barbot et al., 2013), the 25° of change of azimuth of the SAF from the Central segment to the Big Bend would create a strike-slip rate along the Mojave of ~ 30 mm/yr.

The average posterior locking depth of the SAF (20 ± 3.5 km) is slightly deeper than the seismogenic depth of 15 km estimated from the maximum depth of earthquakes (Hauksson et al., 2012) but comparable to the locking depth of 20 km adopted by McCaffrey (2005) based on a regional misfit between a block model and GPS data. The

difference of rheology between the Los Angeles sedimentary basin and the Mojave block may explain the contrast of locking depths between the SAF and the PH ramp. Locking depth below the LA sedimentary basin may be underestimated as we do not take into account these rheological effects (Argus *et al.*, 2005), while viscoelastic effects may decrease the San Andreas strike-slip rate in comparison to simple elastic models (Tong *et al.*, 2014). However, dip-slip rates obtained by our exploration are in good agreement with the paleo-seismological and geological slip rates without the need of introducing viscoelastic effects. Below LA, paleoseismology indicates [0.4 – 1.7] mm/yr and [0.6 – 1.6] mm/yr of quaternary slip rates on the PHT (Shaw *et al.*, 2002; Dolan *et al.*, 2003) and the EPT (Shaw et Suppe, 1996; Oskin *et al.*, 2000), respectively, while long-term slip rates of the central SMT are within the range of [2.0 – 5.5] mm/yr (Dolan *et al.*, 1995; Walls *et al.*, 1998). In comparison, we constrain 2.5 ± 1.0 mm/yr on the frontal ramp at the roots of PHT and the EPT, creeping until 3.5 ± 2.5 km-depth, and 2.7 ± 0.9 mm/yr of creep below the Sierra Madre thrusts up to 3 ± 2.5 km-depth, at the front of the San Gabriel ranges. Note that these inverted dip-slip rates at depth, perpendicular to the profile, might be released at the surface by pure thrust motion or by strike-slip on oblique faults, as for instance the Raymond and San Jose faults extending west-southwest and forming a complex three-dimensional system (Walls *et al.*, 1998).

Posterior PDFs show that the strike-slip rate of the SAF does not trade-off with its locking depth but correlates with the strike-slip rate of the PH ramp (Fig. S9, S10). GPS data provide a reference on the horizontal component of ground displacement. Far-field strike-slip rate, $SS_{SAF} + SS_{PH}$, and shortening rate, V_{short} , are identically constrained with and without InSAR data (Fig. S6 and S7). This shows that the GPS velocity field is dense enough to constrain the deformation gradient and thus the locking depth of the SAF. We also observe a correlation of the locking depth of the SAF with the parameters H_{SG} and D_{SG} , and thus the dip angle of the SG ramp (Fig. S9). Overall, the posterior correlation matrix indicates strong correlations between parameters D and H of the various dislocations as they control the geometry of the ramps and the amount of dip-slip motion. Small variations of dip angles results in significant changes in vertical velocities. Without InSAR data, parameters H and D of the SG, SM and PH ramps are not well constrained as they indicate posterior PDFs close to the prior uniform distributions (Fig. S6). Average posterior model indicates a deeper depth for the tip of SG ramp and a vertical gradient that concentrates at the front of the Puente Hills ranges (Fig. S7). Due to a high sensitivity to vertical movements, InSAR data force the partitioning of the shortening rates between the SM and the PH ramps, which is in

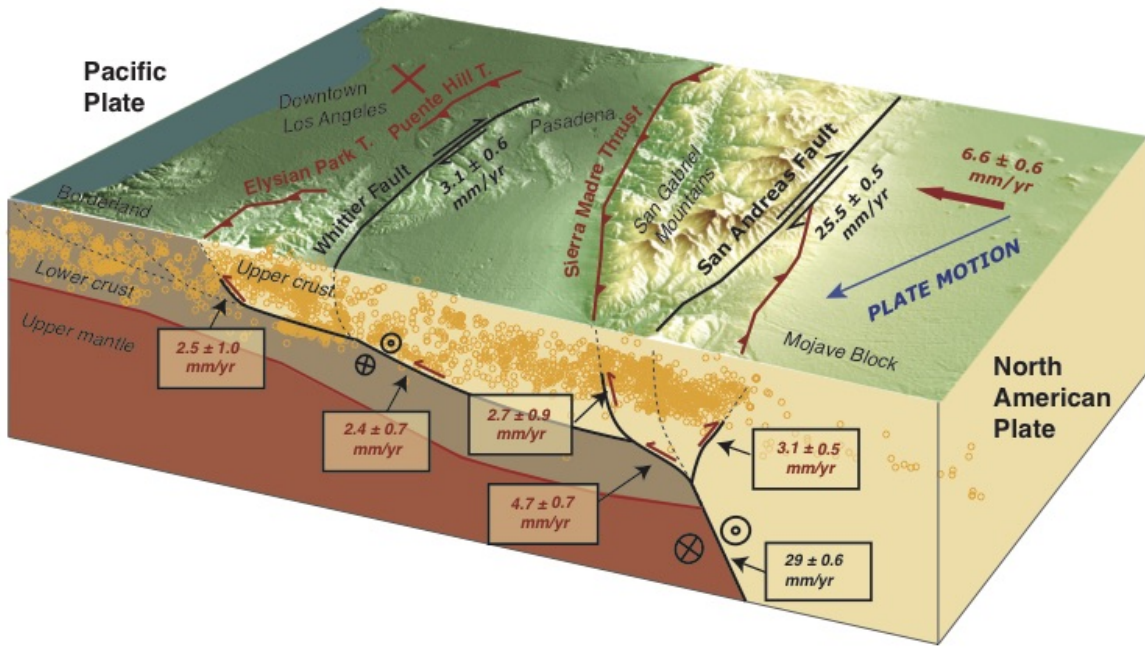


FIGURE 3.3 – Three-dimensional schematic block model across the SGM (after [Fuis et al., 2001a](#)) superimposed to the digital elevation model, the seismicity (yellow dots), the Moho model (red line) and interpreted active faults summarizing the average interseismic strike-slip (back arrows) and dip-slip (red arrows) rates extracted from the Bayesian exploration. Shallow faults (dashed lines) that formed a complex 3-dimensional system at the surface ([Plesch et al., 2007](#)) are locked during the interseismic period while the ramp-décollement system (solid lines) decouples the upper-crust from the lower crust and partitioned the observed uniform velocity field (blue vector) at the down-dip end of the structures.

agreement with the differential topography and vertical velocity between the SGM and the LA Basin (Fig. 6.1A), as well as the long-term respective slip rates of the SMT and the PHT ([Dolan et al., 1995](#)). In comparison to previous studies, by inverting both GPS and InSAR data simultaneously, we improve the sampling of the surface displacement field, especially in the vertical direction, better constraining the geometry of the ramp-décollement system and the intervening slip rates at depth.

The 3.1 ± 0.5 mm/yr of slip along the back-thrust structure is not associated with any identified surface trace north of the SGM but may correspond to the extension of the North Frontal Thrusts below the San Bernardino mountains (Fig. 6.1). However, it is difficult to conclude about the nature of this structure, which might represent distributed deformation formed in a fault-bend fold ([Suppe, 1983](#)), or a backthrust part of a flower structure (Fig. 3.11). The structure accommodates the slip incompatibility between the

shortening rate (V_{short}) and the ramp (V_{SG}) to conserve motion across the fault network. It is required to fit fault-perpendicular and vertical GPS velocities and the displacement gradient in InSAR data north of the SAF.

At greater depth, the local convergence across the profile may be accommodated by shear zone extending northward of the SAF (e.g., [Bowman et al., 2003](#)), following the old suture zone formed by the subduction of the Farallon Plate beneath the NAP that connects the Carrizo plain in the north to the Gulf of California in the south ([Teyssier et Tikoff, 1998](#); [Fuis et al., 2012](#); [Wang et al., 2013](#); [Pikser et al., 2012](#)). In this scenario, slip on this mantle structure might not create detectable surface displacements due to the large differences in viscosity between the upper mantle and the lower crust, the isostatic effects of this long-wavelength slab or the low angle of this deep-seated structure. In an alternative scenario, the upper-mantle boundary between the North America and the Pacific plate may follow the San Andreas fault from the Central segment, in the north, to the SJF, in the south. In this case, the transpressional bend may only reside in the crust and may not be associated with motion in the mantle. Our proposed model is compatible with both scenarios, which cannot be differentiated from geodetic studies alone.

3.10 Conclusion

We develop a novel way to explore the compatibility of geodetic velocities with a long-term kinematic model that conserves motion along and across a fault system. We apply the method to understand slip partitioning around the Big Bend of the SAF and the loading of buried faults below the LA metropolitan area. We start from a simplified prior geometry of connected faults beneath the SGM section of the PAP-NAP plate boundary. Using the conservation of motion across fault junctions as a prior constraint, we then propagate the far-field GPS field on the ramp-décollement system and explore the parameter space of fault geometries and slip rates that satisfy the InSAR and GPS velocity fields. Our most likely model suggests the existence of a flat décollement below Metropolitan Los Angeles bounded by two steeper ramps under the Sierra Madre and the Puente Hills that are creeping below a shallow locking depth. The proposed fault network geometry and kinematics also includes slip along a SW-dipping backthrust connecting to the SAF and accommodating part of convergence between the Mojave block and the San Gabriel ranges. This study underlines the importance of understanding first-order fault geometry for geodetic models ([Daout et al., 2016c](#); [Qiu et al., 2016](#)) and represents

another step forward towards bridging the gap between earthquake cycle modeling and structural geology.

3.11 Supplementary Material

Slip-partitioning model

The closure equation that describes the stability of a two-dimensional transform FFF triple junction ([McKenzie et Morgan, 1969](#)) separating three blocks A, B, and C can be written in vector form as :

$$\mathbf{V}_1 + \mathbf{V}_2 + \mathbf{V}_3 = \mathbf{0} \quad (3.3)$$

where \mathbf{V}_1 represents the velocity of block A with respect to block B (\mathbf{V}_2 for B/C and \mathbf{V}_3 for C/A, respectively). Assuming rigid blocks and that the triangular wedge C is uplift and not tilted ([Fig. 3.4](#)), we can project equation (3.3) on the horizontal and vertical axes and write :

$$\begin{aligned} V_1 \cos(\gamma - \alpha) &= V_2 \cos \gamma - V_3 \cos \beta \\ V_1 \sin(\gamma - \alpha) &= V_2 \sin \gamma - V_3 \sin \beta \end{aligned} \quad (3.4)$$

where V_1 , V_2 and V_3 are the amplitudes of the vectors \mathbf{V}_1 , \mathbf{V}_2 and \mathbf{V}_3 , respectively, and angles α , β , and γ are defined in [Fig. 3.4](#). The ratio of velocities on the fault segments are controlled by the geometry :

$$\begin{aligned} \frac{V_2}{V_1} &= \frac{\sin(\beta - \gamma + \alpha)}{\sin(\beta - \gamma)}; \\ \frac{V_3}{V_1} &= \frac{\sin \alpha}{\sin(\beta - \gamma)}. \end{aligned} \quad (3.5)$$

The modeled two-dimensional fault system is represented in [Fig. 3.5](#). The PP' profile is perpendicular to the direction of the Mojave segment of the SAF ([Fig. 3.5a](#)). The dip-direction velocities on fault segments must satisfy equation (3.5) at each junction, as we detail below.

- 1. Triple junction between the SAF, the San Gabriel (SG) ramp and the Back-Thrust (BT) fault.** The “far-field” horizontal convergence between the Mojave

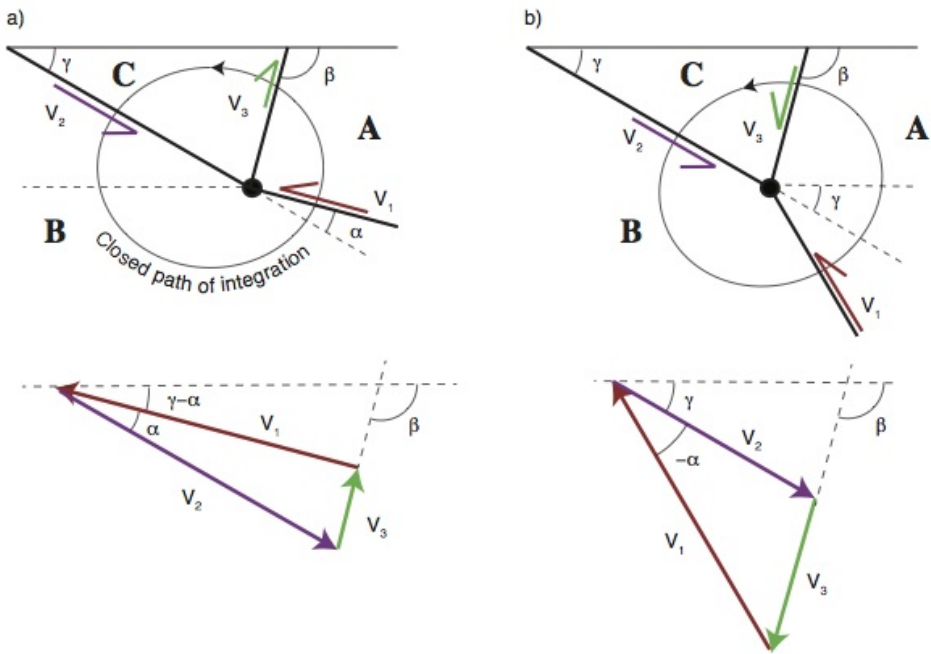


FIGURE 3.4 – Conservation of motion along a triple junction. Vectors summation enforcing the conservation of motion along a triple junction separating three blocks A, B and C in a case of (a) reverse back-thrust fault and (b) normal back-thrust fault. Top) Geometry of the triple junction ; the vectors indicate the relative displacement velocity across the fault assuming the block across the fault fixed. Bottom) Odograph of the above triple junction following a close path of integration. To conserve motion in the system, the velocity vectors form a closed triangle and the vector amplitudes obey the law of cosines.

Block (MB) and Los Angeles (LA), V_{short} , is equal to \mathbf{V}_1 (Fig. 3.5a,b). In this case, as α_1 is set to γ_1 (Fig. 3.5b), equation (3.5) simplifies to :

$$\frac{V_{\text{SG}}}{V_{\text{short}}} = \frac{\sin \beta_1}{\sin(\beta_1 - \gamma_1)}$$

$$\frac{V_{\text{BT}}}{V_{\text{short}}} = \frac{\sin \gamma_1}{\sin(\beta_1 - \gamma_1)}$$

2. Triple junction between the SG ramp, the Sierra Madre (SM) ramp, and the flat décollement. This corresponds to the geometry of Fig. 3.5b. With the velocity notations of Fig. 3.5c and $\gamma_2 = 0$, equation (3.5) becomes :

$$\frac{V_{\text{Decol}}}{V_{\text{SG}}} = \frac{\sin(\beta_2 + \alpha_2)}{\sin \beta_2},$$

$$\frac{V_{\text{SM}}}{V_{\text{SG}}} = \frac{\sin \alpha_2}{\sin \beta_2}.$$

3. Junction between the flat décollement and the PH ramp. In this case slip on the PH ramp is equal to the projection of the convergence on the flat décollement, such as

$$\frac{V_{\text{PH}}}{V_{\text{Decol}}} = \cos \gamma_3.$$

The differential vertical velocity between V_{Decol} and V_{PH} is here assumed to be accommodated by folding in the hanging wall (Suppe, 1983) in agreement with the sedimentary setting in the Los Angeles Basin and the shallow depth.

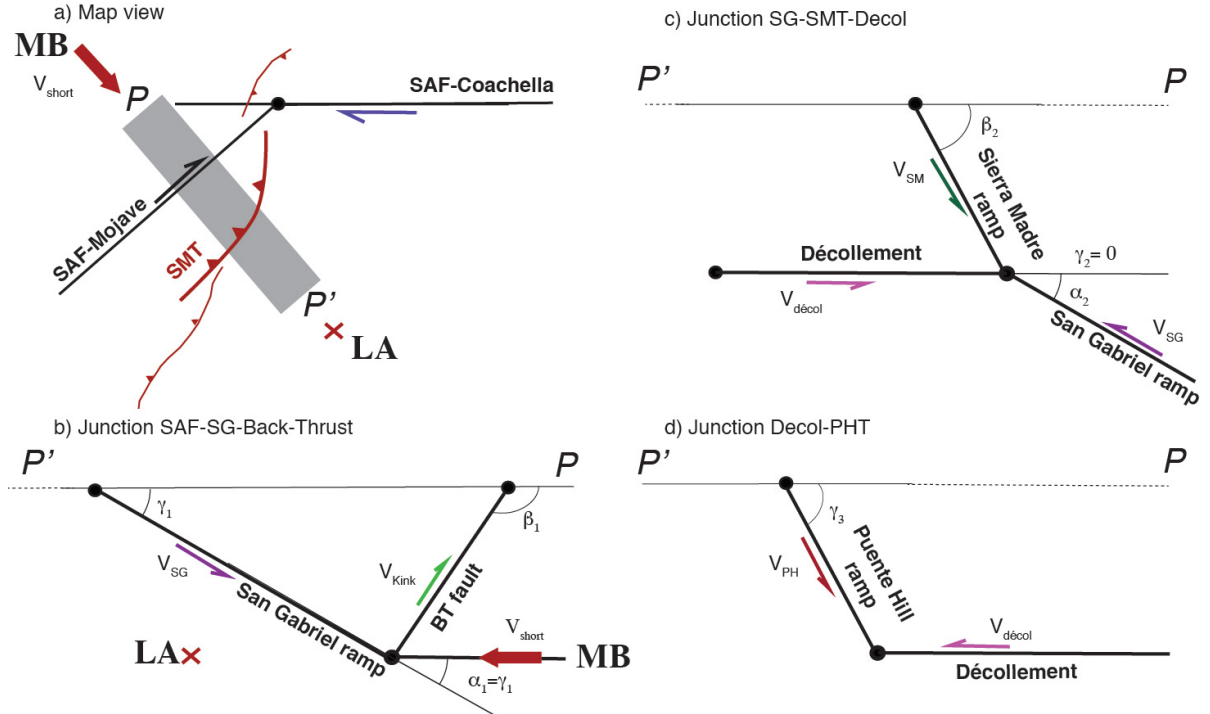


FIGURE 3.5 – Conservation of motion across the Big Bend. a) Schematic map-view of the San Andreas Big Bend illustrating how the local horizontal shortening perpendicular to the Mojave segment of the SAF is partitioned. b,c,d) Cross sections across the triple junctions and fault bends of the fault system along the P'P profile. MB : Mojave Block ; LA : Los Angeles ; SMT : Sierra Madre Thrust ; SM : Sierra Madre ; SG : San Gabriels ; décol : Décollement ; PH : Puente Hills.

GPS data

GPS data are from the Plate Boundary Observatory (PBO). We select stations encompassing the profile and decompose the horizontal displacements into the SAF-parallel and SAF-perpendicular components (Table S1).

TABLE 3.1 – GPS vectors used in the model. GPS station names encompassing the profile sorted by their fault-perpendicular distances to the SAF, as well as their relative velocities and uncertainties (σ). Horizontal vectors are projected into the N63°W SAF-parallel (U_{par}) and SAF-perpendicular (U_{perp}) components to better visualize relative far-field shearing and shortening across the profile.

| Station name | distance (km) | U_{perp} (mm/yr) | U_{par} (mm/yr) | U_v (mm/yr) | σ_{par} | σ_{perp} | σ_v |
|--------------|---------------|---------------------------|--------------------------|---------------|-----------------------|------------------------|------------|
| AZU1 | -88.108 | 6.837 | 25.943 | -0.033 | 1.155 | 1.292 | 3.4 |
| BKMS | -81.198 | 6.503 | 25.644 | -0.131 | 0.733 | 0.768 | 2.44 |
| CGDM | -77.281 | 7.023 | 24.939 | -0.288 | 1.553 | 1.587 | 3.74 |
| CHMS | -72.265 | 5.680 | 24.089 | -1.156 | 1.195 | 1.127 | 4.08 |
| CPBN | -60.034 | 6.678 | 26.571 | 0.290 | 0.448 | 0.413 | 1.82 |
| CRHS | -54.984 | 3.444 | 22.677 | -0.655 | 0.955 | 0.944 | 2.28 |
| ECCO | -51.554 | 3.892 | 22.437 | -0.444 | 1.260 | 1.145 | 4.02 |
| HIVI | -46.731 | 3.839 | 21.294 | -0.526 | 3.422 | 2.528 | 5.02 |
| LASC | -35.556 | 2.889 | 20.170 | -1.931 | 1.089 | 0.941 | 2.40 |
| LORS | -28.864 | 2.696 | 19.362 | -0.549 | 0.460 | 0.403 | 1.62 |
| P470 | -26.759 | 2.211 | 19.016 | -0.481 | 0.588 | 0.656 | 2.64 |
| P574 | -20.804 | 2.791 | 19.247 | 0.815 | 0.431 | 0.340 | 1.0 |
| P575 | -15.978 | 2.255 | 17.384 | 0.836 | 0.598 | 0.644 | 0.72 |
| P581 | -11.846 | 1.569 | 15.602 | 1.131 | 0.246 | 0.429 | 2.30 |
| P582 | -8.673 | 0.829 | 14.672 | 0.261 | 0.256 | 0.244 | 6.00 |
| P583 | 1.124 | 1.861 | 11.698 | -0.397 | 0.374 | 0.408 | 1.32 |
| P586 | 9.350 | 1.703 | 8.960 | 0.192 | 1.187 | 1.255 | 2.96 |
| P587 | 18.141 | 1.601 | 7.350 | -0.412 | 0.305 | 0.259 | 0.84 |
| P588 | 18.737 | 0.948 | 7.054 | 0.136 | 1.760 | 1.387 | 2.18 |
| P590 | 29.175 | 1.077 | 5.414 | -0.31 | 0.220 | 0.220 | 0.64 |
| P605 | 30.649 | 0.338 | 5.211 | 0.123 | 0.300 | 0.300 | 0.7 |
| PBPP | 31.117 | 1.704 | 5.625 | -1.123 | 0.643 | 0.529 | 1.86 |
| PHLB | 33.267 | 0.808 | 5.564 | -0.616 | 0.510 | 0.419 | 1.50 |
| PKRD | 51.829 | 1.588 | 3.223 | -1.277 | 1.271 | 1.191 | 4.94 |
| PVRS | 55.877 | 0.283 | 2.131 | -0.475 | 0.909 | 0.931 | 2.68 |
| RHCL | 64.199 | 1.025 | 1.783 | -0.786 | 0.974 | 1.267 | 4.24 |
| SCIA | 71.324 | 1.017 | 1.978 | -1.539 | 0.696 | 0.627 | 1.54 |
| SPMS | 84.452 | 0.000 | 0.000 | -0.924 | 0.652 | 0.573 | 2.58 |

InSAR Data

InSAR velocity map from track 170 is from [Liu et al. \(2014b\)](#). SAR data of ERS and Envisat satellites from 1992 to 2010 for interferograms were processed using a modified version of JPL/Caltech ROI_PAC software package. Major processing steps include topography phase correction based on 2-arc SRTM digital elevation model, baseline re-estimation for orbital error correction (when applicable), phase unwrapping, filtering and geocoding. For the ERS-2 data after 2001 that have Doppler issue due to gyroscope failure, we employ a maximum entropy approach to solve Doppler ambiguity and identify all usable ERS-2 interferometric pairs. For Envisat ASAR sensor, interferograms are corrected from the effect of the long-term local oscillator frequency drift defined by ([Mankovich et Larsen, 2013](#)). Comparison with GPS shows that this correction reduces the RMS error between InSAR and GPS velocities to less than 2mm/yr ([Liu et al., 2014b](#)). Since orbital ramp error is in general small and limited to a few acquisitions ([Fattah et Amelung, 2014a](#)), we corrected them through baseline re-estimation with the constraint of a priori GPS based deformation model. The number of the pairs with such correction is much less than the total number of interferograms that went into the analysis. This ensures that the influence of the priori model is negligible. We use a variant of the Small Baseline Subset (SBAS) InSAR time series inversion approach to solve for LOS time series and mean deformation rate ([Sansosti et al., 2010](#)). In the time series inversion we incorporated topography dependent troposphere delay correction, residual DEM error and earthquake offset estimate, and employed spatiotemporal filtering to remove high frequency turbulent troposphere noise ([Samsonov, 2010; Liu et al., 2014b](#)).

Inversion method

We design a kinematic inversion sufficiently complex to account for the three-dimensional displacement field, while remaining simple enough to constrain the main parameters controlling deformation in this area. A higher complexity might be required to explain the cloud of seismicity in Southern California and the numerous fault traces observed at the surface. Accordingly, the SAF might change its dip angle toward the surface and other secondary faults might branch off to the proposed ramp-décollement system. However, during the interseismic period these faults are locked and do not produce interseismic deformation.

The model is two-dimensional along a profile perpendicular to the N63°W azimuth of the San Andreas Fault. Strike-slip component of slip only influences the profile-

perpendicular component, while the dip-slip components on the dipping planes affects the profile-parallel and vertical components. As semi-infinite strike-slip dislocations predict the same surface strain for any dip angle (Fig. 3.6), longitudinal components of slip along the dipping dislocations control the amount of shortening and uplift for each blocks.

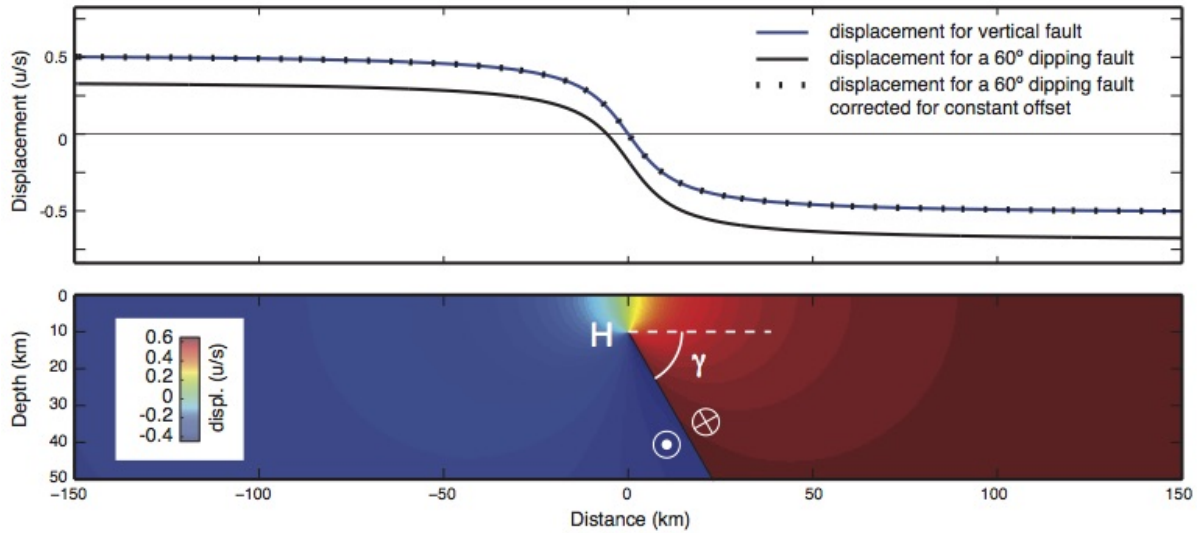


FIGURE 3.6 – Similarity of surface displacements due to widely varying dip angles (γ) for long strike-slip faults (Segall, 2010)

The model parameters include the free parameters enumerated in Table 6.2 for the geometry, the slip rates and the InSAR ramp. We also include the GPS reference frame in the model.

The data vector, \mathbf{d} , is made of the LOS displacement rates, the horizontal GPS velocities projected into profile-perpendicular and profile-parallel components and GPS vertical velocities.

A data covariance matrix, \mathbf{C}_D , is constructed to take into account the error structure on both the GPS and InSAR data. The GPS part of the matrix contains only diagonal elements. As we observe underestimated uncertainties for GPS vectors, we scale the errors by a factor of 20 (green histogram in Fig. 3.7a) based on the magnitude of the residuals of a initial inversion using GPS data only (blue histogram in Fig. 3.7a). The InSAR part of the matrix includes both diagonal and off-diagonal elements to represent the spatial correlation of the noise. Residuals of a initial inversion using InSAR data only show a normal distribution centered on zero. The larger residuals probably correspond to the

ground subsidence signal in the LA Basin (Bawden *et al.*, 2001; Argus *et al.*, 2005; Hu *et al.*, 2016) that may be included in the InSAR profile. From this data-model residuals, we compute empirical covariance as a function of the distance between InSAR points on the residual velocity map (Lohman et Simons, 2005; Sudhaus et Sigurjón, 2009) (black dots Fig. 3.8). We then estimate the best-fit exponential function (red line in Fig. 3.8) to build the full data covariance (Jolivet *et al.*, 2015a), such as :

$$C_{ij} = \sigma^2 e^{-\frac{\|\mathbf{x}_i - \mathbf{x}_j\|}{\lambda}} \quad (3.6)$$

where C_{ij} is the covariance matrix, $\lambda = 4.3$ km is a characteristic length scale of noise, $\sigma = 1.4$ mm/yr is the covariance of the measurement, and \mathbf{x}_i is the position of pixel i (Fig. S1) (Jolivet *et al.*, 2012; Daout *et al.*, 2016c). The correlated noise, σ , is close to the 2σ variance of 1.3 mm/yr of the residual velocities between the initial model and the InSAR data (Fig. 3.7b).

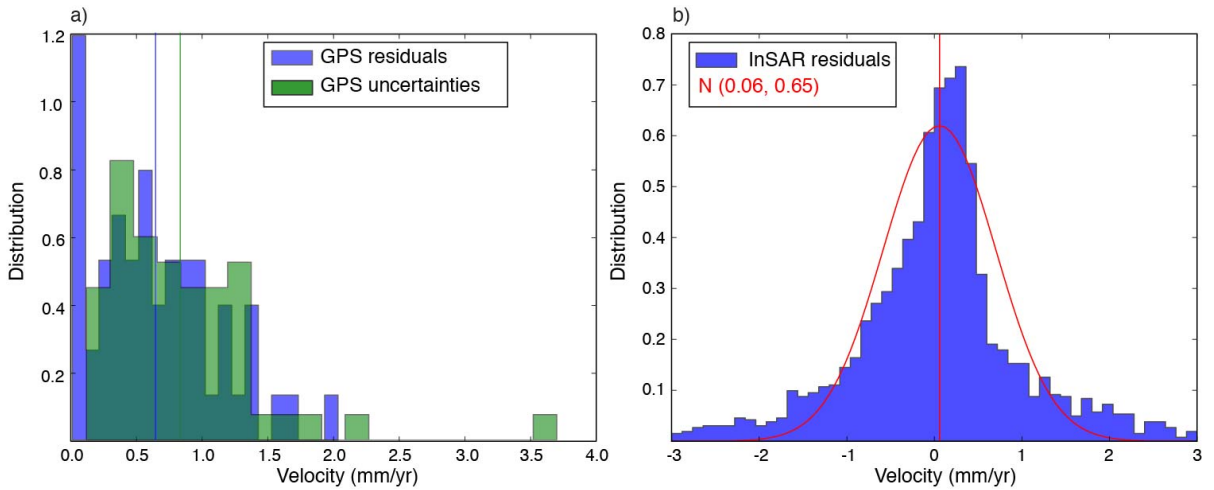


FIGURE 3.7 – Data residuals. a) Distribution of the residuals between a initial model using GPS data only and the GPS data (blue). Comparison with scaled GPS uncertainties (green). b) Distribution of the residual between the model using InSAR data only and the InSAR data.

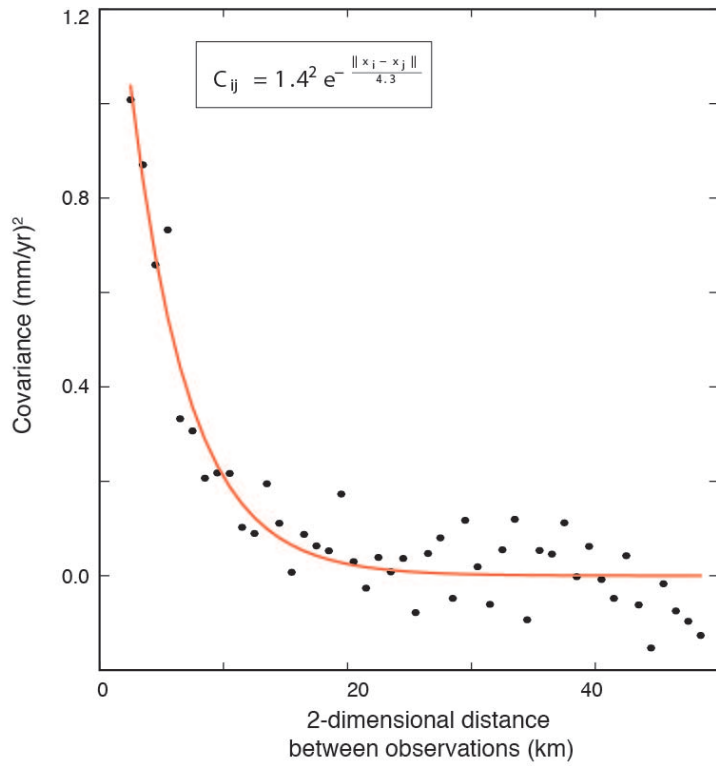


FIGURE 3.8 – InSAR spatial covariance. Two-dimensional empirical covariance and associated best-fit exponential functions for the InSAR data computed from the residual velocity map of a preliminary inversion based on the approach used in [Daout et al. \(2016c\)](#).

Exploration results

We summarize the comparison between prior and posterior distributions in Table 6.2 and Fig. 3.9. We add in Fig. 3.9 a comparison of the PDFs without InSAR data and in Fig. 3.10 the comparison between surface observations and predictions with GPS data only. This shows how GPS data mainly constrain the far-field gradient and the deep-seated rates (SS_{SAF} , SS_{PH} , and V_{short}), while InSAR data improve the constraints on the geometry of the fault system, shrinking the PDFs of the horizontal and vertical distances between dislocations. We also observe that GPS data alone predict a shallower depth for the SG ramp, while adding InSAR data increase the dip angle of the SG ramp. Finally, note that without the conservation of motion, the inverse problem does not have enough constraints to resolve all parameters.

GPS and InSAR velocity maps for the data, model and residuals are presented in Fig. 3.11. There is in general a good agreement between observations and predictions.

Residual velocities between GPS vectors and models are less than 1 mm/yr. The fit to the InSAR profile and with the GPS data projected in the LOS direction is satisfactory (Fig. 2B). However, GPS and InSAR model misfit differ at a distance of -60 and -80 km from the SAF, corresponding to a large portion of residual negative LOS motion in map view near the coast. The LOS residuals have a circular shape in map view, corresponding to areas of ground subsidence due to the hydrological water pumping in the Los Angeles Basin ([Bawden et al., 2001](#); [Argus et al., 2005](#); [Hu et al., 2016](#)). Interestingly, the Puente Hills and the Palos Verdes Faults delimit these water reservoirs.

Fig. 3.12 gives the posterior correlation coefficient matrix, illustrating the trade-off between all the model parameters. Fig. 3.13 shows the correlations between our inferred slip rates and the locking depths. We observe trade-offs between parameters D and H as these two parameters control dip angles and thus the amount of dip-slip motion imposed by the conservation of motion (Fig. 3.12, Fig. 3.13). Unlike single fault models, the SAF strike-slip rate does not indicate strong correlations with other parameters such as the locking depth of the fault. This may be due to the dense GPS velocity field or other constraints imposed by the connectivity of segments and slip preservation through junctions. We observe a correlation between the San Andreas strike-slip rate and the Puente Hills/Whittier fault strike-slip rate. Dip slip rates of the back-thrust and San Gabriel segments are correlated to their locking depths (Fig. 3.13).

TABLE 3.2 – Summary of the prior and posterior probabilities. \mathcal{N} and \mathcal{U} define normal and uniform distributions, respectively. SS_{SAF} : strike-slip rate along the San Andreas semi-infinite dislocation ; SS_{PH} : strike-slip rate along the Puente Hills semi-infinite dislocation ; V_{short} : shortening rate between the Mojave Block and LA ; H_{SAF} : depth of the tip of the SAF dislocation ; D_{SG} , H_{SG} : horizontal and vertical distances between the tip of the SAF dislocation and the tip of the San Gabriel dislocation ; D_{BT} , H_{BT} : horizontal and vertical distances between the tip of the SAF dislocation and the tip of the back-thrust dislocation ; $D_{\text{décol}}$: horizontal distances between the tip of the San Gabriel dislocation and the tip of the décollement dislocation ; D_{SM} , H_{SM} : horizontal and vertical distances between the tip of the San Gabriel dislocation and the tip of the Sierra Madre dislocation ; D_{PH} , H_{PH} : horizontal and vertical distances between the tip of the décollement dislocation and the tip of the Puente Hills dislocation. InSAR ramp corresponds to the linear coefficient.

| variables SGP | prior | posterior |
|--|----------------------------|--------------------------------|
| $SS_{\text{SAF}} + SS_{\text{PH}}$ (mm/yr) | $\mathcal{N}(26, 5)$ | $\mathcal{N}(28.6, 0.5)$ |
| V_{short} (mm/yr) | $\mathcal{N}(7, 1.5)$ | $\mathcal{N}(6.6, 0.6)$ |
| H_{SAF} (km) | $\mathcal{U}(0, 40)$ | $\mathcal{N}(20., 3.5)$ |
| D_{SG} (km) | $\mathcal{U}(0, 40)$ | $\mathcal{N}(25.5, 4)$ |
| H_{SG} (km) | $\mathcal{U}(0, 20)$ | $\mathcal{N}(12, 3.5)$ |
| D_{BT} (km) | $\mathcal{U}(-20, 20)$ | $\mathcal{N}(-7.5, 2.5)$ |
| H_{BT} (km) | $\mathcal{U}(0, 20)$ | $\mathcal{N}(6.5, 3)$ |
| $D_{\text{décol}}$ (km) | $\mathcal{U}(5, 45)$ | $\mathcal{N}(13, 6)$ |
| D_{SM} (km) | $\mathcal{U}(0, 20)$ | $\mathcal{N}(4., 3.)$ |
| H_{SM} (km) | $\mathcal{U}(0, 20)$ | $\mathcal{N}(5., 2.5)$ |
| SS_{PH} (mm/yr) | $\mathcal{U}(0, 10)$ | $\mathcal{N}(3.1, 0.6)$ |
| D_{PH} (km) | $\mathcal{U}(5, 25)$ | $\mathcal{N}(15, 5)$ |
| H_{PH} (km) | $\mathcal{U}(0, 20)$ | $\mathcal{N}(4.5, 2.5)$ |
| InSAR ramp (mm/yr/km) | $\mathcal{U}(-0.03, 0.03)$ | $\mathcal{N}(0.0084, 0.00065)$ |

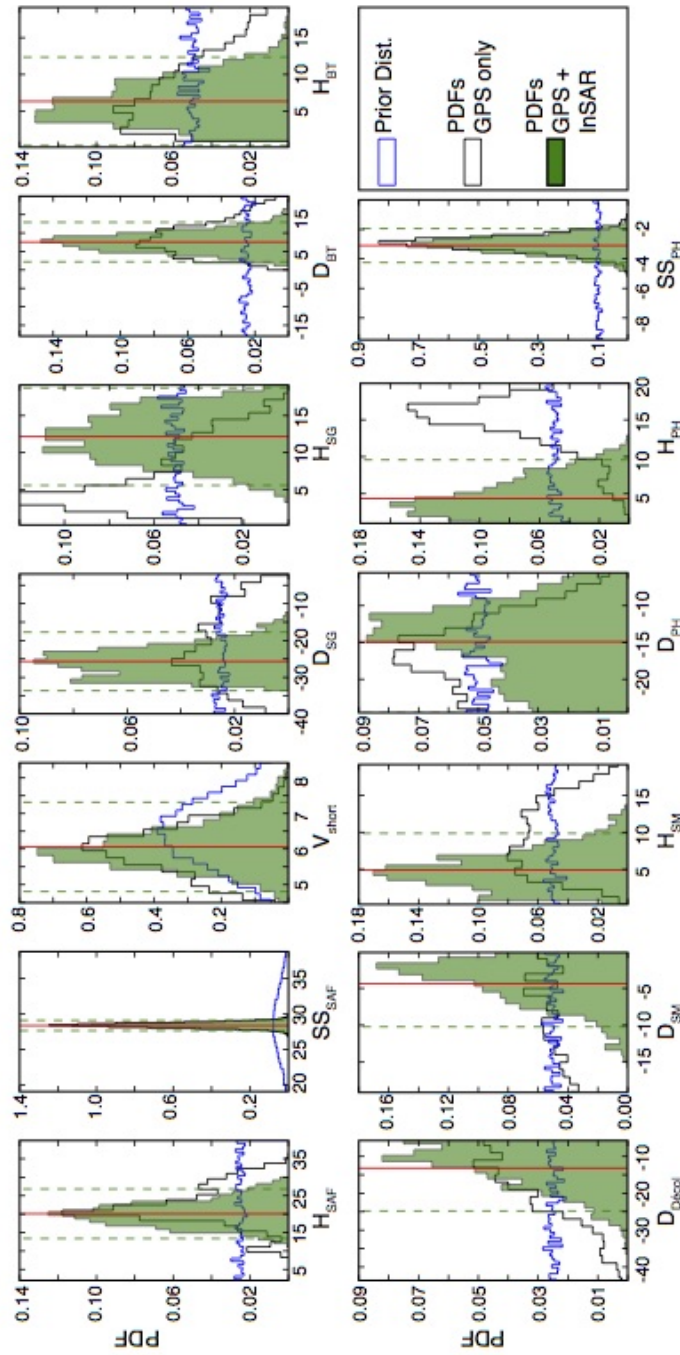


FIGURE 3.9 – Comparison between prior (unfilled blue histograms) and PDFs of the parameters without (unfilled black histograms) and with InSAR data (green histograms).

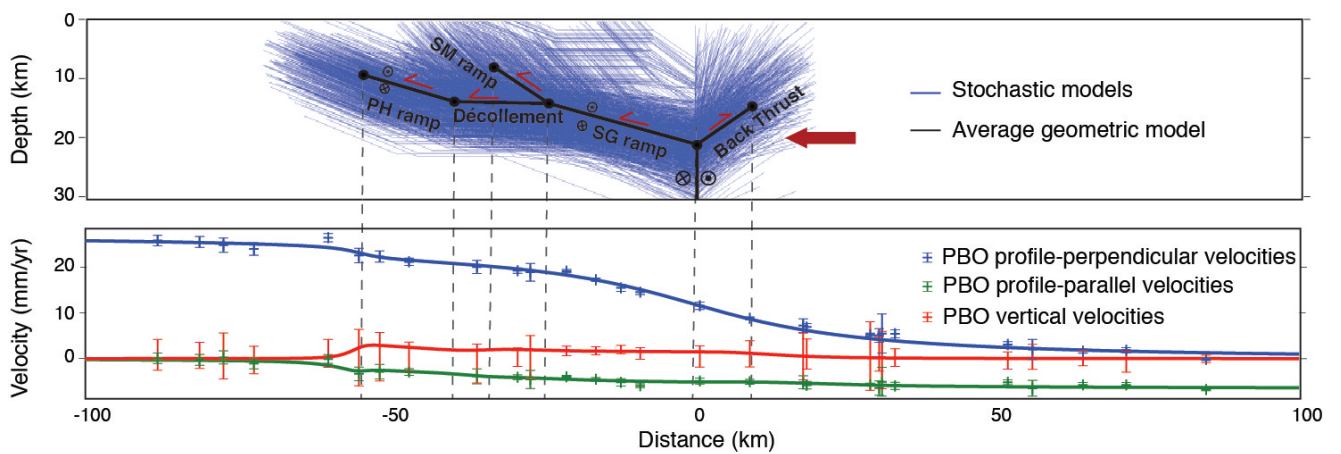


FIGURE 3.10 – Same as Fig.2 with a data vector made only of horizontal and vertical GPS vectors. Top : Posterior geometries in agreement with the data (blue lines) and average geometry (black lines). Bottom : Profile-perpendicular (blue markers), profile-parallel (green markers), and vertical (red markers) GPS velocities with their associated uncertainties and average model obtained (blue, green and red lines) along profiles. Without InSAR data, the geometry of the ramp-décollement system is not well constrained. Average posterior model predicts a concentration of the vertical and profile-parallel gradient at the front of the PHT.

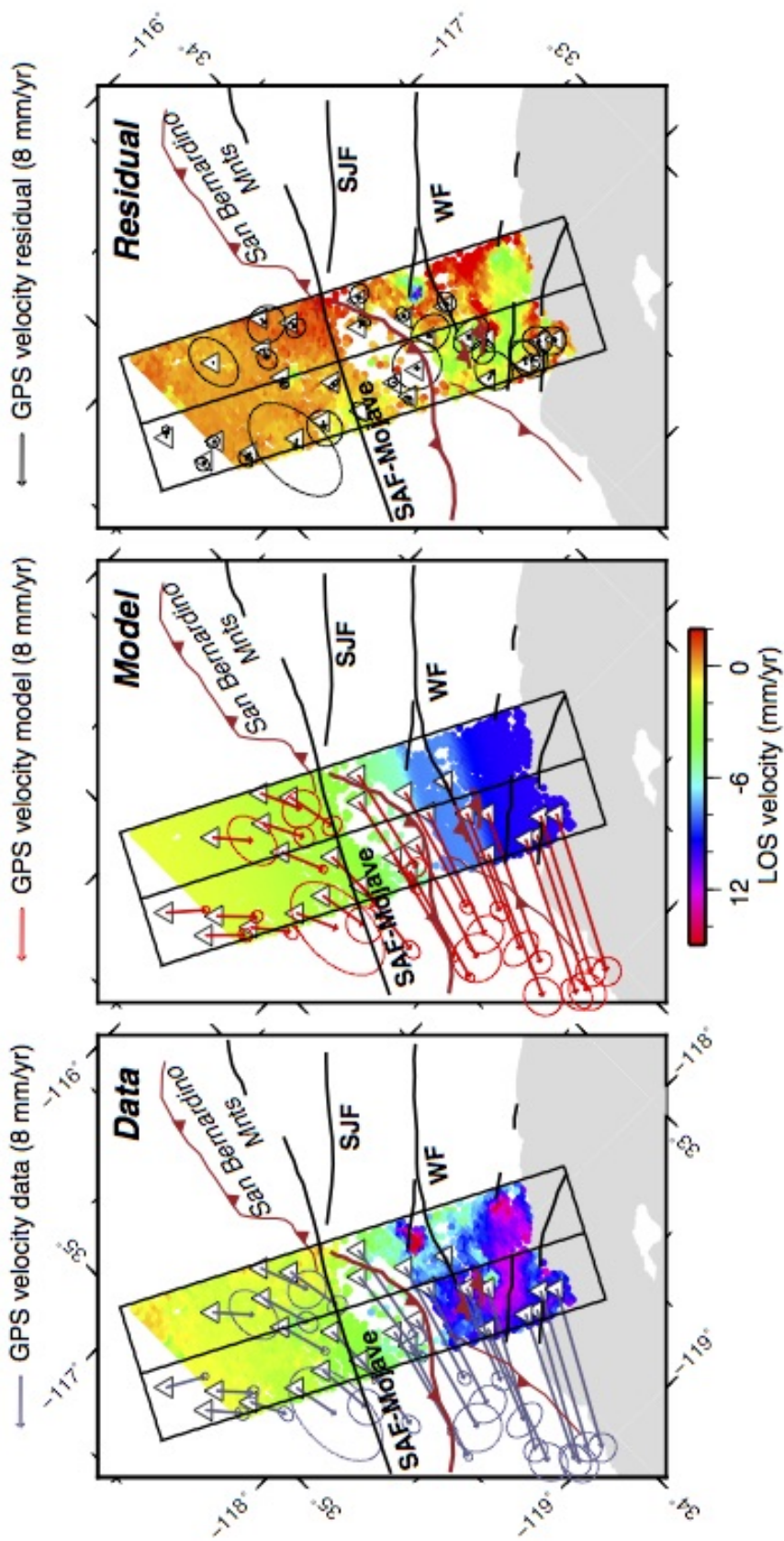


FIGURE 3.11 – Comparison between data and model from the Bayesian inversion. Left : GPS (in the dislocation model reference frame) and down-sampled InSAR data used for the inversion. InSAR data are down-sampled with Generic Mapping Tools (GMT) with a longitudinal and latitudinal increment of 0.02° , and 0.03° , respectively ([Wessel et Smith, 1991](#)), and then collapsed in the fault-perpendicular direction. Middle : Modelled displacements associated to the maximum likelihood of the posterior probability distribution. Right : Residuals between the forward model and the observations.

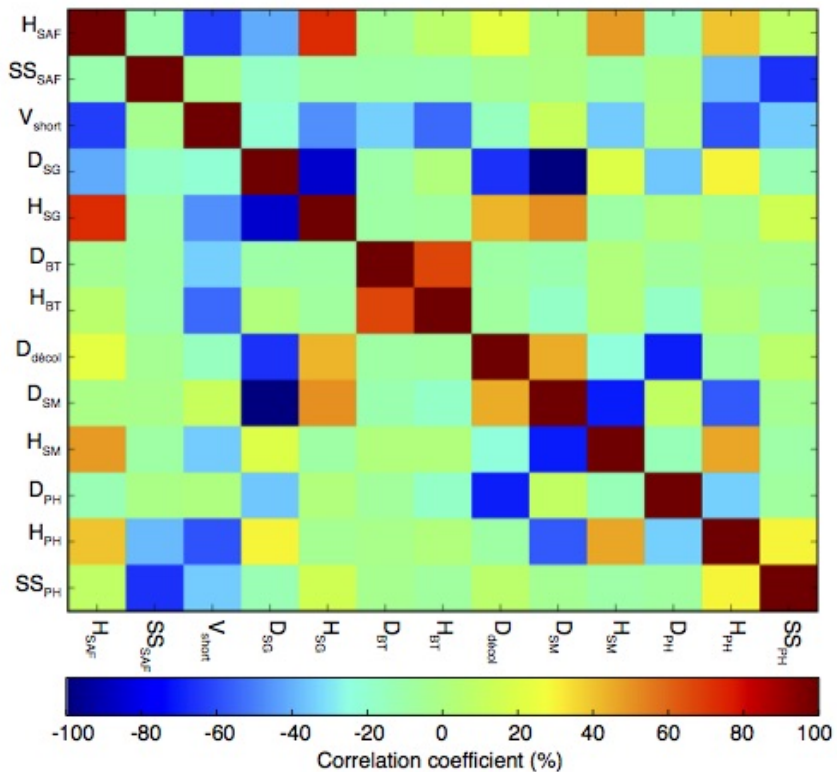


FIGURE 3.12 – Posterior covariance matrix. Correlation coefficients for all free parameters. PH : Puente Hills, SG : San Gabriel, décol : Décollement, SM : Sierra Madre.

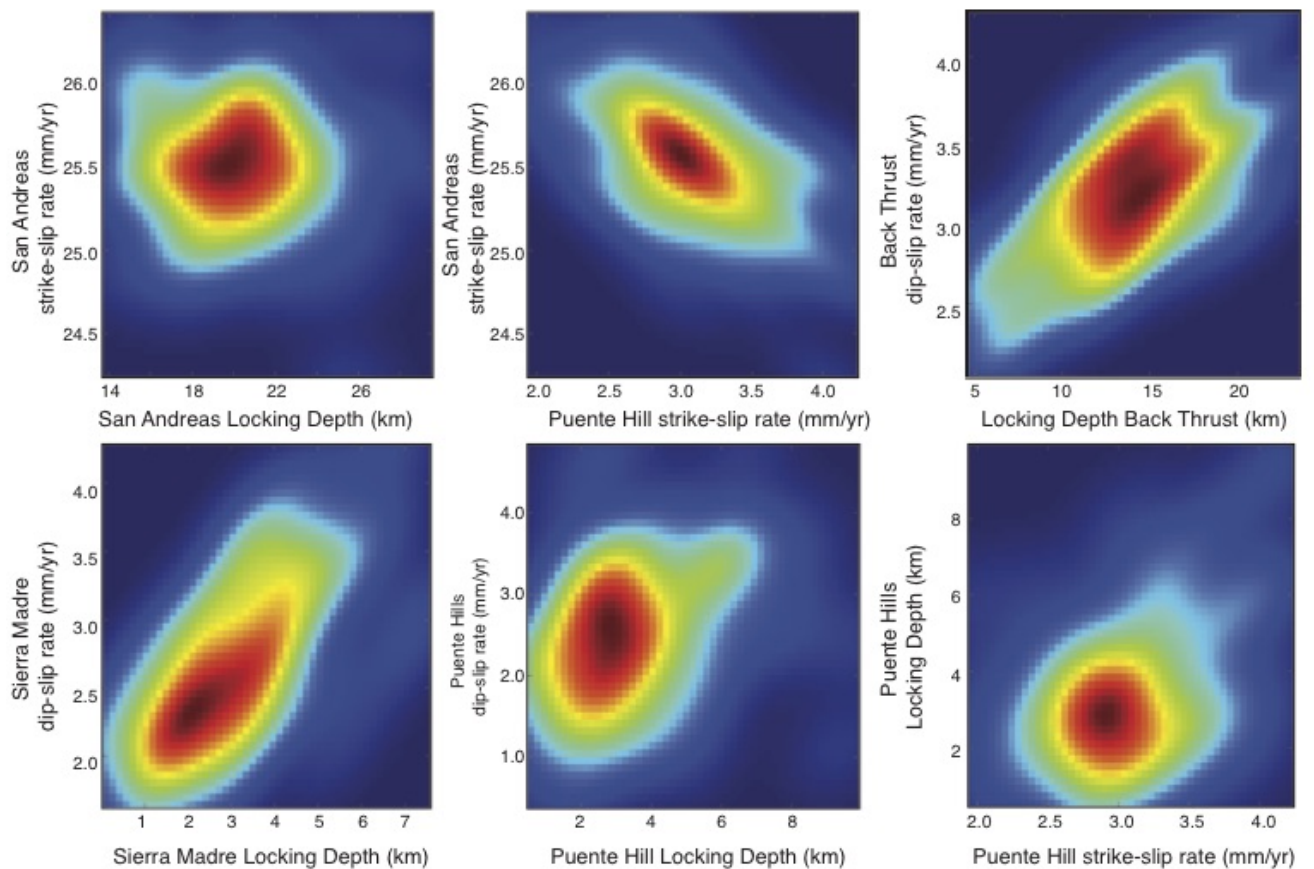


FIGURE 3.13 – Joint pdfs between slip rates and locking-depths showing correlations between SS_{SAF} and SS_{PH} or DS_{BT} and LD_{BT} or DS_{SM} and LD_{SM} .

Deuxième partie

Traitement et Analyses InSAR au Nord-Ouest Tibet

Chapitre 4

Uncertainties retrieval of InSAR derived ground velocity maps after atmospheric delay correction : case example of the Altyn Tagh Fault, Tibet

Sommaire

| | | |
|-----|--|-----|
| 4.1 | Introduction | 126 |
| 4.2 | Data set and formation of wrapped interferograms | 129 |
| 4.3 | Atmospheric corrections before unwrapping | 130 |
| 4.4 | Time series of delays elevation ratios | 133 |
| 4.5 | Atmospheric delays analysis | 135 |
| 4.6 | Validation of the ERA-I derived uncertainties using empirical estimate | 137 |
| 4.7 | Conclusion | 139 |

Preface

La faille de l'Altyn Tagh est au coeur du débat sur la manière dont le plateau Tibétain se déforme. Dans cette partie nord-ouest du plateau difficile d'accès, peu d'études se sont attachées à extraire par InSAR le signal tectonique (Elliott *et al.*, 2008; Wang *et al.*, 2012) en raison des nombreux défis méthodologiques. Les auteurs se confrontèrent aux ambiguïtés entre la déformation corrélée au saut topographique entre le Tarim et le Tibet et l'atmosphère stratifiée. Seule l'étude d'Elliott *et al.* (2008) réussit à dérouler la phase au travers la bordure du plateau mais se limita à sa déformation en champ proche (50km de part et d'autre) en raison des difficultés de déroulement, au Nord, dans la zone de dunes et, également au sud, dans le plateau, dus aux cycles de gel et dégel des sédiments recouvrant le pergélisol. De plus, cette étude n'appliqua aucune correction atmosphérique sur les interférogrammes. Dans ce premier chapitre, je me focaliserai sur la quantification de l'impact des corrections atmosphériques sur le gradient au travers de la faille de l'Altyn Tagh. Pour cela, je réalisera une comparaison systématique entre les corrections empiriques (Cavalié *et al.*, 2008; Doin *et al.*, 2015), estimant la relation entre la phase et la topographie avec les corrections prédictives ERA-Intérim (Doin *et al.*, 2009; Jolivet *et al.*, 2011), utilisant des modèles atmosphériques afin de prédire les délais stratifiés. J'analyserai également la variabilité des modèles atmosphériques journaliers de part et d'autre de la faille afin de mieux cerner les limites du modèle et de mieux quantifier ses incertitudes. Une partie de ces travaux ont été publiés dans le proceedings de la conférence "Dragon 3 Final Results and Dragon 4 Kick-Off" sous le titre "Multi Temporal InSAR Analysis in Northwestern Tibet" (Daout *et al.*, 2016b).

4.1 Introduction

Interferometric Synthetic Aperture Radar (InSAR) is a powerful tool to map precisely and over large areas, the surface deformation of the earth (Bürgmann *et al.*, 2000; Hooper *et al.*, 2012). This technique has been widely employed in earthquake sciences (Peltzer et Rosen, 1995; Lasserre *et al.*, 2005; Pathier *et al.*, 2003; Rousset *et al.*, 2016), volcanic dike intrusions (Pedersen et Sigmundsson, 2006; Cervelli *et al.*, 2002), landslides monitoring (Hilley *et al.*, 2004), urban subsidence (Amelung *et al.*, 1999; Fruneau et Sarti, 2000; López-Quiroz *et al.*, 2009) or water vapor mapping (Hanssen *et al.*, 1999). However, for small deformations such as interseismic deformation, the main source of error is linked to the atmospheric delay.

The atmospheric signal is divided into a stratified component, which is correlated to the topography, and a turbulent delay (Hanssen, 2001). The effect of turbulent patterns being random both in space and time can be attenuated by data stacking of independent data or time series filtering. In contrary, time series analysis of the stratified tropospheric delay shows that it is dominated by a seasonal term (Cavalié *et al.*, 2007; Doin *et al.*, 2009) with an amplitude depending on variation of temperature, pressure, and relative humidity. The stratified tropospheric delay in interferograms reaches few centimeters per kilometer of elevation, and thus may overprint any small deformations. Correcting this signal is thus one of the most important processing step, first, to prevent unwrapping errors in mountainous areas and, second, to reach an accuracy of a few millimeters per year on ground displacement velocities.

Two main classes of methods have been developed to correct for this signal. The first one is empirical and exploits the information in the SAR data correlated to the topography(Cavalié *et al.*, 2008; Lin *et al.*, 2010; Shirzaei et Bürgmann, 2012; Tymofyeyeva et Fialko, 2015; Bekaert *et al.*, 2015; Doin *et al.*, 2015). It has demonstrated its success in numerous case studies but may remove signal when the tectonic signal is strongly correlated with topography. The second one requires external data such as GPS delay measurements (Williams *et al.*, 1998; Webley *et al.*, 2002; Li *et al.*, 2006), satellite multispectral imagery (Li *et al.*, 2012), meteorological data (Delacourt *et al.*, 1998) or global atmospheric models (Doin *et al.*, 2009; Jolivet *et al.*, 2011, 2014b). These methods have shown in some cases to be equally efficient and do not present the disadvantages of empirical methods. However, they are principally limited by the spatial resolution, availability, and accuracy of the external data.

Here, we focus on the atmospheric delay corrections across the Altyn Tagh Fault (ATF) system, at the north-western boundary of the Tibetan plateau. The Altyn Tagh fault's slip rate is at the heart of a debate of how Tibet, thus continents deform (England et Molnar, 1997b; Tapponnier *et al.*, 2001). The debate was fueled by discrepancies between the interseismic slip rate derived from geological observations (Peltzer *et al.*, 1989; Mériaux *et al.*, 2004; Cowgill *et al.*, 2009; Mériaux *et al.*, 2012), from geodetic measures (Wright *et al.*, 2004; Elliott *et al.*, 2008; He *et al.*, 2013) and from numerical models (Peltzer et Saucier, 1996; Meade, 2007a; Thatcher, 2007; DeVries et Meade, 2013). Precise InSAR mapping of strain across the fault becomes thus critical. The elevation variation, between the Tarim desert north of the Altyn Tagh fault (<1000 m) and the mountain ranges across and south of the fault (\sim 5000 m), leads to a significant Atmospheric Phase Screen (APS) varying with elevation, within the interferograms. Furthermore, the topo-

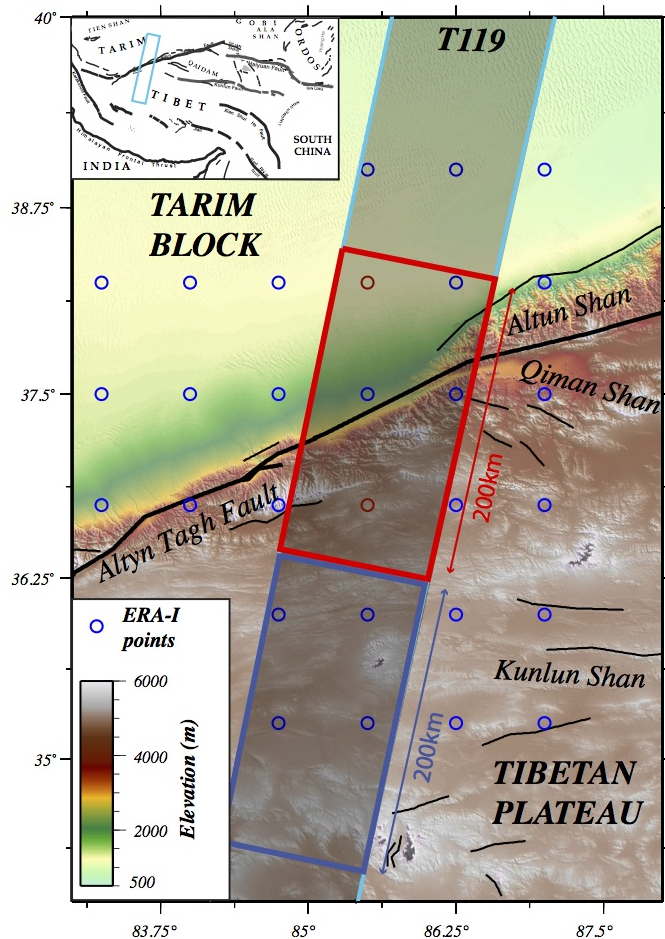


FIGURE 4.1 – Surface traces of the satellite of the track 119 superimposed to the Digital Elevation Model, major fault traces and the ERA-I atmospheric grid. The red and blue boxes delimitate the fault zone and the southern zone, respectively. Insert : location of the track acquired along a descending orbit

graphic step across the ATF does not present deeply incised valleys or gullies, which could help differentiate atmospheric signal from tectonic signal. As mentioned above, the accuracy of InSAR measurements across the fault is strongly altered by incomplete removal of atmospheric delays. For example, Elliott *et al.* (2008) introduced a tropospheric delay correction based on ERA40 Global Atmospheric Model. However, he finally did not use this prediction to correct the interferometric phase and empirically re-estimated the atmospheric delay, at the end of the processing, by inverting it on the velocity map jointly with the fault displacement rate. This operation results in a large uncertainty estimation of 11 ± 10 mm/yr of strike-slip rate motion along the fault.

In this study, we systematically compare empirical atmospheric corrections to pre-

dictions of a global atmospheric model. The objective of this work is to quantify the impact of these corrections on the relative velocity gradient across the ATF, and derive a method to estimate their uncertainties. We first describe the SAR data processing up to the formation of the wrapped interferograms. We then focus on the comparison of empirical and predictive corrections of the atmospheric delays and propose a method to extract uncertainties on time series acquisitions as well as realistic uncertainties on the fault interseismic velocity.

4.2 Data set and formation of wrapped interferograms

We process the complete Envisat archive data along the 1000 km-long and 100 km-wide Envisat track 119 acquired along a descending orbit between 2003 and 2011 (Fig. 4.1). The track begins in the Tarim Basin to the north, crosses the ATF with a topographic jump of more than ~ 5000 m, and extends after the terminaison of the Kunlun fault to the south. To obtain deformation time series in this natural environment and limit the phase decorrelation effects, we process the data with the New Small Baselines Subset chain (Doin *et al.*, 2011) based on the ROIPAC software (Rosen *et al.*, 2004).

From the raw data, we first compute all Single Look Complex (SLCs) images with a common band in Doppler : (1) we estimate the frequency Doppler band, associated to each image in function of the range, and its median value (Doppler centroid) and (2) choose a frequency in common to all images that will be used to produce all SLCs. We then project the SRTM DEM (Farr et Kobrick, 2000) in the radar geometry of a master image and model geometric phase delay of all images relative to the master using DEM and precise orbits before the interferogram generation. We coregister all SLCs relative to a single master image taking into account the DEM. In azimuth the transformation is quadratic derived from the measured offsets while in range the transformation is based on the DEM simulation and the orbits with an adjustment by a constant derived from image matching. We then form the 146 differential interferograms in 2x10 looks and estimate a uniform linear ramp in range to remove the residual orbital errors and the clock drift (Lauknes *et al.*, 2011; Fattah et Amelung, 2014b; Zhang *et al.*, 2014). The network includes 41 images connecting with redundancy all acquisitions either with large B_{perp} and low B_t or low B_{perp} and large B_t (black lines in Fig. 4.2). We employ a series of corrections before unwrapping that reduces the variance of the wrapped phase

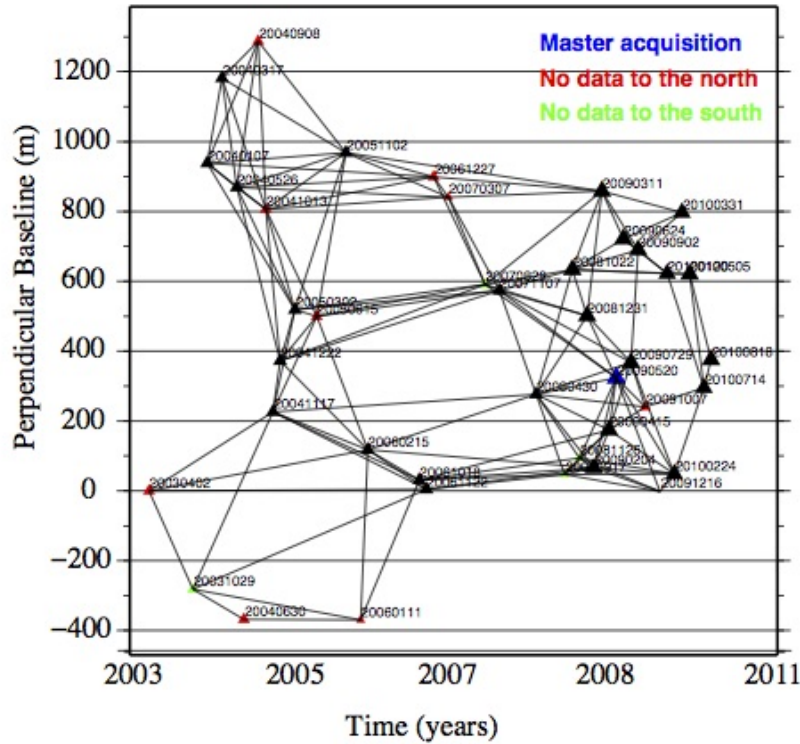


FIGURE 4.2 – Computed interferograms for the 41 images of the track T119. Triangles point to SAR acquisitions and are colored according to their spatial extent : black triangles for whole coverage, red and green triangles for images covering the southern (north respectively) part of the track.

(Grandin *et al.*, 2012; Daout *et al.*, 2016c). In the next sections, we will only focus on the comparison between an empirical correction, which estimates the relationship between the wrapped phase and the elevation, with a predictive correction from a global atmospheric model (ERA Interim from ECMWF) (Doin *et al.*, 2009; Jolivet *et al.*, 2011, 2014b).

4.3 Atmospheric corrections before unwrapping

ERA-I provides estimates of temperature, water vapor partial pressure, and geopotential height every six hours at different pressure levels on a 0.7° grid from 1989 to present (Dee *et al.*, 2011). Integrated path delays at acquisition times are derived at one (Doin *et al.*, 2009) or at all (Jolivet *et al.*, 2011, 2014b) ERA-I points encompassing a SAR scene, using vertical profiles of these variables. The delay is then mapped on the

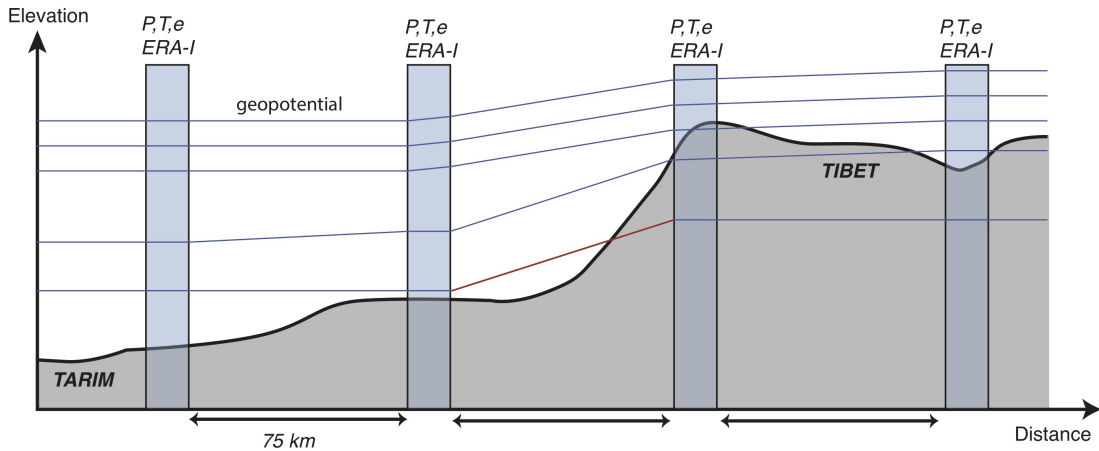


FIGURE 4.3 – Schematic representation of the ERA-I atmospheric models (blue vertical rectangles) across the Tibetan margin and their horizontal interpolations. We also highlight in red one example of interpolation between a grid point at low (Tarim) and a grid point under the ground at high (Tibet) elevation that might not be completely reliable and could result in some artefacts in the model.

radar scene using a Digital Elevation Model (DEM). When several ERA-I points are used, bilinear interpolation in the horizontal direction is performed on the vertical profiles (Fig. 4.3). We suppose that the delay between the satellite and the ground varies laterally due to an inhomogeneous stratification of the atmospheric layering predicted by the ERA-I models.

To extract an empirical phase elevation relationship, we estimate local phase gradients on wrapped interferograms (Doin *et al.*, 2015). The estimation is done by searching the phase versus elevation ratio, $\frac{\delta\phi}{\delta z}$, that maximizes the coherence of the residual phase in small sub-windows. The choice of local estimation within small windows is motivated by the minimization of possible trade-offs with the deformation, which is also correlated to the topography. Doing so, we hope to catch local phase-elevation ratio due to local valleys or gullies instead of the long-wavelength phase-elevation ratio produced by the Altyn Tagh fault deformation. We then select sub-windows with good coherence and with a differential topography within the sub-window, Δz , larger than 150 m and decrease the weight of ratio values that are clear outliers by applying a median filter. Ratios may also be selected within a defined area. In a next step, the median of these ratios is computed to get :

$$\phi = az + b \quad (4.1)$$

with a, b two constants. The choice of a mean relationship is also motivated by the minimization of the possible trade-off with the deformation. The estimated phase delay map, linear with elevation, is finally used to correct the original wrapped interferograms.

Fig. 4.4 shows one example of a wrapped interferogram with a temporal baseline of 2.4 years and a perpendicular baseline of 72 m before and after an empirical and predictive atmospheric correction. Before the correction the short wavelength topographic structures are highlighted by phase changes, especially in the Altun Shan, and the mean delay elevation ratio ($\frac{\delta\phi}{\delta z}$), calculated on small windows of $6 \times 20 \text{ km}^2$, reaches -0.005 rad/km . In many interferograms, the delay elevation ratios show a linear or quadratic correlation with elevation, as illustrated in Fig. 4.4. In this example, after both corrections, this stratified signal is in majority removed and the delay elevation ratio is close to zero. However, some interferograms are not successfully corrected in one case or the other.

To illustrate the possible trade-off of the empirical atmospheric correction with the tectonic signal, we simulate 3 years of strike-slip motion on a vertical half-infinite dislocation aligned with the Altyn Tagh Fault surface trace (Fig. 4.5a) and estimate the delay elevation correlation on the synthetic interferogram (Fig. 4.5c-d). All phase-elevation ratios estimated within the Tibetan plateau with an altitude higher than 4 km are close to zero, while below this altitude, the ratios have a quadratic relationship with elevation. The mean of all delay elevation ratios is close to zero (Fig. 4.5c), and the correction does not affect the tectonic signal (Fig. 4.5e). However, this estimation might be more representative of the delay elevation ratios in the Tibetan plateau than of the delay between the Tibetan plateau and the Tarim basin, $\Delta\phi_{Tibet-Tarim}$. In contrary, adjusting delay elevation ratios with a linear or higher order relationship with elevation (Fig. 4.5d) could lead by integration to a more representative value of $\Delta\phi_{Tibet-Tarim}$. However, we clearly see on Fig. 4.5f that it removes drastically all the tectonic signal across the fault. Employing a power law relationship with elevation (Bekaert *et al.*, 2015), should lead to a similar trade-off. A wavelet transform analysis (Lin *et al.*, 2010; Shirzaei et Bürgmann, 2012) could exploit the spatial heterogeneity of the phase-elevation relationship but depends on the completness of the unwrapped signal in the area of interest. This synthetic example shows the ambiguity of these methods in a case where the deformation is strongly correlated to a large topographic feature. In comparison, predictive corrections do not have this disadvantage but suffer from the lack of accuracy in the daily delay

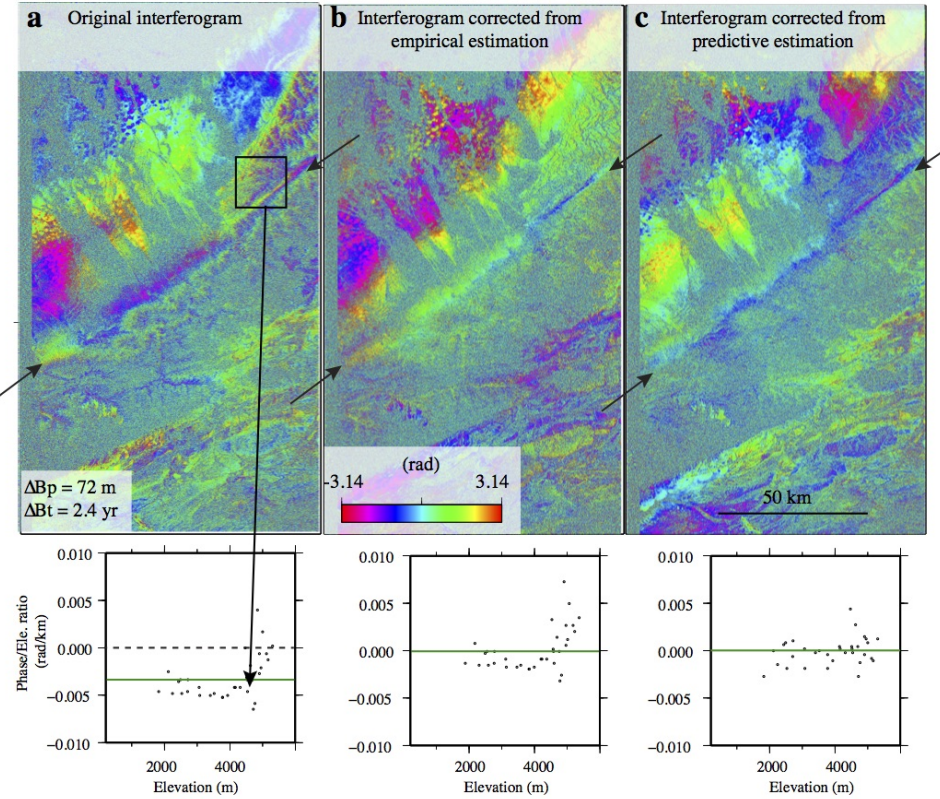


FIGURE 4.4 – Examples of an empirical correction based on the estimation of the local phase-elevation ratio (b) and of predictive correction from ERA-I models (c) on a wrapped interferogram with a temporal baseline of 2.4 years and a perpendicular baseline of 72 m (a). Top : Wrapped phase before and after corrections. Bottom : comparison of the local delays elevation ratio as a function of elevation before and after corrections. Each dot corresponds to a local estimate in a sub-window. The green line shows the mean of all computed ratios used for the empirical correction.

estimation.

4.4 Time series of delays elevation ratios

We compare here empirical and ERAI models in order to discuss the trends associated to stratified atmospheric delays, induced by an imperfect sampling of the seasonal atmospheric signal, that will impact velocity maps. That for, we estimate on small windows for all interferograms the average delay elevation ratios on original wrapped interferograms ($(\frac{\delta\phi}{\delta z})|_{EMP}$), on ERAI models ($(\frac{\delta\phi}{\delta z})|_{ERAI}$), and on interferograms corrected from ERAI. Time series inversion of these delay elevation ratios for each interferogram, S_l , yields the delay

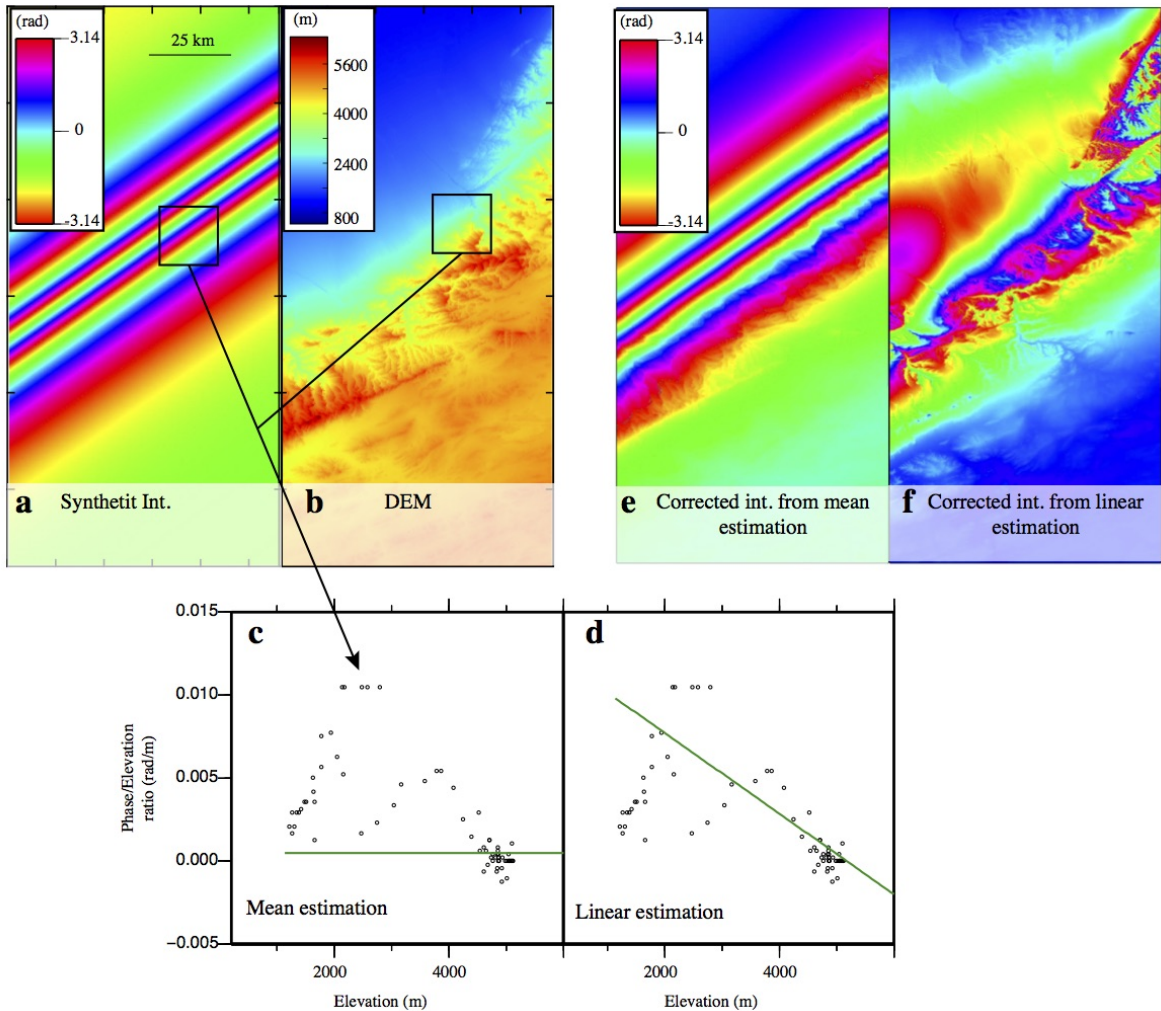


FIGURE 4.5 – Empirical delay elevation relationship estimated on a synthetic interferogram with a temporal baseline of 3 years and simulated a strike-slip motion of 15 mm/yr on the Altyn Tagh Fault. (a) Synthetic interferogram. (b) Digital Elevation Model. (c) Delay-elevation ratios. The green line corresponds to the average. (d) as (c) but the green line is the linear estimation. Using a mean delay elevation ratio does not remove tectonic signal (e), while, estimating a linear relationship removes the majority of the tectonic signal (e) on the synthetic interferogram.

elevation ratio at each acquisition date, S_i^{EMP} (Doin *et al.*, 2009). We estimate separately these ratios for the fault zone and the southern zone of the track and plot them as a function of acquisition time (Fig. 4.6). In the fault area (Fig. 4.6), we observe a good match between the empirical and the ERAI derived ratios (blue and green lines have the same oscillations). Despite this agreement, we do not observe any temporal trend in the empirical ratios extracted from the original interferograms, while the ERAI model predicts a negative trend. Accordingly, ratios extracted from interferograms corrected from

ERA-I model present a positive trend with less variability. The effects of the correction on the velocity map and gradient across the fault is directly linked to this linear trend calculated around the fault zone. Using the ERA-I model correction, we add roughly to the original map ~ 0.11 rad/km/yr across the fault zone, which corresponds roughly to adding ~ 1.5 mm/yr right lateral LOS motion for a 3 km elevation difference on both sides of the fault. Here, applying the empirical correction does not change the LOS motion across the fault. The question is to estimate what extent we believe one or the other correction. By contrast, on the southern zone (Fig. 4.6), we observe that the estimation is dominated by a strong seasonal signal of ~ 6 rad/km of amplitude, not predicted by the atmospheric models neither in amplitude nor in phase. In this area, the empirical estimation of the tropospheric delay is thus masked and made difficult by a larger seasonal signal, which may come from the freeze-thaw cycles of the permafrost active layer (cf. chapter 5). In the central part of the plateau, correcting for the permafrost signal is essential to avoid bias the empirical estimation, correctly unwrap interferograms from north to south and isolate bedrock pixels that are not affected by the permafrost signal.

In the following, our objective is to provide an error bound on ERA-I delay estimate based on its temporal variability and on the comparison with empirical measurements. The procedure is quite complex mainly because we do not have a direct access on the integrated empirical delay between Tarim and Tibet.

4.5 Atmospheric delays analysis

We first analyse the daily time series of the delays predicted by ERA-I between two points located in the Tarim basin (N38.25E85.5) and the Tibetan plateau (N36.75E85.2), at an altitude of 1,4 and 4,5 km, respectively (Fig. 5.8). We also compute an average model, S_{avg}^{ERA-I} , computed on 7-days sliding windows, and the envelope of its associated standard deviation σ_k^{ERA-I} . We observe within the Tarim basin (Fig. 5.8a) a strong daily variability of ~ 30 rad that overprints the seasonality, while within the Tibetan plateau (Fig. 5.8b), the ERAI model predicts a regular seasonal signal with ~ 15 rad of amplitude and with a higher variability in summer (~ 5 rad) than in winter ($\sim 1 - 2$ rad). The delay differences (Fig. 5.8c, ~ 20 rad = ~ 8.9 cm) shows a slight seasonal signal and a strong daily variability. The delays at acquisition dates (shown with blue circles in Fig. 5.8) are sometimes clearly outside the envelope. Indeed, ERAI may not well predict the very quick variations in delay that are associated to abrupt changes in humidity and, to a lesser extent, in temperature. We thus use the 7 days standard variation, σ_k^{ERA-I} ,

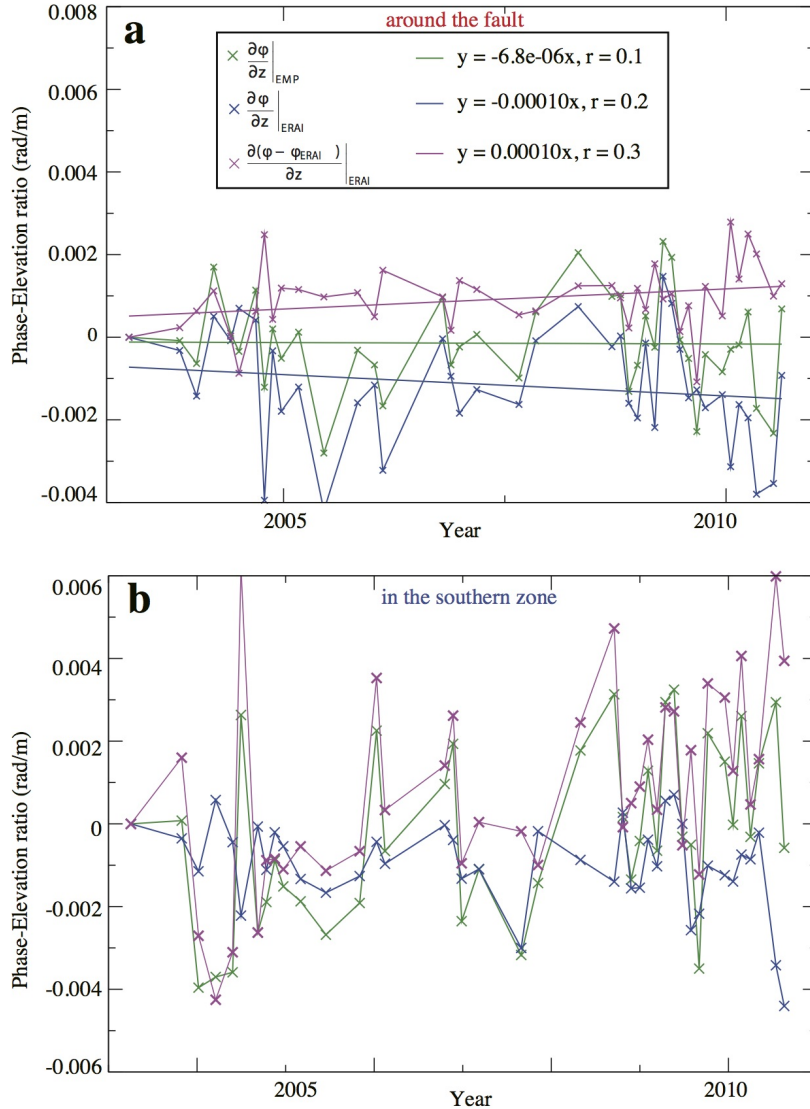


FIGURE 4.6 – Delay/elevation ratio plotted as a function of time for the track 119, for the original interferograms (green crosses), the ERAI models (blue crosses) and the interferograms corrected from ERAI (purple crosses). Top : Average delay elevation ratio in the fault zone (red box in Fig. 4.1). Bottom : Average delay elevation ratio in the southern zone of the track (blue box in Fig. 4.1). A positive multi-annual trend indicates that the delay increases with elevation, mimicking a deformation away from satellite at hight elevation (right lateral movement).

centered on the date k , as a proxy for possible errors in ERAI prediction than those within the 1σ enveloppe. Furthermore, some computed delays that appear as outliers in the time series may be more prone to an erroneous prediction by ERAI. We therefore

4.6 Validation of the ERA-I derived uncertainties using empirical estimate

define a proxy, σ_p , for the uncertainty on S_i^{ERAII} for each acquisition date i , such as :

$$\sigma_{p,i}^{ERAII} = \sigma_i^{ERAII}, \text{ if } |S_i^{ERAII} - S_{avg}^{ERAII}| < \sigma_i^{ERAII}, \quad (4.2)$$

$$\sigma_{p,i}^{ERAII} = |S_i^{ERAII} - S_{avg}^{ERAII}|, \text{ otherwise.} \quad (4.3)$$

In short, if the daily acquisition, S_i^{ERAII} , is close to the sliding window average model, S_{avg}^{ERAII} , and within the envelope, σ_i^{ERAII} , then the error, $\sigma_{p,i}^{ERAII}$, is equal to the standard deviation at the date i , σ_k^{ERAII} . Otherwise, if the daily acquisition, S_i^{ERAII} , is an outlier (i.e., $|S_i^{ERAII} - S_{avg}^{ERAII}| > \sigma_k^{ERAII}$) then the error, $\sigma_{p,i}^{ERAII}$, is equal to its absolute distance to the average. The error bar proxies on the relative delay between Tibet and Tarim at each acquisition date are drawn on Fig. 5.8c. Note that a few acquisitions have a σ_p^{ERAII} value clearly larger than others. We assume that their ERAI corrections are less reliable than for other acquisitions. Note also that the average σ_p^{ERAII} (~ 2.1 rad) is lower by a factor 3 than the absolute S^{ERAII} variability (~ 5.9 rad).

What do we infer from these analysis on the uncertainty on the relative velocity across the ATF? First, we note that, if the data were not corrected from stratified atmospheric delays, we would expect a bias, δv , corresponding to the trend in rad/yr across the S_i^{ERAII} values (blue circles in Fig. 5.8c). Secondly, we observe that the sign and amplitude of this trend will strongly depend on the data sampling (relatively random). Thus the uncertainty on the trend, $\sigma_{\delta v}$, if no corrections were applied, corresponds to the total phase delay variability (~ 5.9 rad). After ERAI correction uncertainties are reduced and we expect that the bias will be in most part removed.

4.6 Validation of the ERA-I derived uncertainties using empirical estimate

The purpose of this section is to discuss the reliability of the dispersion proxy previously defined in the equation 4.3.

We first compare the delay elevation ratios extracted from original interferograms and inverted into time series, $\frac{\delta\phi}{\delta z}|_{EMP}$, with that obtained from the ERAI delay maps, $\frac{\delta\phi}{\delta z}|_{ERAII}$ (Fig. 4.8a). The dispersion of the empirical ratios obtained in various interferogram sub-windows is also inverted into time series assuming errors coming from both dates in the interferogram add up. It is displayed as error bars on the vertical axis on

Fig. 4.8a. This dispersion may be due to (a) lateral and upward variations in the atmospheric stratification, (b) turbulent atmospheric delays, and (c) coherence loss. Note also that empirically derived $\frac{\delta\phi}{\delta z}|_{EMP}$ may trade-off with orbital residue or deformation.

We observe a very good agreement in between both estimations. In order to extract a relationship between $\frac{\delta\phi}{\delta z}|_{EMP}$ and $\Delta\phi_{Tibet-Tarim}^{EMP}$, and extract uncertainties, $\sigma_{\frac{\delta\phi}{\delta z}|_{ERAII}}$, on the delay elevation ratios of the ERAI maps, we examine the relationship between the phase difference between Tibet and Tarim, $\Delta\phi_{Tibet-Tarim}$, and the average delay elevation ratios, $\frac{\delta\phi}{\delta z}|_{ERAII}$, on ERAI. (Fig. 4.8b). We observe a linear relation expressed by :

$$\Delta\phi_{Tibet-Tarim}^{ERAII} = 2615 * \frac{\delta\phi}{\delta z}|_{ERAII} - 164. \quad (4.4)$$

Some acquisitions are clear outliers in Fig. 4.8b, indicating spatial variability of the atmospheric delays (Doin *et al.*, 2009; Bekaert *et al.*, 2015). This relation is used to compute an empirical estimate for the $\Delta\phi_{Tibet-Tarim}^{EMP}$ from $\frac{\delta\phi}{\delta z}|_{EMP}$ and the standard deviation $\sigma_{\Delta\phi_{Tibet-Tarim}}^{EMP}$ from $\sigma_{\frac{\delta\phi}{\delta z}|_{ERAII}}$. Inversely it yields an estimate of $\sigma_{\frac{\delta\phi}{\delta z}|_{ERAII}}$ from the previously calculated error, $\sigma_{\Delta\phi_{Tibet-Tarim}}^{ERAII}$ (Cf section 4.5). We then compare empirical delays between Tarim and Tibet, $\Delta\phi_{Tibet-Tarim}^{EMP}$, with the ERAI predicted delay, $\Delta\phi_{Tibet-Tarim}^{ERAII}$ (Fig. 4.8c). Fig. 4.8c presents more outliers than Fig. 4.8b, due to the lateral heterogeneities in atmospheric conditions. These outliers also have a large σ_p^{ERAII} value. Both suggest that ERA-I for these dates may not provide an accurate delay map estimate. Note that the 1σ error bars in Fig. 4.8a-c encompass with few exception the defined regression lines, suggesting that they represent a conservative estimate of errors. To further clarify this, we plot on Fig. 4.8d, the time series of the delays. The error bars overlap except for the seven outliers within the 1σ uncertainty for ERAI delays. This suggest that the 7-days variability proxy for error on ERAI prediction is conservative. We then display histogram of InSAR derived delay, $\Delta\phi_{Tibet-Tarim}^{EMP}$, minus the delays predicted at acquisition dates, $\Delta\phi_{Tibet-Tarim}^{ERAII}$, and normalized by the σ_{ERAII} uncertainty (Fig. 4.8e). Values are in average null and are concentrated within the $[-1.1, 1.1]$ 1σ deviation, suggesting that the $\sigma_{\Delta\phi_{Tibet-Tarim}}^{ERAII}$ computed from 7 days variability of the ERAI models is not under-estimated and is a good proxy for the uncertainties in the ERA-I predictions.

Using the derived error bars, $\sigma_{\Delta\phi_{Tibet-Tarim}}^{ERAII}$ and $\sigma_{\Delta\phi_{Tibet-Tarim}}^{EMP}$, we finally compute the velocity gradient due to the atmosphere predicted by both empirical (Fig. 4.9a) and ERA-I corrections (Fig. 4.9b). We also derive their respective uncertainties, propagating errors on the images to an error on the velocity gradient between the two ERA-I points separated by 3100 m of topography. After weighting, both stacks (Fig. 4.9) predict

a right lateral gradient across the fault. ERA-I subtracts 2.12 mm/yr between the two ERA-I points, with an uncertainty, $\sigma_{\Delta v}^{ERA\text{I}}$, of 0.82 mm/yr, while the empirical correction add 0.54 mm/yr of left-lateral motion across the fault, with a $\sigma_{\Delta v}^{EMP} = 0.73$ mm/yr.

ERA-I stack of Fig. 4.9b indicates a very strong gradient within the Tarim basin not predicted by empirical corrections (Fig. 4.9a). Moreover, the predicted gradient is not clearly correlated to the topography and shows some strong patterns at the foot of the topographic feature. In these areas, we may wonder if artefact could come out from the lateral interpolation of ERA-I points at low (Tarim) and high (Tibet) elevations. We thus also produce on an other data set of interferograms corrected from an ERA-I prediction derive from only one vertical profile located in the Tarim basin (Doin *et al.*, 2009). It corresponds to the point in the Tarim basin (N38.25E85.5) used for the atmospheric analysis (Fig. 5.8a). In the further tectonic analysis of the chapter 6, our data will be compared to this other scenario to verify that ERA-I does not introduce any additional signal in the final velocity gradient. The stack of this correction derived from one ERA-I point is also available in the Fig. 4.9c.

4.7 Conclusion

We analyse the stratified atmospheric signal across one of the biggest topographic feature in Tibet bounding the Tibetan plateau, to the south, and the Tarim basin, to the north. Under sampling of the seasonal atmospheric signal, due to limited acquisitions and low temporal resolution, creates a linear bias in the time series in trade-off with the secular tectonic deformation across the fault-system. Empirical and predictive estimations of this stratified delay match at first order but also reveals some differences. Across this large-scale topographic feature, empirical estimations may partially trade-off with the deformation. Moreover, the estimation is more representative of the delay elevation ratio within the Tibetan plateau than the delay elevation across the topographic feature due to the few points in the Tarim basin that present topographic gradient and high coherence. To partially solve the problem, we should test, in the future, smaller sub-windows parallel to the ATF. In comparison, ERA-I predictions do not have this disadvantage but suffer from lack of accuracy, more particularly within the Tarim basin, where daily delays indicate a strong daily variability. We thus propose a method to extract uncertainties for ERA-I predictions as well as for empirical estimations and show that these first order discrepancies are within their error bars. We compare uncertainties on the linear trend across the fault, without atmospheric correction ($\sigma_{\delta v}$), with ERAI

corrections ($\sigma_{\delta v}^{ERA\text{I}}$), and with empirical corrections ($\sigma_{\delta v}^{\text{EMP}}$) and show that ERA-I and empirical corrections decreases the ambiguity between the tectonic deformation and the atmospheric signal and that the predicted ERA-I velocity gradient is within the error bar of the empirical derived velocity gradient.

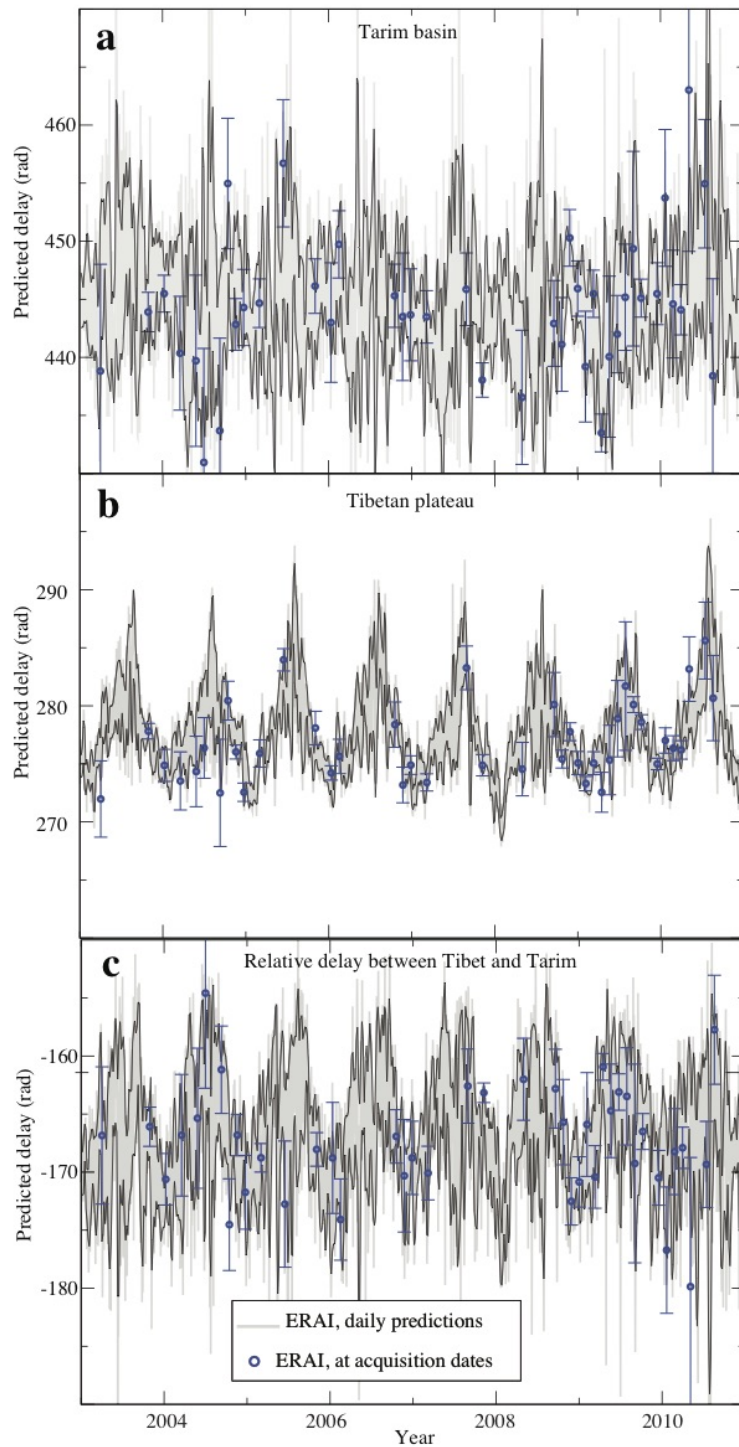


FIGURE 4.7 – Phase delay time series, S_i^{ERA1} (blue circles), plotted as the function of time superimposed to the daily model (grey lines) and the 7-days sliding windows standard deviation σ^{ERA1} (black lines). a) Relative delay in between the satellite and the Tarim basin (N38.25E85.5) located at 1400 m hight. b) Relative delay in between the satellite and the Tibetan plateau (N36.75E85.2) located at 4500 m hight. c) Relative delay in between the Tibetan plateau and the Tarim Basin (two red circles in Fig. 4.1).

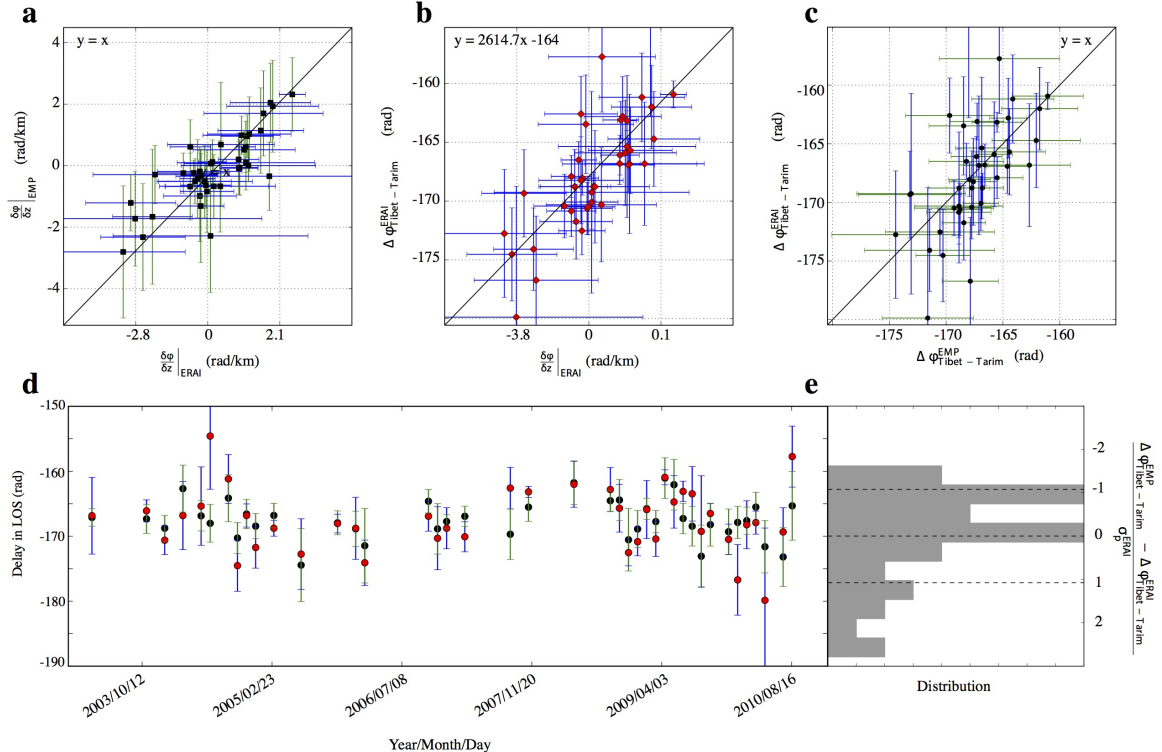


FIGURE 4.8 – Comparison of the delay/elevation ratios estimated on the data and those predicted by the ERAI models. a) Comparison between the delays elevation ratio estimated on the ERAI maps and estimates on the original interferograms. b) Comparison between predicted ERAI phase delay between Tarim and Tibet, S_i^{ERA1} , and estimated delays elevation ratio on the computed ERAI maps. c) Comparison between predicted ERAI phase delay between Tarim and Tibet, S_i^{ERA1} , and deduced phase delays from the empirical estimation, S_i^{SAR} d) Relative delays elevation ratio for the ERAI model and the data plotted as a function of time. e) Distribution function for InSAR derived ratios minus the predicted ratios normalized by the dispersion proxy for ERAI delay ratios.

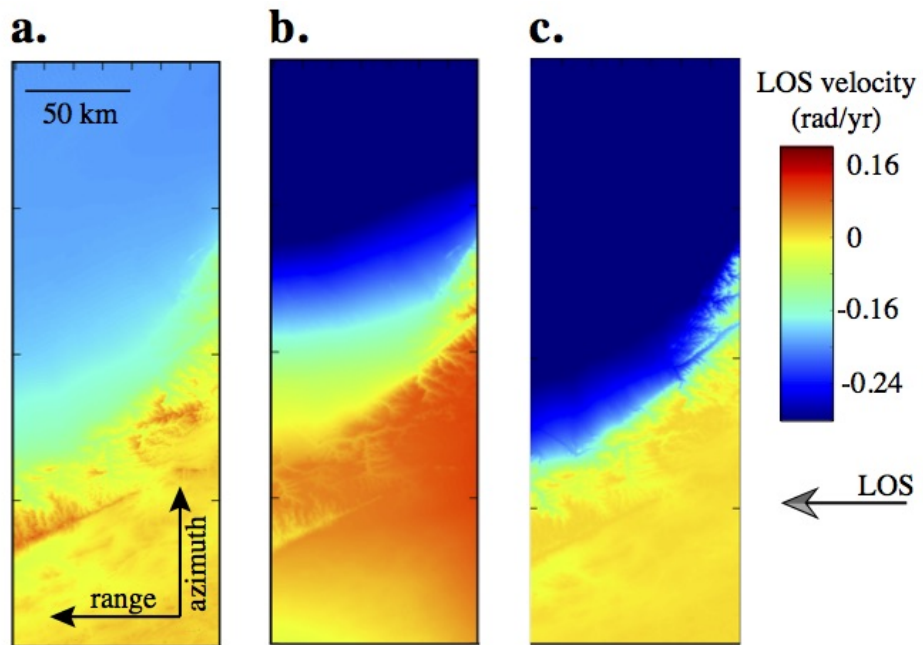


FIGURE 4.9 – Comparison of the three atmospheric stack corrections derived from empirical estimations ([Doin et al., 2015](#)) (a), ERA-I models with lateral variability ([Jolivet et al., 2011](#)) (b), and ERA-I models with only one point located in the Tarim basin ([Doin et al., 2009](#)) (c). The three velocity gradients are obtained by weighting each images with their respective uncertainties derived from the atmospheric analysis. A gradient increasing with elevation simulates a right-lateral movement.

Chapitre 5

Large scale InSAR monitoring of permafrost freeze-thaw cycles on the Tibetan Plateau

Sommaire

| | | |
|------------|--|-----|
| 5.1 | Introduction | 146 |
| 5.2 | Data processing | 148 |
| 5.3 | Results and Discussions | 149 |
| 5.3.1 | Amplitude of the seasonal ground movements | 149 |
| 5.3.2 | Months of subsidence peak | 150 |
| 5.3.3 | Multi-annual trend of ground subsidence | 155 |
| 5.4 | Conclusion | 156 |
| 5.5 | Supplementary Materials | 157 |

Preface

Dans le chapitre précédent, une analyse séparée des relations phase-topographie dans la zone de faille et dans le cœur du plateau, met en évidence dans le plateau un signal saisonnier de très forte amplitude non corrélé avec les modèles atmosphériques. Déjà introduits par [Taylor et Peltzer \(2006\)](#) puis par [Doin et al. \(2015\)](#), ces signaux correspondent aux cycles de gel et dégel des sédiments recouvrant le pergélisol. Les forts taux de déformations dans ces basins compliquent fortement le déroulement de la phase et par conséquent l'obtention d'un signal continu au travers le plateau. Pourtant l'extraction d'un signal de déformation sur une grande distance présente un intérêt tout particulier afin de capturer la grande longueur d'onde de la déformation, ainsi que la géométrie de la terminaison de la faille du Kunlun. Pour palier ce problème, je m'intéresse dans ce chapitre à l'extraction et la quantification du signal associé au pergélisol, afin de dérouler correctement les interferogrammes, sur une distance de plus de 800 km de long, et d'isoler les points stables des points affectés par le pergélisol pour l'étude tectonique qui suivra. En plus de cette cartographie du permafrost, cette étude m'a conduit à analyser le signal de déformation et la réponse du permafrost aux variations climatiques saisonnières et séculaires sur 8 années d'étude. Ce travail a été accepté dans le journal « Geophysical Research Letter », sous le titre « Large scale InSAR monitoring of permafrost freeze-thaw cycles on the Tibetan Plateau » de S. Daout, M.P. Doin, G. Peltzer, A. Socquet, et C. Lasserre ([Daout et al., 2017](#)).

5.1 Introduction

Permafrost, occurring where the mean ground temperature is below 0°, occupies a large fraction (20-25%) of the Earth's continental surface ([Brown et al., 2000](#); [French et al., 2007](#)). It is of fundamental importance in various domains : as an impermeable and hard layer, it controls ground moisture and water transport, evaporation, vegetation growing, and evapotranspiration. It also affects the ground thermal budget through freezing/thawing, latent heat, and conductivity effects ([Outcalt et al., 1990](#)). Finally, it is a major reservoir of water and organic matter that decays into greenhouse gases such as carbon dioxide and methane ([Christensen et al., 2004](#)). The complex interactions and feedback between increased air temperature, ground temperature, and permafrost evolution must be taken into account in climate models ([Oelke et Zhang, 2007](#); [Cheng et Wu, 2007](#); [Riseborough et al., 2008](#)).

The upper layer of the permafrost is subject to seasonal freezing and thawing. It is strongly deforming and cracking due to the volume change associated with water-ice phase changes in pores and lenses of its active layer, leading to the development of characteristic geomorphic patterns defining circle or polygon-shape cracks, palsas, and pingos. The thickness of the active layer (ALT) and the quantity of water/ice stored in it varie spatially and inter-annually, scaling with the amplitude of the ground displacement. Ground cohesion and movement affect infrastructure stability (eg. buildings foundations, railways (Qingbai *et al.*, 2002; Chang et Hanssen, 2015), etc...) and thus the socioeconomic development of the area. Inferring the active layer properties from air temperature is a difficult exercice as it depends on local thermal properties, snow cover, soil layering and water availability (Smith et Riseborough, 1996). The ALT is usually measured "in situ" by probing (Zorigt *et al.*, 2016; Cheng et Wu, 2007) or through geo-physical investigations such as temperature sensors or ground penetrating radar (Hinkel *et al.*, 2001; Wu *et al.*, 2010). Estimating ALT variations over broad regions can be done by interpolating probe data using vegetation index maps compiled from remotely sensed data (Nelson *et al.*, 1997), ground resistivity (Pastick *et al.*, 2013), or relative elevation (Gangodagamage *et al.*, 2014). However, in situ measurements are sparse, making their interpolation inaccurate. Hence, the systematic mapping of ground movements observed by InSAR over broad areas should provide unprecedented insights into characterizing permafrost active layer properties in many regions.

Multi-temporal radar interferometry (MT-InSAR) in natural environment (Hooper *et al.*, 2004; Berardino *et al.*, 2002) is providing new opportunities to map and measure these seasonal surface displacements, as it has been shown on relatively limited spatial extent in Alaska (e.g., Liu *et al.*, 2010; Short *et al.*, 2011; Liu *et al.*, 2012, 2014a, 2015; Schaefer *et al.*, 2015) or in Tibet (e.g., Chang et Hanssen, 2015). However, over broad areas, the approach suffers from major limitations including decorrelation created by cryoturbation of the surface or snow cover, strong phase gradients leading to unwrapping errors, and temporal decorrelation. Previous InSAR studies of permafrost behavior have identified these challenges but circumvent the problem by focusing on small areas ($< 5000 \text{ km}^2$) and sometimes, because of snow cover, using only acquisitions acquired during the thawing season. In this paper, we show that MT-InSAR data can be used to retrieve the permafrost related deformation through the entire seasonal cycle over a wide area ($\sim 240 \times 250 \text{ km}^2$) with a high spatial and temporal resolution. The demonstration is done on the north-western part of the Tibetan plateau where permafrost occupies around 70% of the land (Brown *et al.*, 2000). With an average elevation of $\sim 5 \text{ km}$, the

study area is covered with a succession of east-west trending, flat sedimentary basins, separated by narrow mountain ranges reaching 6 km in height, leading to an extensive zone of discontinuous permafrost ([Fort et van Vliet-Lanoe, 2007](#)).

In the following sections, we first describe how we process single interferograms and improve phase unwrapping across permafrost areas. The interferograms are then combined to construct a timeline of ground movement maps covering 8 years. Finally, we discuss observed cross-correlations between observable parameters and possible implications for processes involved in the freeze-thaw cycle and permafrost evolution.

5.2 Data processing

We process the complete Envisat data archive along four \sim 240 km-long and 100 km-large overlapping descending tracks (162, 391, 119 and 348) between 2003 and 2011 (Insert Fig. 5.1). To construct deformation time series, we use the New Small Baselines Subset (NSBAS) chain ([Doin et al., 2011, 2015](#)) based on the ROI_PAC software ([Rosen et al., 2004](#)). The networks of the 495 interferograms are shown in Figs. S1 and S2, and in Table S1.

Before the critical step of phase unwrapping, which is prone to many errors, we apply three important corrections to the wrapped phase of all interferograms in order to improve the data signal to noise ratio (SNR). (1) We remove the phase delay based on an Atmospheric Phase Screen (APS) using the global atmospheric re-analysis model, ERA-Interim ([Dee et al., 2011; Doin et al., 2009; Jolivet et al., 2011](#)) (Figs. S3b and S4). As we are here at an elevation of \sim 5000 m in a dry environment, turbulent APS is moderate with respect to what could be seen at lower elevation (Fig. S4). (2) We then estimate a linear term in range to remove the residual orbital errors and the effect of the clock drift ([Fattah et Amelung, 2014b; Zhang et al., 2014](#)) (Fig. S3c). (3) We correct the effect of Digital Elevation Model (DEM) errors ([Ducret et al., 2014](#)) (Fig. S3d). These corrections significantly reduce the noise on the wrapped phase for further processing (e.g [Grandin et al., 2012; Daout et al., 2016c](#)). However, we observe in the corrected phase several zones of narrow deformation and phase discontinuity, sometimes exceeding half a cycle, near the edge of sedimentary basins, making phase unwrapping difficult in these areas (Figs S3d, S7a,b, S8a). These patterns are principally observed on interferograms built from pairs of images acquired at different seasons.

In order to unwrap the phase with confidence across the edges of sedimentary basins

in all interferograms, we implement an iterative unwrapping procedure by removing from the phase a template of the deformation signal based on the Principal Component Analysis (PCA) of a first sub-series of correctly unwrapped interferograms (see Supplement Information, Figs S5, S6) (e.g., [Strozzi et Wegmüller, 1999](#); [Yun et al., 2007](#); [Pinel et al., 2008](#); [López-Quiroz et al., 2009](#)). After the unwrapping of the reduced phase (Figs. S7c,d, S8b), the template is added back to each interferogram to reconstruct the full unwrapped phase signal (Fig. S7e).

The series of unwrapped interferograms is then inverted to construct a timeline of LOS displacement maps ([Doin et al., 2015](#)) (Fig S9a). To avoid any confusion with the long wavelength tectonic signal, the ground displacement in the basins is referenced to the bedrock as defined by the PCA template (Fig. S10).

5.3 Results and Discussions

The multi-annual displacement of the ground in the sedimentary basins is dominated by a seasonal signal corresponding to ground upheaval in winter and spring and subsidence in summer and autumn (Fig. S9a). We adjust a sine function plus a linear trend to the 2003-2011 displacement data of each image pixel (Fig. S9b) to estimate the average amplitude of the seasonal signal (Fig. 5.1), the month of the maximum subsidence (Fig. 5.2), and the multi-annual ground velocity (Fig. 6.3). Independent estimates of these quantities in areas of overlap between adjacent satellite tracks indicate a remarkable consistency in map view as confirmed by the small associated uncertainties (Fig. S11, Supplement Information). A sinusoidal function offers a first order, linear fit to the data and is used here to map lateral variations of the amplitude of the seasonal signal and the time of the maximum subsidence. We also discuss a more physical model based on the degree-day integrated over the freezing and thawing periods ([Stefan, 1891](#)).

5.3.1 Amplitude of the seasonal ground movements

The amplitude of the seasonal signal ranges between 0 mm and 12 mm with uncertainties lower than 1.5 mm (Figs. 1A, S11a). The arid climate of Tibet and the short period of positive temperatures explain the relatively small amplitude compared to places like Alaska where the seasonal signal reaches up to 4 cm (e.g., [Liu et al., 2010](#)). Zones where the average amplitude of the seasonal signal exceeds 2.5 mm coincide with the narrow

and elongated basins between the east-west mountain ranges (Figs. 1A, 1B, S12a). The ruggedness of the terrane computed using the SRTM elevation data highlights the flat sedimentary basins in and around our study area (Fig. S12b). The boundaries of the basins match almost perfectly the 2.5 mm contour of the displacement map (Fig. 5.1D, Fig. S12c). The superimposition of amplitude on the Google Earth imagery further indicates the detailed correspondance with the sedimentary basins (Fig. S12d). The upper layer of the sedimentary basins is mostly composed of unconsolidated material ranging from fine silt to coarser gravel sediments and conglomerates emplaced in alluvial fans (Pan *et al.*, 2004). The high porosity of these sediments compared to bedrock implies a large water storage capacity resulting in ground deformation during the freeze-thaw cycle.

The spatial variability of the amplitude of the seasonal deformation is controlled by the water content and thermal properties of the ground upper layer and ultimately by spatial variations of the ALT. The ALT should decrease with decreasing mean temperature or cumulative thawing-degree-day (DDT) as the elevation increases (Riseborough *et al.*, 2008). A negative correlation between the amplitude of the seasonal signal and the elevation could thus be expected. Although a negative correlation may be apparent in the dense part of the amplitude-elevation scatter plot (Fig. 5.1C), the amplitude of the signal does not show a systematic dependence to elevation. In addition, the amplitude of the seasonal movement is large on flat surfaces and decreases on slopes where less water is permanently stored compared to the center of basins (Fig. 5.1C). These observations suggest that the amplitude of the seasonal movements is mostly controlled by the moisture content in the soils of sedimentary basins (Fort *et van Vliet-Lanoe*, 2007). Assuming a 9% expansion coefficient for the water-ice phase change, a 1 m column of porous sediments containing 10% of water would raise the ground by 9 mm, within the range of observed values in the Tibetan basins. A moderate porosity of 3-12% corresponds to high gravel content whereas higher volumetric water content can be found in silts or clays (Liu *et al.*, 2014a; Schaefer *et al.*, 2015). The bedrock however, has a very low porosity and is thus not significantly deformed through the freeze-thaw cycle.

5.3.2 Months of subsidence peak

The maximum subsidence (end of the ice thawing period) for areas of high seasonal deformation (above 2.5 mm) (Fig. 5.2A) is observed between September and November with uncertainties typically less than 15 days (Fig. S11b). The histogram (Fig. 5.2B)

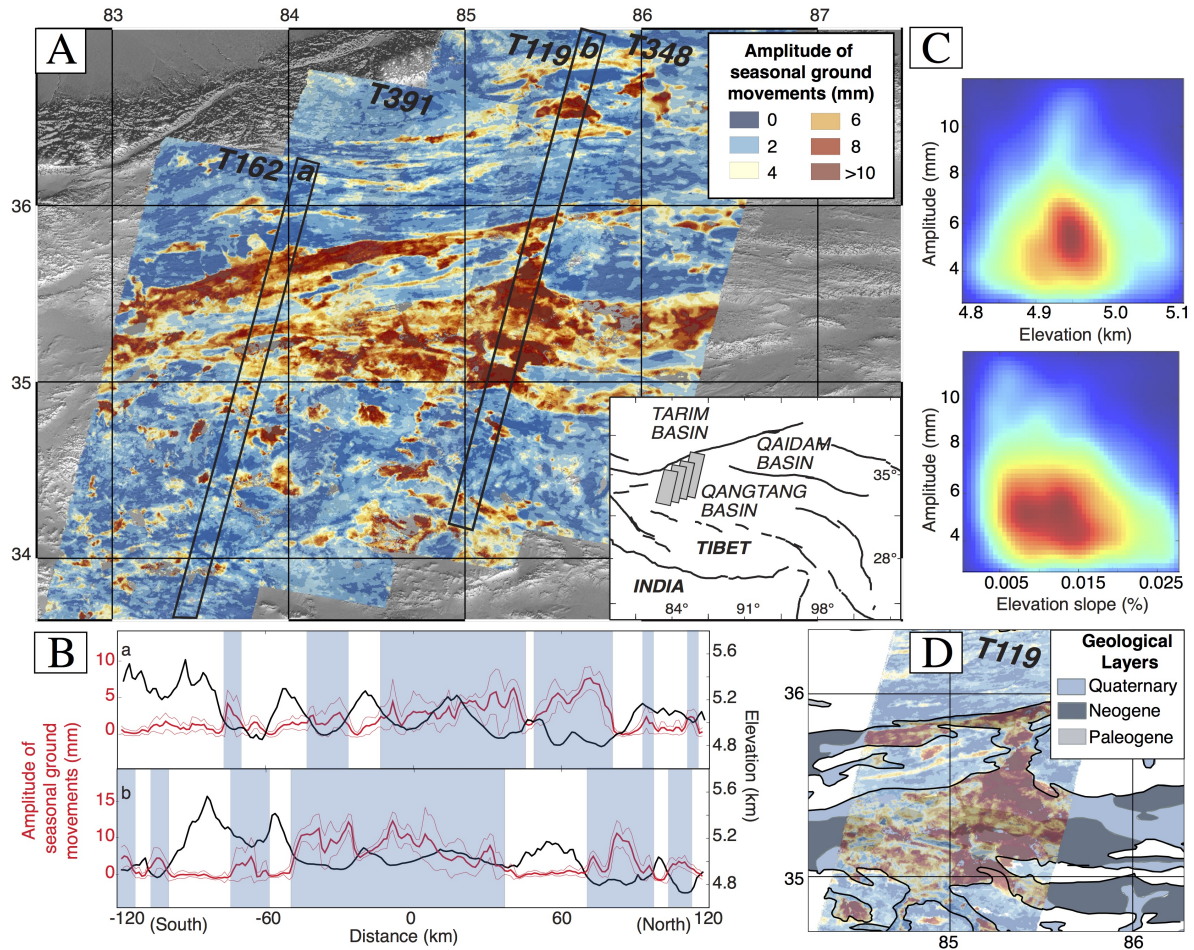


FIGURE 5.1 – A : Map of the amplitude of the seasonal ground movements extracted from InSAR time series analysis of four independent tracks, superimposed on the elevation (SRTM). Bottom right inset : location of the four tracks acquired along descending orbits. B : Profiles of amplitude of seasonal deformation and elevation along tracks 162 (a) and 119 (b). Areas where seasonal signal is larger than 2.5 mm are emphasized by light blue shade and correspond to valleys. C : Density plots showing the correlation between amplitude of the seasonal movements and elevation or terrain elevation slope. D : Zoom on the amplitude of the seasonal deformation for track 119 superimposed on the geological map ([Pan et al., 2004](#)).

shows a slightly skewed distribution, peaking on the 18th of October. Few patches with outlier values and amplitude lower than 4 mm (in red in Fig. 5.2A) are concentrated in rugged terranes. The timing of maximum subsidence for low amplitude signal (below 2.5 mm) have a relatively homogeneous distribution and are considered as non significant and influenced by residual atmospheric delays or noise. Air temperature extracted from ERA-I reanalysis, if fitted by a sinusoid, is maximum on the 14th of July, thus 97 days before the observed active layer thawing maximum (Fig. 5.2B). This maximum is thus

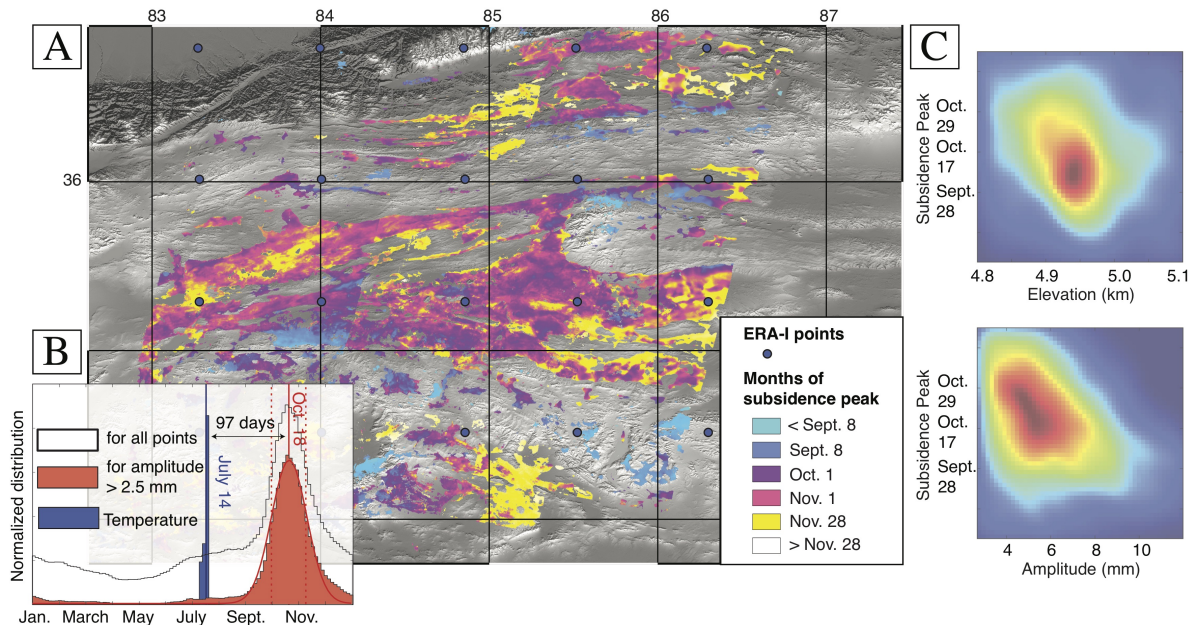


FIGURE 5.2 – A : Month of the seasonal subsidence peak (maximum subsidence) superimposed on shaded elevation (SRTM). We only show points for which the seasonal amplitude is greater than 2.5 mm (A). Blue dots display the ERA-I atmospheric grid used in this study. B : Histograms of date of subsidence peak for all pixels (white) and for pixels affected by a seasonal deformation grater than 2.5 mm (red) compared to that of temperature maxima derived from ECMWF model at all ERA-I points. C : Density plots showing the correlation between the date of subsidence peak and elevation or the amplitude of the seasonal movements.

delayed at the very end of the warm season.

Maximum ground subsidence occurs when the whole active layer is thawed, so when the temperature is maximum at depth. This maximum is delayed with respect to the surface ground temperature due to downward heat diffusion time. Assuming an equality between surface and ground temperatures, the subsidence lag in a purely diffusive model is proportional to seasonal amplitude of the surface temperature, T_a , and to the mean annual air temperature, MAAT, such as (Anderson et Anderson, 2010) : lag (in day) = $-365/2\pi*\ln(-MAAT/T_a)$, increasing linearly with ALT. For instance, at an elevation of 5085 m in our study area ($N35.25^\circ$, $E86.25^\circ$), $T_a = 11.2^\circ$, and $MAAT = -7.3^\circ$ (Fig. 5.3A) imply a lag of 25 days between surface temperature and melting maxima. The measured time lag of 95 ± 20 days between air temperature and subsidence maxima is much larger than the lag predicted by a purely diffusive model.

The difference between surface air temperature and ground temperature depends on the absorption of solar radiation, the lithology, the snow cover in winter and the vegeta-

tion in summer (Lunardini, 1991; Smith et Riseborough, 1996). Moreover, in presence of freezing and thawing of significant amounts of soil moisture, the release and absorption of the latent heat of fusion of the soil water dominates the ground heat budget (Riseborough *et al.*, 2008). To help understanding its spatial variations, we correlate the lag time of maximum subsidence with the elevation and the amplitude of the seasonal movement. We first observe a slight anti-correlation between the maximum subsidence lag and the elevation (Fig. 5.2C), that may be partially explained by a shortening of the warm season, and thus a decrease of the ALT with increasing elevation. Secondly, areas of large seasonal amplitude correspond to an early thawing period with a maximum subsidence occurring in October compared to those of low amplitude with a maximum subsidence in November (Fig. 5.2C).

To explain this observation and better characterize the seasonal deformation pattern, we compute the detrended and normalized seasonal signal as follows : $\phi_{seas}(t) = (d(t) - Vt)/A$, where $d(t)$ is InSAR measurements, V is the multi-year linear trend, and A the amplitude of the seasonal deformation. Fig. 5.3B shows the median and the standard deviation of the 12-month wrapped seasonal signal at each acquisition time. We distinguish between pixels with low amplitude ($2.5 \text{ mm} < A < 8 \text{ mm}$) and those with high amplitude ($A > 8 \text{ mm}$) to separate slope from flat terrains. Note that there is no ground movement in the winter time when the active layer is entirely frozen, a marked departure from the simplistic sinusoid curve. To better describe the seasonal behavior of the active layer, we compute a deformation model, which is -by interval- proportional to the square root of the cumulative degree-day of thawing (DDT) or freezing (DDF) and constant during the time where the active layer is entirely frozen (Harlan et Nixon, 1978; Leppäranta, 1993). In contrast with previous studies (e.g Liu *et al.*, 2012, 2014a, 2015; Schaefer *et al.*, 2015), our observations cover the full season cycle over the course of 8-years allowing us to accurately estimate the model parameters (Fig. 5.3B, see supplementary material).

Over areas of large seasonal amplitude movements, the ground starts to subside in mid-May, shortly after the surface temperature passes over 0°C and ends subsiding in mid-October, about two weeks after the surface temperature returns to freezing (Fig. 5.3). This pattern suggests a saturated soil in which the water is stored up to a shallow depth bellow the surface. In contrast, over areas of moderate seasonal amplitude movements, the subsidence period appears to be delayed by 1-2 months compared to areas of larger movements (Fig. 5.3). There, the subsidence starts in mid-July, approximately when the surface air temperature reaches its maximum and ends subsiding in late November, well into the freezing season at the surface. This pattern can be explained by a non saturated

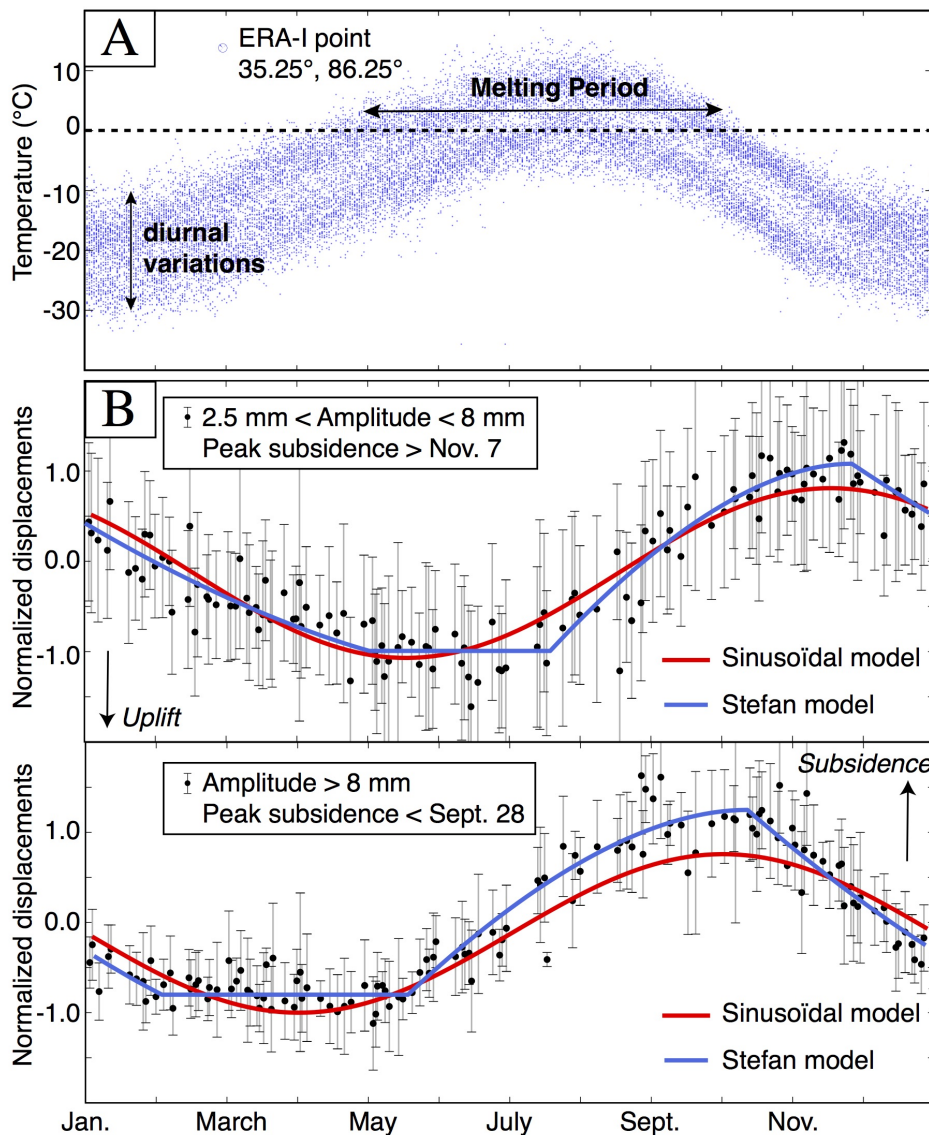


FIGURE 5.3 – A : Time series of air (2 m surface) temperature for one ERA-I point. B : Normalized seasonal evolution at data acquisition times over study area. Top graph shows pixels with seasonal movement amplitude between 2.5 and 8 mm and bottom graph amplitude greater than 8 mm. Superimposed curves are predictions of sinusoidal and Stefan models adjusted data (see text). Adjusted coefficients of Stefan model are : $t_c=\text{May } 26$, $t_1=\text{July } 19$, $t_2=\text{Nov. } 24$, $c=-1.0 \text{ mm}$, $A_t=1.6 \text{ mm.}(\text{yr.}^{\circ})^{-1/2}$, $A_f=0.8 \text{ mm.}(\text{yr.}^{\circ})^{-1/2}$ (top), and $t_c=\text{Feb. } 10$, $t_1=\text{May } 19$, $t_2=\text{Oct. } 12$, $c=-0.8 \text{ mm}$, $A_t=1.5 \text{ mm.}(\text{yr.}^{\circ})^{-1/2}$, $A_f=1 \text{ mm.}(\text{yr.}^{\circ})^{-1/2}$ (bottom).

soil in which the ground water is stored in the bottom part of the active layer, therefore responding later to the freezing and thawing downward progressing fronts.

These findings also explain the observed anti-correlation between amplitude and

phase of the ground movements (Fig. 5.2C), a pattern that cannot be explained by a diffusive model in a homogeneous medium. The aridity of the climate prevailing in northwestern Tibet and the topography of the terrain result in a spatially uneven distribution of ground water, which in turns controls the distribution and behavior of the permafrost active layer (Fort et van Vliet-Lanoe, 2007).

5.3.3 Multi-annual trend of ground subsidence

The multi-annual trend of the ground LOS velocity, restricted to areas of high seasonal deformation amplitude (>2.5 mm), is low and ranges from -2 to 3 mm/yr with isolated areas subsiding up to 4 mm/yr (Fig. 6.3A). Uncertainties are lower than 0.5 mm/yr for all pixels, except in track 348, which includes less acquisitions than other tracks (Figs. S2, S11c). We rule out a significant contribution from horizontal movements to the LOS velocity (possible downslope movement of the soil due to gelifluction or frost creep) because the observed LOS velocity is mostly insensitive to the terrane slope direction (Fig. 6.3C). The observed trend therefore suggests either a long term ground subsidence (range increase) and uplift (range decrease).

The long-term temperature increase over Tibet from 2003 to 2011 is of 0.04-0.05°/yr (Dee et al., 2011). If the surface temperature was the sole controlling parameter of the velocity trend, it would affect the basins rather uniformly. However, we observe large spatial variations within basins in the long-term velocity map (Fig. 6.3A). An ALT increase would primarily increase the amplitude of the seasonal oscillations, keeping constant the maximum uplift level during the winter season, a pattern that is not observed in the time series of individual pixels (Fig. 6.3B). A possible explanation of lateral variations in the long-term ground displacement rate, is the combined effects of basin drainage and ice loss due to temperature increase. In the case of drained sediments, the ice melting during the warm season should result in a water/ice volume loss in the soil, increasing the long-term subsidence rate. On the other hand, endorheic basins may collect more water during the thawing season than they loose by evaporation or percolation to greater depth, resulting in a long-term uplift trend.

We also observe a multi-annual tendency toward thawing for lower elevation basins (Fig. 6.3C), indicating a dependence to the ALT. Other specific ground conditions such as snow and vegetation cover may also influence the long-term trend. Further modeling would be necessary to assess the correlation of temperature increase, as well as these multiple parameters with regionally observed ground movement trend. For comparison,

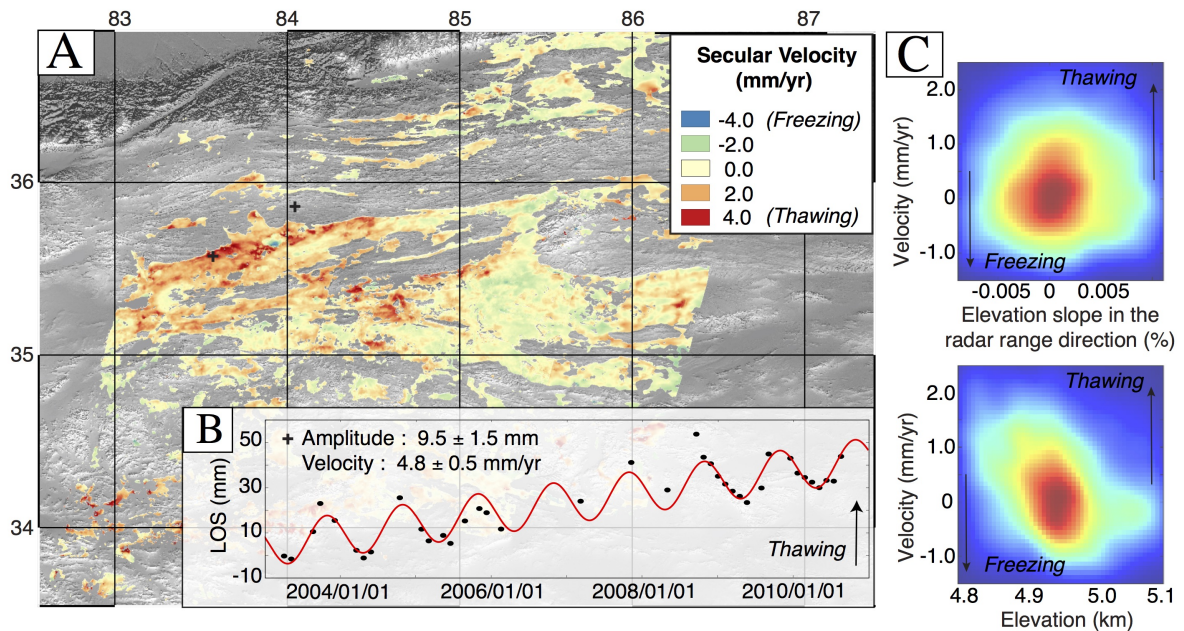


FIGURE 5.4 – A : Map of long-term ground velocity in LOS direction shown at pixels with amplitude of seasonal movement >2.5 mm (Fig. 5.1A). B : Relative displacement time series with best fit sine functions between the two 5×5 pixels windows labeled by cross sign on map A. LOS increase represents ground subsidence. C : Density plots showing correlation between multi-annual trend and terrane slope along radar range direction (top left) and elevation (bottom left). Positive (resp. negative) velocity indicates ice thawing (resp. freezing).

north of the Siling Co Lake in Central Tibet, at lower elevations and where the water content might not be the limiting factor to the permafrost related deformation, InSAR measurements indicate higher long-term subsidence rates than this study, reaching a centimeter per year (Doin *et al.*, 2015). Chang et Hanssen (2015) measured vertical rates up to 10 mm/yr on the Qinghai-Tibet Railway, where the permafrost is there defined as sporadic (Brown *et al.*, 2000).

5.4 Conclusion

With an unprecedented spatial and temporal sampling, MT-InSAR data provide new insights into the dynamics of the permafrost active layer over a $60,000 \text{ km}^2$ area in north-western Tibet. An 8-years timeline of the surface movement, sampling evenly the entire seasonal cycle reveals that the amplitude of the ground movements associated with the freeze-thaw cycle is strongly influenced by the nature of the terrain and the edaphic

condition. Unconsolidated sediments in basins show larger amplitude of seasonal movement compared to exposed bedrock. Spatial variations of the amplitude and phase of the seasonal ground movements appear to be controlled by the ground water availability of the sediments rather than by the thickness of the active layer. Large ground oscillations (> 8 mm) are observed over flat terrains in the centers of basins whereas smaller ground oscillations (2.5-8 mm) occur on slopes where less water is available in the soil. A degree-day integrated model adjusted to the data indicates that the subsidence occurs during the period of diurnal temperature are superior to 0° over areas of large movement and that the pattern is delayed by one to two months for the areas of smaller movements. In addition to the seasonal signal, a multi-annual trend of up to 3 mm/yr of subsidence is observed in limited areas and may be due to long-term changes in ground water supply and basin drainage. The recent launch of new SAR systems (Sentinel-1a/b) with systematic acquisitions and shorter revisit time (down to 6 days) will allow scientists to better characterize the seasonal and inter-annual deformation response of the frozen ground to air temperature, solar radiation and precipitation. Our study showed the potential of long temporal series of InSAR observations, opening new avenues of research on permafrost dynamics and climate.

5.5 Supplementary Materials

Methods

This method section provides additional text and figures explaining and illustrating all the processing steps of the SAR data. We take as example the Envisat track 119, but applied the same processing scheme for all tracks. The purpose of this section is to optimize the retrieval of the permafrost signal within the interferograms and to provide a method for systematic InSAR processing in permafrost area.

Interferogram network : For the four tracks we first define an optimal small baseline interferometric network connecting with redundancy all acquisitions using perpendicular baseline constraint, B_{perp} , and temporal baseline constraint, B_t (Fig. 5.5). Note that some interferograms present either large B_{perp} and low B_t or low B_{perp} and large B_t . We then average all interferograms at 2 and 10 looks in the range and azimuthal directions, respectively. Number of images and interferograms we used for each track are summarized

MESURE DU PERMAFROST DU PLATEAU TIBÉTAIN PAR INSAR

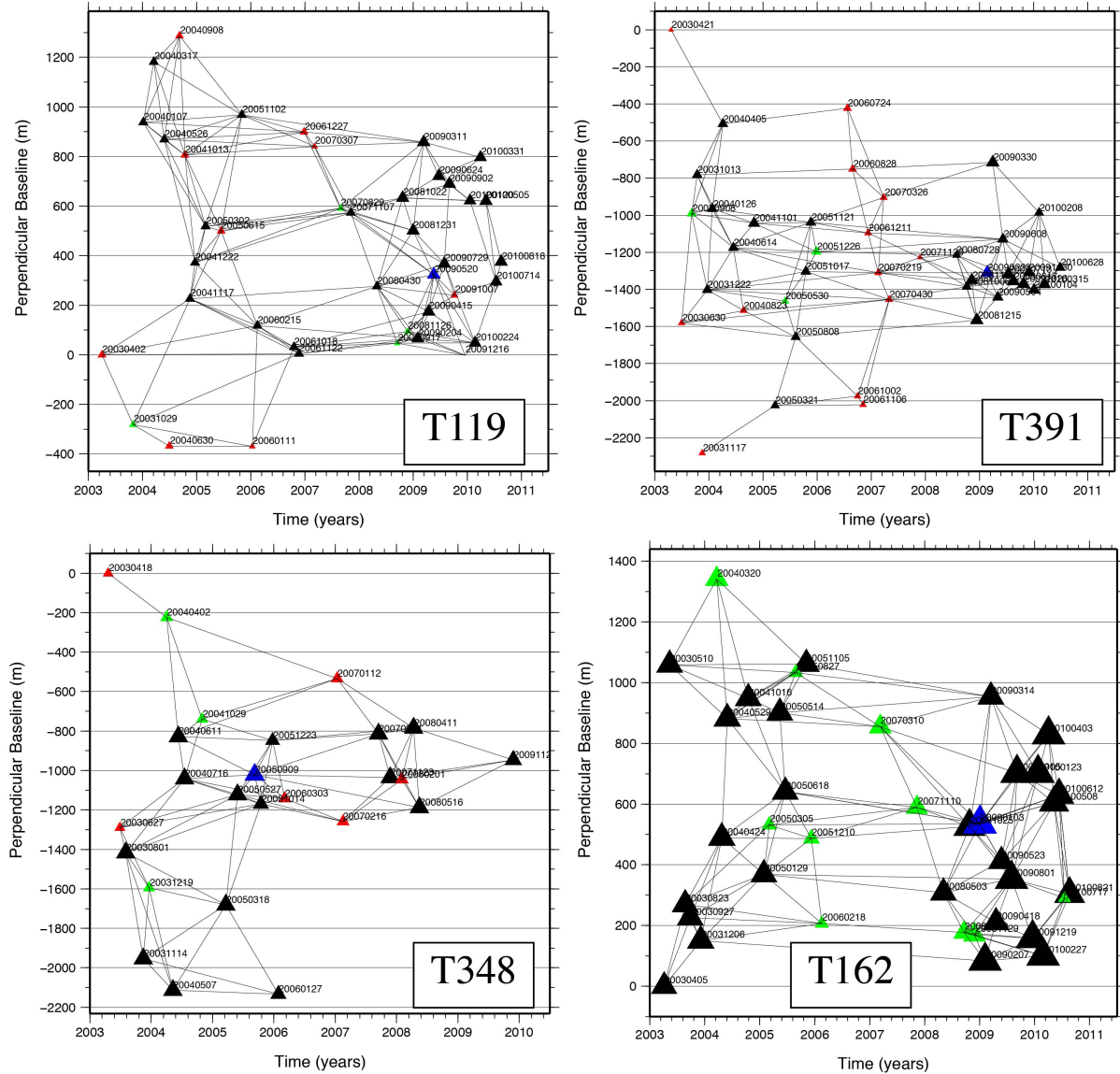


FIGURE 5.5 – Computed interferograms for the four tracks. Triangles are SAR acquisitions with sizes and colors according to their spatial extent : black triangles for a full coverage, green triangles for images covering the northern part of the track only, and red colors for images covering the southern part only. The master image is shown with a blue triangle.

in Table S1 and (Fig. 5.6). Except for track 348, all pixels are covered by more than 30 images.

Corrections before phase unwrapping : The processing is based on a series of corrections before unwrapping that reduces the variance of the wrapped phase. Fig. 5.7 presents an example of a long temporal baseline wrapped interferogram on track 119 before and after this series of corrections, which includes the stratified atmospheric delay

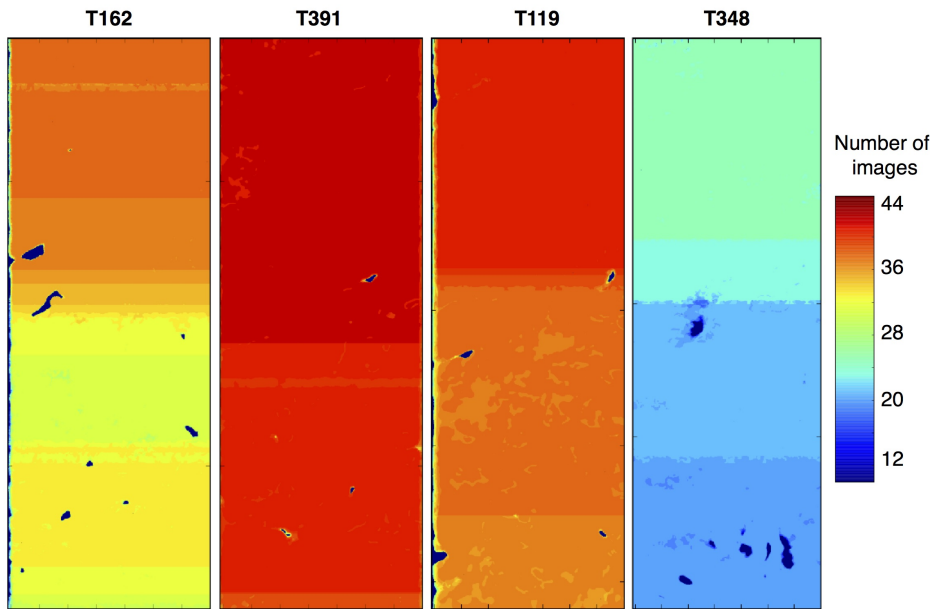


FIGURE 5.6 – Number of images per pixel for the 4 tracks.

correction using global atmospheric re-analysis model, ERA-Interim ([Doin et al., 2009](#); [Jolivet et al., 2011, 2014b](#)) (computed by the European Center for Medium-Range Weather Forecast (ECMWF)), the linear term correction in the range direction to correct for residual orbital errors, and local Digital Elevation Model (DEM) error correction. DEM errors are after estimated based on the relationship between interferometric phase and perpendicular baseline ([Ducret et al., 2014](#)).

ERA-I provides estimates of temperature, water vapor partial pressure, and geopotential height every six hours at different pressure levels on a 0.7° grid from 1989 to present ([Dee et al., 2011](#)). Path delays at each acquisition time are derived from vertical profiles of these variables at several ERA-I points encompassing a SAR scene. The delay is then mapped on the radar scene by integration for each pixel from a Digital Elevation Model (DEM) to the satellite elevation ([Doin et al., 2009](#)). To quantify the amplitude of this tropospheric signal within the Tibetan plateau, we plot the relative delay between the valleys (4800 m) and the mountain ranges (5400 m) for one ERA-I point located in the Tibetan plateau ($36^\circ, 85.5^\circ$) (Fig. 5.8). The integrated path delays between the two elevations are computed relatively to the first date as function of time since each new year to better visualize the seasonal pattern (Fig. 5.8). The prediction indicates a slight seasonal pattern, peacking at the beginning of February, and a variability of 3.1 mm, smaller than the permafrost related signal. We correct interferograms

TABLE 5.1 – Table summarizing the number of images and interferograms per track.

| Tracks | # of Images | # of Interferograms |
|--------------|-------------|---------------------|
| T348 | 41 | 146 |
| T119 | 25 | 75 |
| T162 | 44 | 132 |
| T162 | 38 | 142 |
| Total | 148 | 495 |

from this predicted stratified atmospheric phase screen. Note that within the Tibetan plateau, we cannot compute for validation the residual phase-elevation correlation after ERA-I correction as the phase-elevation correlation is difficult to separate from permafrost signal in the valleys. Note also that this correction does not correct non-stratified patterns with wavelength lower than 75 km. However, the effect of turbulent patterns, being random both in space and time, are attenuated by data stacking in the following time series analysis.

Unwrapping procedure : To help the unwrapping, we implement a specific iterative procedure that consists in using a spatial template for deformation. This approach is standard in InSAR processing and has already been applied for land subsidence (e.g., [Strozzi et Wegmüller, 1999](#); [López-Quiroz et al., 2009](#)) or volcanic studies (e.g., [Yun et al., 2007](#); [Pinel et al., 2008](#)) in presence of complex and large deformation. We here extract the template from a Principal Component Analysis (PCA) decomposition. We produce a first series of unwrapped interferograms and check their reliability computing the misclosure of the interferometric network. If large, we then check visually the corresponding interferogram and correct its unwrapping error by setting manually a high priority bridge along another unwrapping path with less fringe gradients. For some interferograms, this last operation was not possible due to the high fringe rates and we thus did not select them to compute the PCA. We then perform the PCA from a selection of successfully unwrapped interferograms (presenting a low misclosure), $\mathcal{C} = \mathcal{U} * \lambda * \mathcal{V}$, where \mathcal{U} is the eigenvector matrix of the covariance matrix, \mathcal{C} , between interferograms centered around the zero phase, λ , is the eigenvalue matrix, and \mathcal{V} , is the transformation matrix from the interferograms basis to the principal component basis. \mathcal{C} is computed using only unwrapped pixels. Note that as the no data mask is slightly different from one interferograms to the other, \mathcal{C} is not perfectly positive definite. The deformation pattern we are interested in pops up in the first or second component (Fig. 5.9a). Temporal inversion of the corresponding eigenvector shows, as expected, a seasonal signal.

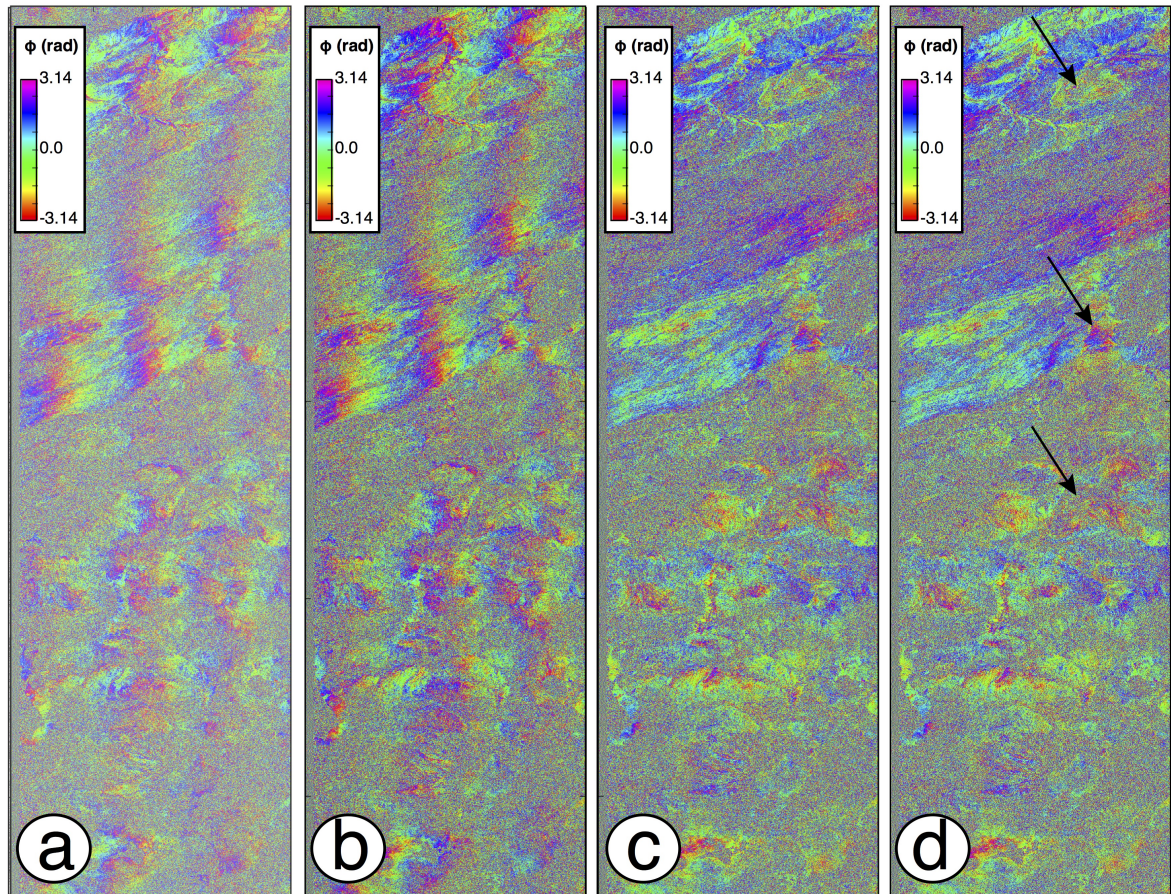


FIGURE 5.7 – Example of corrections on the wrapped phase for a small B_{perp} of 50 m and long temporal baseline interferogram between the two images acquired in November 17, 2004 and April 30, 2008 for track 119. a) Original interferogram in 4x20 looks. b) Interferogram after ERAI correction. c) Interferogram after range ramp correction. d) Interferogram after local DEM errors correction. (a), (b) and (c) are superimposed to the coherence, while (d) is superimposed to the phase colinearity. Arrows point out some areas with strong phase discontinuities.

The comparison of the deformation pattern extracted from PCA with elevation and google earth imagery shows that deformation is concentrated in basins and that "basement" can be considered, on average, as non deforming. We must thus insure that the deformation template extracted from PCA map is on average referenced to zero on basement. To do so, we extract a N-S profile (Fig. 5.9b) and observe that PCA values on basement pixels have far less scatter than the PCA values on basin pixels. To define a N-S reference curve, we fit across the median of pixels selected in areas with less scatter (red median) a cubic ramp in azimuth (blue line in Fig. 5.9b). This ramp in azimuth is removed from the PCA as shown in Fig. 5.9c.

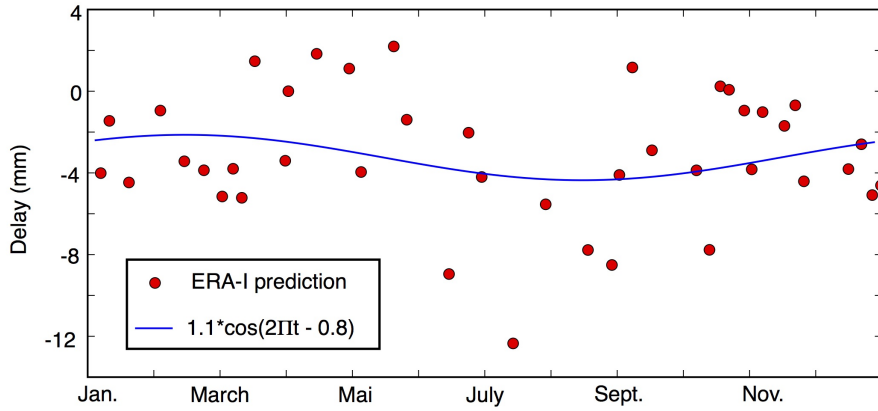


FIGURE 5.8 – Time series of the predicted tropospheric delay for a ERA-I point located within the Tibetan plateau (36° , 85.5°) between elevations of 4800 m and 5400 m. The standard deviation of the stratified atmospheric signal predicted by ERA-I is 3 mm, which is smaller than the permafrost related signal, and with slight seasonal pattern picking at the beginning of February.

We repeat the operation for the four tracks and observe a good spatial continuity of the extracted deformation shape on the overlapping areas that correlates with the low elevation basins (Fig. 5.10).

Then, following López-Quiroz *et al.* (2009), we use the PCA map as a deformation template to help unwrapping in high fringe rate areas. We estimate a best-fit scaling coefficient between the deformation template and the wrapped phase (by maximizing the complex coherence of the residue), and remove the scaled template from the original interferogram (Fig. 5.11, Fig. 5.12). Before corrections (Fig. 5.11a,b), black arrows point out typical patterns of deformation dominating the wrapped phase. After correction, these patterns are in majority removed (Fig. 5.11c) and the phase is more easily unwrapped (Fig. 5.11d).

In addition to this iterative procedure, unwrapping process is performed using a specific scheme. First, we multilook by a factor of 8 in range and 40 in azimuth, replacing the amplitude of the interferograms by the colinearity as defined by Pinel-Puyssegur *et al.* (2012) (Fig. 5.11a). At the difference of the coherence, which assume that all pixels have the same role and give high coherence for bright pixels, the colinearity takes into account the fact that phase ought to vary smoothly with space. The criterion is made of two terms : one measuring the closeness a point comparing to its neighborhood while

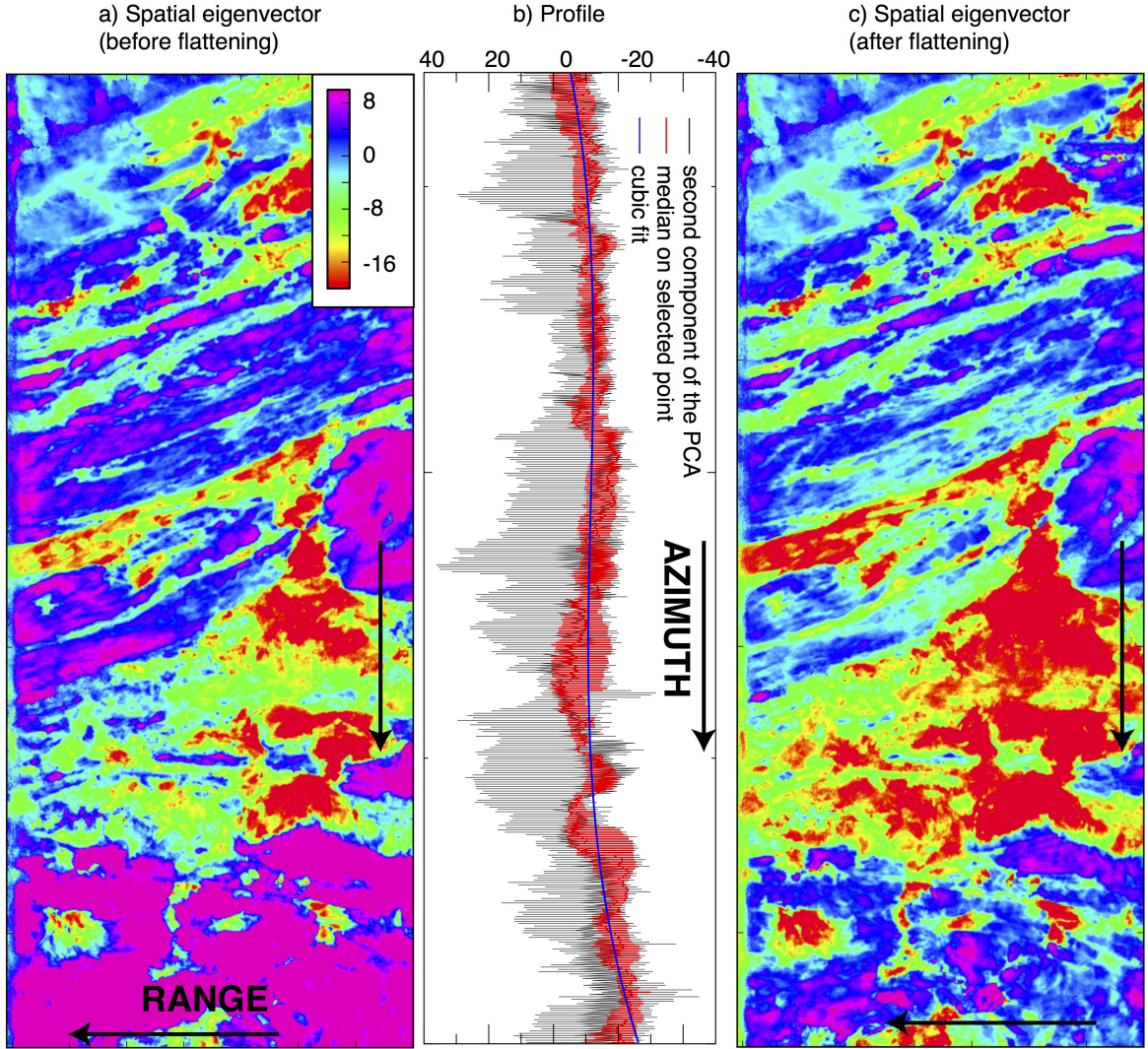


FIGURE 5.9 – Second component of the PCA decomposition for track 119. a) Spatial eigenvector. b) Eigenvector profile (black lines). The bedrock is characterized by relatively more positive values than the basins that show more scatter. Cubic ramp (blue line) estimated from the median computed on selected points on "bedrock" (red line). c) Spatial eigenvector after flattening from the cubic ramp to reference at zero on basement.

the other term estimates the noise level of the pixel and its neighborhoods.

We then low pass filter using the average temporal coherence as weight (Fig. 5.11b). In contrast to the cut-tree algorithm (Rosen *et al.*, 2004), here we impose an unwrapping path going from the high to low coherence areas defined by the filter, avoiding unwrapping to propagate into incoherent areas, as snow-capped mountain ridges or across areas of very high rate. Unwrapping is performed in adjoining sub-regions above a coherence threshold. Each newly unwrapped area is added to already unwrapped areas. The cohe-

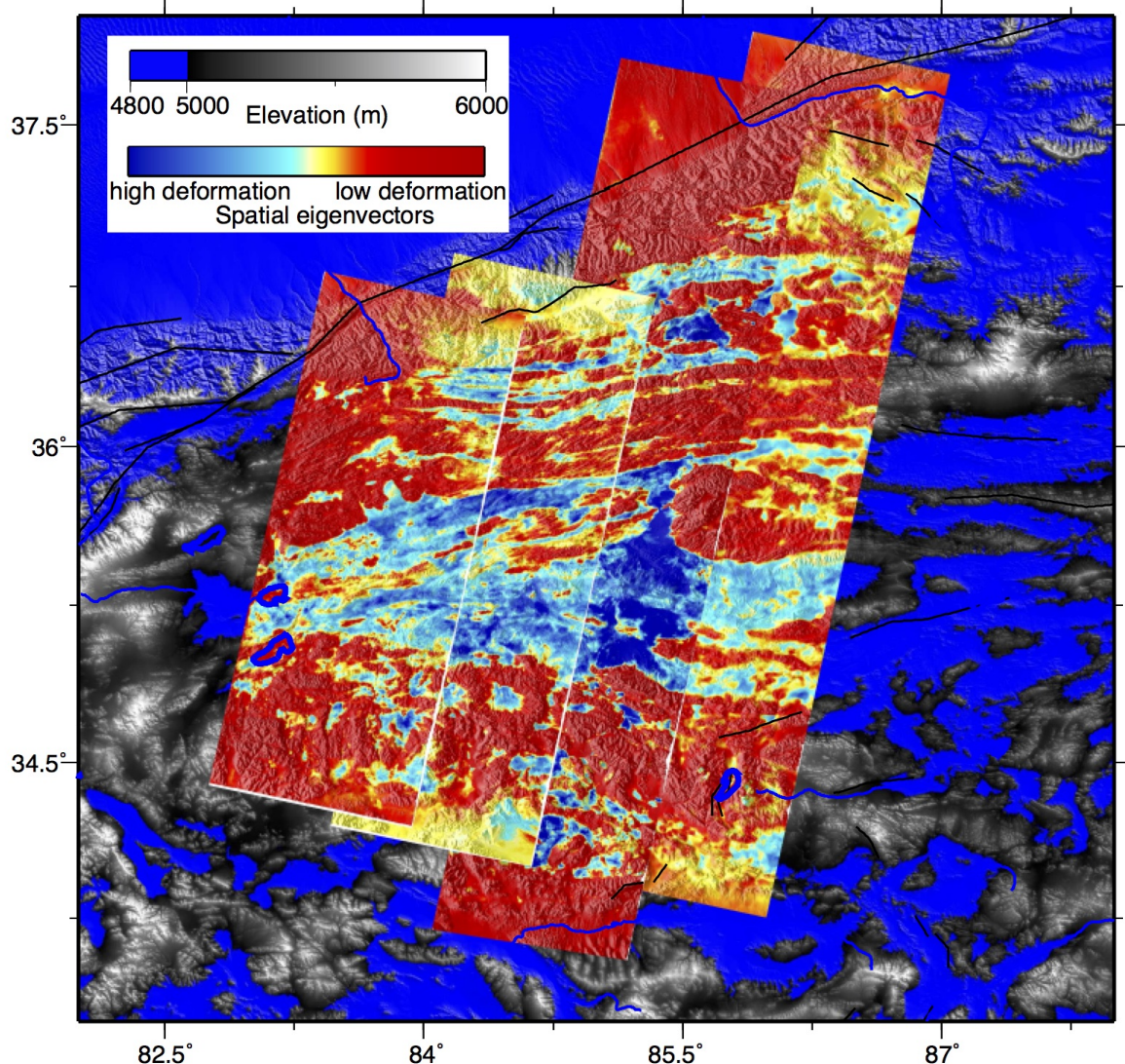


FIGURE 5.10 – Spatial eigenvectors associated to the PCA component that presents a strong seasonality. Blue patterns are deforming areas while red colors highlight stable areas. These maps are used as templates to unwrap interferograms.

rence threshold progressively decreases to propagate unwrapping further away (Grandin *et al.*, 2012; Doin *et al.*, 2015; Daout *et al.*, 2016c). If necessary, high priority bridges are set manually by visual inspection of interferograms.

We finally reintroduce the scaled template previously removed (Fig. 5.11e). Note that if the computed template was not in agreement with the interferograms, the scaling factor between both would tend to be zero. This would lead to a small but inappropriate correction of wrapped interferograms and an increasing of the unwrapping errors. We

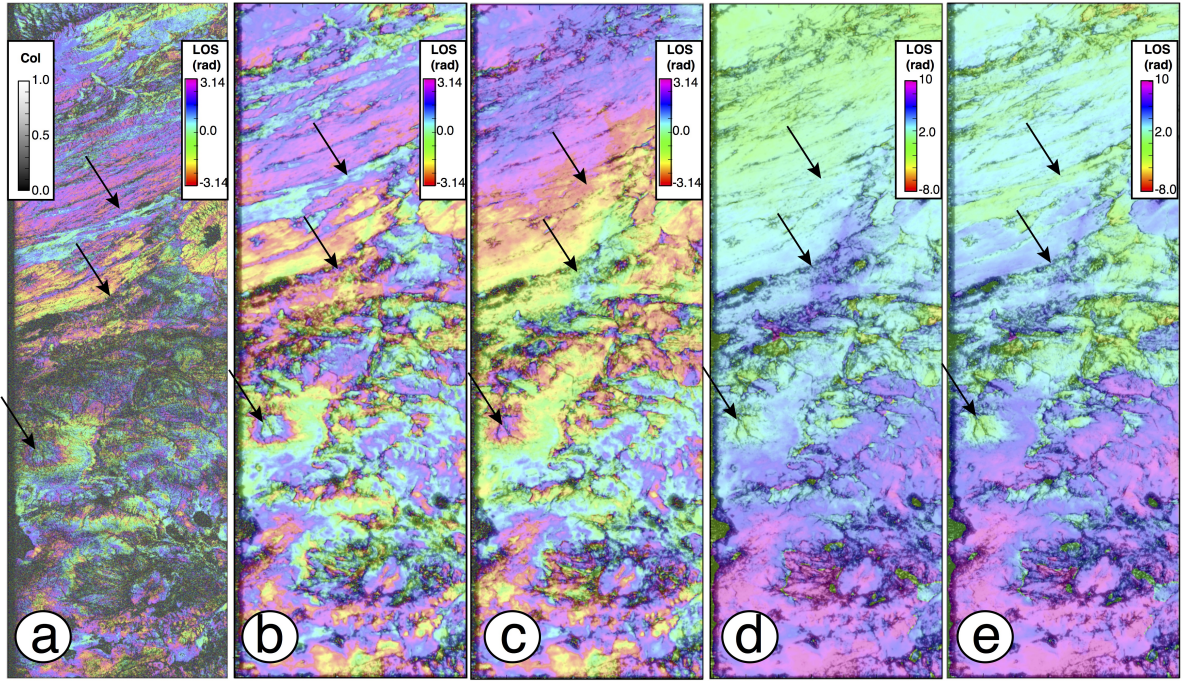


FIGURE 5.11 – Example of unwrapping procedure for an interferogram of track 119. The interferogram is formed between the two images acquired on November 11, 2007 and April 30, 2008, for the track 119. Arrows highlight some examples of areas with strong phase discontinuities, where our procedure succeeds in unwrapping the phase. a) Interferogram in 8x40 looks superimposed to the phase colinearity ([Pinel-Puyssegur et al., 2012](#)). b) Filtered interferogram superimposed to the coherence associated to the filter averaging process. c) Interferogram corrected using the PCA deformation template. d) Unwrapped interferogram. e) Unwrapped interferograms after re introducing the scaled PCA shape.

checked this by computing the misclosure of the unwrapped interferogram network at each iterations, which remain small for most pixels (< 0.5 rad). Doing so, we successfully produce wide, continuous and high quality unwrapped interferograms covering the northwestern part of the Tibetan plateau.

Fig. 5.12 shows three examples of wrapped and unfiltered interferograms presenting strong permafrost related deformation. Before corrections (Fig. 5.12a), black arrows point out typical patterns of deformations dominating the wrapped phase. After correction (Fig. 5.12b), these patterns are in majority removed and the phase is easily unwrapped.

Time series analysis : At the end of the processing, interferograms are inverted into successive phase delays maps (Fig. 5.13a). This step is crucial as it allows to check the consistency of each interferogram and thus detect the residual unwrapping errors ([López-Quiroz et al., 2009; Doin et al., 2011](#)). Times series analysis is then iterated again until

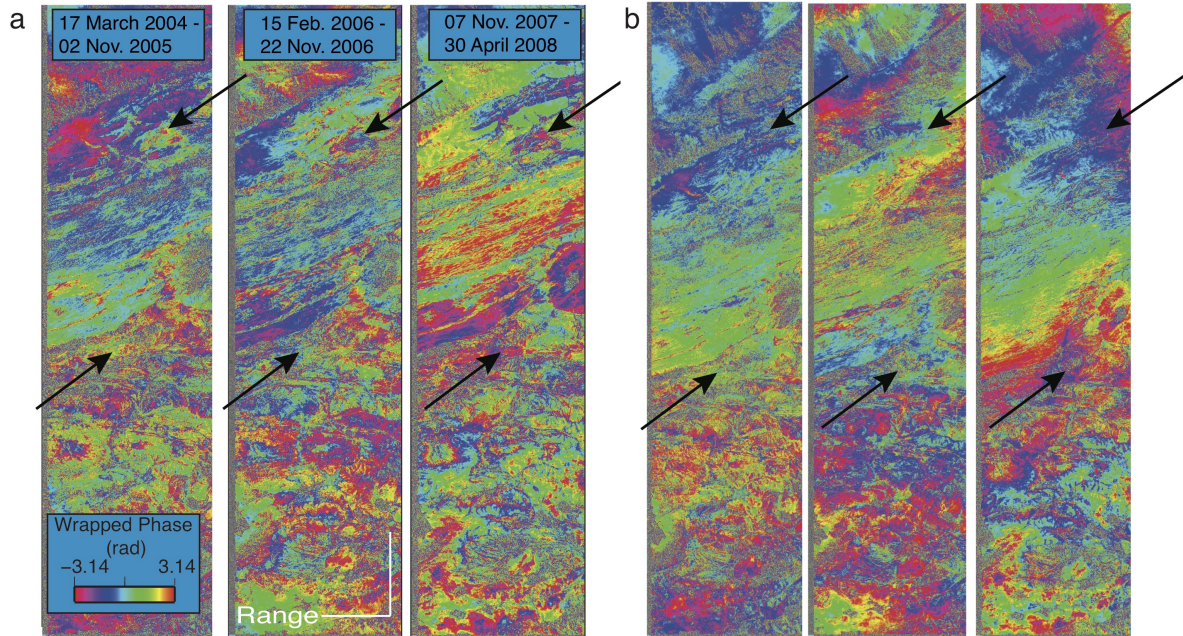


FIGURE 5.12 – **Example of three unfiltered interferograms on track 119.** a) Wrapped interferograms after the series of correction explained in Fig. 5.7. b) Unwrapped interferograms from which PCA template of Fig. 5.9c has been removed to reduce locally the phase gradient and facilitate unwrapping.

no large network inconsistencies remain (Doin *et al.*, 2015). To refer the maps to a stable bedrock, we first mask the deformation areas using a threshold on the previous deformation shape extracted from the PCA (Fig. 5.10), and estimate a cubic ramp in azimuth and a quadratic ramp in range on bedrock areas for each phase delays maps to remove possible tectonic signal (that could be of the order of a few mm/yr in the LOS). So no single reference points are used but we set on average regional reference on non deforming pixels (Fig. 5.14). After correction of this large scale reference surface, we derive a linear term, V , a DEM error coefficient, α , a cosinus term, β_2 , and a sinus term, β_1 , such as :

$$\phi^k = Vt_k + \alpha B_{\perp}^k + \beta_1 * \sin wt_k + \beta_2 * \cos wt_k. \quad (5.1)$$

We solve the inverse problem, $\mathbf{d} = \mathbf{Gm}$, where \mathbf{d} is the data vector made of the phase displacements, and \mathbf{m} is the vector of model, with the least square solution and then produce amplitude ($\sqrt{\beta_1^2 + \beta_2^2}$), temporal lag ($\arctan \frac{\beta_1}{\beta_2}$) and ground velocity (V) deformation maps. Model and residual maps are also shown in Fig. 5.13b,c. Note that here no temporal smoothing have been applied to ϕ^k . We also compute, for each pixel i

and for each parameter j , an error, $\sigma_m^{i,j}$, equal to :

$$\sigma_m^{i,j} = \sqrt{\frac{N}{N-M} (\sigma_d^i)^2 (\mathbf{G}^T \mathbf{G})_j^{-1}}, \quad (5.2)$$

where N is the number of data, M the number of parameter, $(\sigma_d^i)^2$ is the RMS phase residual for each pixel j, and $(\mathbf{G}^T \mathbf{G})_j^{-1}$ is the diagonal j , and then produce amplitude ($\sqrt{\sigma_{\beta_1}^2 + \sigma_{\beta_2}^2}$), temporal lag ($\frac{\sigma_{\beta_1}|\beta_2| + \sigma_{\beta_2}|\beta_1|}{\sigma_{\beta_1}^2 + \sigma_{\beta_2}^2}$) and ground velocity (σ_v) error maps (Fig. 5.15). Computed errors are clearly lower than the measured deformation, with higher errors for track 348 that contains less images (Fig. 5.6).

Data Analysis

Comparisons : To characterize the spatial patterns of the observed signal, we superimpose its amplitude for track 119 on elevation, topography ruggedness, geological map and google earth imagery (Fig. 5.16). The deformation correlates with areas of low topography (Fig. 5.16a) and even more strikingly of low ruggedness (Fig. 5.16b). We observe an almost perfect match between the boundaries of the deforming area and those of the Cenozoic sediments (Fig. 5.16c), made from fine silt to coarser gravel sediments and conglomerates (Pan *et al.*, 2004). Superimposition of amplitude on the Google Earth imagery similarly suggests that deformation is restricted to sedimentary basins (Fig. 5.16d).

Stefan model : The Stefan deformation model $m(t)$ (Stefan, 1891; Leppäranta, 1993) of Fig. 3B is defined as follow :

$$m(t_c < t < t_1) = c, \quad (5.3)$$

$$m(t_1 < t < t_2) = A_t * \sqrt{DDT(t)} + c, \quad (5.4)$$

$$m(t_2 < t < t_c) = -A_f * \sqrt{DDF(t)} + A_t * \sqrt{DDT(t_2)} + c, \quad (5.5)$$

where A_t and A_f are the thawing and freezing coefficients, respectively, $DDT(t)$ and $DDF(t)$ are the cumulative degree-day of thawing and freezing (time integrals of the ground temperature above or below zero), respectively, t_1 , t_2 , and t_c define the beginning of the thawing period, the beginning of the freezing period and the end of the freezing period, respectively, and c is a constant. Note that the SNR in the normalized curve of movements >8 mm is larger than that of the curve of movements <8 mm (Fig. 3B).

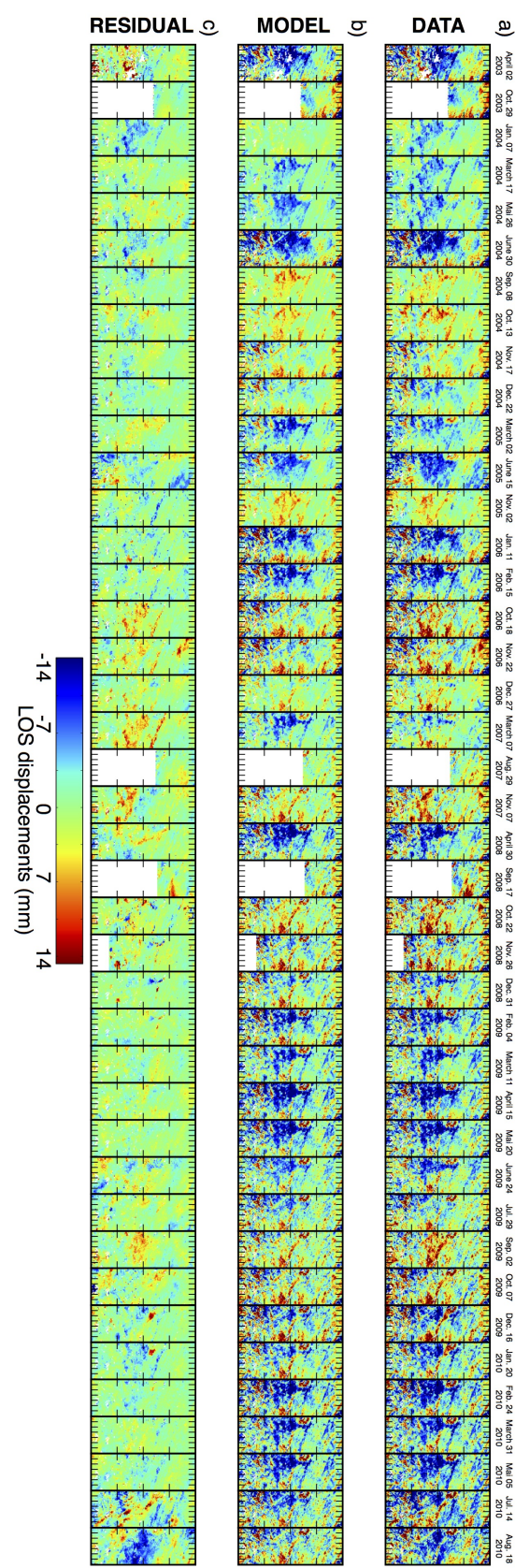


FIGURE 5.13 – Time series of delay maps (a), models (b) and residuals (c) for track 119. One color cycle correspond to a LOS delay of 2.8 cm.

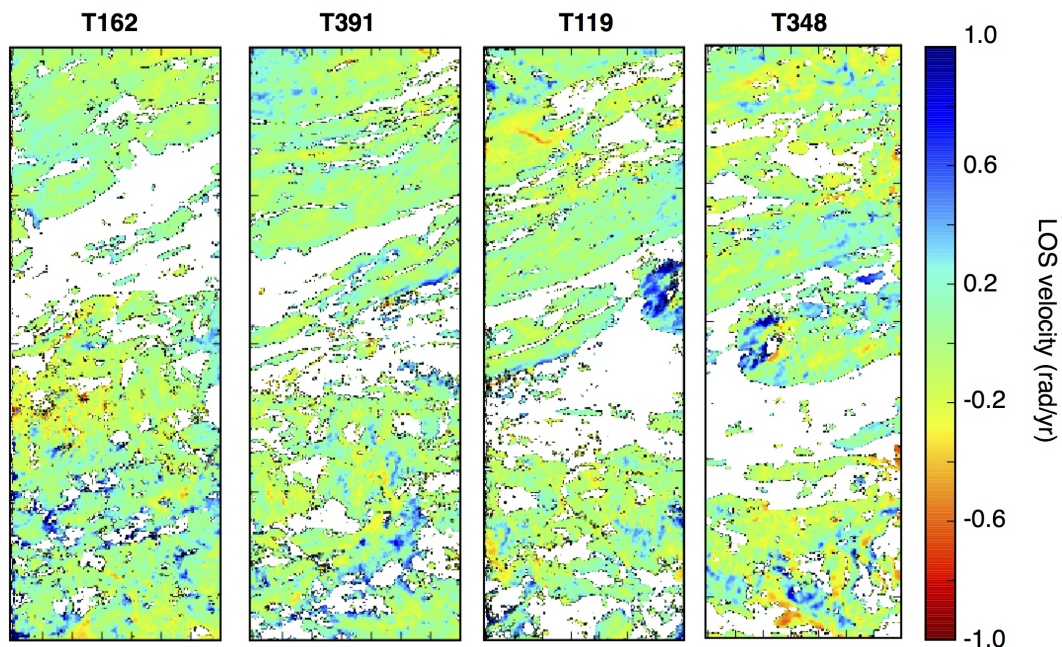
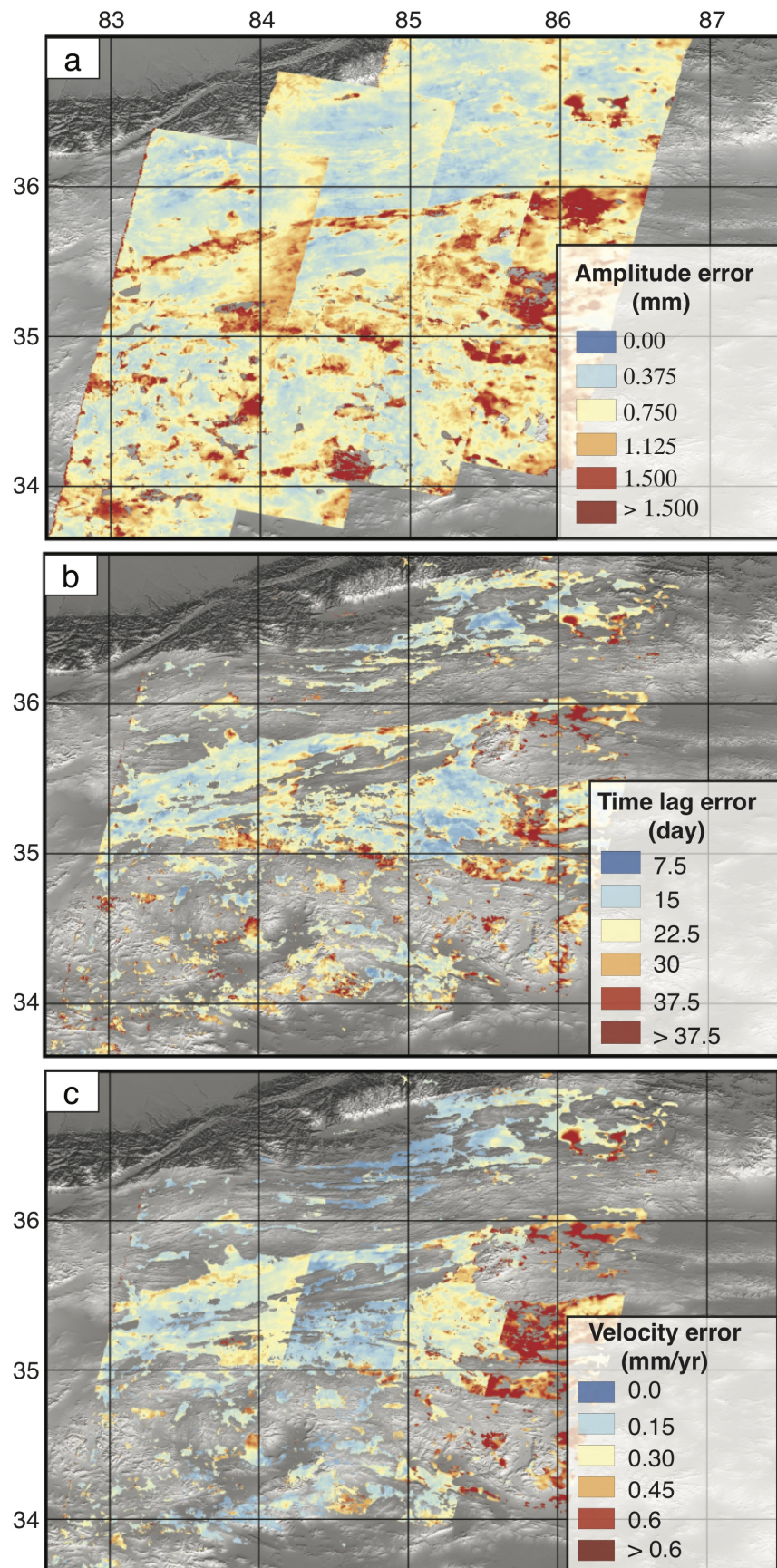


FIGURE 5.14 – Long-term ground velocity of the defined bedrock for the 4 tracks after referencing.



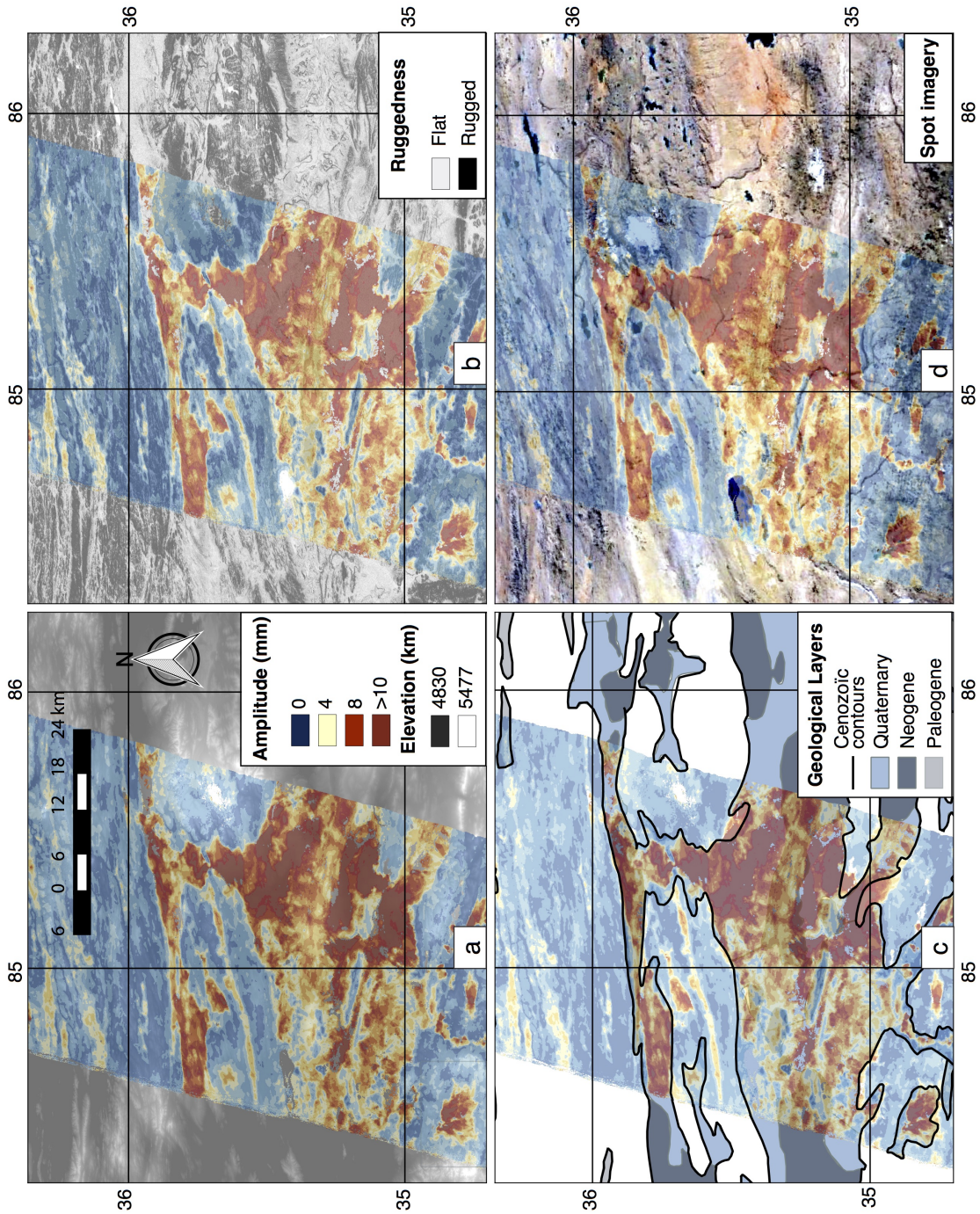


FIGURE 5.16 – Zoom on the amplitude of the seasonal deformation for track 119 superimposed on DEM SRTM (a), on topography ruggedness index (b), on the geological map (Pan *et al.*, 2004) (c), and on CNES/Spot imagery from Google Earth (d).

Chapitre 6

Large scale interseismic deformation in North Western Tibet

Sommaire

| | | |
|------------|--|------------|
| 6.1 | Introduction | 175 |
| 6.2 | InSAR processing | 178 |
| 6.2.1 | Tests on atmospheric corrections | 183 |
| 6.2.2 | Tests on residual orbital ramps | 184 |
| 6.3 | Analysis of the tectonic signal | 186 |
| 6.3.1 | GPS data | 186 |
| 6.3.2 | InSAR velocity field | 188 |
| 6.3.3 | 2D model | 196 |
| 6.4 | Discussions and Conclusions | 201 |

Preface

En raison des nombreuses ambiguïtés entre délais atmosphériques, rampes résiduelles orbitales et déformation tectonique, traiter des données au travers de la faille de l'Altyn Tagh (ATF) s'avère complexe. Les travaux de Wright *et al.* (2001), d'Elliott *et al.* (2008), de Wang *et al.* (2012) et de Garthwaite *et al.* (2013) effectués dans cette zone furent confrontées à ces difficultés. De mon point de vue, ces études ne furent pas totalement satisfaisantes pour les raisons qui suivent. Tout d'abord, la faible cohérence au pied de l'ATF et dans les bassins sédimentaires obligèrent ces auteurs à parfois "deviner" le saut de phase au travers de l'ATF et à masquer une partie non négligeable des scènes SAR. Cela à également restreint la zone étudiée et donc le champs lointain. Ce dernier est important pour contrer le trade-off entre déformation intersismique et rampe orbitale. Ensuite, les auteurs décidèrent d'inverser conjointement en fin de traitement les rampes orbitales, les délais corrélés à la topographie et un modèle de glissement de faille, à partir des cartes de vitesses obtenues. Ce choix annule de fait l'application d'une correction atmosphérique stratifiée aux interférogrammes. Même si ce choix paraît compréhensible, il entraîne toutefois une barre d'erreurs importante sur la carte de vitesse obtenue au travers l'ATF (voir chapitre 4).

Pour ma part, comme déjà évoqué pour le traitement au niveau de la faille d'Haiyuan (cf. chapitre 2), je contre le problème de la mauvaise cohérence et du déroulement par une approche spécifique basée sur une série de corrections sur la phase enroulée dans le but de limiter le nombre d'erreur lors de la phase critique de déroulement. Une attention toute particulière sur ce signal m'a permis de dérouler de façon continue la phase au travers ces zones à forts gradients interférométriques et d'isoler les zones stables non affectées par le pergélisol (chapitre 5). L'analyse des prédictions ERA-Intérim, comparée aux estimations empiriques, me conduit à extraire des incertitudes sur ces corrections. J'utilise ces erreurs pour pondérer les acquisitions dans l'obtention de la carte de vitesse (chapitre 4). Les interférogrammes à faibles lignes de bases temporelles et perpendiculaires, s'analysent ensuite en série temporelle. Cette étape conduit à dériver la série temporelle des déplacements, mais aussi à vérifier la fermeture du réseau interférométrique et permet in fine la détection de toute erreur de déroulement. Enfin, comme évoqué dans ce chapitre, je complète par l'étude du trade-off des rampes orbitales avec la carte de déformation.

Cette démarche, effectuée par tâtonnements se présente comme une succession de corrections influençant le résultat final. Elle peut ainsi naturellement attirer la méfiance et la confusion du lecteur. Cependant, contrairement aux précédentes études qui n'évoquent

quasiment pas ces difficultés somme toute majeures, les nombreux tests systématiques effectués permettent de pousser au maximum les limites de l'interférométrie radar et d'en extraire un protocole de traitement, et d'obtenir un résultat le plus rigoureux possible. Par conséquent, la carte de vitesse qui en résulte se présente comme l'unique résultat, à ma connaissance, déclinant une carte de vitesse intersismique continue sur une grande longueur d'onde, et cohérente sur quatre fauchées chevauchantes, dans une zone quasi inaccessible jusqu'alors par InSAR.

6.1 Introduction

The present-day tectonics in Asia results from the India-Eurasia collision, some 50 million years ago. Since the beginning of the collision, which continues at the present time at a speed of 4 cm/yr, more than 2,500 km of convergence between the Indian and Asian continents have been absorbed, resulting in the deformation of the whole Central and Eastern Asia ([Molnar et Tapponnier, 1975b](#); [Tapponnier et Molnar, 1977](#)). To accommodate such a large amount of shortening, an area of more than ten million square kilometers is mobilized, from the collision front to over 3000 km to the north and east. The high ranges of the Himalayas and the Tien Shan, culminating respectively over 8000 m and 6000 m, and the Tibetan plateau at an altitude of 5000 m on average, are the most spectacular features of the deformation related to the India-Asia collision. The collision zone is also characterized by the existence of major active faults, mostly thrust faults (as along the Himalayan, Longmen Shan and Qilian Shan fronts that bound the Tibetan plateau to the south, east and northeast, respectively, or in the Tien Shan farther north), and strike-slip faults (such as the Red River fault in southeastern Asia, the Karakorum fault in western Tibet, or the Altyn Tagh, Kunlun and Haiyuan faults in northern Tibet). These faults, some exceeding 1000 km-long, can produce devastating M~8 earthquakes, including strike-slip events (e.g. 1920 Haiyuan ([Deng et al., 1986](#)) and 2001 Kokoxili earthquakes ([Lasserre et al., 2005](#))) and thrust events (e.g. 1927 Gulang ([Gaudemer et al., 1995](#)) and 2008 Wenchuan earthquakes ([Shen et al., 2009](#))). However, their role in the accommodation of the deformation of the lithosphere is still controversial.

Estimates of slip velocity across these faults based on short-term (~ 10 yr) or quaternary (~ 2 Myr) averages are often inconsistent (Fig. 6.1). Geodetic measurements estimate 9 to 11 mm/yr across the Altyn Tagh Fault (ATF) ([Elliott et al., 2008](#); [He et al., 2013](#)), while neotectonic slip rate estimates range from 11.5 to 26 mm/yr ([Cowgill et al., 2009](#); [Mériaux et al., 2004, 2005](#)). This discrepancy has resulted in an active debate about

the role of crustal flow and the degree of strain localization throughout the lithosphere (Meyer *et al.*, 1998; England et Molnar, 1997a). The first class of models, based on geological observations, represent the deformation mostly localized on major lithospheric faults with both the Indian and Tarim lithospheric mantle subducting simultaneously under Tibet, re-activating old south and north-dipping suture zones (Peltzer et Tapponnier, 1988; Matte *et al.*, 1996; Tapponnier *et al.*, 2001). In these models, present-day deformation would be accommodated by crustal thickening along accretionary wedges decoupling crustal blocks and simultaneously extruding toward the East along major left-lateral strike-slip faults (e.g the Altyn Tagh, the Kunlun and the Haiyuan Faults) (Meyer *et al.*, 1998; Gaudemer *et al.*, 1995; Lasserre *et al.*, 1999, 2001). However, the low geodetic velocities observed on strike-slip faults in and around Tibet have conducted some authors to support a 'soft Tibet' model. In this second class of models the deformation of the Tibetan lithosphere is continuous and controlled by ductile flow, mostly driven by gravitational forces (England et Houseman, 1989; England et Molnar, 1997a,c). This view of the tectonics of Asia, neglects all observations of Quaternary faulting along major structures. (e.g., Mattauer, 1986; Tapponnier *et al.*, 2001). A third class of models involves a low viscosity layer ($< 10^{18}$ Pa/s) between the lower crust and the upper mantle (Royden *et al.*, 1997; Ryder *et al.*, 2007; Wen *et al.*, 2012; Huang *et al.*, 2014). This 'channel flow' would bring material participating to the growing of the flat topography, limiting the role of crustal thickening.

Slip rates on these faults, which are known to produce large earthquakes, are thus at the heart of the debate of how wide continents deform. For instance, a high slip rate on the ATF (Peltzer *et al.*, 1989; Mériaux *et al.*, 2004; Xu *et al.*, 2005; Mériaux *et al.*, 2005, 2012) would accommodate large parts of the India-Asia convergence, leaving negligible convergence within Tibet, and would transfer most of the convergence to the thrust and fold systems in the Qaidam basin and the Qilian Shan (Tapponnier *et al.*, 2001; Lasserre *et al.*, 2007; Jolivet *et al.*, 2008). In contrast, low rates on the ATF (Bendick *et al.*, 2000; Zhang *et al.*, 2004; Meade, 2007b; Wallace *et al.*, 2004; He *et al.*, 2013) would require a larger slip rate on some faults within the Tibetan plateau, a view, which led some authors to interpret the deformation as continuous throughout the collision zone (England et Houseman, 1989; England et Molnar, 1997a; Ge *et al.*, 2015).

Geodetic data provide unique information to characterize the present-day deformation of Tibet. Because of the difficulty of field access, GPS data from Tibet are mostly concentrated in the Eastern part of the plateau. Major faults such as the ATF, the Kunlun, and the Karakorum Jiali Fault Zone (KJFZ) fault systems are poorly sampled

by GPS data in the near field. Interferometric Synthetic Aperture Radar (InSAR) has a great potential because the technique can provide continuous maps of deformation throughout broad regions and therefore precisely constrain the interseismic loading and its lateral variations. However, because of the many data processing challenges, only a few studies attempted to measure interseismic deformation in the western part of Tibet ([Wright et al., 2004](#); [Peltzer et al., 2006](#); [Lasserre et al., 2007](#); [Elliott et al., 2008](#); [Wang et al., 2012](#); [Garthwaite et al., 2013](#)). Firstly, due to coherence loss in the sand dunes along the South of the Tarim, north of the ATF, and in the sedimentary basins of the plateau, south of the ATF, [Elliott et al. \(2008\)](#), restricted his study to near-field of the fault. The far-field signal is however critical to constrain accurately fault slip rates because of trade-off between strike-slip and converging components of movement. [Wang et al. \(2012\)](#) and [Garthwaite et al. \(2013\)](#) the first attempts to process long radar tracks across the Tibetan plateau. However, limited by the contribution of non-tectonic signals (atmosphere, permafrost...), they did not succeed at providing a continuous velocity map in various zones. For example, [Wang et al. \(2012\)](#) did not unwrap the phase across the ATF and studied separately the northern and the southern parts of the track. Secondly, as these authors were strongly limited by the trade-off between the deformation, residual orbital ramps, and atmospheric delays, they did not correct interferograms from the tropospheric signal and inverted simultaneously these various parameters together with the slip rates on faults, from their obtained velocity map. This mathematical operation results in high uncertainties on velocity gradients due to the strong trade-off in the inversion and the different parameter types. Moreover, not correcting interferograms from atmospheric delays leads to high uncertainties on the velocity gradient across the ATF (cf. chapter [4](#)).

In this study, we focus on the northwestern part of the Tibetan plateau between longitude 82.5° and 87° . We process 800 km-long interferograms from the Tarim Basin, north of the Altyn Tagh Fault, to the central part of Tibet (Fig. [6.1](#)). The area is bounded by two geometrical complexities. At the eastern part, the ATF fault branches off at depth with the Altun Shan to the North and the Qilian Shan to the South. The study area also integrates the western termination of the Kunlun Fault, which divides into two branches and broke during the 1997, M \sim 8 Manyi earthquake ([Peltzer et al., 1999](#); [Ryder et al., 2007](#)). The western part of the study area connects to the western Kunlun Shan Range, which represents one of the high mountain ranges of Central Asia with altitudes peaking at 6500-7500 m. At this place, a convergence movement between the Tarim block and Tibet is suggested by the quaternary deformation of the sediments along the southern

edge of the Tarim. Its foreland extends to the Mazar Tagh range along a décollement, that reaches up to the middle part of the Tarim basin over a width of about 500 km (Matte *et al.*, 1996; Wittlinger *et al.*, 1998; Coudroy *et al.*, 2009). Recent earthquakes, as the Mw 6.4, 2015 Pishan earthquake that broke a blind thrust north of the western Kunlun Shan, underline the strain accumulation along these deep thrusts system (Lu *et al.*, 2016; Sun *et al.*, 2016) that now need to be considered into kinematic models.

We identified two main processing challenging for systematic InSAR processing in this area. (1) South of the ATF the plateau is structured by narrow, E-W mountain ranges reaching elevations of \sim 6000 m, bounding quaternary sedimentary basins at an elevation of \sim 4400 m. These sedimentary basins contain permanent ice, called permafrost, with an active upper layer affected by the seasonal freeze-thaw cycle resulting in the upheaval and subsidence of the soil and other cryoturbations processes degrading the coherence of the radar signal (chapter 5). Moreover, (2) the elevation difference, between the Tarim Basin north of the Altyn Tagh Fault (ATF) (<1 km) and the mountain ranges across and south of the fault (~ 5 km), leads to a high sensitivity of interferograms to changes of atmospheric conditions between dates of image acquisitions. The differential tropospheric delay in interferograms reaches few centimeters per kilometer of elevation, and thus overprints any small deformations. Correcting this signal across the topographic edge of the plateau is thus one of the most important processing step to prevent unwrapping errors and to reach a precision of a few millimeters per year on ground displacement velocities. Here, thanks to a specific focus on the permafrost related deformation signal (chapter 5) and to a careful analysis of the atmospheric signal across the high plateau margin (chapter 4), we successfully unwrap interferograms from north to south, isolate bedrock pixels that are not affected by the permafrost signal and propagate estimated errors on atmospheric correction through the time series analysis to weight each acquisition in relation to its atmospheric uncertainty. We then use the redundancy of the overlapping tracks to re-estimate long-wavelength orbital ramps and thus successfully produce wide and continuous velocity maps covering the northwestern part of the Tibetan plateau.

6.2 InSAR processing

We process the complete Envisat archive data along four 800 km-long and 100 km-large Envisat overlapping tracks (162, 391, 119 and 348) acquired along descending orbits between 2003 and 2011 (Fig. 6.1). To obtain deformation time series in this natural

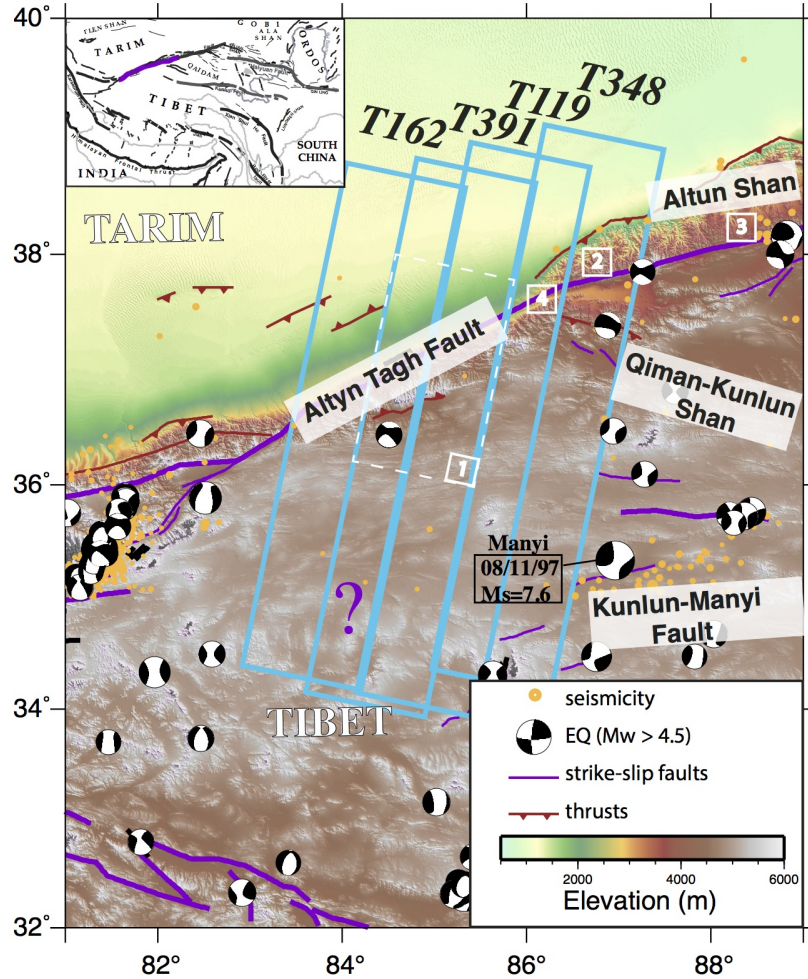


FIGURE 6.1 – Surface traces of four overlapping Envisat descending tracks 162, 391, 119 and 348 in cyan superimposed to Digital Elevation Model (Farr et Kobrick, 2000), moment tensor of earthquakes of magnitude > 4.5 (in Aki and Richards convention) and the seismicity from 1992 to 2014 form USGS (orange dots). Fault traces are from Replumaz et Tapponnier (2003) and from personal communications of Jerome Van der Woerd. Previous investigations of the ATF's slip rate include (1) InSAR velocity map from ERS data of Elliott et al. (2008) (11 ± 10 mm/yr), geological measurements ($10^4 - 10^5$ yrs) from Cowgill et al. (2009) (11.5 ± 2.5 mm/yr) (2) and Mériaux et al. (2004) (26 ± 6 mm/yr) (3), and a GPS velocity profile from He et al. (2013) (9 ± 4 mm/yr) (4).

environment and limit the phase decorrelation effects, we process 484 differential interferograms with the New Small Baselines Subset chain (NSBAS) (Doin et al., 2011, 2015) based on the ROI_PAC software (Rosen et al., 2004). We define an optimal small baseline interferometric network connecting with redundancy all acquisitions either with large B_{perp} and low B_t or low B_{perp} and large B_t (Fig. 5.5).

To prevent propagating errors from the large baselines interferogram, the processing is based on a series of corrections before unwrapping that reduce the variance of the wrapped phase (chapter 2). Those include atmospheric corrections on the wrapped interferograms using a global atmospheric re-analysis model ERA-Interim from ECMWF (Doin *et al.*, 2009; Dee *et al.*, 2011; Jolivet *et al.*, 2011) (chapter 4), a uniform linear ramp correction in range to remove the residual orbital errors and the clock drift (Fattahai et Amelung, 2014b; Zhang *et al.*, 2014), and a correction of the effect of local Digital Elevation Model (DEM) errors before unwrapping (Ducret *et al.*, 2014). Furthermore, as described in Chapter 5, to prevent from unwrapping errors within the plateau due to the freeze and thaw cycles of the sediments, we decrease the fringe rate before unwrapping using a spatial template for seasonal deformation, extracted from a Principal Component Analysis (PCA). We successfully unwrap interferograms from north to south and mask areas with a seasonal movement larger than >2.5 mm/yr, in order to isolate bedrock pixels that are not affected by the permafrost signal.

We also test different phase filters to help the unwrapping across the alluvial fans and sand dunes, north of the ATF. We observe an improvement of the unwrapping capability using two successive filters (Fig. 6.2) weighted by the average temporal coherence extracted from the DEM correction (Fig. 6.2d). We first replace the coherence of the interferograms by the colinearity as defined by Pinel-Puyssegur *et al.* (2012). Following López-Quiroz *et al.* (2009), we then unwrap a smooth phase obtained with a strong low-pass filter (Fig. 6.2b) in order to help connecting areas separated by decorrelated zones. The unwrapping path goes from the high to the low coherence areas defined by the filter. We then compute the complex phase difference between the smooth set of interferogram and a second set, less-filtered interferograms (Fig. 6.2c). The residual high frequency signal is assumed to be between $-\pi$ and π and added to the previous unwrapped phase. We observe an improvement of the unwrapping capability across the alluvial fans and a reduction of unwrapping errors (Fig. 6.2e).

We then estimate an azimuthal ramp for each unwrapped interferograms. Depending on the footprint of both acquisitions used to compute interferogram, the ramp is thus estimated with a linear or a quadratic term and is valid within the footprint extension. The inversion into time series of these ramps to obtain a ramp per acquisition is thus slightly unusual and implies extrapolation outside the valid interval with a decreasing weight (Doin *et al.*, 2015). At the end, all the ramps present a small quadratic coefficient.

We then analyse the time series the set of deramped unwrapped interferograms (López-Quiroz *et al.*, 2009; Doin *et al.*, 2011, 2015) and check the consistency of each

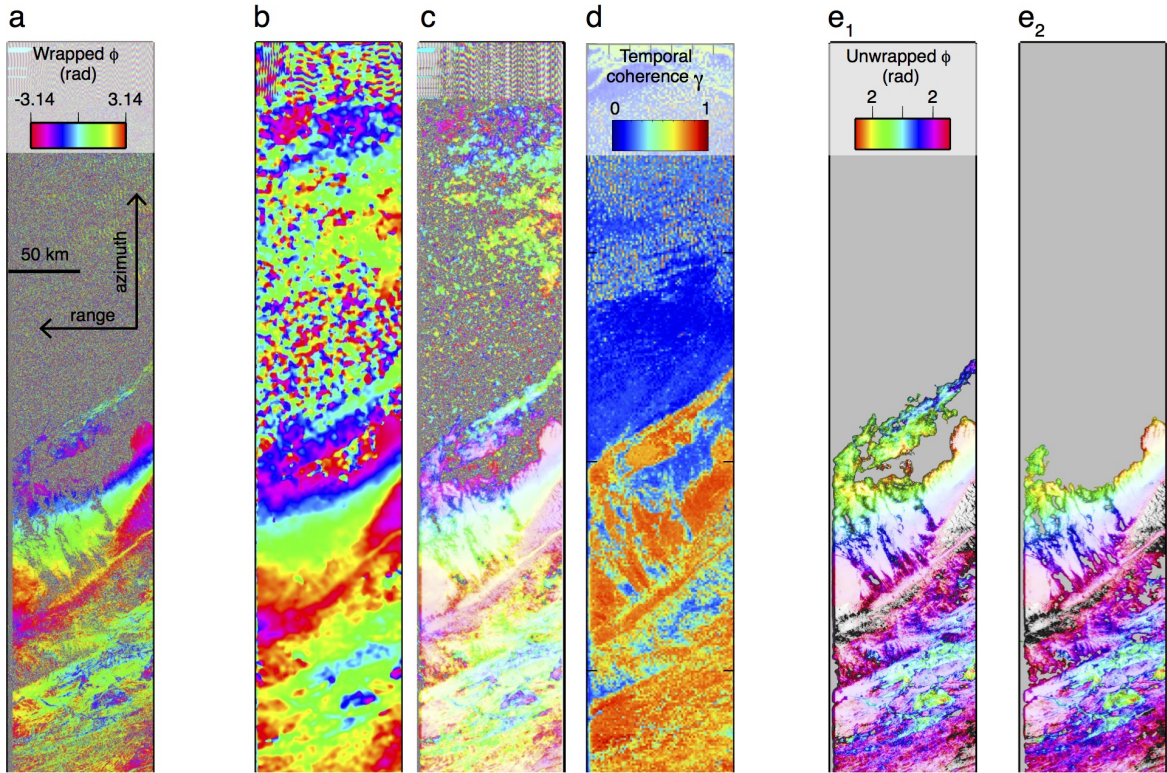


FIGURE 6.2 – Example of an unwrapping procedure accros the dunes. a : Multi-looked interferograms formed with the two images taken on Nov. 17, 2004 and on April 30, 2008. b, c : low pass filters weighted by the average temporal coherence, γ , extracted from the DEM correction (d). e : Two unwrapped interferograms obtained with an unwrapping path depending on phase colinearity as defined by Pinel-Puyssegur *et al.* (2012) (e₁) or on interferogram coherence (e₂).

interferogram within the network. The misclosure of the interferometric network is computed for each interferogram. If large, we visually check the corresponding interferogram. We observe some long interferograms with high discrepancies for pixels located at a distance larger than $\sim 150\text{ km}$ from the ATF to the north. We thus decide to apply a mask on this northern part of the interferograms. The maximal RMS of final network inconsistencies at the end of this procedure is lower than $\sim 0.7\text{ rad}$ for all interferograms.

Incremental phase delay of each date relative to the preceding date is solved by a least square method. We observe on some tracks (mostly tracks 119 and 348), residual ramps in range that form a continuous quadratic term homogeneously from north to south of the track. These residual ramps in azimuth may come from residual clock drift. To finally extract the ground velocity displacement, we thus refer each map, i , to the stable bedrock (defined by the permafrost map) and remove on this bedrock a quadratic

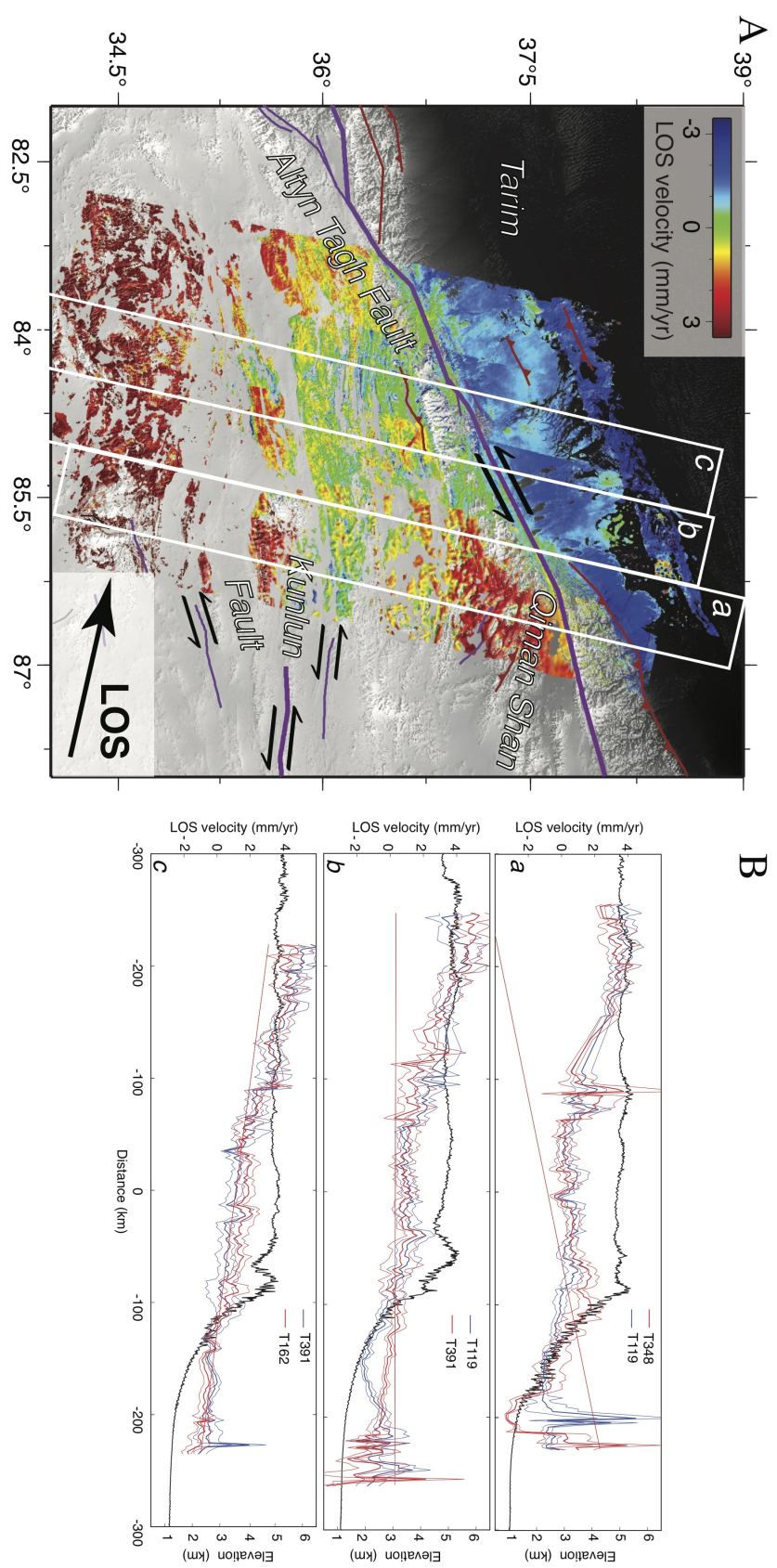


FIGURE 6.3 – Line Of Sight velocity maps for four tracks 348, 119, 391 and 162 (A) with three profiles in the overlapping areas of the four tracks (B). Red continuous lines correspond to estimated linear ramps minimizing the differences between the tracks. Positive motion is toward the satellite. Faults traces as Fig. 6.1.

ramp in range per acquisition. Note that this ramp correction is not a problem as it is uniform on all the track. We then derive a linear term, V , and a DEM error coefficient, α , by expressing the radar phase as :

$$\phi^i = Vt_i + \alpha B_{\perp}^i. \quad (6.1)$$

Equation 6.1 is weighted by the proxy for ERA-I correction uncertainty obtained for each image, i , from the previous atmospheric analysis (chapter 4). We first flatten the velocity map of track 119 by a linear gradient in azimuth on the bedrock pixels located south of the ATF and north of the Kunlun faults prolongation (Fig. 6.1). We then take track 119 as a reference and apply linear ramp corrections in sequence on the overlapping areas of the four successive tracks.

The resulting velocity map and along-track profiles within the overlapping areas (Fig. 6.3) show the overall movement of Tibet (red-green tones toward the satellite), with respect to the Tarim block (blue tones away from the satellite), with a strong gradient along the edge of the plateau between the ATF and the distal part of the alluvial fans. Active deformation is visible on the eastern part of the map near latitude 36°N. It is important to note that many areas on the Tibetan side have been marked based on the large seasonal signal associated with the active layer in the permafrost. In addition, the part of the track covered by track 348 is less reliable because only 24 acquisitions were available for this track and several of them were shorter than the N-S extend of the map.

Besides these caveats, the map shows for the first time the continuous deformation field across a 400 km-long section of the ATF, uncovered by GPS data.

6.2.1 Tests on atmospheric corrections

In the previous atmospheric analysis (chapter 4), initial analysis of the daily predictions between two points within the Tarim basin and the Tibetan plateau, has revealed some abrupt gradients and strong patterns within the Tarim basin at the foot of the topographic feature (Figs. 4.9b, 6.4b). In order to verify whether some artefact could come out of the lateral interpolation of ERA-I data between grid points at low (Tarim) and high (Tibet) elevation (red line in Fig. 4.3), we perform a test with an other set of data corrected with an ERA-I prediction derived from only one ERA-I point encompassing the radar scene and located within the Tarim basin (Doin *et al.*, 2009) (Figs.

4.9c, 6.4c). The resulting velocity map and along-track profiles are shown in (Fig. 6.5). The map show the same features, north of the ATF, indicating that they did not result from the interpolation in the atmospheric correction. Besides, minor differences between (Fig. 6.3) and (Fig. 6.5), the two maps are in good agreement.

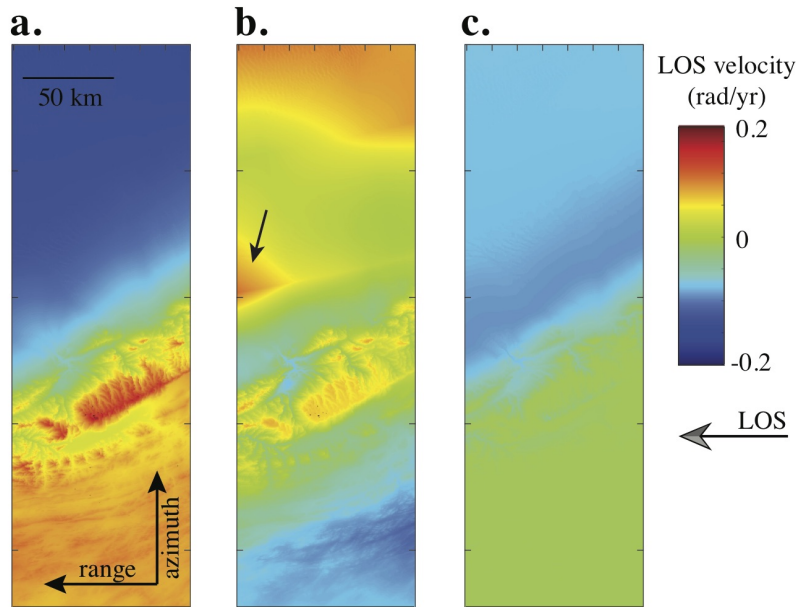


FIGURE 6.4 – Comparison of the three atmospheric stack corrections for track 391 derived from empirical estimations (Doin *et al.*, 2015) (a), ERA-I models with lateral variability (Jolivet *et al.*, 2011) (b), and ERA-I models with only one point located in the Tarim basin (Doin *et al.*, 2009) (c). The three velocity gradients are obtained by weighting each images with their respective uncertainties derived from the atmospheric analysis (chapter 4) and show some artefact signal at the foot of the topographic feature (black arrow) for the ERA-I correction with lateral variability (b).

6.2.2 Tests on residual orbital ramps

To remove the second order discrepancies between the tracks that could arise from residual ramp in azimuth at long-wavelength, we finally estimate a quadratic ramp in azimuth, which minimizes the differences between the overlapping areas between adjacent tracks. We plot the resulting map, the three 600 km-long and 50 km profiles, as well as the estimated azimuthal ramps in the Fig. 6.6. Note that the quadratic ramps have a rather small curvature across the ATF, making the ramp correction linear for a distance smaller than 150 km, thus a distance higher than the wavelength of the tectonic deformation. In

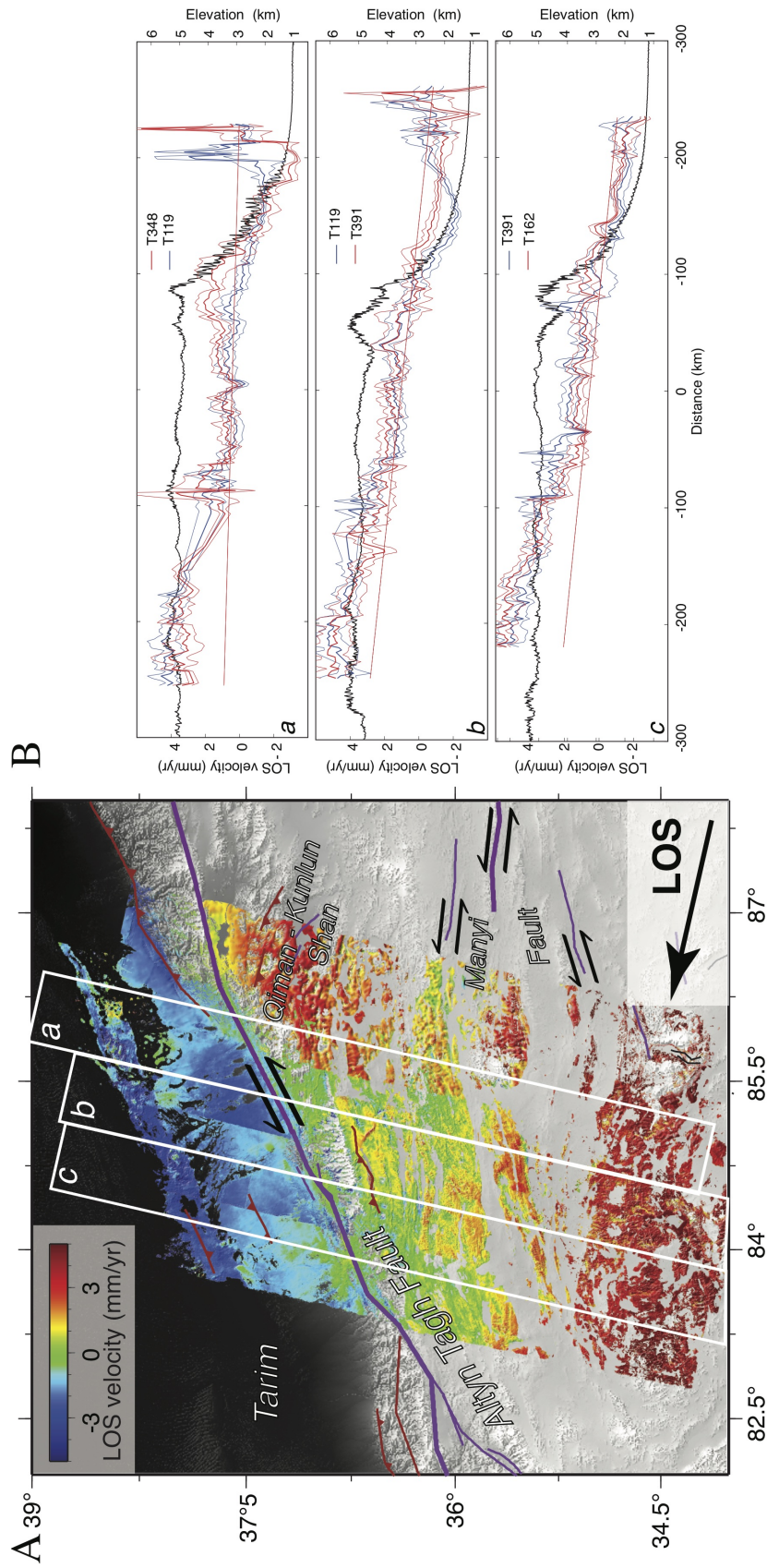


FIGURE 6.5 – Line Of Sight velocity maps for four tracks 348, 119, 391 and 162 obtained with only one ERA-I point in the Tarim Basin (A) with three profiles in the overlapping areas of the four tracks (B). Positive motion is toward the satellite. Faults traces as Fig. 6.1.

addition, as the data are projected in the azimuthal direction of the tracks, we minimize the trade-offs between the deformation and the long-wavelength ramps. We are thus quite confident that this last operation does not remove or add any tectonic signal.

This operation slightly improves the consistency in the overlapping areas and reveals a smooth velocity field on both the Tibetan and the Tarim sides (Fig. 6.6).

6.3 Analysis of the tectonic signal

6.3.1 GPS data

We first compare our velocity map with GPS data provided by [He et al. \(2013\)](#), which includes 17 campaign stations measured 2-3 times between 2009 and 2011, as well as the regional data set around the Tibetan Plateau provided by [Liang et al. \(2013\)](#), which includes 750 continuous and campaign stations (cf. Chapter 2). In Fig. 6.7, we superimpose the stations locations to the amplitude of the ground seasonal deformation derived in Chapter 5. We observe that some stations are located within sedimentary basins that undergo strong seasonal deformation (e.g. AT05, AT10, AT11, J343, J344) or are located very close to the fault system. [He et al. \(2013\)](#) referred the GPS stations to the Tarim block by minimizing only three velocities of the sites AT12, AT13 and AT16 (Fig. 6.7). Note that the stations AT13 is very close to the ATF while stations AT12 and AT16 are from either side of the observed gradient of deformation of our InSAR velocity field in the Tarim Basin (Fig. 6.6). Note also that stations AT08, AT10, AT09 and AT11 are located at the terminaison of the Kunlun-Manyi fault, which experienced the 1997, M~8 Manyi earthquake and presents active seismicity (Fig. 6.1), while stations AT01, AT02, AT03 and AT03A are within the Qiman Shan thrust system.

In order to compare the GPS field of [Liang et al. \(2013\)](#) with the GPS solution of [He et al. \(2013\)](#), we rotate the ITRF solution of [Liang et al. \(2013\)](#) with respect to the Tarim block, north of the ATF. We select stations I033, I398, I064, XJTZ, I065, I066 and I065 located in the Tarim Basin and far from the Altyn Tagh fault system. Following the method described in Chapter 2, we invert for an Euler pole by minimizing the L1 norm of this subset of stations and apply the rotation to all GPS stations (Fig. 6.8). To better visualize the gradient across the Altyn Tagh fault system, we also decompose in the Table 6.1 the horizontal velocity field of the two networks into the ATF-parallel and ALT-perpendicular components. Both networks from [Liang et al. \(2013\)](#) and [He et al.](#)

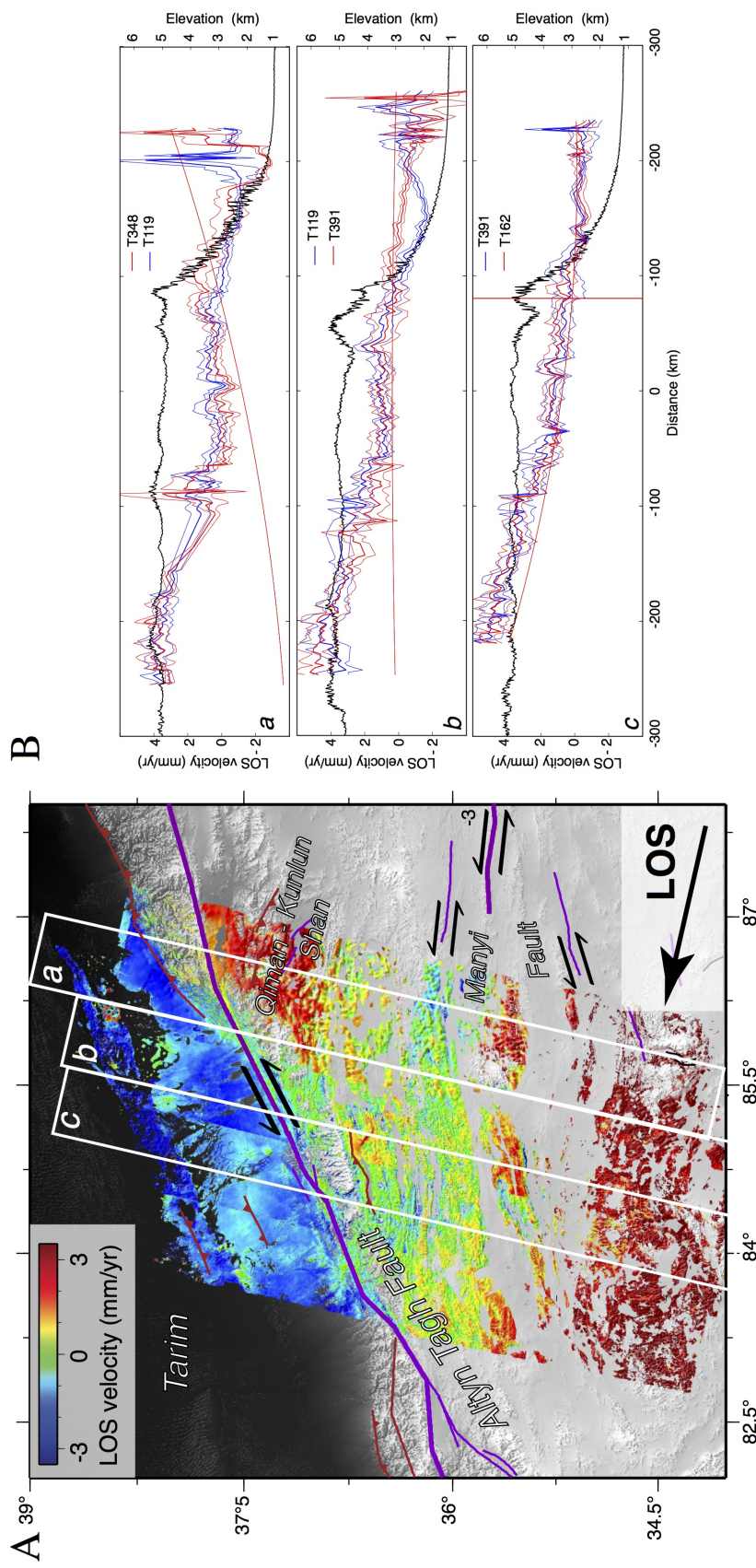


FIGURE 6.6 – As Fig. 6.3 but with a quadratic ramp in azimuth that minimizes the differences between the overlapping areas between adjacent tracks.

(2013) of Fig. 6.8B are thus referred to the Tarim block and indicate relatively consistent velocity vectors (Fig. 6.7, Table 6.1).

The velocity gradient from He *et al.* (2013) shows a left-lateral far-field motion of ~ 11 mm/yr centered on the ATF and ~ 2 mm/yr of convergence between station AT16 and AT09. Surprisingly, GPS vectors indicate some divergence between GPS station in the Tarim AT13, AT12, AT16 and stations south of the ATF : AT14, AT15, AT01, AT02, AT03, AT03A and AT04. These stations might thus be influenced by a left-lateral or a thrust movement of the Qiman-Kunlun Shan. At the terminaison of the northern branch of the Kunlun Fault the signal is unclear and does not indicate clear strike-slip or shortening gradient. However, at least AT05 and AT11 stations are located in the basin with strong seasonal deformation (Fig. 6.7). Within the Tarim basin, we observe a small strike-slip component between the two stations AT12 and AT16, but a right lateral movement between stations AT13 and AT16.

GPS stations I035, XJRQ, I400, I398, and I033 from Liang *et al.* (2013) clearly show the shortening north of the Altun Shan. Surprisingly, relative velocities between stations I064 and XJTZ and stations JB46 and XJQM indicate a right lateral motion of ~ 2 mm/yr and a shortening motion of about 1 mm/yr, while differential velocities between station I412 and stations I064 and XJTZ shows a strike-slip and shortening components of 0.7 mm/yr and 1.5 mm/yr, respectively. The only far-field stations in the Tibetan plateau (J343 and J344) do not present consistent velocity gradients and might strongly be influenced by the seasonal deformation of the permafrost active layer (Fig. 6.7).

6.3.2 InSAR velocity field

The LOS velocity maps provide a continuous view of the surface displacement field over a broad ($400\text{ km} \times 400\text{ km}$) area, along and west of the GPS transect of He *et al.* (2013) and underlines four velocity gradients (Fig. 6.9).

(1) The strain pattern across the ATF shows an offset of $\sim 1.5 - 2$ mm/yr of relative movement between the two sides projected in the line of sight of the Envisat satellite (Fig. 6.9B). This direction of shear is consistent with a left-lateral movement on the ATF.

(2) As previously mentioned, our data reveal a linear offset consistent on all the tracks, at the base of the alluvial fans along the northern piedmont of the Altyn Shan,

TABLE 6.1 – GPS velocity field from [Liang *et al.* \(2013\)](#) and [He *et al.* \(2013\)](#) around our study area after referencing to the Tarim block and sorted by their fault-perpendicular distances to the ATF. Horizontal vectors are projected into the N66°E ATF-parallel (U_{par}) and ATF-perpendicular (U_{perp}) components to better visualize relative far-field shearing and shortening across the profile.

| Station name | distance (km) | U_{perp} (mm/yr) | U_{par} (mm/yr) |
|--------------|---------------|---------------------------|--------------------------|
| AT11 | -220.911 | 3.298 | -5.967 |
| AT09 | -192.194 | 2.265 | -11.287 |
| AT10 | -163.903 | 1.990 | -11.340 |
| AT08 | -148.806 | 1.990 | -11.340 |
| AT07 | -113.102 | 1.609 | -8.926 |
| AT05 | -100.736 | -0.248 | -3.951 |
| AT04 | -56.459 | -0.926 | -8.104 |
| AT03 | -36.872 | -2.695 | -10.699 |
| AT03A | -34.073 | -2.695 | -10.699 |
| AT02 | -24.226 | -1.582 | -7.659 |
| AT01 | -18.384 | -0.946 | -5.862 |
| AT15 | 6.046 | -1.002 | -2.914 |
| AT14 | 10.313 | -0.989 | -2.614 |
| AT13 | 22.189 | 0.079 | 0.326 |
| AT12 | 54.782 | -0.128 | -1.246 |
| AT16 | 113.569 | 0.000 | 0.000 |
| J344 | -189.451 | 8.820 | -8.119 |
| J343 | -155.694 | 0.749 | -5.719 |
| I415 | 17.345 | 2.408 | -3.688 |
| I412 | 22.690 | 0.704 | -1.517 |
| I069 | 43.433 | 3.815 | 2.176 |
| I035 | 71.036 | -0.547 | 1.010 |
| JB46 | 79.741 | -0.779 | 1.595 |
| I034 | 81.083 | -2.671 | 0.368 |
| XJRQ | 81.425 | -2.671 | 0.368 |
| XJQM | 84.136 | -0.788 | 1.599 |
| I067 | 85.809 | 3.163 | 3.047 |
| I066 | 96.009 | 1.112 | 0.950 |
| I065 | 188.026 | 1.016 | 1.496 |
| XJTZ | 239.505 | 0.009 | -0.004 |
| I064 | 246.401 | 0.000 | 0.000 |

trending parallel to the Altyn Tagh Fault trace (Fig. 6.9, Fig. 6.10). Such a signal is in agreement with either a left lateral or south-side up movement. As this signal follows the oasis located at the base of the fans that form a small topographic step, we have to rule

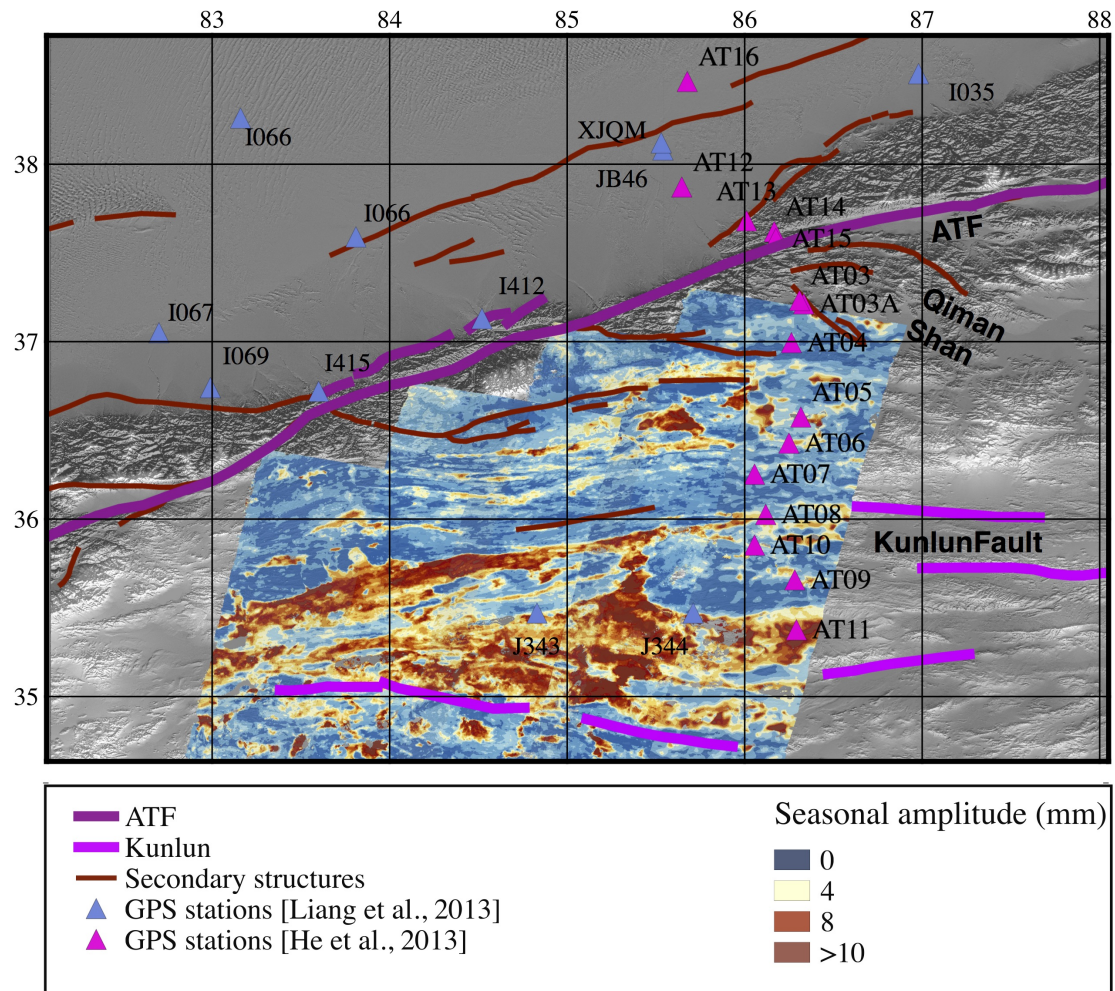


FIGURE 6.7 – GPS stations from [He et al. \(2013\)](#) (pink triangles) and from [Liang et al. \(2013\)](#) (blue triangles) superimposed to the amplitude of the seasonal deformation derived in Chapter 5. Fault traces derived from Fig. 6.1 and our InSAR velocity map.

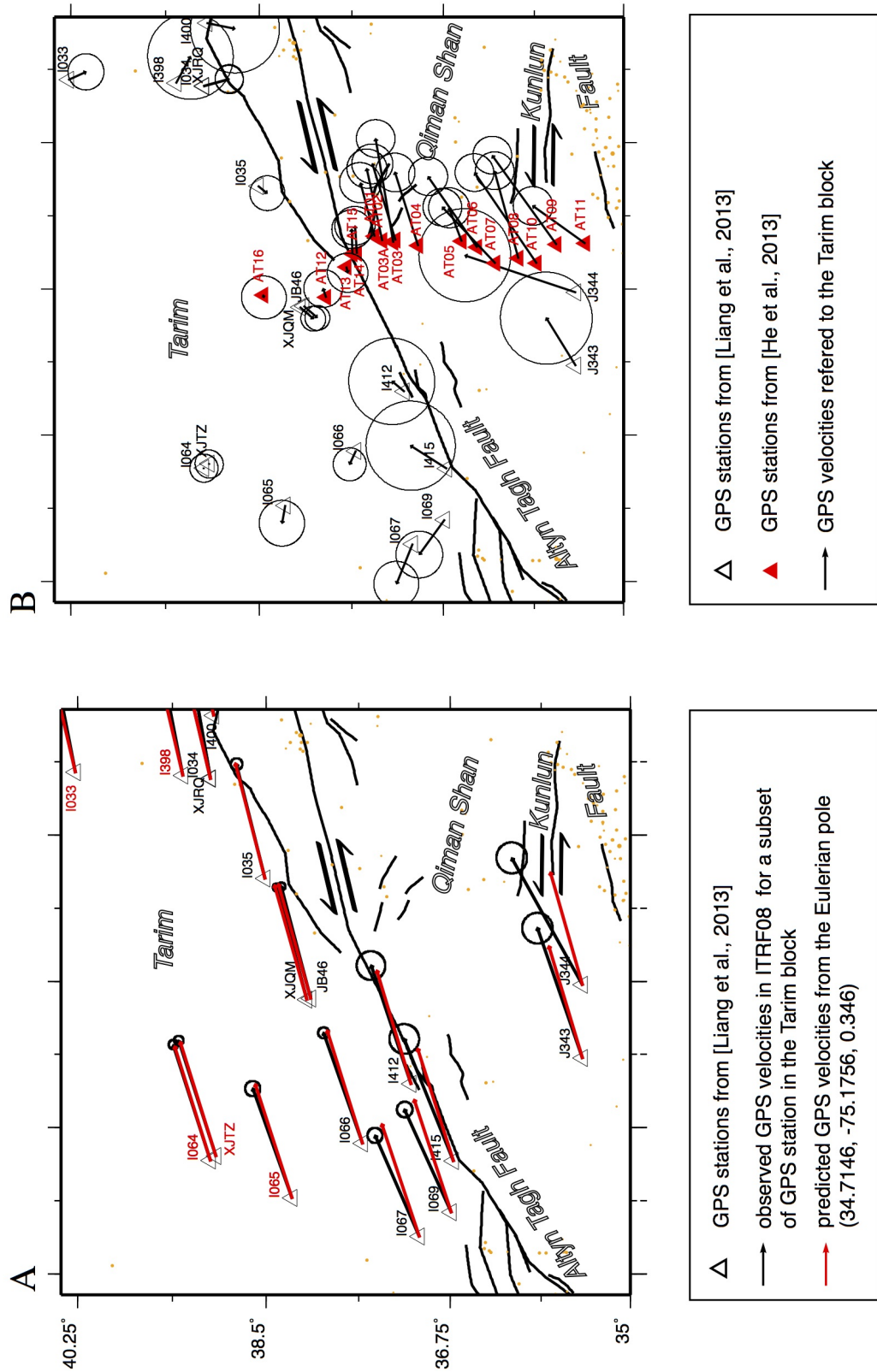


FIGURE 6.8 – GPS referencing to the Tarim block. (A) Subset of 7 reference stations (in red) used to define a reference frame within the Tarim block. (B) Residual velocities between the observations and the predictions from [Liang et al. \(2013\)](#) network (black triangles) superimposed with the GPS solution of [He et al. \(2013\)](#) (red triangles).

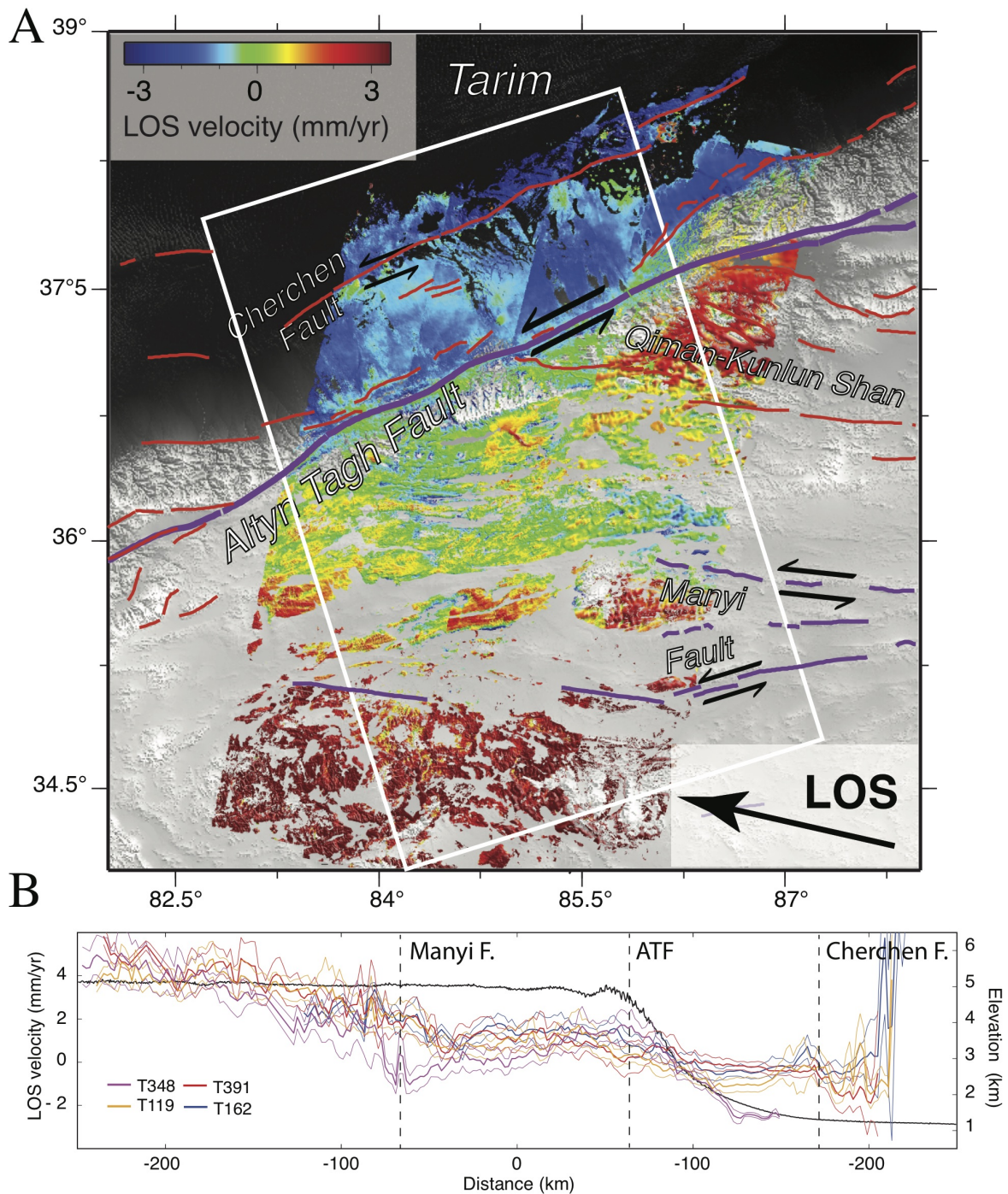


FIGURE 6.9 – A : Line Of Sight velocity maps of the four tracks 348, 119, 391 and 162 after a quadratic ramp correction with interpreted fault traces from the observed signal. Positive motion is toward the satellite. B : ATF-perpendicular profile encompassing the four tracks and underlying the four velocity gradients associated from the South to the North to the Manyi, the Kunlun, the Altyn Tagh and the Cherchen Faults.

out possible contribution from deformation associated with a hydrologic process in the soil of the oasis. To characterize the temporal behavior of this signal, we performed a PCA decomposition from the time series of images of tracks 391 (Fig. 6.10). We observe that the deformation in the Tarim (Fig. 6.10B1) pops-up in the linear component of the PCA (Fig. 6.10B2). This PCA thus confirms that the deformation along the Tarim structure is not seasonal and probably not related to the hydrology of the oasis soil. Note that the first component looks like a DEM error with discontinuities associated to the different sizes of the images, while the second component contains the residual atmospheric signal.

If the deformation observed at the base of the fans has a tectonic origin (probably associated to the Chechen Fault (Fig. 6.9)), the velocity gradient indicates either a left-lateral shear or the uplift of the southern block on a south-dipping fault, or a combination of both. Active convergence across this section of the ATF system is suggested by a system of NE striking, north dipping thrust faults cutting across a 50 km-wide alluvial fan centered at N37.4, E84.4 (Fig. 6.10A, Fig. 6.11). The ASTER visible and mid-infrared band combination image highlights the older terraces of the fan uplifted with respect to the active channels along two fault lines and topography profile indicates an uplift of up to 15 m of the northern compartment against the faults (Fig. 6.11A). Finally, the velocity map shows a differential movement of up to 1 mm/yr across the faults (Fig. 6.11B), consistent with the north side up movement. These findings show that the thrust faults are currently being elastically loaded as a result of a small amount of convergence between Tibet and the Tarim block. A convergence movement between the Tarim block and Tibet is also suggested by the quaternary deformation of the sediments along the southern edge of the Tarim (Fig. 1.16). In addition, the Mw 6.4, 2015 Pishan earthquake, which broke a blind thrust north of the Western Kunlun Shan (Lu *et al.*, 2016; Sun *et al.*, 2016) also indicates a compressional axis in a direction perpendicular to the ATF. These thrusts may connect to the Mazar Tagh, further North, contributing to the uplift the southern part of the Western Kunlun Shan (Fig. 6.9) and may branch at depth along a décollement at the root of the ATF into the single Kunlun lithospheric boundary (Matte *et al.*, 1996; Wittlinger *et al.*, 1998) (Fig. 1.14, Fig. 1.15).

(3) We also observe 50 km South of the ATF, mostly on tracks 119 and 348, a velocity gradient toward the satellite, probably associated to thrust faults along the Qiman-Kunlun Shan that may branch with the deep part of the ATF from the south forming a typical flower structure (Fig. 6.9). This signal is consistent with the differential shortening GPS velocity gradient previously observed between stations AT13, AT12, AT16 and

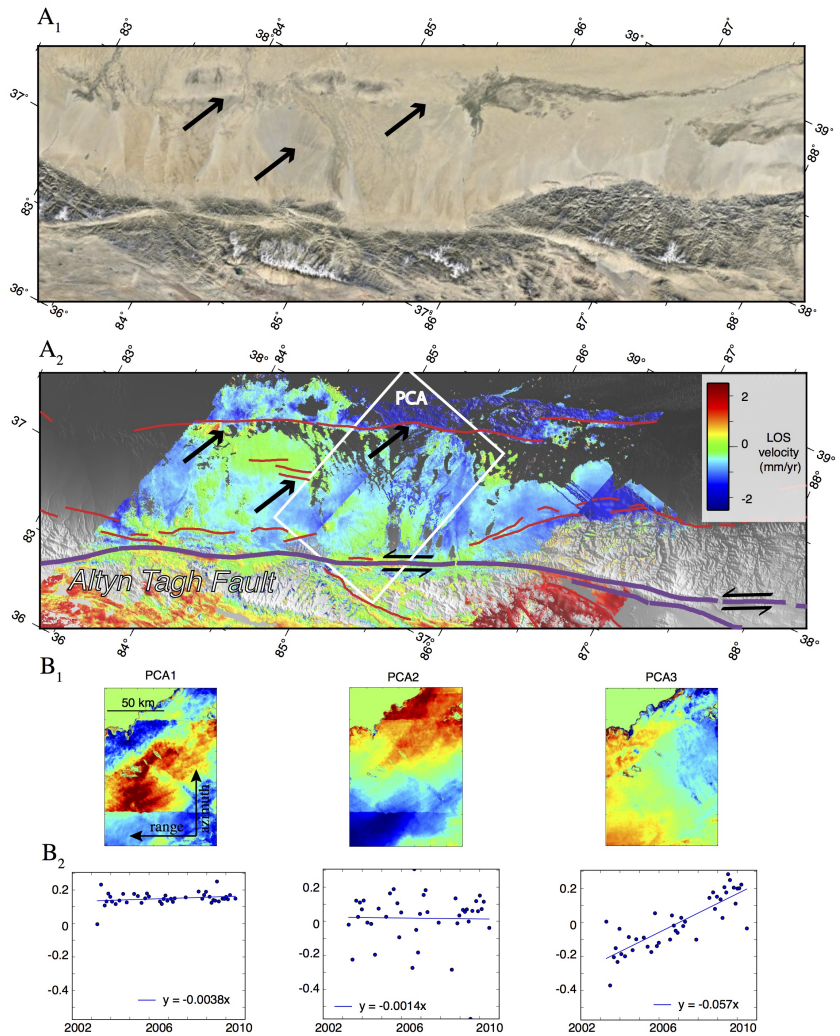


FIGURE 6.10 – A : Zoom around the Tarim basin from a google earth image (A1) and Fig. 6.6 (A2). White boxe indicates the areas where we compute the PCA from images of the track 391 while the arrows point out active deformation markers in the Tarim. B1 : Spacial eigenvectors associated to three first components of the PCA. B2 : Temporal eigenvectors of the three first components. The tectonic signal pop-ups in the third component of the PCA.

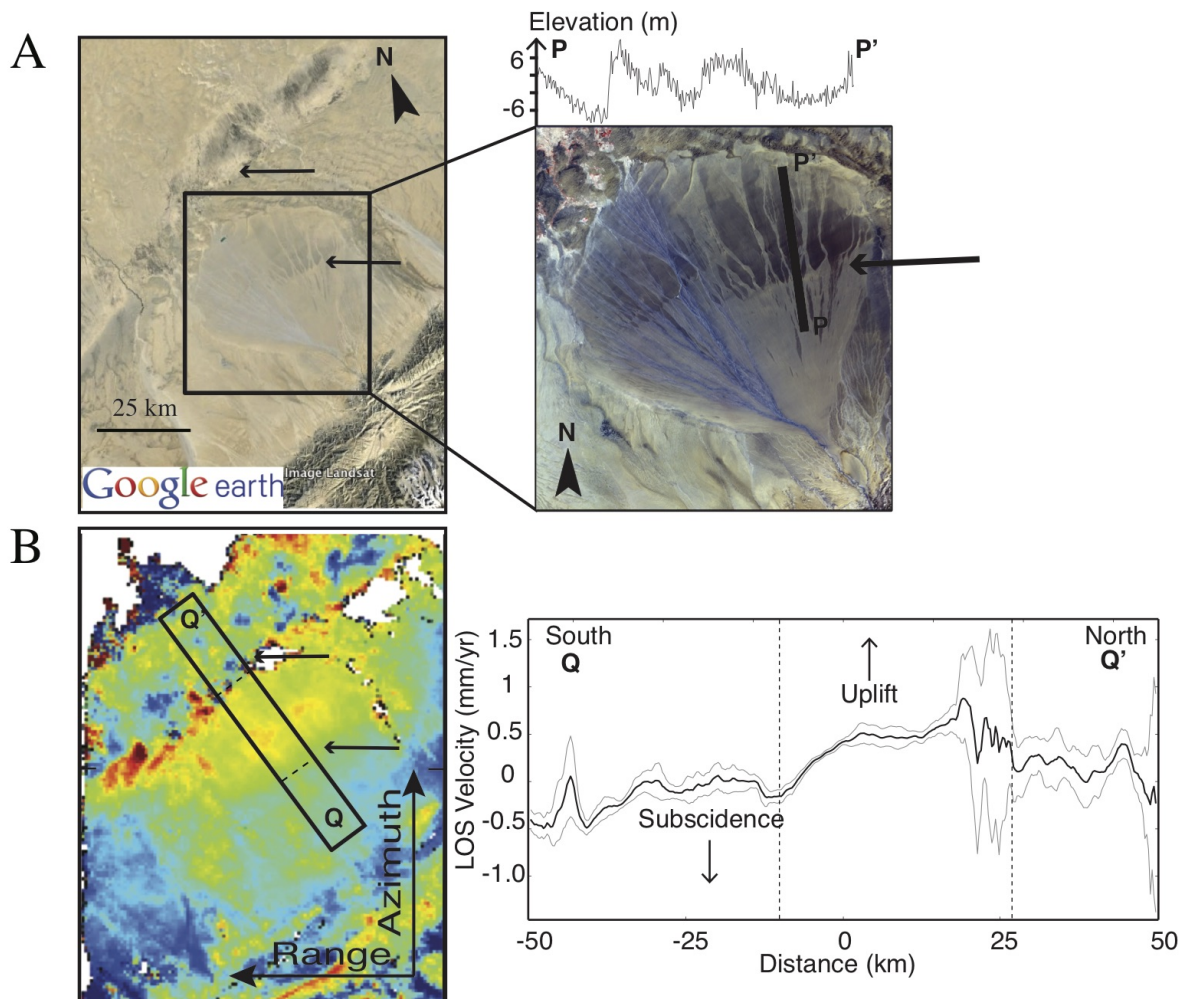


FIGURE 6.11 – A : Zoom around north dipping thrust faults cutting an alluvial fan in the Tarim Basin from a google earth image and an ASTER image. PP' is a topographic profile (DEM SRTM ([Farr et Kobrick, 2000](#))). B : Comparison with the velocity map obtained from track 162 with associated profile.

stations south of the ATF : AT14, AT15, AT01, AT02, AT03, AT03A and AT04.

(4) Finally, the velocity maps indicate a ~ 3 mm/yr velocity step at the south-western termination of the Manyi/Kunlun fault system, ~ 150 km-south of the ATF on the Eastern part and ~ 100 km south of the ATF on the Western part (Fig. 6.9). This signal is also consistent with left-lateral motion or south-side up movement. It might also be associated with some post-seismic deformation subsequent to the 2001, M 7.9 Kokoxili ([Lasserre et al., 2005](#)) or the 1997, M 7.6 Manyi earthquake ([Peltzer et al., 1999](#)) on this fault (Fig. 6.1). The southern branch might follows the Jinsha suture connecting to the Gozha fault father west while the northern branch of the fault might follows the Kunlun suture, connecting to the Karakax (Fig. 1.11). Because the Manyi/Kunlun fault is oriented parallel to the LOS trend ($\sim N90^\circ$ azimuth), the signal appears stronger than the signal associated to the ATF in map view. In the absence of any field measurements or additional data in this remote area, it is however difficult to conclude about the nature of the signal.

6.3.3 2D model

In order to constrain the loading rate of the Altyn Tagh Fault system, we consider a 200 km-large and 400 km-long profile across the central segment of the ATF that encompass the two GPS networks and the three velocity maps T119, T391, and T162. The model includes a vertical dislocation modeling the ATF, as well as a ramp structure modeling the rigid block located between the Cherchen and the Altyn Tagh Fault, which accommodates the far-field shortening. We allow for two half-infinite strike-slip dislocations on the two structures (SS_{ATF} , SS_{ramp}), such that the deep-seated strike-slip motion below the ATF locking depth that controls the far-field motion is equal to the sum of strike-slip rates on the two dislocations, $SS_{\text{SAF}} + SS_{\text{PH}}$. We also invert for a shortening component across the fault system (V_{short}), while we assume that the dip-slip motion on the creeping ramp is equal to the projection of the shortening rate (cf. chapter 2 for more details on the model). We also estimate the depth of the two dislocations, H_{ATF} and H_{ramp} , as well as the horizontal distance to the ATF and the tip of the ramp, D_{ramp} . We define for all parameters a uniform prior distribution. For instance, the prior probability for no convergence across the system is the same than an a-priori convergence of 1 mm/yr.

Following chapters 2 and 3, we explore the range of models allowed by geodetic data and derive the posterior probability describing the full ensemble of possible models,

TABLE 6.2 – Summary of the prior and posterior probabilities for a model with GPS data only, or with InSAR data only, or with both InSAR and GPS data. \mathcal{U} defines uniform distribution. SS_{ATF} : strike-slip rate along the Altyn Tagh semi-infinite dislocation ; SS_{ramp} : strike-slip rate along the creeping ramp ; H_{ATF} : depth of the tip of the ATF dislocation ; D_{ramp} : horizontal distances between the tip of the ATF dislocation and the tip of the ramp ; H_{ramp} : locking depth of the ramp ; V_{short} : shortening rate between Tarim and Tibet

| variables | prior | post. GPS | post. InSAR | post. GPS+InSAR |
|----------------------------|------------------------|--------------------------|--------------------------|--------------------------|
| SS_{ATF} | $\mathcal{U}(0, 20)$ | $\mathcal{N}(9, 2.)$ | $\mathcal{N}(10.6, 1.5)$ | $\mathcal{N}(10.2, 1.4)$ |
| H_{ATF} (km) | $\mathcal{U}(0, 30)$ | $\mathcal{N}(21, 6.5)$ | $\mathcal{N}(26, 3.5)$ | $\mathcal{N}(25, 3.5)$ |
| SS_{ramp} (mm/yr) | $\mathcal{U}(0, 10)$ | $\mathcal{N}(2.8, 1.8)$ | $\mathcal{N}(3.5, 0.6)$ | $\mathcal{N}(3.6, 0.6)$ |
| D_{ramp} (km) | $\mathcal{U}(40, 120)$ | $\mathcal{N}(71, 22)$ | $\mathcal{N}(80, 1)$ | $\mathcal{N}(80, 1)$ |
| H_{ramp} (km) | $\mathcal{U}(0, 30)$ | $\mathcal{N}(12, 7)$ | $\mathcal{N}(10, 2)$ | $\mathcal{N}(10, 2.5)$ |
| V_{short} (mm/yr) | $\mathcal{U}(0, 5)$ | $\mathcal{N}(-2.8, 1.3)$ | $\mathcal{N}(-3.3, 0.3)$ | $\mathcal{N}(-3.4, 0.3)$ |

$p(\mathbf{m}|\mathbf{d})$, that explain the observations, \mathbf{d} , and agree with a prior boundaries, $p(\mathbf{m})$, with a Bayesian approach ([Minson et al., 2013](#); [Jolivet et al., 2015a](#); [Lin et al., 2015](#)), such as

$$p(\mathbf{m}|\mathbf{d}) \propto p(\mathbf{m}) \exp \left[-\frac{1}{2} (\mathbf{d} - \mathbf{g}(\mathbf{m}))^T \mathbf{C}_D^{-1} (\mathbf{d} - \mathbf{g}(\mathbf{m})) \right], \quad (6.2)$$

where \mathbf{d} is the data vector, \mathbf{m} is the vector of model parameters, \mathbf{C}_D is the covariance matrix of the data, and $\mathbf{g}(\mathbf{m})$ is the surface displacements predicted from model \mathbf{m} . The model parameters include the ones previously described for geometry and slip rates and the InSAR and GPS reference frames. We add an unknown azimuth linear trend to InSAR data that ties far-field LOS velocities to GPS data.

We compare three models inverting various data set. In the first model, the data vector is made of only GPS vectors from [He et al. \(2013\)](#) and [Liang et al. \(2013\)](#) encompassing the profile. In the second model, the data vector is made of the three LOS velocities corrected from the quadratic ramp, while the third model includes both GPS and InSAR data.

We do not take into account track 348 presenting higher velocity gradient across the ATF in comparison to the three other tracks. For the GPS data, we select coherent stations according to the previous analysis (cf. section 6.3.1). We remove stations AT05 and AT11 presenting inconsistent velocities and located in the basin with clear seasonal deformation, as well as stations AT14, AT15, AT01, AT02, AT03, AT03A and AT04 that

are probably influenced by the Qiman-Kunlun Shan thrust system. Although stations J343 and J344 also present inconsistent velocities and are located within the basin with strong seasonal deformation, we did not remove them as they are the only far-field stations in the Tibetan Plateau from [Liang *et al.* \(2013\)](#) network.

The data covariance matrix contains only diagonal elements. For GPS data, we take the 2σ error provided by the authors, and associate a uniform uncertainty of 1 mm/yr for all InSAR data, corresponding roughly to the scatter of the LOS points in the profiles.

The comparison between the prior and posterior PDFs for the three models is summarized in Table 6.2, while the average posterior model and the comparison between observations and predictions is available in profile in the Fig. 6.12. The comparison between surface observations and predictions from the mean value of the posterior model are also shown in the Fig. 6.13

The model with GPS data alone and with InSAR data alone indicate an ATF strike-slip rate of 9 ± 2 mm/yr and 10.6 ± 1.5 mm/yr, locked until 21 ± 6.5 km-depth and 26 ± 3.5 km-depth, respectively. The strike-slip rate on the ramp structure is of 2.8 ± 1.8 mm/yr and 3.5 ± 0.6 mm/yr with a locking depth of 12 ± 7 km and 10 ± 2 km, respectively. We observe that with GPS data alone, only the posterior PDFs of SS_{ATF} and V_{short} resemble normal distribution while all other parameters are not really well constrained with posterior PDFs close to uniform distributions. In contrary, InSAR data alone constrain all parameters, except for the locking depth of the ATF that show asymmetric posterior distribution centered on the maximum limit. In addition, posterior PDFs with GPS data alone are much more wider than with the information enclosed in the InSAR-derived information. GPS vectors do not clearly indicate strike-slip neither shortening deformation in the Tarim, which are poorly fitted by the model. In contrary, with its high sensitivity to vertical displacements and its high spatial resolution, InSAR captures remarkably well the gradient of deformation associated to creeping ramp, which is in good consistency on the four tracks. However, with InSAR data alone, the trade-off between the long-wavelength residual ramp and the deformation results in a not very well constrained locking depth.

The model with GPS and InSAR data indicates a solution close to the model with InSAR data only. The average posterior model shows a locking depth of 25 ± 3.5 km and 10 ± 2.5 km for the ATF and the creeping ramp respectively (Fig. 6.12). These depths are associated with a strike-slip rates of 10.2 ± 1.4 mm/yr and 3.6 ± 0.6 mm/yr for the two half-infinite dislocations, respectively, indicating a deep-seated strike-slip

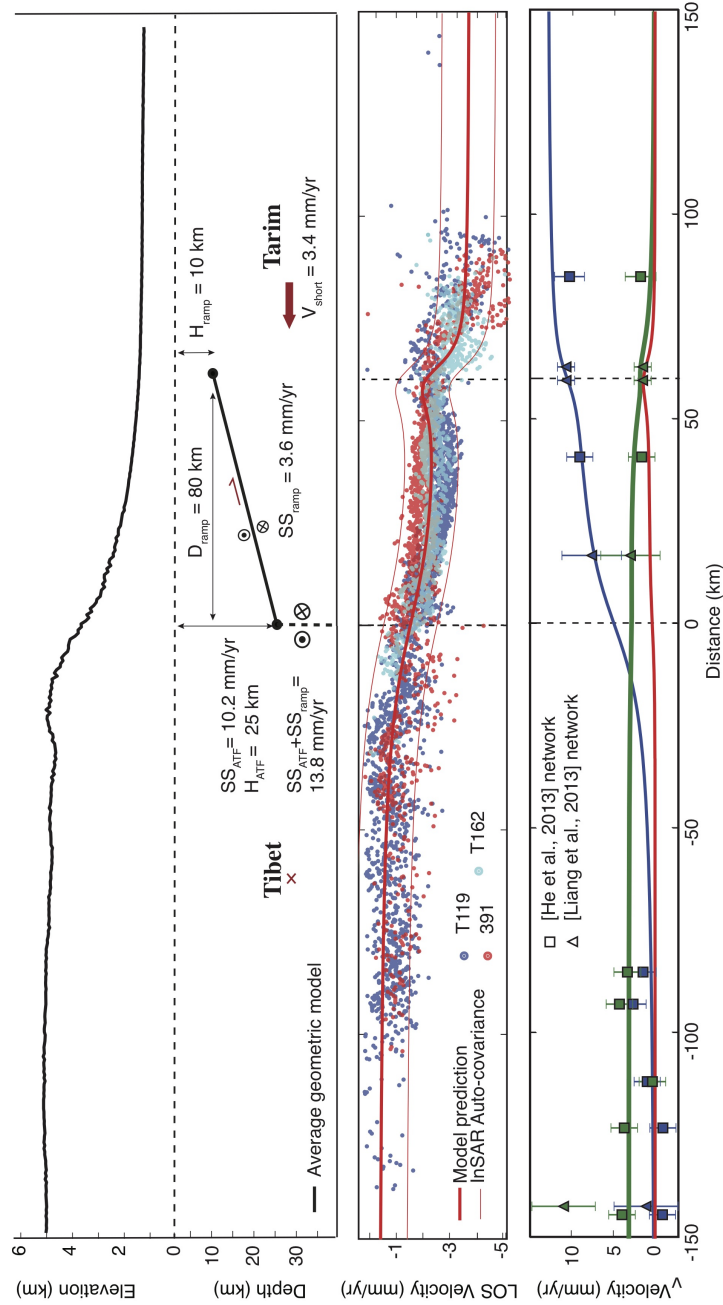
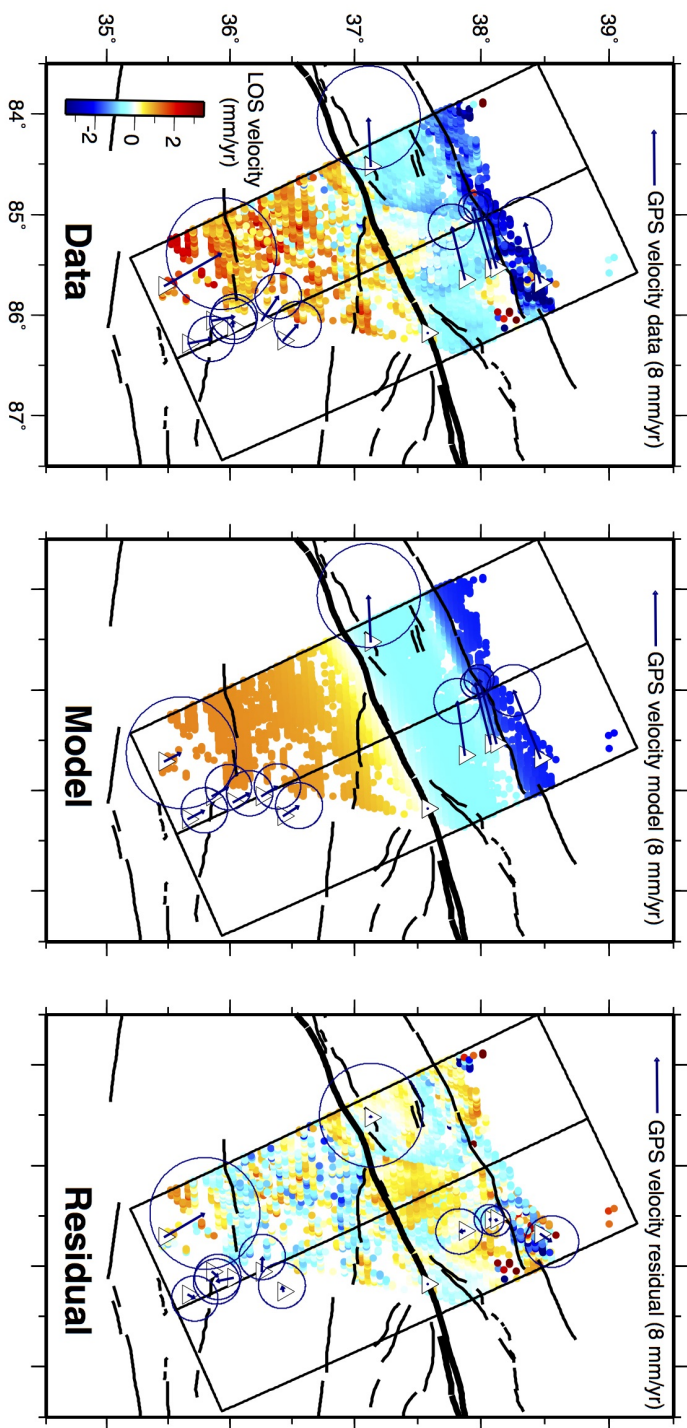


FIGURE 6.12 – Inversion model and results for the western (A) and eastern (B) profiles. Top : topography (black line), average posterior fault geometry and slip rates. Middle : LOS velocities (blue, red and cyan points). Bottom : profile-parallel (green square markers) and profile-perpendicular (blue square markers) GPS velocities. Average model obtained (corresponding blue and green lines) along profiles. (Fig. 6.7).

FIGURE 6.13 – Comparison between data and model from the Bayesian inversion. Left : GPS and down-sampled InSAR data used for the inversion. InSAR data are down-sampled with Generic Mapping Tools (GMT) with a latitudinal and longitudinal increment of 0.018° , and 0.046° , respectively (Wessel et Smith, 1991), and then collapsed in the fault-perpendicular direction. Middle : Modeled displacements associated to the maximum likelihood of the posterior probability distribution. Right : Residuals between the forward model and the observations.



motion below the ATF of about \sim 14 mm/yr. All parameters are well constrained while the predicted velocity profile fits relatively well all InSAR and GPS data. In this model, GPS data limits the trade-off between the InSAR long-wavelength residual ramp and the deformation and thus helps to constrain the horizontal slip-rates, while the combination of InSAR and GPS together fixes the fault-system geometry. However, the question is to determine how to weight the GPS data in comparison to the InSAR velocity maps. Campaign GPS data in this area of Tibet should be treated with caution as they are affected by atmospheric delays and as our permafrost map indicates that many stations might be affected by the non-tectonic signal. Unlike our InSAR data that are made of more than 40 acquisitions spanning 8 years, the campaign GPS velocity vectors are derived from only 2-3 measurement campaigns between 2009 and 2011. In addition, note that the ITRF solution provided by [He et al. \(2013\)](#) clearly indicates large inconsistency in comparison to the ITRF solution of [Liang et al. \(2013\)](#) for close stations, highlighting the difficulty to find stable rotation pole due to the large trade-off between the interseismic deformation and the predicted velocity from the Eulerian pole.

This 2-dimensional model has the advantage to be simple enough to enable constraining the non-linear geometrical parameters controlling the average deformation in this area. However, the velocity field highlights the kinematical complexity of the study area due to the Altun Shan or the Qiman-Kunlan Shan thrusts or to the Manyi Fault. These faults are trending obliquely to the Altyn Tagh Fault and would thus require a 3-dimensional model to estimate their contribution in the observed surface deformation.

6.4 Discussions and Conclusions

Due to the large trade-off between atmospheric delays, residual orbital ramps and tectonic deformation, processing InSAR data across the ATF is challenging. Our present approach is based on a series of corrections on the wrapped phase that aims at enhancing the signal-to-noise ratio before unwrapping, limiting the possible errors during this critical phase of processing. We identified four main processing challenges for systematic InSAR processing in Tibet.

The first challenge is associated to decorrelation, in particular across alluvial fans and sand dunes in the Tarim basin. Specific filtering and unwrapping procedures were dedicated to recover the far field signal in the Tarim basin, improving the recovery of the ATF displacement rate. In order to impose unwrapping path stable in time, we took into ac-

count the average temporal coherence in the unwrapping. The second challenge concerns the effects of hydrological and permafrost seasonal changes in the highest elevation areas of Tibet. A specific focus on permafrost related deformation (chapter 5) allows us to : (1) correctly unwrap interferograms from north to south, in particular across sedimentary basins, (2) quantify the temporal behavior of the freeze-thaw cycles, and (3) isolate bedrock pixels that are not affected by the permafrost signal for further tectonic analysis. The third difficulty is linked to the quadratic residual orbital ramps for interferograms longer than 300 km-long. To improve the estimation, we mask dunes areas located at a northern distance larger than \sim 150 km from the ATF, as well as sedimentary basins with more than 2.5 mm/yr of seasonal deformation. We invert these ramps into time series analysis and impose the closure of the signal within the interferometric network. Finally, we take advantage of the overlapping areas to re-estimate residual ramps on the velocity maps and provide consistent signal on several tracks at both long and short wavelengths. The fourth challenge is enhanced by the 4 km topographic step from the Tarim Basin to the Tibetan plateau. We compare empirical ([Cavalié et al., 2007](#); [Doin et al., 2015](#)) and predictive ([Doin et al., 2009](#); [Jolivet et al., 2011](#)) corrections of atmospheric delays and propagate errors on its correction through the time series analysis to estimate the tectonic velocities.

Despite these difficulties, we provide here the first velocity map continuous over a \sim 150000 km^2 wide area from the Tarim basin to the central part of the Tibetan plateau, crossing the topographic features as well as the sedimentary basins. A novel and surprising result is the observation of a clear line of concentrated deformation within the northern piedmont of the Altyn Shan, trending parallel to the Altyn Tagh Fault (ATF) trace. Such a signal is consistent with both a left-lateral or south-side up movement on a structure, 70 km north of the ATF. The wide and high resolution InSAR signal also illuminates active thrusting in the Tarim block, south of the linear and shallow structure, in agreement with geomorphological markers. The radar displacements shows 1 mm/yr of uplift of the hanging wall of the thrust fault across an alluvial fan, north of the ATF (Fig. [6.10A](#)). These findings suggest that the transpressive deformation along this northern edge of Tibet may be decoupled into transform and compressive deformation on deep-seated structures, which may merge at depth into a single lithospheric boundary.

An other interesting result is the observation of a localized gradients of deformation at the northwestern and south western terminaison of the Manyi Fault, where the block boundaries were here previously roughly defined due to large data gaps. These results redefine the block boundaries and will add new constraints on elastic strain accumulation

that should strongly increase the value of 3-dimentional kinematic block models in this area particularly devoid of GPS measurements.

The ~ 14 mm/yr of slip rate derived in the model in this segment of the ATF appears quite reasonable in comparison to geological slip rates (Mériaux *et al.*, 2004; Cowgill *et al.*, 2009) and slip predicted by fault kinematic. The ATF can be viewed as a transform fault transferring the convergence in the Western Kunlun to the Easter Kunlun, the Qaidam Basin and the Qilian Shan. It is therefore plausible that the left-lateral slip along the ATF decreases from west to east as the movement is absorbed by successive compressive structures on the south side of the fault. The current slip rate of 10 mm/yr on the ATF is well estimated by InSAR along the eastern section (Jolivet *et al.*, 2008). An higher rate of slip on the ATF along its western section is thus consistent with the kinematic interpretation and would suggest than around 4 mm/yr of slip is transferred to the Qilian Shan thrusts, which corresponds to the shortening observed in the northeastern part of the Tibetan plateau (Wang *et al.*, 2001; Zhang *et al.*, 2004). Because of the difficulty to conduct GPS measurements in the western part of the plateau, it is likely that the answer to this open question will be unambiguously answered when a multi-year time series of InSAR data will be available on both ascending and descending tracks, providing a way of separating east-west and vertical movements. The ESA, Sentinel-1 satellites are currently building up the archive for this endeavor.

Conclusions et perspectives

Le but de ces travaux a consisté à mesurer, caractériser et modéliser la déformation actuelle grâce à des observations tectoniques et géodésiques sur des zones à fortes complexités géométriques et présentant un fort taux de partitionnement de la déformation. Cartographier la localisation de la déformation et comprendre le fonctionnement de ces complexités géométriques sont des démarches importantes tant sur le plan intellectuel que sociale afin de mieux quantifier et intégrer l'ensemble des aléas de ces zones actives.

Une partie importante de cette thèse repose sur le développement d'une méthodologie InSAR dédiée à la mesure de faibles déformations sur des zones naturelles étendues et montagneuses à partir des archives du satellite Envisat. Les difficultés de traitement rencontrées résident principalement au niveau des délais atmosphériques corrélés aux gradients topographiques ainsi qu'aux fortes décorrélations temporelles associées à la végétation, aux zones sableuses ou aux cycles de gel et dégel du permafrost. Pour remédier à ces problèmes, le traitement s'appuie sur une série de corrections appliquées aux interférogrammes enroulés et sur l'analyse en série temporelle d'interférogrammes à faibles lignes de bases. Avant le déroulement, les interférogrammes subissent ainsi une correction des délais atmosphériques et des erreurs locales de topographie, et ce, afin de diminuer la variance de la phase interférométrique et d'exploiter la haute résolution du signal pour en extraire les signaux parasites contenus dans des gammes de fréquences autres que la déformation. A la suite, une série de filtres améliore le rapport signal sur bruit à travers les zones de reliefs ou les dunes. Les corrections augmentent significativement la continuité de la phase et limitent grandement les erreurs lors de l'étape critique de déroulement.

Une attention toute particulière sur la déformation associée au permafrost m'a conduit à dérouler correctement les interférogrammes dans le coeur du plateau Tibétain sur une zone de plus de 150000 km². Il fut ainsi possible d'isoler les zones stables non affectées par le permafrost pour améliorer le référencement des images. Cette étude a également

CONCLUSION ET PERSPECTIVES

conduit à quantifier le comportement temporel de la couche active recouvrant le permafrost associée à des cycles de gel et dégel. Ainsi, une déformation hétérogène mais géographiquement limitée aux vastes bassins allongés d'est en ouest et remplis de sédiments du Cénozoïque a été mise en évidence. Des modèles simples de diffusion n'apportent pas d'explication à ces observations de surface, qui suggèrent au contraire que la quantité d'eau et l'altitude sont les facteurs principaux contrôlant la réponse du sol gelé au forçage climatique. Une fois corrigées de ces signaux parasites, les cartes de déplacements tectoniques obtenues localisent précisément la déformation dans des zones difficiles d'accès en mettant en évidence les changements de partitionnement de la déformation. Au nord ouest Tibet, la carte de vitesse image la terminaison ouest de la faille du Kunlun et son interaction avec la faille de l'Altyn Tagh, à un endroit où la frontière des blocs est jusqu'à présent mal-connue. Les données obtenues mettent aussi en exergue une déformation active dans le Tarim dans une zone également difficile d'accès où les décalages géomorphologiques sont souvent recouverts par les dunes. Par conséquent, ces résultats soulignent le potentiel de l'InSAR pour une mesure précise, à distance et sur de grandes zones, de la déformation actuelle. Elles viennent compléter les mesures à plus long-terme de terrain. Une comparaison des données acquises avec des études géomorphologiques, tectoniques et des interprétations de données sismiques ouvre de nombreuses perspectives de modélisation et apporte, entre autre, une meilleure caractérisation de la déformation à court terme.

Ces travaux démontrent le potentiel de la géodésie spatiale appliquée aux Sciences de la Terre. Le lancement des nouveaux satellites SAR (série Sentinel-1, ALOS-2) constitue aujourd'hui un tournant majeur dans le domaine de la géodésie spatiale et une opportunité à saisir. La nouvelle génération de satellites SAR proposent de nouvelles données acquises à des fréquences plus rapprochées (chaque semaine) et à grande échelle. D'une part, ces données présentent une meilleure qualité de mesure avec notamment des orbites plus précisément connues. Par ailleurs, un meilleur échantillonnage des cycles saisonniers atmosphériques diminue les ambiguïtés entre le biais linéaire introduit par l'atmosphère stratifiée et la déformation séculaire du sol. Il s'agit ensuite d'une opportunité pour couvrir aisément de grandes zones affectées par de la déformation et de mieux contraindre la nature des déformations profondes. Ces nouvelles données offrent également des perspectives uniques pour la cartographie des petites déformations transitoires tectoniques ou hydrologiques. Elles apporteront notamment une mesure systématique des distributions du permafrost et un échantillonnage plus détaillé du comportement saisonnier et des réponses inter-annuelles de la couche active en réponse aux changements climatiques.

Aussi, un meilleur échantillonnage de l'ensemble des phases du cycle sismique sera un élément clef dans la connaissance de leurs caractéristiques spatiales et temporelles. Ceci débouchera sur une meilleure détection des changements subtils de déformation durant les diverses phases ou sur l'identification des zones de possibles initiations de grands séismes. Ces volumes de données ouvriront enfin des perspectives, visant à mieux contraindre les modèles inverses de source, et à améliorer la comparaison avec les modèles physiques du cycle sismique.

De meilleures mesures de surface détermineront-elles, pour autant, comment et sous quelle forme les contraintes emmagasinées aujourd’hui seront relâchés demain ? Quels facteurs favoriseront la rupture d'un nouveau segment, la réactivation d'une ancienne faille de surface, un relâchement sous forme de glissement lent ou bien la déformation distribuée sur une grande zone ? Notre vision sur quelques dizaines d'années du comportement intersismique d'un système de failles permet-elle d'en comprendre son cycle sismique sur quelques milliers d'années ? Pas complètement, assurément. Seules des études complémentaires portant sur la géométrie des structures et sur le comportement rhéologique des roches présentes, intégrées dans un contexte géodynamique et tectonique, apporteront une meilleure estimation de l'aléa sismique d'une zone active. Dans cette perspective, mon deuxième axe de recherche a consisté à introduire des contraintes de géologie structurale dans les modèles géodésiques, et ce, afin de mieux contraindre la cinématique et la géométrie des structures profondes. De par sa forte sensibilité aux déplacements verticaux et sa grande résolution spatiale, l'InSAR apporte des informations complémentaires au GPS bien adapté à l'exploration de la géométrie des structures profondes. Jusqu'à présent, les modèles intersismiques se limitaient souvent à des plans verticaux sans aucunes liaisons entre eux. Les modèles développés dans ce travail intègrent la complexité géométrique des structures présentes dans un même système et prennent en compte des contraintes de connectivité extraites des modèles géologiques. Ainsi, j'ai pu quantifier, au Tibet et en Californie, la compatibilité des observations actuelles de surface avec des modèles structuraux long-termes. En Californie, une introduction des lois de conservation du mouvement dans les modèles constraint la cinématique et la géométrie des chevauchements aveugles se développant dans la région de Los Angeles. Ces lois constituent un cadre novateur pour réconcilier les données de déformations actuelles avec les informations de géologie structurale. Nos observations et nos modèles renforcent l'importance de la géométrie des failles de San Andreas, d'Haiyuan, de l'Altyn Tagh et du Kunlun. Ces failles imposantes tant par leurs morphologies que par la topographie qu'elles délimitent, s'enracinent très probablement sur une frontière lithosphérique unique en disposant de

CONCLUSION ET PERSPECTIVES

fait la force d'orchestrer le partitionnement de la convergence des plaques et la tectonique régionale. L'intégration des modèles structuraux avec les observations et mesures du comportement actuel des failles se présente ainsi comme une pièce essentielle du puzzle. En parallèle, une meilleure intégration des processus mécaniques de déformation sera indispensable à notre comprehension du comportement des zones actives et de leurs aléas sismiques.

Bibliographie

- ALTAMIMI, Z., COLLILIEUX, X. et MÉTIVIER, L. (2011). ITRF2008 : an improved solution of the international terrestrial reference frame. *Journal of Geodesy*, 85(8):457–473. [79](#)
- AMELUNG, F., GALLOWAY, D. L., BELL, J. W., ZEBKER, H. A. et LACZNIAK, R. J. (1999). Sensing the ups and downs of Las Vegas : InSAR reveals structural control of land subsidence and aquifer-system deformation. *Geology*, 27(6):483–486. [126](#)
- ANDERSON, R. S. et ANDERSON, S. P. (2010). *Geomorphology : The mechanics and chemistry of landscapes*. Cambridge University Press. [152](#)
- ARGUS, D. F. et GORDON, R. G. (2001). Present tectonic motion across the Coast Ranges and San Andreas Fault system in central California. *GSA Bull.*, 113(12):1580–1592. [50](#)
- ARGUS, D. F., HEFLIN, M. B., PELTZER, G., CAMPE, F. et WEBB, F. H. (2005). Interseismic strain accumulation and anthropogenic motion in metropolitan Los Angeles. *J. Geophys. Res.*, 110(B04401). [52](#), [95](#), [104](#), [113](#), [115](#)
- ARMIJO, R., TAPPONNIER, P., MERCIER, J. et HAN, T.-L. (1986). Quaternary extension in southern tibet : Field observations and tectonic implications. *Journal of Geophysical Research : Solid Earth*, 91(B14):13803–13872. [28](#), [34](#)
- ASTIZ, L. et SHEARER, P. M. (2000). Earthquake locations in the inner continental Borderland, offshore southern California. *Bull. Seism. Soc. Am.*, 90:425–449. [96](#)
- ATWATER, T. M. (1998). Plate tectonic history of southern California with emphasis on the western Transverse Ranges and northern channel islands. [96](#)
- BARBOT, S., AGRAM, P. et MICHELE, M. D. (2013). Change of apparent segmentation of the San Andreas Fault around Parkfield from space geodetic observations across multiple periods. *J. Geophys. Res.* [103](#)

BIBLIOGRAPHIE

- BAWDEN, G. W., THATCHER, W., STEIN, R. S., HUDDNUT, K. W. et PELETZER, G. (2001). Tectonic contraction across Los Angeles after removal of groundwater pumping effects. *Nature*, 412:812–815. [113](#), [115](#)
- BEKAERT, D., HOOPER, A. et WRIGHT, T. (2015). A spatially-variable power-law tropospheric correction technique for InSAR data. *J. Geophys. Res. : Solid Earth*. [127](#), [132](#), [138](#)
- BENDICK, R., BILHAM, R., FREYMUELLER, J., LARSON, K. et YIN, G. (2000). Geodetic evidence for a low slip rate in the altyn tagh fault system. *Nature*, 404(6773):69–72. [38](#), [176](#)
- BERARDINO, P., FORNARO, G., LANARI, R. et SANSOSTI, E. (2002). A new algorithm for surface deformation monitoring based on small baseline differential SAR interferograms. *Geoscience and Remote Sensing, IEEE Transactions on*, 40(11):2375–2383. [22](#), [147](#)
- BEVIS, M. et BROWN, A. (2014). Trajectory models and reference frames for crustal motion geodesy. *J. of Geodesy*, 88(3):283–311. [62](#), [79](#)
- BOCK, Y., WDOWINSKI, S., FANG, P., ZHANG, J., WILLIAMS, S., JOHNSON, H., BEHR, J., GENRICH, J., DEAN, J., DOMSELAAR, M. v. et al. (1997). Southern California permanent GPS geodetic array : Continuous measurements of regional crustal deformation between the 1992 Landers and 1994 Northridge earthquakes. *J. Geophys. Res. : Solid Earth*, 102(B8):18013–18033. [95](#)
- BOURNE, S., ENGLAND, P. et PARSONS, B. (1998). The motion of crustal blocks driven by flow of the lower lithosphere and implications for slip rates of continental strike-slip faults. *Nature*, 391(6668):655–659. [15](#), [50](#)
- BOWMAN, D., KING, G. et TAPPONNIER, P. (2003). Slip partitioning by elastoplastic propagation of oblique slip at depth. *Science*, 300(5622):1121–1123. [15](#), [31](#), [52](#), [94](#), [95](#), [106](#)
- BROWN, J., HINKEL, K. et NELSON, F. (2000). The circumpolar active layer monitoring (CALM) program : Research designs and initial results 1. *Polar geography*, 24(3):166–258. [146](#), [147](#), [156](#)
- BRUNE, J. N., HENYET, T. L. et ROY, R. F. (1969). Heat flow, stress, and rate of slip along the San Andreas Fault, California. *J. Geophys. Res.*, 74(15). [50](#)

- BÜRGMANN, R., ROSEN, P. A. et FIELDING, E. J. (2000). Synthetic aperture radar interferometry to measure earth's surface topography and its deformation. *Annual Review of Earth and Planetary Sciences*, 28(1):169–209. [126](#)
- ÇAKIR, Z., ERGINTAV, S., ÖZENER, H., DOGAN, U., AKOGLU, A. M., MEGHRAOUI, M. et REILINGER, R. (2012). Onset of aseismic creep on major strike-slip faults. *Geology*, 40(12):1115–1118. [76](#)
- CAVALIÉ, O., DOIN, M.-P., LASSERRE, C. et BRIOLE, P. (2007). Ground motion measurement in the Lake Mead area, Nevada, by differential synthetic aperture radar interferometry time series analysis : Probing the lithosphere rheological structure. *J. Geophys. Res. (1978–2012)*, 112(B3). [22](#), [63](#), [69](#), [82](#), [127](#), [202](#)
- CAVALIÉ, O., LASSERRE, C., DOIN, M.-P., PELETZER, G., SUN, J., XU, X. et SHEN, Z.-K. (2008). Measurement of interseismic strain across the Haiyuan fault (Gansu, China), by InSAR. *Earth Planet. Sci. Lett.*, 275:246–257. [23](#), [41](#), [59](#), [64](#), [72](#), [73](#), [126](#), [127](#)
- CERVELLI, P., SEGALL, P., AMELUNG, F., GARBEIL, H., MEERTENS, C., OWEN, S., MIKLIUS, A. et LISOWSKI, M. (2002). The 12 september 1999 upper east rift zone dike intrusion at kilauea volcano, Hawaii. *J. Geophys. Res. : Solid Earth (1978–2012)*, 107(B7):ECV–3. [126](#)
- CHAMPAGNAC, J.-D., YUAN, D.-Y., GE, W.-P., MOLNAR, P. et ZHENG, W.-J. (2010). Slip rate at the north-eastern front of the Qilian Shan, China. *Terra Nova*, 22(3):180–187. [75](#), [76](#)
- CHANG, L. et HANSSEN, R. (2015). Detection of permafrost sensitivity of the Qinghai–Tibet railway using satellite radar interferometry. *International Journal of Remote Sensing*, 36(3):691–700. [147](#), [156](#)
- CHAUSSARD, E., BÜRGMANN, R., FATTABI, H., NADEAU, R., TAIRA, T., JOHNSON, C. et JOHANSON, I. (2015). Potential for larger earthquakes in the east san francisco bay area due to the direct connection between the Hayward and Calaveras faults. *Geophysical Research Letters*, 42(8):2734–2741. [51](#), [100](#)
- CHAUSSARD, E., JOHNSON, C., FATTABI, H. et BÜRGMANN, R. (2016). Potential and limits of InSAR to characterize interseismic deformation independently of GPS data : Application to the southern San Andreas Fault system. *Geochemistry, Geophysics, Geosystems*, 17(3):1214–1229. [51](#)

BIBLIOGRAPHIE

- CHENG, G. et WU, T. (2007). Responses of permafrost to climate change and their environmental significance, Qinghai-Tibet Plateau. *J. Geophys. Res. : Earth Surface*, 112(F2). [146](#), [147](#)
- CHILES, J.-P. et DELFINER, P. (2009). *Geostatistics : modeling spatial uncertainty*, volume 497. John Wiley & Sons. [68](#), [84](#)
- CHRISTENSEN, T. R., JOHANSSON, T., ÅKERMAN, H. J., MASTEPANOV, M., MALMER, N., FRIBORG, T., CRILL, P. et SVENSSON, B. H. (2004). Thawing sub-arctic permafrost : Effects on vegetation and methane emissions. *Geophysical research letters*, 31(4). [146](#)
- CORBETT, E. (1984). *Seismicity and crustal structure of Southern California : tectonic implications for the transfer of Baja California to the Pacific Plate and estimates of the Pacific-North America motion*. Thèse de doctorat, Calif. Inst. of Technol., Pasadena, Calif. [96](#)
- COUDROY, T., LI, H., van der WOERD, J., BARRIER, L., SIMOES, M., TAPPONNIER, P., MAINSANT, G., PAN, J. et THUIZAT, R. (2009). Deformation and propagation of the western kunlun foreland into the tarim basin (xinjiang, china). In *AGU Fall Meeting Abstracts*, volume 1, page 0771. [178](#)
- COWGILL, E., GOLD, R. D., XUANHUAN, C., XIA-FENG, W., ARROWSMITH, J. R. et SOUTHON, J. (2009). Low quaternary slip rate reconciles geodetic and geologic rates along the altyn tagh fault, northern Tibet. *Geology*, 37:647–650. [127](#), [175](#), [179](#), [203](#)
- CROUCH, J. K. et SUPPE, J. (1993). Late cenozoic tectonic evolution of the Los Angeles basin and inner California Borderland : A model for core complex-like crustal extension. *Geol. Soc. of Am. Bull.*, 105:1415–1434. [95](#), [96](#), [97](#)
- DAOUT, S., BARBOT, S., PELETZER, G., DOIN, M.-P., LIU, Z. et JOLIVET, R. (2016a). Constraining the kinematics of metropolitan los angeles faults with a slip-partitioning model. *Geophysical Research Letters*. [94](#)
- DAOUT, S., DOIN, M.-P., LASSEUR, C., PELETZER, G. et SOCQUET, A. (2016b). Multi temporal insar analysis in northwestern tibet. In *Dragon 3 Final Results and Dragon 4 Kick-Off*, volume 739, page 69. [126](#)

- DAOUT, S., DOIN, M.-P., PELTZER, G., SOCQUET, A. et LASSEUR, C. (2017). Large scale insar monitoring of permafrost freeze-thaw cycles on the tibetan plateau. *Geophysical Research Letters*. [146](#)
- DAOUT, S., JOLIVET, R., LASSEUR, C., DOIN, M.-P., BARBOT, S., TAPPONNIER, P., NOCQUET, J.-M., JIANBAO, S., SHEN, Z., QINGLIANG, W. *et al.* (2014). Slip partitioning along the haiyuan fault system. In *Dragon 3Mid Term Results*, volume 724, page 52. [59](#)
- DAOUT, S., JOLIVET, R., LASSEUR, C., DOIN, M.-P., BARBOT, S., TAPPONNIER, P., PELTZER, G., SOCQUET, A. et SUN, J. (2016c). Along-strike variations of the partitioning of convergence across the Haiyuan fault system detected by InSAR. *GJI*, 205(1):536–547. [59](#), [100](#), [106](#), [113](#), [114](#), [130](#), [148](#), [164](#)
- DAVIS, T. L., NAMSON, J. et YERKES, R. F. (1989). A cross section of the Los Angeles area : Seismically active fold and thrust belt, the 1987 Whittier Narrows earthquake, and earthquake hazard. *J. Geophys. Res. : Solid Earth (1978–2012)*, 94(B7):9644–9664. [96](#)
- DEE, D., UPPALA, S., SIMMONS, A., BERRISFORD, P., POLI, P., KOBAYASHI, S., ANDRAE, U., BALMASEDA, M., BALSAMO, G., BAUER, P. *et al.* (2011). The ERA-Interim reanalysis : Configuration and performance of the data assimilation system. *Quarterly J. the Royal Meteorological Society*, 137(656):553–597. [130](#), [148](#), [155](#), [159](#), [180](#)
- DELACOURT, C., BRIOLE, P. et ACHACHE, J. (1998). Tropospheric corrections of SAR interferograms with strong topography. application to Etna. *Geophysical Research Letters*, 25(15):2849–2852. [127](#)
- DENG, J. et SYKES, L. R. (1997). Evolution of the stress field in southern California and triggering of moderate-size earthquakes : A 200-year perspective. *J. Geophys. Res.*, 102(B5):9859–9886. [95](#)
- DENG, Q., SHEFA, C., FANGNIN, S., SHILONG, Z., YIPENG, W., WEIQI, Z., DECHENG, J., BURCHFIELD, B., MOLNAR, P., ROYDEN, L. *et al.* (1986). Variations in the geometry and amount of slip on the Haiyuan (Nanxihaushan) fault zone, China and the surface rupture of the 1920 Haiyuan earthquake. *Earthquake Source Mechanics*, pages 169–182. [59](#), [175](#)

BIBLIOGRAPHIE

DEVRIES, P. M. et MEADE, B. J. (2013). Earthquake cycle deformation in the Tibetan plateau with a weak mid-crustal layer. *J. Geophys. Res.*, 118(6):3101–3111. [38](#), [76](#), [127](#)

DOIN, M.-P., LASERRE, C., PELTZER, G., CAVALIÉ, O. et DOUBRE, C. (2009). Corrections of stratified tropospheric delays in SAR interferometry : Validation with global atmospheric models. *J. Applied Geophysics*, 69:35–50. [63](#), [69](#), [126](#), [127](#), [130](#), [134](#), [138](#), [139](#), [143](#), [148](#), [159](#), [180](#), [183](#), [184](#), [202](#)

DOIN, M.-P., LODGE, F., GUILLASO, S., JOLVET, R., LASERRE, C., DUCRET, G., GRANDIN, R., PATHIER, E. et PINEL, V. (2011). Presentation of the small baseline nsbas processing chain on a case example : The Etna deformation monitoring from 2003 to 2010 using envisat data. *Proc. ESA Fringe.* [22](#), [24](#), [64](#), [78](#), [82](#), [84](#), [129](#), [148](#), [165](#), [179](#), [180](#)

DOIN, M.-P., TWARDZIK, C., DUCRET, G., LASERRE, C., GUILLASO, S. et JIANBAO, S. (2015). InSAR measurement of the deformation around Siling Co Lake : Inferences on the lower crust viscosity in central Tibet. *J. Geophys. Res. : Solid Earth*, 120(7):5290–5310. [23](#), [24](#), [36](#), [46](#), [63](#), [81](#), [126](#), [127](#), [131](#), [143](#), [146](#), [148](#), [149](#), [156](#), [164](#), [166](#), [179](#), [180](#), [184](#), [202](#)

DOLAN, J. F., CHRISTOFFERSON, S. A. et SHAW, J. H. (2003). Recognition of paleoearthquakes on the Puente Hills blind thrust fault, California. *Science*, 300(5616):115–118. [50](#), [104](#)

DOLAN, J. F., SIEH, K., ROCKWELL, T. K., YEATS, R. S., SHAW, J., SUPPE, J., HUFFTILE, G. J. et GATH, E. M. (1995). Prospects for Larger or More Frequent Earthquakes in the Los Angeles Metropolitan Region. *Science*, 267:199–205. [95](#), [104](#), [105](#)

DUCRET, G., DOIN, M.-P., GRANDIN, R., LASERRE, C. et GUILLASO, S. (2014). DEM corrections before Unwrapping in a Small Baseline Strategy for InSAR Time Series Analysis. *Geoscience and Remote Sensing Letters, IEEE*, 11:696–700. [22](#), [23](#), [44](#), [63](#), [69](#), [79](#), [148](#), [159](#), [180](#)

DUPUTEL, Z., AGRAM, P. S., SIMONS, M., MINSON, S. E. et BECK, J. L. (2014). Accounting for prediction uncertainty when inferring subsurface fault slip. *Geophysical Journal International*, page ggt517. [33](#)

- ELLIOTT, J. R., BIGGS, J., PARSONS., B. et WRIGHT, T. J. (2008). InSAR slip rate determination on the altyn tagh fault, northern Tibet, in the presence of topographically correlated atmospheric delays. *J. Geophys. Res.*, 35. 38, 41, 45, 126, 127, 128, 174, 175, 177, 179
- ENGLAND, P. et HOUSEMAN, G. (1989). Extension during continental convergence, with application to the Tibetan plateau. *Journal of Geophysical Research : Solid Earth*, 94(B12):17561–17579. 36, 176
- ENGLAND, P. et MOLNAR, P. (1997a). Active Deformation of Asia : From Kinematics to Dynamics. *Science*, 278:647–650. 36, 176
- ENGLAND, P. et MOLNAR, P. (1997b). Active deformation of asia : From kinematics to dynamics. *Science*, 278:647–650. 127
- ENGLAND, P. et MOLNAR, P. (1997c). The field of crustal velocity in Asia calculated from Quaternary rates of slip on faults. *J. Geophys. Res.*, 130:551–582. 36, 176
- FARR, T. G. et KOBRECK, M. (2000). Shuttle Radar Topography Mission produces a wealth of data. *Eos Trans. AGU*, 81(48):583–585. 129, 179, 195
- FATTAHI, H. et AMELUNG, F. (2014a). InSAR uncertainty due to orbital errors. *Geophys J. Int.*, 199(1):549–560. 111
- FATTAHI, H. et AMELUNG, F. (2014b). InSAR uncertainty due to orbital errors. *Geophysical Journal International*, 199(1):549–560. 129, 148, 180
- FERRETTI, A., PRATI, C. et ROCCA, F. (2000). Nonlinear subsidence rate estimation using permanent scatterers in differential SAR interferometry. *IEEE Transactions on Geoscience and Remote Sensing*, 38(5):2202–2212. 22
- FIALKO, Y. (2006). Interseismic strain accumulation and the earthquake potential on the southern San Andreas Fault system. *Nature*, 441:968–971. 52
- FIALKO, Y., SANDWELL, D., SIMONS, M. et ROSEN, P. (2005). Three-dimensional deformation caused by the Bam, Iran, earthquake and the origin of shallow slip deficit. *Nature*, 435(7040):295–299. 31
- FITCH, T. J. (1972). Plate convergence, transcurrent faults, and internal deformation adjacent to southeast asia and the western Pacific. *Journal of Geophysical research*, 77(23):4432–4460. 14

BIBLIOGRAPHIE

- FORT, M. et van VLIET-LANOE, B. (2007). Permafrost and periglacial environment of western tibet. *Landform analysis*, 5:25–29. [148](#), [150](#), [155](#)
- FRENCH, H. M., DEM ITROFF, M., FORMAN, S. L. et NEWELL, W. L. (2007). A chronology of Late-Pleistocene permafrost events in southern New Jersey, Eastern USA. *Permafrost Periglacial Process.*, 18(1):49–59. [146](#)
- FRUNEAU, B., PATHIER, E., RAYMOND, D., DEFFONTAINES, B., LEE, C., WANG, H., ANGELIER, J., RUDANT, J., CHANG, C. *et al.* (2001). Uplift of tainan tableland (SW Taiwan) revealed by SAR interferometry. *Geophys. Res. Lett.*, 28(16):3071–3074. [27](#)
- FRUNEAU, B. et SARTI, F. (2000). Detection of ground subsidence in the city of Paris using radar interferometry : isolation of deformation from atmospheric artifacts using correlation. *Geophysical Research Letters*, 27(24):3981–3984. [126](#)
- FUIS, G., RYBERG, T., GODFREY, N., OKAYA, D. et MURPHY, J. (2001a). Crustal structure and tectonics from the Los Angeles basin to the Mojave desert, southern California. *Geology*, 29:15–18. [50](#), [51](#), [97](#), [105](#)
- FUIS, G., RYBERG, T., LUTTER, W. et EHLIG, P. (2001b). Seismic mapping of shallow fault zones in the san gabriel mountains from the Los Angeles region seismic experiment, southern California. *J. Geophys. Res. : Solid Earth (1978–2012)*, 106(B4):6549–6568. [97](#)
- FUIS, G., SCHEIRER, D. S., LANGENHEIM, V. E. et KOHLER, M. D. (2012). A new perspective of the geometry of the San Andreas Fault in southern California and its relationship to the lithospheric structure. *Bull. Seism. Soc. Am.*, 102:236–251. [50](#), [97](#), [106](#)
- FUIS, G. S., CLAYTON, R. W., DAVIS, P. M., RYBERG, T., LUTTER, W. J., OKAYA, D. A., HAUKSSON, E., PRODEHL, C., MURPHY, J. M., BENTHIEN, M. L. *et al.* (2003). Fault systems of the 1971 San Fernando and 1994 Northridge earthquakes, southern California : Relocated aftershocks and seismic images from larse ii. *Geology*, 31(2):171–174. [97](#)
- FUIS, G. S., KOHLER, M. D., SCHERWATH, M., BRINK, U. T., VAN AVENDONK, H. J. et MURPHY, J. M. (2007). A comparison between the transpressional plate boundaries of south island, new zealand, and southern california, usa : The alpine and san andreas fault systems. *A Continental Plate Boundary : Tectonics at South Island, New Zealand*, pages 307–327. [51](#)

- FUKUDA, J. et JOHNSON, K. M. (2008). A fully Bayesian inversion for spatial distribution of fault slip with objective smoothing. *Bulletin of the Seismological Society of America*, 98(3):1128–1146. [33](#)
- FURLONG, K. et HUGO, W. D. (1989). Geometry and evolution of the San Andreas Fault zone in Northern California. *J. Geophys. Res.*, 94(B3):3100–3110. [49](#), [94](#)
- GANGODAGAMAGE, C., ROWLAND, J. C., HUBBARD, S. S., BRUMBY, S. P., LILJEDAHL, A. K., WAINWRIGHT, H., WILSON, C. J., ALTMANN, G. L., DAFFLON, B., PETERSON, J. et al. (2014). Extrapolating active layer thickness measurements across arctic polygonal terrain using lidar and ndvi data sets. *Water resources research*, 50(8):6339–6357. [147](#)
- GARTHWAITE, M. C., WANG, H. et WRIGHT, T. J. (2013). Broadscale interseismic deformation and fault slip rates in the central Tibetan plateau observed using InSAR. *Journal of Geophysical Research : Solid Earth*, 118(9):5071–5083. [42](#), [45](#), [174](#), [177](#)
- GAUDEMER, Y., TAPPONIER, P., MEYER, B., PELETZER, G., SHUNMIN, G., ZHITAI, C., HUAGUNG, D. et CIFUENTES, I. (1995). Partitionning of crustal slip between linked, active faults in the eastern Qilian Shan, and evidence for a major seismic gap, the "Tianzhu gap", on the western Haiyuan Fault, Gansu (China). *Geophys. J. Int.*, 120: 599–645. [35](#), [38](#), [39](#), [43](#), [52](#), [53](#), [59](#), [60](#), [64](#), [67](#), [74](#), [75](#), [76](#), [94](#), [95](#), [175](#), [176](#)
- GE, W.-P., MOLNAR, P., SHEN, Z.-K. et LI, Q. (2015). Present-day crustal thinning in the southern and northern tibetan plateau revealed by gps measurements. *Geophysical Research Letters*, 42(13):5227–5235. [176](#)
- GRANDIN, R., DOIN, M.-P., BOLLINGER, L., PINEL-PUYSSÉGUR, B., DUCRET, G., JOLIVET, R. et SAPKOTA, S. N. (2012). Long-term growth of the Himalaya inferred from interseismic InSAR measurement. *Geology*, 40(12):1059–1062. [23](#), [63](#), [69](#), [81](#), [130](#), [148](#), [164](#)
- GUILLASO, S., LASSERRE, C., DOIN, M., CAVALIÉ, O., SUN, J. et PELETZER, G. (2008). InSAR measurement of interseismic strain in areas of low coherence : Example across the Haiyuan fault (Gansu, China) using a local InSAR adaptive range filter, paper presented at general assembly. *Eur. Geosci. Union, Vienna*. [23](#)
- GUILLASO, S., REIGBER, A., FERRO-FAMIL, L. et POTTIER, E. (2006). Range resolution improvement of airborne SAR images. *IEEE Geoscience and Remote Sensing Letters*, 3(1):135–139. [23](#)

BIBLIOGRAPHIE

- GUO, X., GAO, R., WANG, H., LI, W., KELLER, G., XU, X., LI, H. et ENCARNACION, J. (2015). Crustal architecture beneath the Tibet-ordos transition zone, ne Tibet, and the implications for plateau expansion. *Geophysical Research Letters*, 42(24). [39](#)
- HANSSEN, R. F. (2001). *Radar interferometry : data interpretation and error analysis*, volume 2. Springer Science & Business Media. [22](#), [127](#)
- HANSSEN, R. F., WECKWERTH, T. M., ZEBKER, H. A. et KLEES, R. (1999). High-resolution water vapor mapping from interferometric radar measurements. *Science*, 283(5406):1297–1299. [126](#)
- HARLAN, R. et NIXON, J. (1978). Ground thermal regime. *Geotechnical engineering for cold regions*, pages 103–163. [153](#)
- HAUKSSON, E., YANG, W. et SHEARER, P. (2012). Waveform relocated earthquake catalog for southern California (1981 to 2011). *Bull. Seism. Soc. Am.*, 102:2239–2244. [103](#)
- HE, J., VERNANT, P., CHÉRY, J., WANG, W., LU, S., KU, W., XIA, W. et BILHAM, R. (2013). Nailing down the slip rate of the altyn tagh fault. *Geophys. Res. Lett.*, 40(20):5382–5386. [38](#), [127](#), [175](#), [176](#), [179](#), [186](#), [188](#), [189](#), [190](#), [191](#), [197](#), [201](#)
- HETLAND, E., MUSÉ, P., SIMONS, M., LIN, Y., AGRAM, P. et DiCAPRIO, C. (2012). Multiscale InSAR time series (MInTS) analysis of surface deformation. *Journal of Geophysical Research : Solid Earth*, 117(B2). [22](#)
- HETLAND, E. et SIMONS, M. (2010). Post-seismic and interseismic fault creep II : transient creep and interseismic stress shadows on megathrusts. *Geophys. J Int.*, 181(1):99–112. [38](#), [76](#)
- HILLEY, G. E., BÜRGMANN, R., FERRETTI, A., NOVALI, F. et ROCCA, F. (2004). Dynamics of slow-moving landslides from permanent scatterer analysis. *Science*, 304(5679):1952–1955. [126](#)
- HINKEL, K., DOOLITTLE, J., BOCKHEIM, J., NELSON, F., PAETZOLD, R., KIMBLE, J. et TRAVIS, R. (2001). Detection of subsurface permafrost features with ground-penetrating radar, Barrow, Alaska. *Permafrost Periglacial Process.*, 12(2):179–190. [147](#)
- HOOPER, A. (2008). A multi-temporal InSAR method incorporating both persistent scatterer and small baseline approaches. *Geophysical Research Letters*, 35(16). [22](#)

- HOOPER, A., BEKAERT, D., SPAANS, K. et ARIKAN, M. (2012). Recent advances in SAR interferometry time series analysis for measuring crustal deformation. *Tectonophysics*, 514:1–13. [126](#)
- HOOPER, A., SEGALL, P. et ZEBKER, H. (2007). Persistent scatterer interferometric synthetic aperture radar for crustal deformation analysis, with application to Volcán Alcedo, Galápagos. *J. Geophys. Res. (1978–2012)*, 112(B7). [63](#)
- HOOPER, A., ZEBKER, H., SEGALL, P. et KAMPES, B. (2004). A new method for measuring deformation on volcanoes and other natural terrains using InSAR persistent scatterers. *Geophys. Res. Lett.*, 31(23). [22, 147](#)
- HOWELL, S., SMITH-KONTER, B., FRAZER, N., TONG, X. et SANDWELL, D. (2016). The vertical fingerprint of earthquake cycle loading in southern California. *Nature Geoscience*, 9(8):611–614. [51](#)
- HU, J., DING, X., LI, Z., ZHANG, L., ZHU, J., SUN, Q. et GAO, G. (2016). Vertical and horizontal displacements of Los Angeles from InSAR and GPS time series analysis : resolving tectonic and anthropogenic motions. *J. Geodynamics*. [113, 115](#)
- HU, X., PAN, B., KIRBY, E., GAO, H., HU, Z., CAO, B., GENG, H., LI, Q. et ZHANG, G. (2015). Rates and kinematics of active shortening along the eastern Qilian Shan, China, inferred from deformed fluvial terraces. *Tectonics*. [75, 76](#)
- HUANG, M.-H., BÜRGMANN, R. et FREED, A. M. (2014). Probing the lithospheric rheology across the eastern margin of the Tibetan plateau. *Earth and Planetary Science Letters*, 396:88–96. [36, 176](#)
- IDE, S., BEROZA, G. C., SHELLY, D. R. et UCHIDE, T. (2007). A scaling law for slow earthquakes. *Nature*, 447(7140):76–79. [25](#)
- ITO, Y., OBARA, K., SHIOMI, K., SEKINE, S. et HIROSE, H. (2007). Slow earthquakes coincident with episodic tremors and slow slip events. *Science*, 315(5811):503–506. [25](#)
- JACOBY, G. C., SHEPPARD, P. R. et SIEH, K. E. (1988). Irregular Recurrence of Large Earthquakes Along the San Andreas Fault : Evidence from Trees. *Science*, 241:196–199. [49](#)
- JAEGER, J.-J., COURTILLOT, V. et TAPPONNIER, P. (1989). Paleontological view of the ages of the Deccan Traps, the Cretaceous/Tertiary boundary, and the India-Asia collision. *Geology*, 17(4):316–319. [34, 59](#)

BIBLIOGRAPHIE

- JOLIVET, R. (2011). *Déformation intersismique le long de la faille de Haiyuan, Chine : variations spatio-temporelles contraintes par interférométrie SAR*. Thèse de doctorat, Université de Grenoble. [20](#)
- JOLIVET, R., AGRAM, P. S., LIN, N. Y., SIMONS, M., DOIN, M.-P., PELETZER, G. et LI, Z. (2014a). Improving InSAR geodesy using global atmospheric models. *J. Geophys. Res.*, 119(3):2324–2341. [63](#)
- JOLIVET, R., AGRAM, P. S., LIN, N. Y., SIMONS, M., DOIN, M.-P., PELETZER, G. et LI, Z. (2014b). Improving inSAR geodesy using global atmospheric models. *Journal of Geophysical Research : Solid Earth*, 119(3):2324–2341. [127](#), [130](#), [159](#)
- JOLIVET, R., CANDELA, T., LASSERRE, C., RENARD, F., KLINGER, Y. et DOIN, M.-P. (2015a). The Burst-Like Behavior of Aseismic Slip on a Rough Fault : The Creeping Section of the Haiyuan Fault, China. *Seis. Soc. Am.*, 105(1):480–488. [33](#), [64](#), [72](#), [100](#), [113](#), [197](#)
- JOLIVET, R., CATTIN, R., CHAMOT-ROOKE, N., LASSERRE, C. et PELETZER, G. (2008). Thin-plate modeling of interseismic deformation and asymmetry across the Altyn Tagh fault zone. *Geophysical Research Letters*, 35(2). [176](#), [203](#)
- JOLIVET, R., GRANDIN, R., LASSERRE, C., DOIN, M.-P. et PELETZER, G. (2011). Systematic InSAR tropospheric phase delay corrections from global meteorological reanalysis data. *Geophys. Res. Lett.*, 38(17). [23](#), [44](#), [63](#), [69](#), [79](#), [126](#), [127](#), [130](#), [143](#), [148](#), [159](#), [180](#), [184](#), [202](#)
- JOLIVET, R., LASSERRE, C., DOIN, M.-P., GUILLASO, S., PELETZER, G., DAILU, R., SUN, J., SHEN, Z.-K. et XU, X. (2012). Shallow creep on the Haiyuan Fault (Gansu, China) observed by SAR Interferometry. *J. Geophys. Res.*, 117. [23](#), [25](#), [41](#), [58](#), [59](#), [63](#), [64](#), [72](#), [73](#), [76](#), [81](#), [83](#), [113](#)
- JOLIVET, R., LASSERRE, C., DOIN, M.-P., PELETZER, G., AVOUAC, J.-P., JIANBAO, S. et DAILU, R. (2013). Spatio-temporal evolution of aseismic slip along the Haiyuan fault, China : implications for fault frictional properties. *Earth Planet. Sci. Lett.*, pages 377–378. [23](#), [41](#), [64](#), [72](#)
- JOLIVET, R., SIMONS, M., AGRAM, P., DUPUTEL, Z. et SHEN, Z.-K. (2015b). Aseismic slip and seismogenic coupling along the central San Andreas Fault. *Geophys. Res. Lett.*, 42(2):297–306. [68](#)

- KING, G., KLINGER, Y., BOWMAN, D. et TAPPONNIER, P. (2005). Slip-partitioned surface breaks for the Mw 7.8 2001 kokoxili earthquake, China. *Bulletin of the Seismological Society of America*, 95(2):731–738. [31](#)
- KING, G. et NABELEK, J. (1985). Role of fault bends in the initiation and terminaison of earthquakes rupture. *Science*, 228:984–987. [25](#)
- KLINGER, Y. (2010). Relation between continental strike-slip earthquake segmentation and thickness of the crust. *J. Geophys. Res.*, 115(B07306):19. [31](#)
- KLINGER, Y., MICHEL, R. et KING, G. (2006). Evidence for an earthquake barrier model from Mw 7.8 kokoxili (Tibet) earthquake slip-distribution. *Earth and Planetary Science Letters*, 242(3):354–364. [31](#)
- KOHLER, M. D. (1999). Lithospheric deformation beneath the San Gabriel Mountains in the Southern California Transverse Ranges. *J. Geophys. Res.*, 104(B7):15025–15041. [97](#)
- LACHENBRUCH, A. H. et SASS, J. (1980). Heat flow and energetics of the san andreas fault zone. *Journal of Geophysical Research : Solid Earth*, 85(B11):6185–6222. [29](#)
- LASSERRE, C. (2000). *Fonctionnement sismique, cinématique et histoire géologique de la faille de Haiyuan (Chine)*. Thèse de doctorat, Université Paris-Diderot-Paris VII. [76](#)
- LASSERRE, C., BUKCHIN, B., BERNARD, P., TAPPONNIER, P., ER, Y. G., MOSTINSKY, A. et DAILU, R. (2001). Source parameters and tectonic origin of the 1996 june 1 Tianzhu (Mw=5.2) and 1995 July Yongden (Mw=5.6) earthquakes near the Haiyuan fault (Gansu, China). *Geophys. J. Int.*, 144:206–220. [36](#), [39](#), [58](#), [60](#), [76](#), [176](#)
- LASSERRE, C., CAVALIÉ, O., PELTZER, G., SOCQUET, A., DOIN, M., JIANBAO, S., XIWEI, X., SHEN, Z.-K., QINGLIANG, W. et GAUDEMÉR, Y. (2007). Interseismic strain across the Altyn Tagh and Haiyuan faults at the northern edge of the Tibetan plateau, measured by space geodesy. *Geophysical Research Abstracts CDROM*, 9:10102. [41](#), [176](#), [177](#)
- LASSERRE, C., ER, Y. G., TAPPONNIER, P., MERIAUX, A.-S., der WOERD, J. V., DAOYANG, Y., RYERSON, F. J., FINKEL, R. C. et CAFFEE, M. (2002). Fast late pleistocene slip rate on the leng long ling segment of the Haiyuan fault, qinghai, China. *J. Geophys. Res.*, 107. [38](#), [39](#), [59](#)

BIBLIOGRAPHIE

- LASSERRE, C., MOREL, P.-H., GAUDEM ER, Y., TAPPONNIER, P., RYERSON, F., KING, G., MÉTIVIER, F., KASSER, M., KASHGARIAN, M., LIU, B. *et al.* (1999). Postglacial left slip rate and past occurrence of $M \geq 8$ earthquakes on the western Haiyuan fault, Gansu, China. *J. Geophys. Res. (1978–2012)*, 104(B8):17633–17651. [36](#), [38](#), [39](#), [176](#)
- LASSERRE, C., PELETZER, G., CRAMPÉ, F., KLINGER, Y., Van der WOERD, J. et TAPPONNIER, P. (2005). Coseismic deformation of the 2001 $Mw = 7.8$ Kokoxili earthquake in Tibet, measured by synthetic aperture radar interferometry. *J. Geophys. Res. (1978–2012)*, 110(B12). [25](#), [38](#), [59](#), [126](#), [175](#), [196](#)
- LAUKNES, T. R., ZEBKER, H., LARSEN, Y. *et al.* (2011). InSAR deformation time series using an-norm small-baseline approach. *Geoscience and Remote Sensing, IEEE Transactions on*, 49(1):536–546. [129](#)
- LELOUP, P. H., PHAM, T. T., ARMIJO, R. et LACASSIN, R. (1988). Champs de contraintes et cinématique des chevauchements sud-alpins près de la terminaison de la faille judicarienne. *CR Acad. Sci. Paris, Ser. II*, pages 797–804. [28](#), [29](#)
- LELOUP, P. H., RICARD, Y., BATTAGLIA, J. et LACASSIN, R. (1999). Shear heating in continental strike-slip shear zones : model and field examples. *Geophysical Journal International*, 136(1):19–40. [29](#)
- LEPPÄRANTA, M. (1993). A review of analytical models of sea-ice growth. *Atmosphere-Ocean*, 31(1):123–138. [153](#), [167](#)
- LI, Z., FIELDING, E. J., CROSS, P. et MULLER, J.-P. (2006). Interferometric synthetic aperture radar atmospheric correction : GPS topography-dependent turbulence model. *Journal of Geophysical Research : Solid Earth*, 111(B2). [127](#)
- LI, Z., XU, W., FENG, G., HU, J., WANG, C., DING, X. et ZHU, J. (2012). Correcting atmospheric effects on inSAR with MERIS water vapour data and elevation-dependent interpolation model. *Geophysical Journal International*, 189(2):898–910. [127](#)
- LIANG, S., GAN, W., SHEN, C., XIAO, G., LIU, J., CHEN, W., DING, X. et ZHOU, D. i. (2013). Three-dimensional velocity field of present-day crustal motion of the Tibetan Plateau derived from GPS measurements. *J. Geophys. Res.*, 118(10):5722–5732. [60](#), [61](#), [62](#), [186](#), [188](#), [189](#), [190](#), [191](#), [197](#), [198](#), [201](#)

- LIN, Y., JOLIVET, R., SIMONS, M., AGRAM, P., MARTENS, H., LI, Z. et LODI, S. (2015). High interseismic coupling in the eastern makran (Pakistan) subduction zone. *E. Earth Planet. Sci. Lett.*, 420:116–126. [100](#), [197](#)
- LIN, Y.-n. N., SIMONS, M., HETLAND, E. A., MUSE, P. et DiCAPRIO, C. (2010). A multiscale approach to estimating topographically correlated propagation delays in radar interferograms. *Geochemistry, Geophysics, Geosystems*, 11(9). [127](#), [132](#)
- LINDSEY, E. O. et FIALKO, Y. (2013). Geodetic slip rates in the southern San Andreas Fault system : Effects of elastic heterogeneity and fault geometry. *J. Geophys. Res.*, 118:689–697. [52](#)
- LINDSEY, E. O., SAHAKIAN, V. J., FIALKO, Y., BOCK, Y., BARBOT, S. et ROCKWELL, T. K. (2014). Interseismic strain localization in the San Jacinto fault zone. *Pure and Applied Geophysics*, 171(11):2937–2954. [52](#)
- LISOWSKI, M., SAVAGE, J. C. et PRESCOTT, W. (1991). The Velocity Field Along the San Andreas Fault in Central and Southern California. *J. Geophys. Res.*, 96(B5):8369–8389. [95](#)
- LIU, L., SCHAEFER, K., CHEN, A., GUSMEROLI, A., ZEBKER, H. et ZHANG, T. (2015). Remote sensing measurements of thermokarst subsidence using InSAR. *Journal of Geophysical Research : Earth Surface*, 120(9):1935–1948. [147](#), [153](#)
- LIU, L., SCHAEFER, K., GUSMEROLI, A., GROSSE, G., JONES, B. M., ZHANG, T., PARSEKIAN, A. D. et ZEBKER, H. A. (2014a). Seasonal thaw settlement at drained thermokarst lake basins, arctic Alaska. *Atmospheric Chemistry and Physics*, 8(3):815. [147](#), [150](#), [153](#)
- LIU, L., SCHAEFER, K., ZHANG, T. et WAHR, J. (2012). Estimating 1992–2000 average active layer thickness on the Alaskan north slope from remotely sensed surface subsidence. *Journal of Geophysical Research : Earth Surface*, 117(F1). [147](#), [153](#)
- LIU, L., ZHANG, T. et WAHR, J. (2010). InSAR measurements of surface deformation over permafrost on the North Slope of Alaska. *J. Geophys. Res. : Earth Surface*, 115(F3). [147](#), [149](#)
- LIU, Z., LUNDGREN, P. et SHEN, Z. (2014b). Improved imaging of southern California crustal deformation using InSAR and GPS, SCEC annual meeting. *SCEC contribution*, 2038. [52](#), [97](#), [98](#), [111](#)

BIBLIOGRAPHIE

- LIU-ZENG, J., KLINGER, Y., XU, X., LASERRE, C., CHEN, G., CHEN, W., TAPPONIER, P. et ZHANG., B. (2007). Millennial Recurrence of Large Earthquakes on the Haiyuan Fault near Songshan, Gansu Province, China. *Bull. Seis. Soc. Am.*, 97(1B):14–34. [59](#), [60](#)
- LOHMAN, R. B. et SIMONS, M. (2005). Some thoughts on the use of InSAR data to constrain models of surface deformation : Noise structure and data downsampling. *Geochemistry, Geophysics, Geosystems*, 6(1). [68](#), [85](#), [113](#)
- LÓPEZ-QUIROZ, P., DOIN, M.-P., TUPIN, F., BRIOLE, P. et NICOLAS, J.-M. (2009). Time series analysis of Mexico City subsidence constrained by radar interferometry. *J. Applied Geophysics*, 69(1):1–15. [22](#), [24](#), [63](#), [64](#), [81](#), [82](#), [126](#), [149](#), [160](#), [162](#), [165](#), [180](#)
- LOVELESS, J. et MEADE, B. J. (2011). Partitioning of localized and diffuse deformation in the Tibetan Plateau from joint inversions of geologic and geodetic observations. *Earth Planet. Sci. Lett.*, 303(1):11–24. [73](#), [95](#)
- LU, R., XU, X., HE, D., LIU, B., TAN, X. et WANG, X. (2016). Coseismic and blind fault of the 2015 pishan Mw 6.5 earthquake : Implications for the sedimentary-tectonic framework of the western Kunlun mountains, northern Tibetan plateau. *Tectonics*, 35(4):956–964. [178](#), [193](#)
- LUNARDINI, V. J. (1991). *Heat transfer with freezing and thawing*, volume 65. Elsevier. [153](#)
- LUNDGREN, P. E., HETLAND, A., LIU, Z. et FIELDING, E. J. (2009). Southern San Andreas-San Jacinto fault system slip rates estimated from earthquake cycle models constrained by GPS and interferometric synthetic aperture radar observations. *114(B02403):18*. [51](#)
- MANIGHETTI, I., CAMPILLO, M., SAMMIS, C., MAI et KING, P. (2005). Evidence for self-similar, triangular slip distributions on earthquakes : implications for earthquake and fault mechanics. *J. Geophys. Res.*, 110. [25](#)
- MARINKOVIC, P. et LARSEN, Y. (2013). Consequences of long-term ASAR local oscillator frequency decay-an empirical study of 10 years of data Living Planet Symposium 2013 edinburgh. ESA. [111](#)

- MASSONNET, D., ROSSI, M., CARMONA, C., ADRAGNA, F., PELETZER, G., FEIGL, K. et RABAUTE, T. (1993). The displacement field of the Landers earthquake mapped by radar interferometry. *Nature*, 364(6433):138–142. [18](#)
- MASSONNET, D. et SOUYRIS, J. (2008). *Imaging with synthetic aperture radar*, chapitre 1. EPFL Press. [19](#), [21](#)
- MATTAUER, M. (1986). Intracontinental subduction, crust-mantle décollement and crustal-stacking wedge in the Himalayas and other collision belts. *Geological Society, London, Special Publications*, 19(1):37–50. [35](#), [36](#), [176](#)
- MATTE, P., TAPPONNIER, P., ARNAUD, N., BOURJOT, L., AVOUAC, J., VIDAL, P., QING, L., YUSHENG, P. et YI, W. (1996). Tectonics of western Tibet, between the Tarim and the Indus. *Earth and Planetary Science Letters*, 142(3):311–330. [34](#), [40](#), [41](#), [176](#), [178](#), [193](#)
- MCCAFFREY, R. (2002). Crustal block rotations and plate coupling. *Plate boundary zones*, pages 101–122. [67](#)
- MCCAFFREY, R. (2005). Block kinematics of the Pacific-North America plate boundary in the southwestern United States from inversion of GPS, seismological, and geologic data. *J. Geophys. Res. : Solid Earth*, 110(B7). [51](#), [103](#)
- MCKENZIE, D. et MORGAN, W. (1969). Evolution of triple junctions. *Nature*, 224:125. [31](#), [107](#)
- MCQUARRIE, N. et WERNICKE, B. P. (2005). An animated tectonic reconstruction of the southwestern North America since 36 Ma. *Geosphere*, 1(3). [96](#)
- MEADE, B. J. (2007a). Present-day kinematics at the India-Asia collision zone. *Geology*, 35(1):81. [38](#), [73](#), [127](#)
- MEADE, B. J. (2007b). Present-day kinematics at the India-Asia collision zone. *Geology*, 35(1):81–84. [176](#)
- MEADE, B. J. et HAGER, B. H. (2005). Block models of crustal motion in southern California constrained by GPS measurements. *J. Geophys. Res.*, 110(B03403):19. [51](#), [103](#)

BIBLIOGRAPHIE

- MEADE, B. J., KLINGER, Y. et HETLAND, E. A. (2013). Inference of Multiple Earthquake-Cycle Relaxation Timescales from Irregular Geodetic Sampling of Interseismic Deformation. *Bull. seism. Soc. of Am.*, 103(5):2824–2835. [38](#), [76](#)
- MÉRIAUX, A.-S., RYERSON, F., TAPPONNIER, P., Van der WOERD, J., FINKEL, R., XU, X., XU, Z. et CAFFEE, M. (2004). Rapid slip along the central altyn tagh fault : morphochronologic evidence from Cherchen He and Sulamu Tagh. *Journal of Geophysical Research : Solid Earth*, 109(B6). [37](#), [127](#), [175](#), [176](#), [179](#), [203](#)
- MÉRIAUX, A.-S., TAPPONNIER, P., RYERSON, F., XIWEI, X., KING, G., Van der WOERD, J., FINKEL, R., HAIBING, L., CAFFEE, M., ZHIQIN, X. et al. (2005). The aksay segment of the northern altyn tagh fault : Tectonic geomorphology, landscape evolution, and holocene slip rate. *Journal of Geophysical Research : Solid Earth*, 110(B4). [37](#), [175](#), [176](#)
- MÉRIAUX, A.-S., VAN DER WOERD, J., TAPPONNIER, P., RYERSON, F. J., FINKEL, R. C., LASSERRE, C. et XU, X. (2012). The pingding segment of the altyn tagh fault (91e) : Holocene slip-rate determination from cosmogenic radionuclide dating of offset fluvial terraces. *J. Geophys. Res. : Solid Earth (1978–2012)*, 117(B9). [127](#), [176](#)
- MÉTIVIER, F., ER, Y. G. et MEYER, P. T. B. (2007). Northeastward growth of the Tibet plateau deduced from balanced reconstruction of two depositional areas : The Qaidam and Hexi Corridor basins, China. *Tectonics*, pages 1–20. [59](#)
- METROPOLIS, N., ROSENBLUTH, A. W., ROSENBLUTH, M. N., TELLER, A. H. et TELLER, E. (1953). Equation of state calculations by fast computing machines. *J. chemical phy.*, 21(6):1087–1092. [34](#), [68](#)
- MEYER, B., TAPPONNIER, P., BOURJOT, L., METIVIER, F., ER, Y. G., PELTZER, G., SHUNMIN, G. et ZHITAI, C. (1998). Crustal thickening in Gausu-Qinghai, lithospheric mantle subduction, and oblique, strike-slip controlled growth of the Tibet plateau. *Geophy. J. Int.*, 135. [31](#), [32](#), [34](#), [35](#), [39](#), [59](#), [60](#), [75](#), [176](#)
- MILLER, M. M., MELBOURNE, T., JOHNSON, D. J. et SUMNER, W. Q. (2002). Periodic slow earthquakes from the Cascadia subduction zone. *Science*, 295(5564):2423–2423. [25](#)
- MINSON, S., SIMONS, M. et BECK, J. (2013). Bayesian inversion for finite fault earthquake source models theory and algorithm. *Geophys. J Int.*, page ggt180. [33](#), [67](#), [100](#), [197](#)

- MOLNAR, P. et TAPPONNIER, P. (1975a). Cenozoic tectonics of Asia : effects of a continental collision. *Science*, 189:419–426. [59](#)
- MOLNAR, P. et TAPPONNIER, P. (1975b). Cenozoic tectonics of asia : effects of a continental collision. *Science*, 189(4201):419–426. [34](#), [175](#)
- MOUNT, V. S. et SUPPE, J. (1987). State of stress near the San Andreas Fault : Implications for wrench tectonics. *Geology*, 15(12):1143–1146. [29](#), [50](#), [95](#)
- MOUNT, V. S. et SUPPE, J. (1992). Present-Day Stress Orientations Adjacent to Active Strike-Slip Faults : California and Sumatra. *J. Geophys. Res.*, 97:11995–12013. [95](#), [96](#)
- NAMSON, J. S. et DAVIS, T. L. (1988). Seismically active fold and thrust belt in the san joaquin valley, central California. *Geol. Soc. of Am. Bull.*, 100:257–273. [96](#)
- NELSON, F., SHIKLOMANOV, N., MUELLER, G., HINKEL, K., WALKER, D. et BOCKHEIM, J. (1997). Estimating active-layer thickness over a large region : Kuparuk river basin, Alaska, usa. *Arctic and Alpine Research*, pages 367–378. [147](#)
- NICHOLSON, C., SORLIEN, C. C., ATWATER, T., CROWELL, J. C. et LUYENDYK, B. P. (1994). Microplate capture, rotation of the western Transverse Ranges, and initiation of the San Andreas transform as a low-angle fault system. *Geology*, 22(6):491–495. [96](#)
- OELKE, C. et ZHANG, T. (2007). Modeling the active-layer depth over the Tibetan Plateau. *Arctic, Antarctic, and Alpine Research*, 39(4):714–722. [146](#)
- OKADA, Y. (1985). Surface deformation to shear and tensile faults in a half-space. *Bull. Seismo. Soc. Am.*, 75:1135–1154. [26](#)
- OSKIN, M., SIEH, K., ROCKWELL, T., MILLER, G., GUPTILL, P., CURTIS, M., MCARDLE, S. et ELLIOT, P. (2000). Active parasitic folds on the Elysian Park anticline : Implications for seismic hazard in central Los Angeles, California. *Geol. Soc. Am. Bull.*, 112(5):693–707. [104](#)
- OUTCALT, S. I., NELSON, F. E. et HINKEL, K. M. (1990). The zero-curtain effect : Heat and mass transfer across an isothermal region in freezing soil. *Water Resources Research*, 26(7):1509–1516. [146](#)
- PAN, G.-t., DING, J., YAO, D.-s. et WANG, L.-q. (2004). Geological map of the Qinghai-Xizang (Tibet) Plateau and adjacent areas. *Chengdu Cartographic Publishing House*. [150](#), [151](#), [167](#), [171](#)

BIBLIOGRAPHIE

- PASTICK, N. J., JORGENSEN, M. T., WYLIE, B. K., MINSLEY, B. J., JI, L., WALVOORD, M. A., SMITH, B. D., ABRAHAM, J. D. et ROSE, J. R. (2013). Extending airborne electromagnetic surveys for regional active layer and permafrost mapping with remote sensing and ancillary data, yukon flats ecoregion, central Alaska. *Permafrost and Periglacial Processes*, 24(3):184–199. [147](#)
- PATHIER, E., FRUNEAU, B., DEFFONTAINES, B., ANGELIER, J., CHANG, C.-P., YU, S.-B. et LEE, C.-T. (2003). Coseismic displacements of the footwall of the chelungpu fault caused by the 1999, Taiwan, chi-chi earthquake from inSAR and GPS data. *Earth and Planetary Science Letters*, 212(1):73–88. [126](#)
- PATIL, A., HUARD, D. et FONNESBECK, C. J. (2010). PyMC : Bayesian stochastic modelling in Python. *J. of Statistical Software*, 35(4):1. [34](#), [68](#), [102](#)
- PEDERSEN, R. et SIGMUNDSSON, F. (2006). Temporal development of the 1999 intrusive episode in the eyjafjallajökull volcano, iceland, derived from InSAR images. *Bulletin of Volcanology*, 68(4):377–393. [126](#)
- PELTZER, G., CRAMPÉ, F. et KING, G. (1999). Evidence of nonlinear elasticity of the crust from the mw7. 6 manyi (tibet) earthquake. *Science*, 286(5438):272–276. [177](#), [196](#)
- PELTZER, G. et ROSEN, P. (1995). Surface displacement of the 17 may 1993 eureka valley, California, earthquake observed by SAR interferometry. *Science*, 268(5215):1333. [126](#)
- PELTZER, G. et SAUCIER, F. (1996). Present-day kinematics of asia derived from geologic fault rates. *J. Geophys. Res. : Solid Earth (1978–2012)*, 101(B12):27943–27956. [38](#), [127](#)
- PELTZER, G., SOCQUET, A., LASSERRE, C., MÉRIAUX, A., TAPPONNIER, P. et RYERSON, R. (2006). InSAR observations of interseimsic strain along the central Altyn Tagh fault consistent with holocene slip-rate. *In AGU Fall Meeting Abstracts*, volume 1, page 02. [41](#), [177](#)
- PELTZER, G. et TAPPONNIER, P. (1988). Formation and evolution of strike-slip faults, rifts, and basins during the india-asia collision : An experimental approach. *Journal of Geophysical Research : Solid Earth*, 93(B12):15085–15117. [34](#), [176](#)
- PELTZER, G., TAPPONNIER, P. et ARMIJO, R. (1989). Magnitude of late quaternary left-lateral displacements along the north edge of Tibet. *Science*, 246(4935):1285–1289. [40](#), [127](#), [176](#)

- PIKSER, J. E., FORSYTH, D. W. et HIRTH, G. (2012). Along-strike translation of a fossil slab. *E. Earth Planet. Sci. Lett.*, 331:315–321. [49](#), [106](#)
- PINEL, V., HOOPER, A., la CRUZ-REYNA, D., REYES-DAVILA, G., DOIN, M. *et al.* (2008). Study of the deformation field of two active mexican stratovolcanoes (popocatepetl and colima volcano) by time series of InSAR data. [149](#), [160](#)
- PINEL-PUYSSEGUR, B., MICHEL, R. et AVOUAC, J.-P. (2012). Multi-Link InSAR Time Series : Enhancement of a Wrapped Interferometric Database. *IEEE J. Selected Topics in Applied Earth Observations and Remote Sensing*, 5(3):784–794. [63](#), [80](#), [162](#), [165](#), [180](#), [181](#)
- PLESCH, A., SHAW, J. H. et AL. (2007). Community Fault Model (CFM) for Southern California. *Bull. Seismol. Soc. Am.*, 97(6). [50](#), [95](#), [105](#)
- QIDONG, D., SHEFA, C., FANGNIN, S., SHILONG, Z., YIPENG, W., WEIQI, Z., DECHENG, J., BURCHFIELD, B., MOLNAR, P., ROYDEN, L. *et al.* (1986). Variations in the geometry and amount of slip on the Haiyuan (Nanxihaushan) fault zone, China and the surface rupture of the 1920 Haiyuan earthquake. *Earthquake Source Mechanics*, pages 169–182. [38](#)
- QINGBAI, W., YONGZHI, L., JIANMING, Z. et CHANGEOGRAPHY J. INT.ANG, T. (2002). A review of recent frozen soil engineering in permafrost regions along Qinghai-Tibet Highway, China. *Permafrost Periglacial Process.*, 13(3):199–205. [147](#)
- QIU, Q., HILL, E. M., BARBOT, S., HUBBARD, J., FENG, W., LINDSEY, E. O., FENG, L., DAI, K., SAMSONOV, S. V. et TAPPONNIER, P. (2016). The mechanism of partial rupture of a locked megathrust : The role of fault morphology. *Geology*, 44(10):875–878. [106](#)
- REPLUMAZ, A. et TAPPONNIER, P. (2003). Reconstruction of the deformed collision zone between india and Asia by backward motion of lithospheric blocks. *Journal of Geophysical Research : Solid Earth*, 108(B6). [179](#)
- RISEBOROUGH, D., SHIKLOMANOV, N., ETZELMÜLLER, B., GRUBER, S. et MAR-CHENKO, S. (2008). Recent advances in permafrost modelling. *Permafrost Periglacial Process.*, 19(2):137–156. [146](#), [150](#), [153](#)

BIBLIOGRAPHIE

- ROSEN, P. A., HENSLEY, S., PELETZER, G. et SIMONS, M. (2004). Updated repeat orbit interferometry package released. *Eos, Transactions American Geophysical Union*, 85(5):47–47. [23](#), [63](#), [80](#), [129](#), [148](#), [163](#), [179](#)
- ROUSSET, B., JOLIVET, R., SIMONS, M., LASSEUR, C., RIEL, B., MILILLO, P., ÇAKIR, Z. et RENARD, F. (2016). An aseismic slip transient on the North Anatolian Fault. *Geophysical Research Letters*, 43(7):3254–3262. [25](#), [126](#)
- ROYDEN, L. H., BURCHFIELD, B. C., KING, R. W., WANG, E., CHEN, Z., SHEN, F. et LIU, Y. (1997). Surface deformation and lower crustal flow in eastern Tibet. *science*, 276(5313):788–790. [36](#), [176](#)
- RUBIN, C. M., LINDVALL, S. C. et ROCKWELL, T. K. (1998). Evidence for Large Earthquakes in Metropolitan Los Angeles. *Science*, 281:398–402. [95](#)
- RYDER, I., PARSONS, B., WRIGHT, T. J. et FUNNING, G. J. (2007). Post-seismic motion following the 1997 manyi (Tibet) earthquake : InSAR observations and modelling. *Geophysical Journal International*, 169(3):1009–1027. [36](#), [176](#), [177](#)
- SALYARDS, S. L., SIEH, K. E. et KIRSCHVINK, J. L. (1992). Paleomagnetic measurement of nonbrittle coseismic deformation across the San Andreas Fault at Pallett Creek. *J. Geophys. Res. B*, 97(B9):12457–12470. [51](#), [103](#)
- SAMSONOV, S. (2010). Topographic correction for alos palSAR interferometry. *Geoscience and Remote Sensing, IEEE Transactions on*, 48(7):3020–3027. [111](#)
- SANDWELL, D. T. et SMITH, W. H. (2009). Global marine gravity from retracked geosat and ers-1 altimetry : Ridge segmentation versus spreading rate. *Journal of Geophysical Research : Solid Earth*, 114(B1). [51](#)
- SANSOSTI, E., CASU, F., MANZO, M. et LANARI, R. (2010). Space-borne radar interferometry techniques for the generation of deformation time series : An advanced tool for earth's surface displacement analysis. *Geophys. Res. Lett.*, 37(20). [111](#)
- SAVAGE, J. et LISOWSKI, M. (1995). Interseismic deformation along the San Andreas Fault in southern California. *J. Geophys. Res. : Solid Earth*, 100(B7):12703–12717. [51](#), [103](#)
- SAVAGE, J. C. (1990). Equivalent strike-slip earthquakes cycles in half-space and lithosphere-asthenosphere earth models. *J. Geophys. Res.*, 95(B4):4873–4879. [99](#)

- SCHAEFER, K., LIU, L., PARSEKIAN, A., JAFAROV, E., CHEN, A., ZHANG, T., GUSMEROLI, A., PANDA, S., ZEBKER, H. A. et SCHAEFER, T. (2015). Remotely sensed active layer thickness (resalt) at barrow, Alaska using interferometric synthetic aperture radar. *Remote Sensing*, 7(4):3735–3759. [147](#), [150](#), [153](#)
- SEGALL, P. (2010). *Earthquake and volcano deformation*. Princeton University Press, Princeton, NJ. [26](#), [27](#), [99](#), [112](#)
- SHAW, J. et SUPPE, J. (1996). Earthquakes hazards of active blind-thrust faults under the central Los Angeles basin, California. *J. Geophys. Res.*, 101:8623–8642. [96](#), [104](#)
- SHAW, J. H., PLESCH, A., DOLAN, J. F., PRATT, T. L. et FIORE, P. (2002). Puente Hills blind-thrust system, Los Angeles, California. *BSSA*, 92(8):2946–2960. [50](#), [104](#)
- SHAW, J. H. et SHEARER, P. M. (1999). An elusive blind-thrust fault beneath metropolitan Los Angeles. *Science*, 283(5407):1516–1518. [96](#)
- SHEN, Z.-K., JACKSON, D. D. et GE, B. X. (1996). Crustal deformation across and beyond the Los Angeles basin from geodetic measurements. *J. Geophys. Res.*, 101: 27957–27980. [51](#), [103](#)
- SHEN, Z.-K., SUN, J., ZHANG, P., WAN, Y., WANG, M., BÜRGMANN, R., ZENG, Y., GAN, W., LIAO, H. et WANG, Q. (2009). Slip maxima at fault junctions and rupturing of barriers during the 2008 wenchuan earthquake. *Nature Geoscience*, 2(10):718–724. [38](#), [59](#), [175](#)
- SHIRZAEI, M. et BÜRGMANN, R. (2012). Topography correlated atmospheric delay correction in radar interferometry using wavelet transforms. *Geophysical Research Letters*, 39(1). [127](#), [132](#)
- SHORT, N., BRISCO, B., COUTURE, N., POLLARD, W., MURNAGHAN, K. et BUDKEWITSCH, P. (2011). A comparison of TerraSAR-X, RADARSAT-2 and ALOS-PALSAR interferometry for monitoring permafrost environments, case study from herschel island, canada. *Remote Sensing of Environment*, 115(12):3491–3506. [147](#)
- SIEH, K. (1978). Slip along the San Andreas Fault associated with the great 1857 earthquake. *Bull. Seism. Soc. Am.*, 68:1421–1428. [49](#), [95](#)
- SIEH, K. E. et JAHNS, R. H. (1984). Holocene activity of the San Andreas Fault at wallace creek, California. *Geol. Soc. Am. Bull.*, 95(8):883–896. [103](#)

BIBLIOGRAPHIE

- SIMONS, M., FIALKO, Y. et RIVERA, L. (2002). Coseismic deformation from the 1999 Mw 7.1 hector mine, California, earthquake as inferred from InSAR and GPS observations. *Bulletin of the Seismological Society of America*, 92(4):1390–1402. [27](#)
- SMITH, B. R. et SANDWELL, D. T. (2006). A model of the earthquake cycle along the San Andreas Fault System for the past 1000 years. 111(B01405):20. [51](#)
- SMITH, M. et RISEBOROUGH, D. (1996). Permafrost monitoring and detection of climate change. *Permafrost Periglacial Process.*, 7(4):301–309. [147](#), [153](#)
- SOCQUET, A., VIGNY, C., CHAMOT-ROOKE, N., SIMONS, W., RANGIN, C. et AMBROSIUS, B. (2006). India and Sunda plates motion and deformation along their boundary in Myanmar determined by GPS. *J. Geophys. Res. : Solid Earth (1978–2012)*, 111(B5). [62](#)
- STEFAN, J. (1891). Über die theorie der eisbildung, insbesondere über die eisbildung im polarmeere. *Annalen der Physik*, 278(2):269–286. [149](#), [167](#)
- STROZZI, T. et WEGMULLER, U. (1999). Land subsidence in mexico city mapped by ERS differential sar interferometry. In *Geoscience and Remote Sensing Symposium, 1999. IGARSS'99 Proceedings. IEEE 1999 International*, volume 4, pages 1940–1942. IEEE. [149](#), [160](#)
- SUDHAUS, H. et JÓNSSON, S. (2011). Source model for the 1997 zirkuh earthquake (Mw= 7.2) in iran derived from jers and ers inSAR observations. *Geophysical Journal International*, 185(2):676–692. [27](#), [33](#)
- SUDHAUS, H. et SIGURJÓN, J. (2009). Improved source modelling through combined use of insar and gps under consideration of correlated data errors : application to the june 2000 kleifarvatn earthquake, iceland. *Geophysical Journal International*, 176(2):389–404. [68](#), [86](#), [113](#)
- SUN, J., JOHNSON, K. M., CAO, Z., SHEN, Z., BÜRGMANN, R. et XU, X. (2011). Mechanical constraints on inversion of coseismic geodetic data for fault slip and geometry : Example from InSAR observation of the 6 october 2008 Mw 6.3 dangxiong-yangyi (tibet) earthquake. *Journal of Geophysical Research : Solid Earth*, 116(B1). [27](#)
- SUN, J., SHEN, Z.-K., LI, T. et CHEN, J. (2016). Thrust faulting and 3d ground deformation of the 3 july 2015 Mw 6.4 pishan, China earthquake from sentinel-1a radar interferometry. *Tectonophysics*. [178](#), [193](#)

- SUPPE, J. (1983). Geometry and kinematics of fault-bend folding. *Am. J. Science*, 283:684–721. [31](#), [32](#), [75](#), [99](#), [105](#), [109](#)
- TAPE, C., PLESCH, A., SHAW, J. H. et GILBERT, H. (2012). Estimating a Continuous Moho Surface for the California Unified Velocity Model. *Seism. Res. Lett.*, 83. [96](#)
- TAPPONNIER, P., MEYER, B., AVOUAC, J. P., PELETZER, G., GAUDEM ER, Y., SHUNMIN, G., HONGFA, X., KELUN, Y., ZHITAI, C., SHUAHUA, C. *et al.* (1990). Active thrusting and folding in the Qilian Shan, and decoupling between upper crust and mantle in northeastern Tibet. *Earth Planet. Sci. Lett.*, 97(3):382–403. [35](#), [39](#), [60](#)
- TAPPONNIER, P. et MOLNAR, P. (1977). Active Faulting and Tectonics in China. *J. Geophys. Res.*, 82(20):2905–2927. [34](#), [59](#), [175](#)
- TAPPONNIER, P., ZHIQIN, X., ROGER, F., MEYER, B., ARNAUD, N., WITTLINGER, G. et JINGSUI, Y. (2001). Oblique stepwise rise and growth of the Tibet plateau. *Science*, 294(5547):1671–1677. [34](#), [35](#), [36](#), [59](#), [60](#), [73](#), [75](#), [127](#), [176](#)
- TARANTOLA, A. et VALETTE, B. (1982). Generalized nonlinear inverse problems solved using the least squares criterion. *Reviews of Geophysics*, 20(2):219–232. [33](#)
- TAYLOR, M. et PELETZER, G. (2006). Current slip rates on conjugate strike-slip faults in central Tibet using synthetic aperture radar interferometry. *Journal of Geophysical Research : Solid Earth*, 111(B12). [41](#), [46](#), [146](#)
- TESHEBAEVA, K., SUDHAUS, H., ECHTLER, H., SCHURR, B. et ROESSNER, S. (2014). Strain partitioning at the eastern pamir-alai revealed through sar data analysis of the 2008 nura earthquake. *Geophysical Journal International*, 198(2):760–774. [31](#)
- TEYSSIER, C. et TIKOFF, B. (1998). Strike-slip partitioned transpression of the San Andreas Fault system : a lithospheric-scale approach. In HOLDSWORTH, R. E., STRACHAN, R. A. et DEWEY, J. F., éditeurs : *Continental Transpressional and Transtensional Tectonics*, pages 143–158. Geological Society, London. [95](#), [96](#), [106](#)
- THATCHER, W. (2007). Microplate model for the present-day deformation of Tibet. *J. Geophys. Res.*, 112(B1):B01401. [73](#), [127](#)
- THOMPSON, S. C., WELDON, R. J., RUBIN, C. M., ABDRAKHMATOV, K., MOLNAR, P. et BERGER, G. W. (2002). Late Quaternary slip rates across the central Tien Shan, Kyrgyzstan, central Asia. *J. Geophys. Res. : Solid Earth (1978–2012)*, 107(B9):ETG–7. [75](#)

BIBLIOGRAPHIE

- THOMPSON, T. B., PLESCH, A., SHAW, J. H. et MEADE, B. J. (2015). Rapid slip-deficit rates at the eastern margin of the Tibetan Plateau prior to the 2008 Mw 7.9 Wenchuan earthquake. *Geophys. Res. Lett.*, 42(6):1677–1684. [76](#)
- TONG, X., SANDWELL, D. T. et SMITH-KONTER, B. (2013). High-resolution interseismic velocity data along the San Andreas Fault from GPS and InSAR. *J. Geophys. Res.*, 118(1-21):21. [95](#)
- TONG, X., SMITH-KONTER, B. et SANDWELL, D. T. (2014). Is there a discrepancy between geological and geodetic slip rates along the San Andreas Fault system ? *J. Geophys. Res. : Solid Earth*, 119(3):2518–2538. [51](#), [52](#), [103](#), [104](#)
- TOPPOZADA, T. R., BRANUM, D. M., REICHLE, M. S. et HALLSTROM, C. L. (2002). San Andreas Fault Zone, California : $M \geq 5.5$ Earthquake History. *Bull. Seism. Soc. Am.*, 92(7):2555–2601. [95](#)
- TRUBIENKO, O., FLEITOUT, L., GARAUD, J.-D. et VIGNY, C. (2013). Interpretation of interseismic deformations and the seismic cycle associated with large subduction earthquakes. *Tectonophysics*, 589:126–141. [76](#)
- TYMOFYEYEVA, E. et FIALKO, Y. (2015). Mitigation of atmospheric phase delays in InSAR data, with application to the eastern California shear zone. *Journal of Geophysical Research : Solid Earth*, 120(8):5952–5963. [127](#)
- VALLAGE, A., KLINGER, Y., GRANDIN, R., BHAT, H. et PIERROT-DESEILLIGNY, M. (2015). Inelastic surface deformation during the 2013 Mw 7.7 Balochistan, Pakistan, earthquake. *Geology*, 43(12):1079–1082. [31](#)
- VAN DER WOERD, J., RYERSON, F., TAPPONNIER, P., GAUDEM ER, Y., FINKEL, R., MÉRIAUX, A.-S., CAFFEE, M., GUOGUANG, Z. et QUNLU, H. (1998). Holocene left-slip rate determined by cosmogenic surface dating on the xidatan segment of the Kunlun fault (qinghai, China). *Geology*, 26(8):695–698. [37](#)
- WALLACE, K., YIN, G. et BILHAM, R. (2004). Inescapable slow slip on the Altyn Tagh fault. *Geophysical Research Letters*, 31(9). [176](#)
- WALLS, C., ROCKWELL, T., MUELLER, K., BOCK, Y., WILLIAMS, S., PFANNER, J., DOLAN, J. et FANG, P. (1998). Escape tectonics in the Los Angeles metropolitan region and implications for seismic risk. *Nature*, 394:356–360. [95](#), [103](#), [104](#)

- WANG, H., WRIGHT, T. et BIGGS, J. (2009). Interseismic slip rate of the northwestern xianshuihe fault from InSAR data. *Geophys. Res. Lett.*, 36(3). [41](#)
- WANG, H., WRIGHT, T. J., YU, Y., LIN, H., JIANG, L., LI, C. et QIU, G. (2012). InSAR reveals coastal subsidence in the pearl river delta, China. *Geophysical Journal International*, 191(3):1119–1128. [38](#), [41](#), [42](#), [45](#), [126](#), [174](#), [177](#)
- WANG, Q., ZHANG, P.-Z., FREYmueller, J. T., BILHAM, R., LARSON, K. M., LAI, X., YOU, X., NIU, Z., WU, J., LI, Y. et al. (2001). Present-day crustal deformation in China constrained by global positioning system measurements. *Science*, 294(5542): 574–577. [34](#), [59](#), [203](#)
- WANG, Y., FORSYTH, D. W., RAU, C. J., CARRIERO, N., SCHMANDT, B., GAHERTY, J. B. et SAVAGE, B. (2013). Fossil slabs attached to unsubducted fragments of the farallon plate. *Proceedings of the National Academy of Sciences*, 110(14):5342–5346. [49](#), [106](#)
- WEBB, T. et KANAMORI, H. (1985). Earthquake focal mechanisms in the eastern Transverse Ranges and San Emigdio Mountains, southern California, and evidence for a regional decollement. *Bull. Seism. Soc. Am.*, 75:735–757. [97](#)
- WEBLEY, P., BINGLEY, R., DODSON, A., WADGE, G., WAUGH, S. et JAMES, I. (2002). Atmospheric water vapour correction to inSAR surface motion measurements on mountains : results from a dense GPS network on mount Etna. *Physics and Chemistry of the Earth, Parts A/B/C*, 27(4):363–370. [127](#)
- WELDON, R. J. et SIEH, K. E. (1985). Holocene rate of slip and tentative recurrence interval for large earthquakes on the San Andreas Fault, cajon pass, southern California. *Geol. Soc. Am. Bull.*, 96(6):793–812. [50](#), [103](#)
- WEN, Y., LI, Z., XU, C., RYDER, I. et BÜRGMANN, R. (2012). Postseismic motion after the 2001 Mw 7.8 kokoxili earthquake in Tibet observed by InSAR time series. *Journal of Geophysical Research : Solid Earth*, 117(B8). [36](#), [176](#)
- WESNOUSKY, S. G. (2006). Predicting the endpoints of earthquake ruptures. *Nature*, 444(7117):358–360. [25](#)
- WESSEL, P. et SMITH, W. H. (1991). Free software helps map and display data. *Eos, Trans. AGU*, 72(41):441–446. [119](#), [200](#)

BIBLIOGRAPHIE

- WHIPPLE, K. X., SHIRZAEI, M., HODGES, K. V. et ARROWSMITH, J. R. (2016). Active shortening within the himalayan orogenic wedge implied by the 2015 gorkha earthquake. *Nature Geoscience*. [97](#)
- WILCOX, R. E., HARDING, T. t. et SEELY, D. (1973). Basic wrench tectonics. *Aapg Bulletin*, 57(1):74–96. [50](#), [97](#)
- WILLIAMS, S., BOCK, Y. et FANG, P. (1998). Integrated satellite interferometry : Tropospheric noise, GPS estimates and implications for interferometric synthetic aperture radar products. *Journal of geophysical research*, 103(B11):27051–27067. [127](#)
- WITTLINGER, G., TAPPONNIER, P., POUPINET, G., MEI, J., DANIAN, S., HERQUEL, G. et MASSON, F. (1998). Tomographic evidence for localized lithospheric shear along the altyn tagh fault. *Science*, 282(5386):74–76. [40](#), [178](#), [193](#)
- WRIGHT, T., PARSONS, B. et FIELDING, E. (2001). Measurement of interseismic strain accumulation across the North Anatolian Fault by satellite radar interferometry. *Geophys. Res. Lett.*, 28(10):2117–2120. [174](#)
- WRIGHT, T. J., PARSONS, B., ENGLAND, P. C. et FIELDING, E. J. (2004). InSAR observations of low slip rates on the major faults of western Tibet. *Science*, 305(5681):236–239. [41](#), [127](#), [177](#)
- WU, Q., ZHANG, T. et LIU, Y. (2010). Permafrost temperatures and thickness on the Qinghai-Tibet Plateau. *Glob. Planet. Chang.*, 72(1):32–38. [147](#)
- XU, X., WANG, F., ZHENG, R., CHEN, W., MA, W., YU, G., CHEN, G., TAPPONNIER, P., VAN DER WOERD, J., MÉRIAUX, A. et al. (2005). Late quaternary sinistral slip rate along the altyn tagh fault and its structural transformation model. *Science in China Series D : Earth Sciences*, 48(3):384–397. [176](#)
- YE, Z., GAO, R., LI, Q., ZHANG, H., SHEN, X., LIU, X. et GONG, C. (2015). Seismic evidence for the North China plate underthrusting beneath northeastern Tibet and its implications for plateau growth. *Earth Planet. Sci. Lett.*, 426:109–117. [39](#), [60](#)
- YULE, D. et SIEH, K. (2003). Complexities of the San Andreas Fault near San Gorgonio Pass : Implications for large earthquakes. *J. Geophys. Res.*, 108:3–23. [96](#)
- YUN, S.-H., ZEBKER, H., SEGALL, P., HOOPER, A. et POLAND, M. (2007). Interferogram formation in the presence of complex and large deformation. *Geophysical Research Letters*, 34(12). [149](#), [160](#)

- ZEBKER, H. A. et ROSEN, P. (1994). On the derivation of coseismic displacement fields using differential radar interferometry : The Landers earthquake. In *Geoscience and Remote Sensing Symposium, 1994. IGARSS'94. Surface and Atmospheric Remote Sensing : Technologies, Data Analysis and Interpretation.*, International, volume 1, pages 286–288. IEEE. [20](#)
- ZHANG, L., DING, X., LU, Z., JUNG, H.-S., HU, J. et FENG, G. (2014). A novel multitemporal InSAR model for joint estimation of deformation rates and orbital errors. *Geoscience and Remote Sensing, IEEE Transactions on*, 52(6):3529–3540. [129](#), [148](#), [180](#)
- ZHANG, P.-Z., SHEN, Z., WANG, M., GAN, W., BÜRGMANN, R., MOLNAR, P., WANG, Q., NIU, Z., SUN, J., WU, J. et al. (2004). Continuous deformation of the Tibetan Plateau from global positioning system data. *Geology*, 32(9):809–812. [176](#), [203](#)
- ZORIGT, M., KWADIJK, J., VAN BEEK, E. et KENNER, S. (2016). Estimating thawing depths and mean annual ground temperatures in the Khuvsgul region of Mongolia. *Environmental Earth Sciences*, 75(10):1–10. [147](#)

